Alma Mater Studiorum - Università di Bologna

DOTTORATO DI RICERCA IN
CHIMICA

Ciclo XXX

Settore Concorsuale: 03/A2

Settore Scientifico Disciplinare: CHIM/02

MODELING PHOTOINDUCED EVENTS
AND NON-LINEAR SPECTROSCOPY IN
COMPLEX MULTICHROMOPHORIC SYSTEMS

Presentata da: Francesco Segatta

Coordinatore Dottorato
Prof. Aldo Roda

Supervisore
Prof. Marco Garavelli
Co-Supervisore
Dr. Simone Taioli

Esame Finale anno 2018

Contents

Abstract

What are the processes activated by light when it impinges on a sample of light-sensitive molecules in mutual interaction? How can this information be accessed from both the experimental and theoretical sides? This work is aimed at answering at these specific questions. In order to accomplish this goal, we use state-of-the-art computational methods and develop novel theoretical approaches for investigating static and dynamical properties of networks of interacting molecular organic chromophores, and compute their spectroscopy. We focus in particular on the simulation of non-linear time-resolved techniques, such as the pump-probe and the two dimensional electronic spectroscopy. These approaches have been proven to be fundamental tools to track the system photoinduced dynamics with extremely high time and spectral resolution and disentangle contributions from different system components. We conclude that the synergic combination of "independent" results from accurate quantum chemical calculations and detailed spectroscopic experiments is the way to reach a reliable map of the activated energy transfer processes and to gain new physical insights into the system properties.

Introduction

The interaction between light and matter is a phenomenon of upmost importance for our life, or even for the existence of life on earth itself. Photosynthesis provides us food and oxygen by means of specialized molecular complexes, using light as the energy source. We can see the world around us because our eyes contain the retinal molecule, a photoreceptor that reacts in the presence of light. Vitamin D, essential for normal bone and teeth development, is formed in the skin of animals through exposure of the chemical 7-dehydrocholesterol to sunlight. Light is absorbed, in the above examples, by specific molecules or groups of molecules, that harvest it temporarily as an electronic excitation, and utilize it to perform specific reactions, and achieve specific functions. The branches of science that study these and similar processes, initiated by the absorption of light, are called *photophysics* and *photochemistry*.
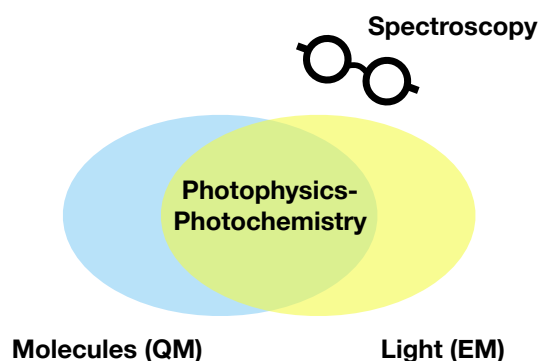
The study of photochemical reactions is experimentally achieved by means of spectroscopic techniques: ground-state absorption allows, e.g., to study the energetics of molecular transitions, and their probability to occur. Non-linear time resolved

spectroscopy (such as pump-probe and two dimensional electronic spectroscopy) utilizes femtosecond control over the multiple pulses that are used to probe the system during its ultrafast evolution. A high density of information is obtained, but to disentangle all measured features and reach a detailed and reliable map of the energy transfer network between the system components is still a challenge. It is therefore often necessary to support experimental measurements with theoretical models.

From the theoretical point of view, the understanding of photophysical and photochemical processes requires: (a) an accurate description of the involved molecular systems (governed by the laws of quantum mechanics), and (b) a way to account for their response to light. The first problem is usually tackled using the computational tools of quantum chemistry, i.e., by solving the Schrödinger equation at some level of approximation, delivering the manifold of system states. The complexity of real systems makes it often necessary to decompose them into computationally feasible parts, which can be later combined to reconstruct the properties of the whole aggregate (Frenkel Exciton model). Moreover, the description of molecular vibrations and environment fluctuations is a key ingredient to properly access system behavior and the energy transfer dynamics between the system components. Light-matter interaction is usually treated via perturbation theory, provided that the external electromagnetic field used to probe the system is weaker than the internal fields that maintain the electrons firmly attached to the molecules. A coherent theoretical framework to study linear and non-linear optical spectroscopy was firstly introduced by Prof. Shaul Mukamel a few decades ago. The so-called *response function* is the key ingredient here, as it incorporates all the information of the molecular response to external light-induced perturbations.

My three years Phd activity has focused on two distinct, while intertwining topics: on the one hand, to reach an accurate and reliable description of the excited state properties of the photoactive molecular system[1]; on the other, to use this information to compute linear and non-linear spectroscopy, eventually comparing the simulations with available experimental measurements, to gain new physical and chemical insight on the properties of the systems under investigation.

The thesis is organized as follows:

Part I is focused on the description of quantum mechanical properties of systems of interacting molecules. The Frenkel Exciton model is introduced, as an effective

---

[1]The terms "molecule", "photoactive molecule" and "chromophore" are interchangeable in this Thesis.

theoretical tool to capture the essential physics of a molecular aggregate, and its connection with the microscopic molecular Hamiltonian is outlined. The role of molecular vibrations and environmental fluctuations is reviewed, and some of the most popular theories for describing intermolecular energy transfer processes are presented.

Part II presents the ample body of experimental and theoretical spectroscopic techniques that have been develop to study molecular systems and access their dynamics. Particular attention is reserved to the so-called two dimensional electronic spectroscopy (2DES), which is one of the most advanced techniques available to disentangle overlapping signals and directly follow energy transfer processes. A novel and very accurate theoretical approach to simulate system dynamics and associated non-linear spectroscopy, developed in collaboration with the research group of Prof. David F. Coker (Boston University, Boston, MA, USA), is eventually outlined.

Part III presents the results obtained by combining accurate molecular computations with the simulation of their spectroscopy. Three examples are reported, and for each of them we compare experimental measurements of non-linear spectroscopy with the corresponding theoretical predictions. In the first example we present a quantum chemistry study of the Light Harvesting complex 2 of the photosynthetic bacterium *rhodopseudomonas acidophila* and the simulation of its 2DES, providing new insight into the comprehension of the measured spectral features. In the second example, by combining experimental investigation and theoretical modeling, we reveal the signatures of the energy transfer process in *xanthorhodopin* (a light-driven transmembrane proton pump with two chromophores), and connect these observations to the microscopic mechanisms underlying them. In the third example we unravel the ultrafast photoinduced dynamics of *trans*-azobenzene and, by a joint experimental and theoretical analysis of time-resolved pump-probe spectra, we deliver a solid explanation for the observed Kasha rule violation.

Part I

From single molecule to molecular aggregates (in their environment)

Introduction

Light harvesting (LH) complexes are aggregates of multiple interacting chromophores, held together in defined geometric arrangements by a protein scaffold. In order to understand the structure-function relationship of such aggregates, it is important to access their quantum mechanical (QM) properties. Indeed it is well known that these multichromophoric complexes exhibit emergent collective behaviors of their components, and therefore these need to be studied *collectively.* At the same time, the necessary balance between accuracy and scalability of computer simulations denies the possibility of a direct investigation of the aggregate as a whole, reducing the applicability domain of computational quantum chemistry approaches to a single (or at most a small number of) chromophoric unit(s). Moreover, not only the large number of chromophores involved, but also the presence of a fluctuating environment that surrounds them, as well as their intra-molecular vibrations, make it even more difficult to access the aggregate's behavior.

In order to tackle such a problem, it is often necessary to decompose it into smaller and simpler pieces, thus reducing the complexity by isolating the important aspects without losing the core physics of the system. One of the models that has been developed for this purpose, is the so-called *Frenkel Exciton model.*

In the Frenkel Exciton model, the aggregate manifold of states is obtained by combining the properties of individual sites with site-site coupling terms. The recovered aggregate manifold of states is called the *excitonic* manifold. Exciton states involve the concerted excitation of an assembly of molecules, which results in a delocalized excitation over multiple chromophores, as opposed to the localized excitation of individual species of the assembly.[1] At the core of the assumptions that make the Frenkel Exciton model applicable, is the fact that the enormous complexity of

an hypothetical wave-function which exactly describes the QM properties of the complete molecular aggregate, can, in many cases of interest, be reduced. This is understood e.g. realizing that electrons belonging to far enough molecules interact as classical objects (i.e. QM effects are not important), and feel each other through classical electrostatic potentials. In other words, the Frenkel Exciton model can be viewed as an *Effective theory*.[1] By introducing this model (and its sensible approximations), one not only reduces the computational cost of the calculations, but also obtains a simpler physical picture of the system under study.

The theory of excitons was first developed by Frenkel for atomic lattices, and then utilized in the molecular crystals field by Davydov.[1, 3] It has also been extensively applied in the study of LH systems[4, 5], to describe their static and dynamical properties. The *exciton strategy* (i.e. the involvement of delocalized states) is for example used by photosynthetic bacteria which live at the bottom of some lakes, to fine-tune their absorption bands through a specific organization of their component chromophores, in order to maximize the harvest of the available light that has not been retained by the leaves of the plants at the surface.[6] Significant interest in the field has been reserved to understand how LH systems use the manifold of excitons, together with intra- and inter-molecular vibrations, to realize very efficient exciton migrations mechanisms.[7] The tremendous efficiency of such *Excitation Energy Transfer* (EET) processes is indeed a very active research topic on both the theoretical and experimental sides, and has received a significant boost with the development and advancement of ultrafast transient spectroscopic techniques, such as the two dimensional electronic spectroscopy (2DES).

The outline of this chapter is as follows: The main ideas behind the Frenkel Exciton modeling, with a particular focus on the physical meaning of its main ingredients, are given. First we introduce the simplest version of the model, which comprise single-molecule electronic states and couplings between them. Then an overview of the quantum chemistry methods necessary to produce the Frenkel Exciton microscopic inputs is presented. Next, we generalize the Frenkel Exciton Hamiltonian in order to include intra- and inter-chromophoric vibrations: these are accounted within the spectral density formalism. Finally, we briefly review some of the transport theories that have been developed for describing the system evolution in time,

---

[1]A beautiful description of Effective Theories is proposed in this quote of H. Georgi: "One of the most astonishing things about the world in which we live, is that there seems to be interesting physics at all scales. To do physics amid this remarkable richness, it is convenient to be able to isolate a set of phenomena from all the rest, so that we can describe it without having to understand everything. Fortunately, this is often possible. We can divide the parameter space of the world into different regions, in each of which there is a different appropriate description of the important physics. Such an appropriate description of the important physics is an Effective theory." [2].

and understand processes such as exciton migration.

We make use of the Frenkel Exciton model in Part III, Chapter 1, to describe the manifold of states of the LH2 complex: site properties are computed at the CASSCF/CASPT2[8, 9] level with the software package Molcas[10]. We implemented the numerical routine that allows to compute the coupling between the chromophores at the transition density level (also computed with CASSCF reference wave-functions). The spectral density function is employed in all of the reported examples to describe the coupling between electronic states and the bath of vibrations (Part III, Chapter 1-3), usually by means of the vertical gradient approach[11] (outlined in Chapter 3). Both Förster and Redfield transport theories are employed to describe the EET pathways in two distinct sector of the LH2 aggregate (Part III, Chapter 1), due to the presence of different coupling strength between the various chromophores of the complex.

Frenkel exciton model

1.1 Basic ingredients

1.1.1 Non-interacting dimer

Consider a couple of non interacting molecules. Each separate system is described by a *local* Hamiltonian, namely $\hat{H}_1$ and $\hat{H}_2$, and by a set of eigenstates, $|0\rangle_1, |1\rangle_1, \ldots, |N_1\rangle_1$ and $|0\rangle_2, |1\rangle_2, \ldots, |N_2\rangle_2$ respectively. The dimer (i.e. the global system) is then described by the *global* Hamiltonian $\hat{H} = \hat{H}_1 + \hat{H}_2$, with eigenstates obtained as direct (Hartree) product of local eigenstates, i.e.

$$
\begin{aligned}
|0\rangle &\equiv |0\rangle_1 |0\rangle_2 \equiv |00\rangle \\
|1\rangle &\equiv |1\rangle_1 |0\rangle_2 \equiv |10\rangle \\
|2\rangle &\equiv |0\rangle_1 |1\rangle_2 \equiv |01\rangle \\
&\vdots \\
|N\rangle &\equiv |N_1\rangle_1 |N_2\rangle_2 \equiv |N_1 N_2\rangle
\end{aligned}
\tag{1.1}
$$

and $N = N_1 \cdot N_2$.

1.1.2 Interacting dimer

Consider now that between the two molecules an interaction term $\hat{H}_{int}$ has been switched on: the global Hamiltonian will now take the form

$$\hat{H} = \hat{H}_1 + \hat{H}_2 + \hat{H}_{int} \tag{1.2}$$

If one supposes that $\hat{H}_{int}$ does not change the electronic structure of each of the two chromophores, or, which is the same, that the two sets of local states remain *good* eigenfunctions of the local systems, then the global states listed above (Hartree product of site basis functions, Eq. (1.1)) are still *good* states for the global system, even if they are no longer eigenstates. In one word, one assumes $\hat{H}_{int}$ to be a small perturbation added to the non-interacting Hamiltonian, i.e., to work in the context of Perturbation Theory (PT). By choosing Hartree products of site states, we are also assuming the overlap of the wave-functions of different sites to be small, and thus that the electrons sitting on different molecules feel each other only through classical electrostatic potentials, with negligible exchange interaction.[1]

Eq. (1.2) can be written in Dirac notation, using the basis of global states listed above. $\hat{H}_1$ thus becomes $\hat{H}_1 = (\epsilon_0^1 |0\rangle \langle 0| + \epsilon_1^1 |1\rangle \langle 1| + \epsilon_2^1 |2\rangle \langle 2| + \dots)$, and a similar expansion holds for $\hat{H}_2$. The interaction term, $\hat{H}_{int}$, is instead written as $\sum_{ijkl} V_{ij,kl} |ij\rangle \langle kl|$. If we consider two-level systems (only $|0\rangle \langle 0|$ and $|1\rangle \langle 1|$ terms in the previous expression) the interacting Hamiltonian reads

$$
\begin{aligned}
\hat{H} = {} & (\epsilon_0^1 + \epsilon_0^2) |00\rangle \langle 00| + (\epsilon_1^1 + \epsilon_0^2) |10\rangle \langle 10| + (\epsilon_1^2 + \epsilon_0^1) |01\rangle \langle 01| + (\epsilon_1^1 + \epsilon_1^2) |11\rangle \langle 11| + \\
& + V_{00,00} |00\rangle \langle 00| + V_{10,10} |10\rangle \langle 10| + V_{01,01} |01\rangle \langle 01| + V_{11,11} |11\rangle \langle 11| + \\
& + V_{00,10} |00\rangle \langle 10| + V_{10,00} |10\rangle \langle 00| + V_{00,01} |00\rangle \langle 01| + V_{01,00} |01\rangle \langle 00| + \\
& + V_{01,10} |01\rangle \langle 10| + V_{10,01} |10\rangle \langle 01| + \\
& + V_{11,10} |11\rangle \langle 10| + V_{10,11} |10\rangle \langle 11| + V_{11,01} |11\rangle \langle 01| + V_{01,11} |01\rangle \langle 11|
\end{aligned} \tag{1.3}
$$

which in matrix form becomes

$$
H = \begin{bmatrix}
\epsilon_0^1 + \epsilon_0^2 + V_{00,00} & V_{00,10} & V_{00,01} & V_{00,11} \\
V_{10,00} & \epsilon_1^1 + \epsilon_0^2 + V_{10,10} & V_{10,01} & V_{10,11} \\
V_{01,00} & V_{01,10} & \epsilon_1^2 + \epsilon_0^1 + V_{01,01} & V_{10,11} \\
V_{11,00} & V_{11,10} & V_{11,01} & \epsilon_1^1 + \epsilon_1^2 + V_{11,11}
\end{bmatrix} \tag{1.4}
$$

This is the most general Hamiltonian one can write for a couple of interacting two-level systems in this basis set, when the Hartree ansatz is correct. On the diagonal the Hamiltonian matrix has energies of the global states (from the energy

---

[1]We note with Kasha[1] that the overlap between site wave-functions of neighboring molecules, will become more and more important when considering higher excited states, whose orbitals will be generally more diffused in space.

$\epsilon_0^1 + \epsilon_0^2 + V_{00,00}$ of the global ground state $|00\rangle$, to the energy $\epsilon_1^1 + \epsilon_1^2 + V_{11,11}$ of the excited state $|11\rangle$), while outside the diagonal it has coupling terms, that allow for a mixing between the states. We note that, in all the systems of interest, we will assume site energies and coupling terms to be real quantities, which implies that the matrix of Eq. (1.4) is symmetric.[2] The coupling $V_{ij,kl}$ is therefore equal to $V_{kl,ij}$. The nature and physical meaning of the various elements of this matrix will be detailed in the following Sections.

1.1.3 Sensible Approximations

At this point, a number of approximations are usually employed: it is very common to consider systems in which the energy gap between the ground state (GS) and the states $|10\rangle$ and $|01\rangle$, as well as between the latter and the state $|11\rangle$, is large. This observation allows the decoupling of these sectors, so that the only off-diagonal terms that survive are those within the different manifolds, and the Hamiltonian can be rewritten as:

$$H = \begin{bmatrix} \epsilon_0^1 + \epsilon_0^2 + V_{00,00} & 0 & 0 & 0 \\ 0 & \epsilon_1^1 + \epsilon_0^2 + V_{10,10} & V_{10,01} & 0 \\ 0 & V_{01,10} & \epsilon_1^2 + \epsilon_0^1 + V_{01,01} & 0 \\ 0 & 0 & 0 & \epsilon_1^1 + \epsilon_1^2 + V_{11,11} \end{bmatrix} \quad (1.5)$$

This approximation relies on the fact that the mixing between states caused by the interaction term $\hat{H}_{int}$ will happen only *within* the manifold of states that are close in energy. We can conveniently focus on the first excitation manifold, so that

$$H = \begin{bmatrix} \tilde{\epsilon}_1 & V_{12} \\ V_{21} & \tilde{\epsilon}_2 \end{bmatrix} \quad (1.6)$$

or equivalently

$$\hat{H} = \tilde{\epsilon}_1 |1\rangle \langle 1| + \tilde{\epsilon}_2 |2\rangle \langle 2| + V_{12} |1\rangle \langle 2| + V_{21} |2\rangle \langle 1| \quad (1.7)$$

where we have subtracted the (constant) GS energy from all the diagonal terms[3], and obtained the excitation energies $\tilde{\epsilon}_1 = \epsilon_1^1 - \epsilon_0^1$, $\tilde{\epsilon}_2 = \epsilon_1^2 - \epsilon_0^2$.

---

[2]Since $\hat{H} = \hat{H}^\dagger$, in the Hartree product basis we have: $H_{ij} = H_{ji}$.

[3]We have also assumed that the diagonal terms $V_{ij,ij}$ cancel out (e.g., $V_{10,10} - V_{00,00} \simeq 0$). We will discuss the role of these terms, and the appropriateness of this assumption, when focusing on each Hamiltonian matrix entry.

The assumptions introduced so far are at the core of the Frenkel Exciton modeling. We summarize them hereafter.

Approximations

- $\hat{H}_{int}$ is a perturbation.
- The system states are expressed on the basis built as Hartree product of site states (i.e., the overlap between site wave functions is assumed to be negligible).
- The different sectors of the Hamiltonian are separated by large energy gaps: each manifold is allowed to mix only within itself.

These approximations can in principle be released, paying the price of a considerable complication of the model presented here. Eq. (1.7) represent the typical exciton model Hamiltonian of a couple of interacting chromophores.

1.1.4   Three 3-level interacting sites

The simplest example in which all the relevant terms that can enter the excitonic model are present, is the case of three 3-level interacting sites. Here the global Hamiltonian is given by $\hat{H} = \hat{H}_1 + \hat{H}_2 + \hat{H}_3 + \hat{H}_{int}$, and $\hat{H}_{int}$ is a sum of two-body inter-chromophore interaction terms (i.e., $\hat{V}_{12} + \hat{V}_{13} + \hat{V}_{23}$ [4]).

The complete list of states that can be built by direct products of site eigenfunctions is (using the compact notation $|0\rangle_1 |0\rangle_2 |0\rangle_3 \equiv |000\rangle$):

$$
\begin{array}{cccc}
\text{GS} & 1^{st} \text{ exc. manifold} & 2^{nd} \text{ exc. manifold} & \text{higher order exc.} \\
|000\rangle \equiv |0\rangle & |100\rangle & |110\rangle & |111\rangle \\
 & |200\rangle & |210\rangle & |211\rangle \\
 & |010\rangle & |120\rangle & |121\rangle \\
 & |020\rangle & |220\rangle & |112\rangle \\
 & |001\rangle & |101\rangle & |221\rangle \\
 & |002\rangle & \vdots & |212\rangle \\
 & & |202\rangle & |122\rangle \\
 & & |011\rangle & |222\rangle \\
 & & \vdots & \\
 & & |022\rangle &
\end{array}
\tag{1.8}
$$

Note that the approximation of large gaps can be wrong for higher lying states of

---

[4] $\hat{V}_{ab} = \left(V_{ab} |a\rangle \langle b| + V_{ba} |b\rangle \langle a| \right)$, a and b being site indexes.

single chromophores (e.g., $|200\rangle$), which may be resonant with states of the second excitation manifold, and should therefore be included in this manifold. Attention should be paid when one needs to introduce many excited states for each chromophore: the higher the energy, the larger the number of close lying states that can mix with each other; moreover, as stated above, the higher states will be more diffuse and thus the negligible overlap hypothesis can breakdown. For this reason, the Frenkel Exciton modeling is usually limited to very few excited states per chromophore.

1.1.5 Interacting multimer

Let us consider a system composed by N sites, where each site has n excited states. The total number of states is given by the formula[5]

$$N_{total} = \sum_{k=0}^{N} \left(\begin{array}{c} N \\ k \end{array} \right) n^k \qquad (1.9)$$

n^k being the k_{th} power of n, and k representing the number of excited chromophores in a given aggregate/global state.

It is therefore natural to partition the excitonic states according to the number of excited sites k: the global GS ($k = 0$) is the state in which none of the sites are excited; the *first excitation manifold* ($k = 1$) includes all the states with just one chromophore excited and all the other in their GS; in the *second excitation manifold* ($k = 2$) all the possible combination of couples of excited sites are considered; then all the triads ($k = 3$) follow, and so on and so forth.[6]

It is apparent that for increasing number of sites and excitations on each site, the total number of states increases exponentially. It is nonetheless often possible to reduce the number of *important* states that have to be considered. First of all, different spectroscopic techniques (linear and non-linear) can be sensibly described by truncating the expansion at $k = 1, 2, 3...$, according to the number of laser pulses which are sent to the system. Secondly, according to the spectral window which will be probed during an experiment, a reduced number of excited states per chromophore (i.e., the one which lies inside the probed window) can be considered.

---

[5]The general formula in which site m has n_m excited states is: $N_{total} = 1 + \sum_i^N n_i + \sum_{i<j}^N n_i n_j + \sum_{i<j<k}^N n_I n_j n_k + \dots$

[6]This definition of the various manifolds holds as far as there is a sufficiently large energy separation between the single chromophore states and the states of couples of excited sites. There can be situations in which higher lying states of single chromophores have energies comparable with that of states of couples of excited sites: they should therefore be removed from the first excitation manifold, and considered in the second excitation manifold.
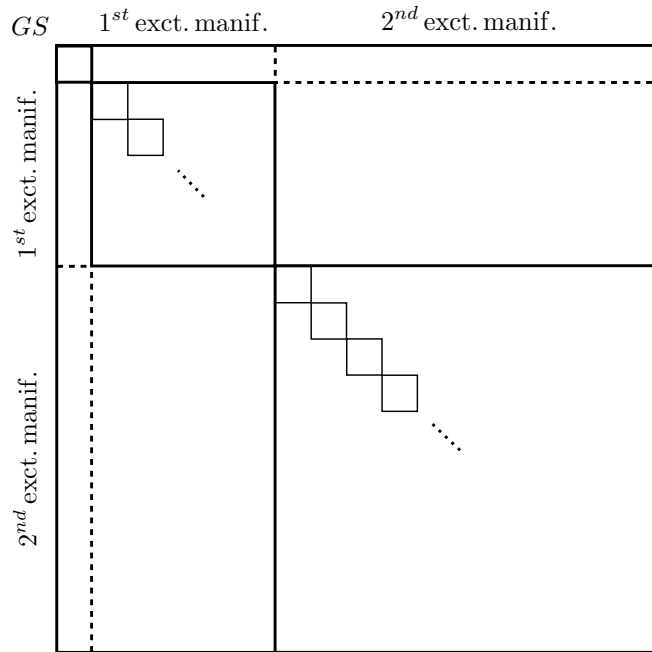
Figure 1.1: Frenkel Exciton Hamiltonian sectors.

The above mentioned approximations hold if the excluded states have a sufficiently large energy gap with the considered states, otherwise they can still influence the simulations by mixing (via interaction) with the manifold of probed states.

In Figure 1.1 we show the different sectors into which it is possible to subdivide the excitonic Hamiltonian, truncating the expansion to the second excitation manifold (states with more than two chromophores excited are excluded, as well as single chromophore states lying too high in energy). The increasing complexity of the matrix for increasing number of excitations is apparent. As already explained, the off-diagonal matrix blocks between the GS, first-excitation, and second-excitation manifolds can be safely assumed to be zero in many cases of interest.

1.1.6   Interacting multimer of two level systems

An aggregate of N two-level systems, according to Eq. (1.9), have N states in the first excitation manifold and $N(N-1)/2$ (i.e., $\sim N^2$) states in the second-excitation manifold. We discuss here some properties of the first-excitation manifold. The system is characterized by the N states $|i\rangle \equiv |0_1 0_2 \ldots 1_i \ldots 0_N\rangle$, and the Frenkel exciton Hamiltonian reads

$$H = \sum_{i}^{N} \epsilon_i |i\rangle \langle i| + \sum_{i \neq j}^{N} V_{ij} |i\rangle \langle j| \qquad (1.10)$$
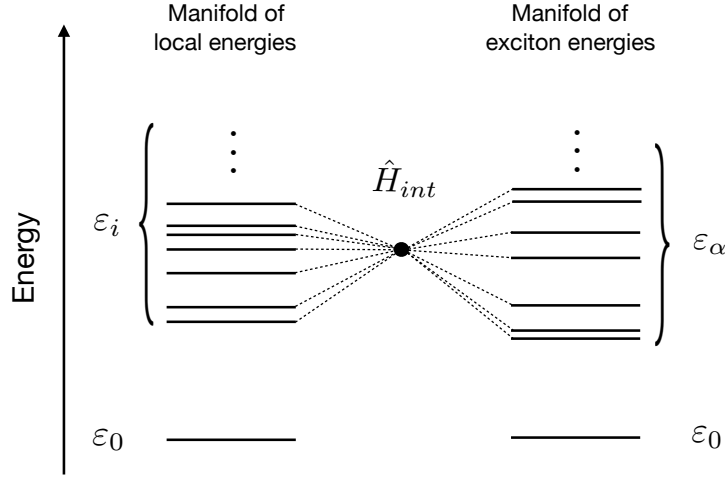
Figure 1.2: Pictorial representation of the transformation of the local manifold of energies ϵ_i caused by the interaction Hamiltonian $\hat{H}_{int}$. The new manifold of *exciton* energies ϵ_α is formed.

where $\epsilon_i = \langle i| \hat{H} |i \rangle$ and $V_{ij} = V_{ji}$.[7] By diagonalizing the Hamiltonian of Eq. (1.10), one obtains new eigenvalues and eigenfunctions, which are called *excitonic energies* and *excitonic states* respectively, given by

$$|\alpha\rangle = \sum_i^N c_{\alpha i} |i\rangle \tag{1.11}$$

$$\epsilon_\alpha = \langle \alpha| \hat{H} |\alpha\rangle = \sum_i^N \sum_j^N c_{\alpha i}^* H_{ij} c_{\alpha j} \tag{1.12}$$

and the coefficients $c_{\alpha i}$ are obtained as a result of the diagonalization. A pictorial representation of the mixing (controlled by $\hat{H}_{int}$) between site states, and the resulting manifold of exciton states, is shown in Figure 1.2.

Not only the energies, but all the properties of the system have to be computed in terms of the new states: if we consider a generic operator $\hat{\mathcal{O}}$, its matrix elements in terms of the excitonic states $|\alpha\rangle$ are expressed as a linear combination of matrix elements of site states as

$$\langle \alpha| \hat{\mathcal{O}} |\beta\rangle = \sum_{i,j}^N c_{\alpha i}^* c_{\beta j} \langle i| \hat{\mathcal{O}} |j\rangle \tag{1.13}$$

A notable operator that will be considered afterwards, is the transition dipole moment $\hat{\boldsymbol{\mu}}$, whose matrix elements between exciton states are related to site transi-

---

[7]And we have assumed the energy of the global ground state $|0\rangle$ to be $\epsilon_0 = 0$.
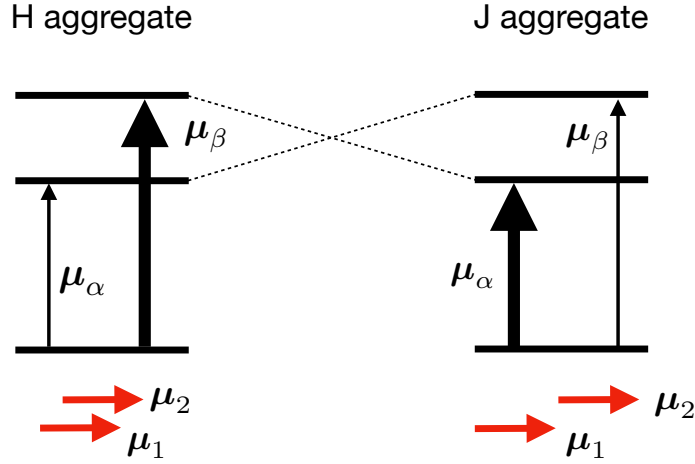
Figure 1.3: Schematic representation of H and J aggregates. $\boldsymbol{\mu}_{1/2}$ are the site dipoles, $\boldsymbol{\mu}_{\alpha/\beta}$ are the exciton dipoles. Even if the energy of the excitons is the same, the different spacial orientation of the dipoles modulates the intensity of the excitons transitions (expressed by the thickness of the black arrows).

tion dipole moments as in Eq. (1.13), i.e.

$$\boldsymbol{\mu}_{\alpha\beta} = \langle\alpha|\,\hat{\boldsymbol{\mu}}\,|\beta\rangle = \sum_{i,j}^{N} c_{\alpha i}^{*} c_{\beta j} \boldsymbol{\mu}_{ij} \tag{1.14}$$

and the transitions from the ground state $|0\rangle$ to a generic exciton $|\alpha\rangle$, are given by[8]

$$\boldsymbol{\mu}_{\alpha} = \langle 0|\,\hat{\boldsymbol{\mu}}\,|\alpha\rangle = \sum_{i}^{N} c_{\alpha i} \boldsymbol{\mu}_{i} \tag{1.15}$$

From a field-matter interaction perspective, we note that the light that impinges on a sample of strongly interacting molecules, probes the excitonic manifold of states, and not the original manifold of states of the isolated chromophores. Moreover the brightness of the excitonic transitions will be proportional to the modulus of the excitonic dipoles, i.e., $|\boldsymbol{\mu}_{\alpha}|^2$. This brightness does not only depend on the coefficients $c_{\alpha i}$ (determined via diagonalization by the Hamiltonian parameters H_{ij}, i.e., by site energies and couplings between the sites), but also on the orientation of the site transition dipoles $\boldsymbol{\mu}_i$, as suggested by Eq. (1.15). A widely studied example of the influence of the orientation of the transition dipoles in the spectra of interacting molecules is that of J and H aggregates (Figure 1.3).[12, 13]

---

[8]Here we simplified the notation by introducing $\boldsymbol{\mu}_{\alpha} \equiv \boldsymbol{\mu}_{0\alpha}$ and $\boldsymbol{\mu}_{0i} \equiv \boldsymbol{\mu}_i$. We have furthermore assumed that the global GS will not mix with all the other states, due to the significant energy gap between itself and all the other states

1.2   Microscopic Origin of the Frenkel Exciton Model

The general expression of the Frenkel Exciton Hamiltonian can be connected to the microscopic Hamiltonian of a system of interacting molecules. We consider for simplicity a two-chromophore system, composed by molecules having respectively $\mathcal{N}_I$ nuclei (described by the positions R, the momenta P and charges Z) and n_{el}^I electrons (r, p, -1), with $I = 1, 2$. The indexes i and $\bar{i}$ run over either electrons or nuclei of molecule 1, while the indexes j and $\bar{j}$ run over either electrons or nuclei of molecule 2. (R, P) are nuclear degrees of freedom (DOFs), while (r, p) are electronic DOFs. The dimer Hamiltonian (in atomic units) then reads

$$
\begin{aligned}
\hat{H}_{full} &= \underbrace{\left[\sum_i^{\mathcal{N}_1} \frac{\hat{P}_i^2}{2M_i} + \sum_i^{n_1} \frac{\hat{p}_i^2}{2} - \sum_{i\bar{i}} \frac{Z_{\bar{i}}}{\left| \hat{\boldsymbol{r}}_i - \hat{\boldsymbol{R}}_{\bar{i}} \right|} + \sum_{i,\bar{i}>i} \frac{1}{\hat{r}_{i\bar{i}}} + \sum_{i,\bar{i}>i} \frac{Z_i Z_{\bar{i}}}{\hat{R}_{i\bar{i}}} \right]}_{\hat{H}_1} + \\[2mm]
&+ \underbrace{\left[\sum_j^{\mathcal{N}_2} \frac{\hat{P}_j^2}{2M_j} + \sum_j^{n_2} \frac{\hat{p}_j^2}{2} - \sum_{j\bar{j}} \frac{Z_{\bar{j}}}{\left| \hat{\boldsymbol{r}}_j - \hat{\boldsymbol{R}}_{\bar{j}} \right|} + \sum_{j,\bar{j}>j} \frac{1}{\hat{r}_{j\bar{j}}} + \sum_{j,\bar{j}>j} \frac{Z_j Z_{\bar{j}}}{\hat{R}_{j\bar{j}}} \right]}_{\hat{H}_2} + \\[2mm]
&+ \underbrace{\left[\sum_{ij} \frac{1}{\hat{r}_{ij}} - \sum_{ij} \frac{Z_i}{\left| \hat{\boldsymbol{R}}_i - \hat{\boldsymbol{r}}_j \right|} - \sum_{ij} \frac{Z_j}{\left| \hat{\boldsymbol{r}}_i - \hat{\boldsymbol{R}}_j \right|} + \sum_{ij} \frac{Z_i Z_j}{\hat{R}_{ij}} \right]}_{\hat{H}_{int}}
\end{aligned} \tag{1.16}
$$

The first two terms (labeled as $\hat{H}_1$ and $\hat{H}_2$, respectively) are responsible for the quantum mechanical properties of the isolated sites, while the last term is the coupling term between sites, responsible of the mixing of the local site properties. In what follows we will apply the Born-Oppenheimer approximation[14] to $\hat{H}_1$ and $\hat{H}_2$, and retain only the electronic parts of those Hamiltonians. In this approximation the nuclear DOFs are held fixed and the electronic problem is solved for each fixed arrangement of nuclei. The electronic properties then become parametrically dependent on the nuclear configuration in the BO approximation. In doing that, we assume that this approximation is alway applicable for all the systems of interest.

The previous equation therefore becomes

$$\hat{H}_{el} = \underbrace{\left[\sum_i^{n_1} \frac{\hat{p}_i^2}{2} - \sum_{i\bar{i}} \frac{Z_{\bar{i}}}{\left| \hat{\boldsymbol{r}}_i - \hat{\boldsymbol{R}}_{\bar{i}} \right|} + \sum_{i,\bar{i}>i} \frac{1}{\hat{r}_{i\bar{i}}} \right]}_{\hat{H}_1} +$$

$$+ \underbrace{\left[\sum_j^{n_2} \frac{\hat{p}_j^2}{2} - \sum_{j\bar{j}} \frac{Z_{\bar{j}}}{\left| \hat{\boldsymbol{r}}_j - \hat{\boldsymbol{R}}_{\bar{j}} \right|} + \sum_{j,\bar{j}>j} \frac{1}{\hat{r}_{j\bar{j}}} \right]}_{\hat{H}_2} +$$

$$+ \underbrace{\left[\sum_{ij} \frac{1}{\hat{r}_{ij}} - \sum_{ij} \frac{Z_i}{\left| \hat{\boldsymbol{R}}_i - \hat{\boldsymbol{r}}_j \right|} - \sum_{ij} \frac{Z_j}{\left| \hat{\boldsymbol{r}}_i - \hat{\boldsymbol{R}}_j \right|} + \sum_{ij} \frac{Z_i Z_j}{\hat{R}_{ij}} \right]}_{\hat{H}_{int}} \qquad (1.17)$$

By (separately) solving the Schrödinger equation for the first two terms of Eq. (1.17), the unperturbed wave functions for the two chromophores (up to a certain number of states) can be obtained, and interaction terms between sites are introduced later via perturbation theory.[9]

Equation (1.17) therefore explains the microscopic origin of the Frenkel Exciton model, in terms of intra- and inter-molecular interactions between electrons and nuclei of the considered aggregate.

1.2.1 Electrostatic environmental effects

Electrostatic environmental effects can also be accounted for in the same microscopic fashion, including one or more $\hat{H}_{env}$ Hamiltonians (of the same form as $\hat{H}_1$ and $\hat{H}_2$), which describe the environmental molecules (such as the proteins surroundings), and a corresponding number of chromophore-environment interaction terms (of the same form of $\hat{H}_{int}$, Eq. (1.17)) for each chromophore.

Let us consider for simplicity a single chromophore C and its environment E: $\hat{H} = \hat{H}_C + \hat{H}_E + \hat{H}_{int}$. If we assume that, in the processes of interest, the environment only acts as an electrostatic embedding (i.e. it is not involved in the interaction with light and it is not significantly affected by the state of the chromophores), its properties are completely described by its ground state. Before solving the electronic structure of the chromophore C, a GS computation can be performed on the environment, and $\hat{H}_{int}$ can be simplified by localizing the electron charge density on

---

[9]The particular case of e.g. a two-level chromophore is here understood by assuming that the solution of the Schrödinger equation returns states with a significant energy gap between the first and all the other excited states, so that one can effectively consider the system to be described by only the GS and the first ES.

its atoms[10], obtaining a point-charges electrostatic potential given by

$$\hat{H}_{int} = \sum_i \sum_e \frac{Z_i \tilde{q}_e}{\hat{R}_{ie}} - \sum_i \sum_e \frac{\tilde{q}_e}{\left| \hat{\boldsymbol{r}}_i - \hat{\boldsymbol{R}}_e \right|} \tag{1.18}$$

where the index i runs over electrons and nuclei of C, while e runs over the localized point charges of the environment, $\tilde{q}_e$.[11]

The first term of Eq. (1.18) is a constant, while the second term of this effective potential can be treated either via perturbation theory, as a correction of the solutions of the unperturbed $\hat{H}_C$ Hamiltonian, or explicitly, inserting it in the $\hat{H}_C$ Hamiltonian as an external electrostatic contribution. In the latter case, the unperturbed molecular states in presence of this effective potential will be different with respect to the "vacuum" unperturbed solutions, and all the site properties will be directly affected by the presence of the environment which changes the reference wave-functions.

Note that the two ways of accounting for the environmental terms are not equivalent, since the DOFs are different in the two cases: in one case these are the atomic wave-functions (DOFs of the quantum chemistry method), which, in the presence of such charges, mix in a different way to produces new molecular orbitals (MOs), and then new electronic states. In the other case, the DOFs are the macroscopic "vacuum" unperturbed states of the chromophore.

In the computations reported in this Thesis, we have always considered the environment as directly included in the quantum chemistry computations of the reference site states.

1.2.2 $\hat{H}_{int}$: a closer look

Let us consider (from now on) a generic system with N sites. The global Hamiltonian is given by the sum $\hat{H} = \left(\sum_{I=1}^{N} \hat{H}_I \right) + \hat{H}_{int}$, and $\hat{H}_I$ is described as in Eq. (1.17).

As discussed before, the most general *inter-molecular* coupling term is given by $\hat{H}_{int} = \sum_{I \neq J} \hat{V}_{IJ}$, where I and J are site indexes and $\hat{V}_{IJ}$ is a two-body Coulomb interaction term; this Coulombic term, as shown in Eqs. (1.16-1.17), can be split in different contributions, namely the electron-electron part, the nuclear-electron part

---

[10]Usually employing the so called ESP (electrostatic potential fitting) method.[15]

[11]The model can be further developed by including also the environmental polarizability.

and the nuclear-nuclear part, i.e.,

$$
\begin{aligned}
\hat{V}_{IJ} &= \hat{V}_{IJ}^{(el-el)} + \hat{V}_{IJ}^{(nuc-el)} + \hat{V}_{IJ}^{(el-nuc)} + \hat{V}_{IJ}^{(nuc-nuc)} = \\
&= \sum_{ij} \frac{1}{\hat{r}_{ij}} - \sum_{ij} \frac{Z_i}{\left| \hat{\boldsymbol{R}}_i - \hat{\boldsymbol{r}}_j \right|} - \sum_{ij} \frac{Z_j}{\left| \hat{\boldsymbol{r}}_i - \hat{\boldsymbol{R}}_j \right|} + \sum_{ij} \frac{Z_i Z_j}{\hat{R}_{ij}}
\end{aligned}
\tag{1.19}
$$

where $i \in I, j \in J$ indexes runs over either electrons or nuclear coordinates of chromophore I and J, respectively.

Consider the matrix element of $\hat{V}_{IJ}$ between two generic global states, i.e.

$$
\langle a_1 b_2 \dots m_I \dots n_J \dots | \hat{V}_{IJ} | a_1' b_2' \dots m_I' \dots n_J' \dots \rangle
\tag{1.20}
$$

where $a\,(a'), b\,(b'), m\,(m'), n\,(n')$ span the manifold of states of chromophores 1, 2, I, J, respectively; this generic term will be different from zero if and only if all the chromophores, except I and J, are in the same state[12], as

$$
\begin{aligned}
\langle \dots m_I \dots n_J \dots | \hat{V}_{IJ} | \dots m_I' \dots n_J' \dots \rangle &= \langle m_I n_J | \hat{V}_{IJ} | m_I' n_J' \rangle \langle a | a' \rangle \langle b | b' \rangle \dots \\
&= \langle m_I n_J | \hat{V}_{IJ} | m_I' n_J' \rangle \delta_{aa'} \delta_{bb'} \dots
\end{aligned}
\tag{1.21}
$$

This result suggests that the coupling between configurations having more than two chromophores in different electronic states is null.

If we explicitly express the term $\langle m_I n_J | \hat{V}_{IJ} | m_I' n_J' \rangle$ in its components, by using Eq. (1.19) and writing the states in terms of multi-electronic spatial wave-functions (at fixed nuclear configurations), we obtain

$$
\begin{aligned}
\langle m_I n_J | \hat{V}_{IJ} | m_I' n_J' \rangle &= \int d\boldsymbol{r}_I d\boldsymbol{r}_J \psi_m^* (\boldsymbol{r}_I) \psi_{m'} (\boldsymbol{r}_I) V_{IJ} (\boldsymbol{r}_I, \boldsymbol{r}_J, R_I, R_J) \psi_n^* (\boldsymbol{r}_J) \psi_{n'} (\boldsymbol{r}_J) = \\
&= \int d\boldsymbol{r}_I d\boldsymbol{r}_J \psi_m^* (\boldsymbol{r}_I) \psi_{m'} (\boldsymbol{r}_I) V_{IJ}^{(el-el)} (\boldsymbol{r}_I, \boldsymbol{r}_J) \psi_n^* (\boldsymbol{r}_J) \psi_{n'} (\boldsymbol{r}_J) \\
&\quad + \delta_{mm'} \int d\boldsymbol{r}_J V_{IJ}^{(nuc-el)} (\boldsymbol{r}_J, R_I) \psi_n^* (\boldsymbol{r}_J) \psi_{n'} (\boldsymbol{r}_J) \\
&\quad + \delta_{nn'} \int d\boldsymbol{r}_I \psi_m^* (\boldsymbol{r}_I) \psi_{m'} (\boldsymbol{r}_I) V_{IJ}^{(el-nuc)} (\boldsymbol{r}_I, R_J) \\
&\quad + \delta_{mm'} \delta_{nn'} V_{IJ}^{(nuc-nuc)} (R_I, R_J)
\end{aligned}
\tag{1.22}
$$

where $\boldsymbol{r}_I = \left(\boldsymbol{r}_1^I, \dots, \boldsymbol{r}_{n_{el}}^I \right)$ and $d\boldsymbol{r}_I = d\boldsymbol{r}_1^I \dots d\boldsymbol{r}_{n_{el}}^I$. These multidimensional integrals can be conveniently expressed in terms of *densities*. Consider for example the

---

[12]This condition is fulfilled if and only if the wave functions of the different chromophores do not overlap in space. In this case, as we have already said, the Coulomb coupling is the unique interaction between the chromophores.

electron-electron contribution, rewritten as

$$V_{IJ}^{(el-el)}(\boldsymbol{r}_I, \boldsymbol{r}_J) = \sum_i^{n_{el}^I} \sum_j^{n_{el}^J} 1/\left|\boldsymbol{r}_i^I - \boldsymbol{r}_j^J\right| = \sum_i \int d\boldsymbol{r}\,\delta(\boldsymbol{r} - \boldsymbol{r}_i^I) \sum_j 1/\left|\boldsymbol{r} - \boldsymbol{r}_j^J\right| \quad (1.23)$$

The corresponding integral in Eq. (1.22) then becomes

$$\sum_i \int d\boldsymbol{r}\, \underbrace{d\boldsymbol{r}_1^I \ldots d\boldsymbol{r}_{n_{el}}^I \psi_m^* \left(\boldsymbol{r}_1^I \ldots \boldsymbol{r}_{n_{el}}^I\right) \psi_{m'}\left(\boldsymbol{r}_1^I \ldots \boldsymbol{r}_{n_{el}}^I\right) \delta(\boldsymbol{r} - \boldsymbol{r}_i^I)}_{\langle\psi_m|\delta(\boldsymbol{r}-\boldsymbol{r}_i^I)|\psi_{m'}\rangle} \sum_j \int d\boldsymbol{r}_J \frac{1}{\left|\boldsymbol{r} - \boldsymbol{r}_j^J\right|} \ldots$$

$$(1.24)$$

We note that, due to the antisymmetry of the site wave-functions and the integration over all the volume for each variable $\boldsymbol{r}_1^I \ldots \boldsymbol{r}_{n_{el}}^I$, all the n_{el}^I terms of the sum over i gives the same result, as

$$\langle\psi_m|\delta(\boldsymbol{r} - \boldsymbol{r}_i^I)|\psi_{m'}\rangle = \langle\psi_m|\delta(\boldsymbol{r} - \boldsymbol{r}_{\bar{i}}^I)|\psi_{m'}\rangle \ \ \forall i, \bar{i} \in (0, \ldots, n_{el}^I) \qquad (1.25)$$

Eq. (1.24) is then equal to

$$\int d\boldsymbol{r}\, \rho_{mm'}^I(\boldsymbol{r}) \sum_j \int d\boldsymbol{r}_J \frac{1}{\left|\boldsymbol{r} - \boldsymbol{r}_j^J\right|} \psi_n^*(\boldsymbol{r}_J)\, \psi_{n'}(\boldsymbol{r}_J) \qquad (1.26)$$

where $\rho_{mm'}^I(\boldsymbol{r}) = n_{el}^I \langle\psi_m|\delta(\boldsymbol{r} - \boldsymbol{r}_1^I)|\psi_{m'}\rangle$. The same kind of transformation can be applied to the $\boldsymbol{r}_J$ part of the integral, so that the various components of Eq. (1.22) can be rewritten in terms of densities, as[16]

$$\begin{aligned}
\langle m_I n_J|\hat{V}_{IJ}|m_I' n_J'\rangle &= \int d\boldsymbol{r}\, d\boldsymbol{r}'\, \rho_{mm'}^I(\boldsymbol{r}) \frac{1}{|\boldsymbol{r} - \boldsymbol{r}'|} \rho_{nn'}^J(\boldsymbol{r}') \\
&\quad - \delta_{mm'} \int d\boldsymbol{r}' \sum_{i \in I} \frac{\rho_{nn'}^J(\boldsymbol{r}')\, Z_i}{|\boldsymbol{R}_i - \boldsymbol{r}'|} \\
&\quad - \delta_{nn'} \int d\boldsymbol{r} \sum_{j \in J} \frac{\rho_{mm'}^I(\boldsymbol{r})\, Z_j}{|\boldsymbol{r} - \boldsymbol{R}_j|} \\
&\quad + \delta_{mm'}\delta_{nn'} \sum_{ij} \frac{Z_i Z_j}{R_{ij}}
\end{aligned} \qquad (1.27)$$

where $\rho_{aa}^I(\boldsymbol{r})$ is the *electronic charge density* of the electronic state a of molecule I, and $\rho_{ab}^I(\boldsymbol{r})$, with $a \neq b$, is the so called *transition charge density* related to the transition between the states a and b of molecule I[16]. According to this scheme, we can distinguish three different kind of interaction terms:

- Density-Density (D-D): terms involving interaction between densities ($m = m'$ and $n = n'$ in the previous equation), for which one should consider all the

GS 1st exct. manif. 2nd exct. manif.
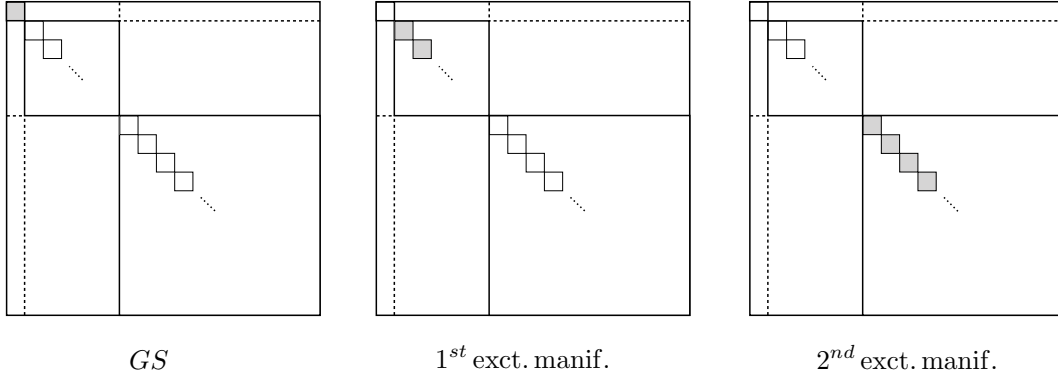
Figure 1.4: The diagonal contributions of the various sectors of the excitonic Hamiltonian.

possible contributions $\hat{V}_{IJ}^{(el-el)}$, $\hat{V}_{IJ}^{(nuc-el)}$, $\hat{V}_{IJ}^{(el-nuc)}$, $\hat{V}_{IJ}^{(nuc-nuc)}$. These terms will enter only in the diagonal of $\hat{H}$;

- Density-Transition Density (D-TRD): terms involving interaction between transition densities (TRDs) and densities (D) (either $m = m'$ and $n \neq n'$ or $m \neq m'$ and $n = n'$), in which only $\hat{V}_{IJ}^{(el-el)}$ and $\hat{V}_{IJ}^{(nuc-el)}$ or $\hat{V}_{IJ}^{(el-nuc)}$ have to be considered;

- Transition Density-Transition Density (TRD-TRD): terms involving interaction between TRDs ($m \neq m'$ and $n \neq n'$), in which only the $\hat{V}_{IJ}^{(el-el)}$ part of the potential is different from zero.

We now develop some of the terms of Eq. (1.27) according to their position in the excitonic Hamiltonian. Since we are interested in the simulation of third-order experiments[13], we will hereafter consider terms up to the second excitation manifold. First we discuss diagonal entries (in order: *GS* diagonal term, *first excitation manifold* diagonal terms, and *second excitation manifold* diagonal terms), and then some off-diagonal entries.

1.2.3 Diagonal Entries

The diagonal elements are those which involve site state energies and D-D interaction terms. For the ground state energy one has:

---

[13]Nonlinear spectroscopy experiments, where three laser pulses interacts with the samples of molecules. The reason why one should stop to the second excitation manifold will become clear in the next Part of the Thesis, in which we describe in detail how to simulate linear and non-linear spectroscopic techniques.
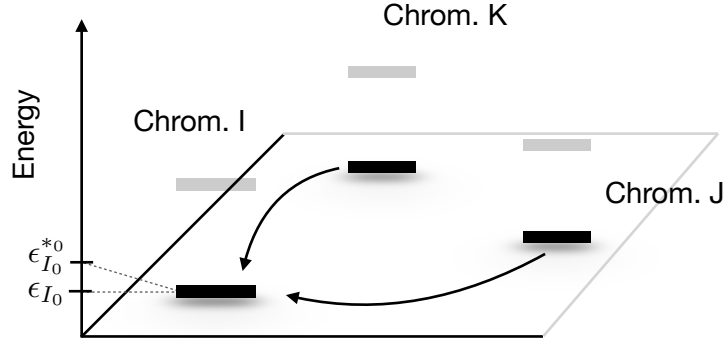
Figure 1.5: Pictorial representation of the terms of Eq. (1.28) for a system of three Chromophores with two levels (for each of them, 0 is the GS and 1 is the unique ES). The chromophores are spatially disposed in the (x,y) plane, and the z axis represents the energy. The GS density of both Chrom. J and Chrom. K interacts with the GS density of Chrom. I, and shifts its energy.

GS:

$$
\begin{aligned}
E_{GS}^* = \langle 0| \hat{H} |0\rangle &= \langle 0| \left(\sum_{I=1}^{N} \hat{H}_I \right) + \hat{H}_{int} |0\rangle = \\
&= \sum_I \epsilon_{I_0} + \langle 0| \hat{H}_{int} |0\rangle = \\
&= \sum_I \left(\epsilon_{I_0} + \sum_{J \neq I} \langle 0_I 0_J | \hat{V}_{IJ} |0_I 0_J\rangle \right) = \\
&= \sum_I \epsilon_{I_0}^{*0}
\end{aligned}
\tag{1.28}
$$

where $\epsilon_{I_0}^{*0}$ is defined as the sum of the ϵ_{I_0} term (the energy of the isolated molecule I in its GS), corrected by the term $\sum_{J \neq I} \langle 0_I 0_J | \hat{V}_{IJ} |0_I 0_J\rangle$, which accounts for the interaction between molecule I (in its GS) and all the other molecules (also in their GS). This is the term $V_{00,00}$ of Eq. (1.4), whose physical meaning is here clarified. This correction ($\epsilon_{I_0} \rightarrow \epsilon_{I_0}^{*0}$) can be interpreted as the "environment-like" effect that the presence of all the molecules (in their GS) have on the GS energy of site I. The global GS energy E_{GS}^* is thus the sum of all the individual site energies $\epsilon_{I_0}^{*0}$.

We note that this environment-like correction can be accounted for by considering the QM region of each molecule as surrounded by point charges (or even polarizable charge distributions), which represent the GS charge density of all the other chromophores. The GS energy of chromophore i, can then be obtained in QM computations which explicitly include this electrostatic embedding of the other chromophores, directly producing the "environmental corrected" $\epsilon_{I_0}^{*0}$ energy, instead
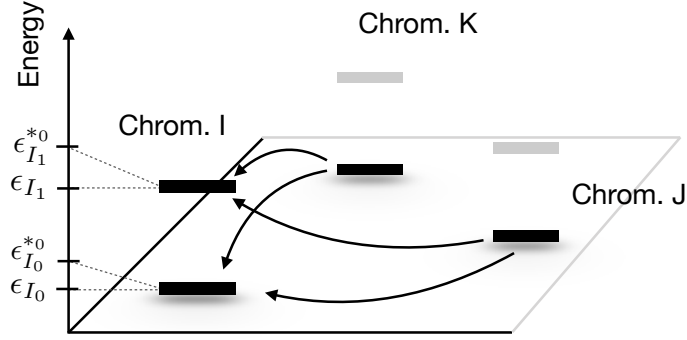
Figure 1.6: Pictorial representation of the terms of Eq. (1.29) for the same system of Figure 1.5. The GS density of both Chrom. J and Chrom. K interacts with both the GS and ES densities of Chrom. I, shifting their energies.

of the vacuum energy ϵ_{I_0}.

First excitation manifold:

$$\langle m_I | \hat{H} | m_I \rangle = \langle m_I | \left(\sum_{I=1}^N \hat{H}_I \right) + \hat{H}_{int} | m_I \rangle = \tag{1.29}$$

$$= \sum_{K \neq I} \epsilon_{K_0} + \epsilon_{I_m} + \langle m_I | \hat{H}_{int} | m_I \rangle =$$

$$= \sum_{K \neq I} \epsilon_{K_0} + \epsilon_{I_m} + \sum_{K \neq I} \sum_{J \neq K, J \neq I} \langle 0_K 0_J | \hat{V}_{KJ} | 0_K 0_J \rangle + \sum_{J \neq I} \langle m_I 0_J | \hat{V}_{IJ} | m_I 0_J \rangle =$$

$$= \sum_{K \neq I} \left(\epsilon_{K_0} + \sum_{J \neq K, J \neq I} \langle 0_K 0_I | \hat{V}_{KJ} | 0_K 0_J \rangle \right) + \left(\epsilon_{I_m} + \sum_{J \neq I} \langle m_I 0_J | \hat{V}_{IJ} | m_I 0_J \rangle \right) =$$

$$\stackrel{\Delta}{=} \sum_K \left(\epsilon_{K_0} + \sum_{J \neq K} \langle 0_K 0_J | \hat{V}_{KJ} | 0_K 0_J \rangle \right) + \epsilon_{I_m}^{*0} - \left(\epsilon_{I_0} + \sum_{J \neq I} \langle 0_I 0_J | \hat{V}_{IJ} | 0_I 0_J \rangle \right)$$

$$= E_{GS}^* + \left(\epsilon_{I_m}^{*0} - \epsilon_{I_0}^{*0} \right)$$

where in Δ we have rewritten the sum over the GS contributions by summing and subtracting the term $\left(\epsilon_{I_0} + \sum_{J \neq I} \langle 0_I 0_J | \hat{V}_{IJ} | 0_I 0_J \rangle \right)$, and defined $\epsilon_{I_m}^{*0} \equiv \epsilon_{I_m} + \sum_{J \neq I} \langle m_I 0_J | \hat{V}_{IJ} | m_I 0_J \rangle$.

The first excitation manifold has therefore diagonal energies given by the sum of the global GS energy E_{GS}^* and terms like $\left(\epsilon_{I_m}^{*0} - \epsilon_{I_0}^{*0} \right)$, which can be interpreted as the amount of energy necessary to promote the given site I from its GS to a certain excited state m (i.e., the $0 \to m$ excitation energy of molecule I) in the presence of the other chromophores in their GS.

The introduced correction of the excitation energy of the $0 \to m$ transition, can be again accounted for by the presence of this electrostatic embedding in the quan-
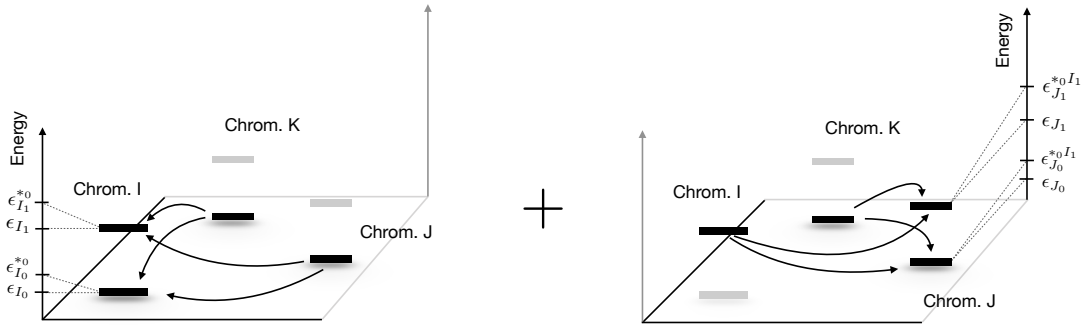
Figure 1.7: Pictorial representation of the term $|0_I 0_J\rangle \to |1_I 0_J\rangle \to |1_I 1_J\rangle$ of Eq. (1.30), for the same system of Figure 1.5. (*Left*) The GS density of both Chrom. J and Chrom. K interacts with both the GS and ES densities of Chrom. I, shifting their energies. (*Right*) The GS density of Chrom. K and the ES density of Chrom. I interact with both the GS and ES densities of Chrom. J, shifting their energies.

tum chemistry computations, containing the GS charges of the other chromophores. *Second excitation manifold*:

$$
\begin{aligned}
\langle m_I n_J | \hat{H} | m_I n_J \rangle &= \langle m_I n_J | \left(\sum_{I=1} \hat{H}_I \right) + \hat{H}_{int} | m_I n_J \rangle = \qquad (1.30) \\
&= \sum_{K \neq I, J} \epsilon_{K_0} + \epsilon_{I_m} + \epsilon_{J_n} + \langle m_I n_J | \hat{H}_{int} | m_I n_J \rangle = \\
&= \dots \\
&= E_{GS}^* + \frac{1}{2} \left[\left(\epsilon_{I_m}^{*0} - \epsilon_{I_0}^{*0} \right) + \left(\epsilon_{J_n}^{*0 I_m} - \epsilon_{J_0}^{*0 I_m} \right) \right] + \\
&\quad + \frac{1}{2} \left[\left(\epsilon_{J_n}^{*0} - \epsilon_{J_0}^{*0} \right) + \left(\epsilon_{I_m}^{*0 J_n} - \epsilon_{I_0}^{*0 J_n} \right) \right]
\end{aligned}
$$

In order to understand the last formula one has to think about the physical process involved in the excitation of two chromophores, say I and J. Two equivalent situations can happen: first I is excited in the presence of all the others in their GS (paying $\epsilon_{I_m}^{*0} - \epsilon_{I_0}^{*0}$ energy), and then J is excited in presence of all the others in the GS except for I, which is in its excited state m (paying $\epsilon_{J_n}^{*0 I_m} - \epsilon_{J_n}^{*0 I_m}$ of energy).[14] Second, the other way round, J is excited ($\epsilon_{J_n}^{*0} - \epsilon_{J_0}^{*0}$) with all the other chromophores in their GS, and then I is excited in presence of J excited and all the other molecules in their GS ($\epsilon_{I_m}^{*0 J_n} - \epsilon_{I_0}^{*0 J_n}$). The first process is schematically described by the sequence of transitions $|0_I 0_J\rangle \to |m_I 0_J\rangle \to |m_I n_J\rangle$, while the

---

[14]Where $\epsilon_{J_n}^{*0 I_m}$ indicates the energy of molecule J in state n in presence of all the other molecules in their GS except for molecule I which is in the state m).
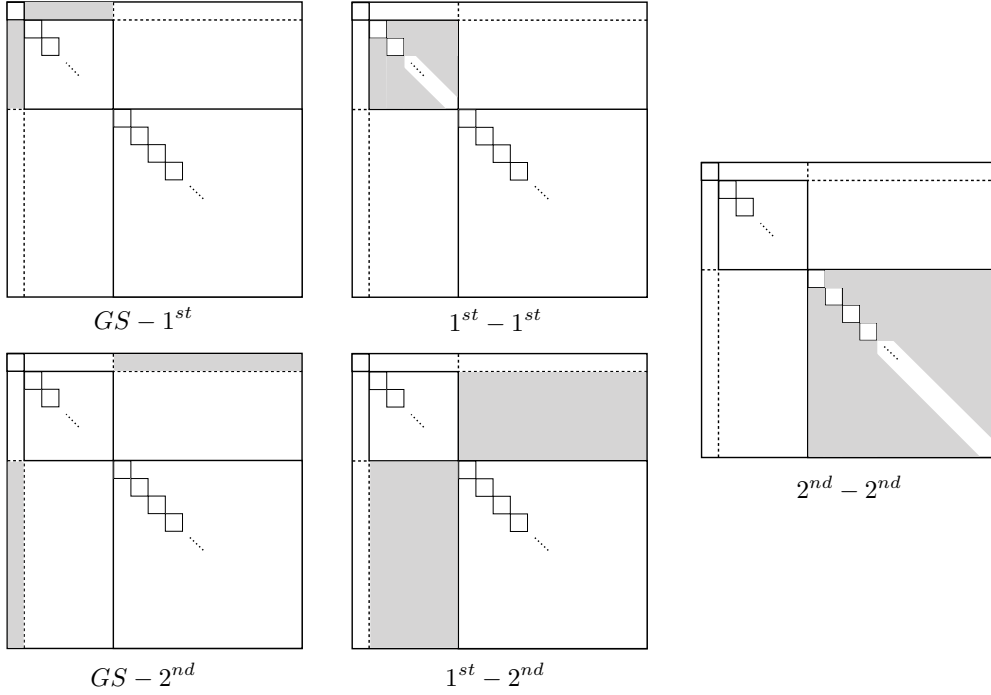
Figure 1.8: The various off-diagonal sectors of the excitonic Hamiltonian.

second process by $|0_I 0_J\rangle \to |0_I n_J\rangle \to |m_I n_J\rangle$.

If one assumes that the ES charge densities of the states of interest are similar to the GS charge density, which implies that $\epsilon_{I_m}^{*0 J_n} \simeq \epsilon_{I_m}^{*0}$, then Eq. (1.30) simplifies to

$$\langle m_i n_j | \hat{H} | m_i n_j \rangle \simeq E_{GS}^* + \left(\epsilon_{I_m}^{*0} - \epsilon_{I_0}^{*0} \right) + \left(\epsilon_{J_n}^{*0} - \epsilon_{J_n}^{*0} \right) \tag{1.31}$$

which is the sum of the global GS plus two terms which account for the necessary energy to excite chromophores I and J in presence of the "environment", given by all the other molecules in their GS.

This last approximation should be carefully checked when the chromophores of interest are very close in space (and therefore sensitive to the local details of their charge distributions) and when the permanent dipole moments of the GS and ES display large differences (as a result of the differences in the charge densities). All the computation of the present Thesis relies on this approximation.

1.2.4   Off-diagonal entries

Off diagonal entries involve both TRD-TRD and D-TRD terms. We order the various off-diagonal elements according to the various sub-sectors of the Hamiltonian, i.e.: *GS-1st excitation manifold, GS-2nd excitation manifold, 1st-1st, 1st-2nd, 2nd-2nd.*

For each given couple of states $|a_A b_B c_C \ldots\rangle$ and $|a'_A b'_B c'_C \ldots\rangle$, one can easily establish which terms of the form $\hat{V}_{IJ}$ will survive when computing the corresponding matrix element, as ruled by Eq. (1.21). We remark that in PT these off diagonal terms are weighted by the inverse of the (unperturbed) energy difference between the two considered states: this means that interaction terms between states of energetically distant manifolds will give very small contributions, which can often be neglected (e.g. we always consider the excitonic GS to be the Hartree product of the site ground states, as it does not mix with the states of the other manifolds). This is the reason why, in presenting the Frenkel Exciton model, we have assumed that the different manifold of states (GS, first-excitation and second-excitation) are decoupled.

We develop here the off-diagonal terms associated to the coupling between states belonging to the first excitation manifold. All the other terms are discussed in the Appendix (Section 5.1).

1st-1st

Two cases have to be considered: the first involves the states $\langle 0_A b_B|$ and $|a_A 0_B\rangle$, and the second involves the states $\langle a_A|$ and $|a'_A\rangle$. Then

- First case:

$$\sum_I \sum_{J \neq I} \langle 0_A b_B | \hat{V}_{IJ} | a_A 0_B \rangle \neq 0 \iff \begin{cases} I = A, J = B \implies \langle 0_A b_B | \hat{V}_{AB} | a_A 0_B \rangle \\ J = A, I = B \implies \text{similar terms} \end{cases}$$

(1.32)

  which translates in the TRD-TRD interaction term given by

$$\int d\boldsymbol{r} \int d\boldsymbol{r}' \frac{\rho^A_{0a}(\boldsymbol{r}) \rho^B_{0b}(\boldsymbol{r}')}{|\boldsymbol{r} - \boldsymbol{r}'|}$$

(1.33)

- Second case (when $a \neq a'$, as the $a = a'$ case has been already considered in the diagonal entries):

$$\sum_I \sum_{J \neq I} \langle a_A | \hat{V}_{IJ} | a'_A \rangle \neq 0 \iff \begin{cases} I = A \implies \sum_{J \neq A} \langle a_A | \hat{V}_{AJ} | a'_A \rangle \\ J = A \implies \text{similar terms} \end{cases}$$

(1.34)

  which again represents the interaction between the TRD related to the $a_A \to a'_A$ transition with all the other molecules in the ground state. This kind of correction is usually already accounted for when, in quantum chemistry

computations, the GS charges of the molecules surrounding A are included as electrostatic embedding contributions.

1.2.5   Summary

In this Chapter we have discussed the microscopic origin of the Frenkel Exciton model, showing the physical meaning of all the terms that enter in the exciton Hamiltonian. We have also explained the rationale behind the approximations usually employed in this approach, which allow to reduce the complexity of the problem and the number of microscopic inputs that have to be computed through quantum chemistry calculations. In the next Chapter we briefly outline the computational quantum chemistry techniques that have been used to obtain the results of this Thesis, and in the following Chapter we disclose the impact of intra- and interchromophoric vibrations on the description of these systems.

Computing the QM quantities of interest

The Frenkel Exciton model, in its regime of validity, provides a powerful tool for evaluate the manifold of states of systems of interacting chromophores. Nonetheless, the accuracy of the obtained manifold stands on the accuracy of the microscopic inputs which should be provided to the model, i.e. by the precision with which we access the QM properties of the aggregate constituents (the single sites/molecules). These are evaluated by solving the time-independent Schrödinger equation of each single chromophore in its environment.

There are a number of methods designed to solve the time-independent Schrödinger equation for a given molecule. We mainly distinguish between *wave-function based* methods and *density based* methods. The former, as suggested by the name, rely on the computation of the multi-electronic wave-function of the system, to a certain level of approximation. Among them, a powerful methodology which provides high accuracy with reasonable computational costs, is the so called Complete Active Space Self Consistent Field (CASSCF) method, usually employed in tandem with second order perturbation theory correction to the energy (CASPT2). *Density based* methods (DFT and TD-DFT methods) do not access the properties of the system through the computation of a wave-function, but rather they exploit the possibility to squeeze all the information contained in the (extremely complex) wave-function $\Psi(\boldsymbol{r}_1 \ldots \boldsymbol{r}_{n_{el}})$ within a (simpler) electron density $\rho(\boldsymbol{r})$. They are in general applicable to larger systems, paying the price of results dependent upon the choice of certain model parameters (i.e. the exchange correlation functional).

The results obtained in this Thesis mainly refer to computations performed with

the CASSCF/CASPT2 methodology, as it is implemented in the Molcas 8.1[10] software package.

In the following Sections we briefly review the main ideas behind the wave-function approach, focusing in particular on the computation of expectation values of interest (as excitation energies or transition dipoles), and reserving special attention to the extraction of transition densities, which enter in the evaluation of the site-site coupling terms.

2.0.1   Solution of the time-independent Schrödinger equation

Our aim is to find the stationary solutions of the (electronic, non-relativistic) time-independent Schrödinger equation

$$\hat{H}_{el}\Psi^{el} = E\Psi^{el} \tag{2.1}$$

where Ψ^{el} is a many-particle electronic wave-function, and $\hat{H}$ is the electronic molecular Hamiltonian, which in the Born-Oppenheimer approximation is given by

$$\hat{H}_{el} = \sum_{i=0}\frac{1}{2}\hat{\nabla}_i^2 - \sum_i\sum_j\frac{Z_i}{\left|\hat{\boldsymbol{R}}_i - \hat{\boldsymbol{r}}_j\right|} + \sum_i\sum_{j>i}\frac{1}{\hat{r}_{ij}} + \sum_i\sum_j\frac{Z_iZ_j}{\hat{R}_{ij}} \tag{2.2}$$

In the Born-Oppenheimer approximation, the electronic wave-function Ψ^{el} explicitly depend on the electrons coordinates and parametrically on nuclear coordinates. A proper electronic wave function must satisfy specific conditions: it has to be anti-symmetric with respect to the swap of any pair of electrons due to Pauli exclusion principle applied to the electrons (fermions), i.e.

$$\Psi^{el}\left(\boldsymbol{x}_1, \boldsymbol{x}_2, \ldots, \boldsymbol{x}_n\right) = -\Psi^{el}\left(\boldsymbol{x}_2, \boldsymbol{x}_1, \ldots, \boldsymbol{x}_n\right) \tag{2.3}$$

where $\boldsymbol{x} = (\boldsymbol{r}, s)$[1]. The multi-electronic wave-function is conveniently obtained starting from orthonormal one-electron molecular spin-orbitals $\chi(\boldsymbol{x})$, where $\chi(\boldsymbol{x})$ can be factorized in its spin $-\alpha(s)$ and $\beta(s)$, i.e., spin up and spin down $-$ and coordinate dependent $-\varphi(\boldsymbol{r})-$ components. These molecular spin-orbitals are combined in so-called Slater determinants to satisfy the antisymmetry principle of Eq. (2.3). The multi-electronic wave-function for a system of n electrons and n spin orbitals χ then reads

---

[1]The generalized coordinate $\boldsymbol{x}$ is defined by the spatial coordinate $\boldsymbol{r}$ and the spin coordinate s.

$$\Psi^{el}\left(\boldsymbol{x}_1, \boldsymbol{x}_2, \ldots, \boldsymbol{x}_n\right) = \frac{1}{\sqrt{n!}}\det\begin{pmatrix} \chi_1\left(\boldsymbol{x_1}\right) & \chi_2\left(\boldsymbol{x_1}\right) & \cdots & \chi_n\left(\boldsymbol{x_1}\right) \\ \chi_1\left(\boldsymbol{x_2}\right) & \chi_2\left(\boldsymbol{x_2}\right) & \cdots & \chi_n\left(\boldsymbol{x_2}\right) \\ \vdots & \vdots & \ddots & \vdots \\ \chi_1\left(\boldsymbol{x_N}\right) & \chi_2\left(\boldsymbol{x_n}\right) & \cdots & \chi_n\left(\boldsymbol{x_n}\right) \end{pmatrix} \tag{2.4}$$

The spatial components of the one-electron molecular orbitals (MOs) $\varphi\left(\boldsymbol{r}\right)$, are obtained as Linear Combination of Atomic Orbitals $A\left(\boldsymbol{r}\right)$ (LCAO), i.e.

$$\varphi_i\left(\boldsymbol{r}\right) = \sum_j c_{ij} A_j\left(\boldsymbol{r}\right) \tag{2.5}$$

The atomic orbitals can be either of Slater type or Gaussian type: the former are hydrogen-like orbitals, and allow to perform accurate integral evaluations, while the latter are represented by gaussian function, which make integral calculation considerably faster. Gaussian type AOs are the most common choice in quantum chemical calculations, as Slater type AOs become quickly difficult to treat for increasing molecular sizes. The use of finite basis sets of AOs, introduces a truncation error in the computations.

2.0.2 Hartree-Fock: zero-th order solution

The zero*th* order solution of the time-independent Schrödinger equation (Eq. 2.1) is the so-called Hartree-Fock (HF) solution. HF makes use of an iterative method (Self-Consistent Field, or SCF), to obtain the *best* determinant of the Slater form (Eq. (2.4)) according to the *variational principle* (where the variational degrees of freedom are the coefficients c_{ij} of Eq. (2.5)). In a system having n_{el} electrons and m AOs, the HF solution comprise $n_{el}/2$ occupied spacial MOs (further on named $\varphi_a, \varphi_b \ldots$) and $m - n_{el}/2$ virtual orbitals (named $\varphi_r, \varphi_s \ldots$).

2.0.3 Configuration Interaction

On the top of the HF solution, it is possible to enhance the flexibility of the multi-electronic wave-function (i.e. span a larger portion of the complete Hilbert space) by adding other Slater determinants. This is obtained by substituting orbitals of the virtual space with orbitals of the occupied space. The physical idea is that of considering configurations in which an electron belonging to an occupied orbital is excited to an orbital of the virtual space. The produced configurations can be

classified according to the number of interchanged spin-orbitals (singly, doubly, triply excited determinants, and so on), and the multi-electronic wave-function then reads

$$\left|\Psi^{el}\right\rangle = c_0 \left|\bar{\chi}_0\right\rangle + \sum_{r,a} c_a^r \left|\bar{\chi}_a^r\right\rangle + \sum_{rs,ab} c_{ab}^{rs} \left|\bar{\chi}_{ab}^{rs}\right\rangle + \dots \tag{2.6}$$

where $\left|\bar{\chi}_0\right\rangle$ is Hartree Fock Slater determinant, $\left|\bar{\chi}_a^r\right\rangle$ are all the possible 1-electron (index r) 1-hole (index a) Slater determinants, $\left|\bar{\chi}_{ab}^{rs}\right\rangle$ are all the possible 2-electrons (indexes r and s) 2-holes (indexes a and b) Slater determinants, and so on and so forth.

The coefficients of the linear combination of Slater determinants of Eq. (2.6) are again determined through the variational principle (so called *Configuration Interaction* (CI) procedure[14]). We note that in the limit of infinite basis functions and full CI (where all the possible interchanges of occupied and virtual orbitals are considered) the exact solution of Eq. (2.1) is obtained. In practice, one always deal with finite basis sets and truncated expansions, such as the CIS (CI-Single[17]), CISD (CI-Singles & Doubles[18]), etc.

The HF solution can also be improved by Møller-Plesset perturbation Theory up to different orders (MP2, MP3, etc.)[19]: the HF wave-function is taken as the unperturbed reference solution, and the coefficients for the different configurations (Eq. 2.6) are determined through (Rayleigh-Schrödinger) perturbation theory.

2.0.4 CASSCF (& RASSCF)

The solutions introduced so far belong to the realm of so-called *single reference* methods: they rely on a single reference, i.e. the HF solution and its MOs (which are the fixed DOFs of the CI expansion). Single reference solutions often fail to describe situations where static electron correlation is important, as happens in the description of electronic excited states. A different class of methods, the so called *multireference methods*, is here introduced.

These methods rely on the simultaneous optimization of both CI coefficients and the MOs, with a procedure called Multi-Configuration SCF (MCSCF)[8]. The MCSCF wave-function is expressed in the same form as the CI one (Eq. 2.6), but only a restricted number of excitations between selected orbital subspaces are considered, including all the needed configurations to give a proper description of the system. This procedure provides a better description of static electron correlation, and the remaining contributions, the so-called dynamical electron correlation, can then be included mainly in two ways: through Multireference Configuration Interaction (MRCI)[20], i.e. the multireference extension of the CI method, or through

the application of perturbation theory on top of the MCSCF-type calculation.

Among the various MCSCF methods, CASSCF[8] is certainly one of the most popular variations. Three different sets of MOs must be considered, belonging to the *inactive*, the *active*, and the *secondary* spaces (see Figure 2.1). While inactive and secondary MOs are fully occupied and unoccupied, respectively, a full list of configurations with flexible occupation number is constructed in what is known as the *Complete Active Space* (CAS). The selection of the active MOs is crucially important in these methods: they must include all the MOs that are relevant to describe with enough flexibility the considered problem. The main drawback of the method is the limited size of the active space that can be accessed, provided by Weyl's Formula:

$$K\left(n, N, S\right) = \frac{2S+1}{n+1} \left(\begin{array}{c} n+1 \\ \frac{1}{2}N - S \end{array} \right) \left(\begin{array}{c} n+1 \\ \frac{1}{2}N + S + 1 \end{array} \right) \tag{2.7}$$

where n is the number of MOs, N the number of electrons, and S is the total spin. The high-cost (factorial) scaling of these methods for increasing number of electrons, active space dimensions and basis sets, requires further development of the theory, as provided by the RASSCF implementation.

The *Restricted Active Space Self Consistent Field* (RASSCF) represent an extension of the CASSCF method. The full active space is here further subdivided in three parts, the so-called RAS1, RAS2 and RAS3 spaces (Figure 2.1). The active orbitals are then redistributed in these three sub-spaces according to the following rules: in RAS1 one inserts fully occupied orbitals and allows a fixed number of possible *holes*; in RAS2 one inserts orbitals with any occupation state, and a full-CI procedure is performed in this space; in RAS3 one inserts empty orbitals, and allows a fixed number of possible *excitations*. The higher the number of *holes* (in RAS1) and *electrons* (*excitations*, in RAS3) the larger the flexibility of such a RASSCF wave-function will be. A schematic representation of the CASSCF and RASSCF subspaces is given in Figure (2.1).

A way to improve the performances of CASSCF/RASSCF, especially when using large basis sets, is based on the Cholesky Decomposition technique[21]. It accelerates the calculation by eliminating or reducing as much as possible the storage and manipulation of two-electron integral matrix[2], with a minimal loss of accuracy.

The CASSCF/RASSCF methodology can be developed in two different flavors: *Single State* (SS-CASSFT) and *State Average* (SA-CASSCF)[22]. SA-CASSCF pro-

---

[2]Two-electron integrals are ubiquitous in quantum chemistry computations. In the AO basis a generic two-electron integral reads: $(\mu\nu|\lambda\sigma) = \int A_\mu(\boldsymbol{r}_1)A_\nu(\boldsymbol{r}_1)\frac{1}{r_{12}}A_\lambda(\boldsymbol{r}_2)A_\sigma(\boldsymbol{r}_2)d\boldsymbol{r}_1 d\boldsymbol{r}_2$
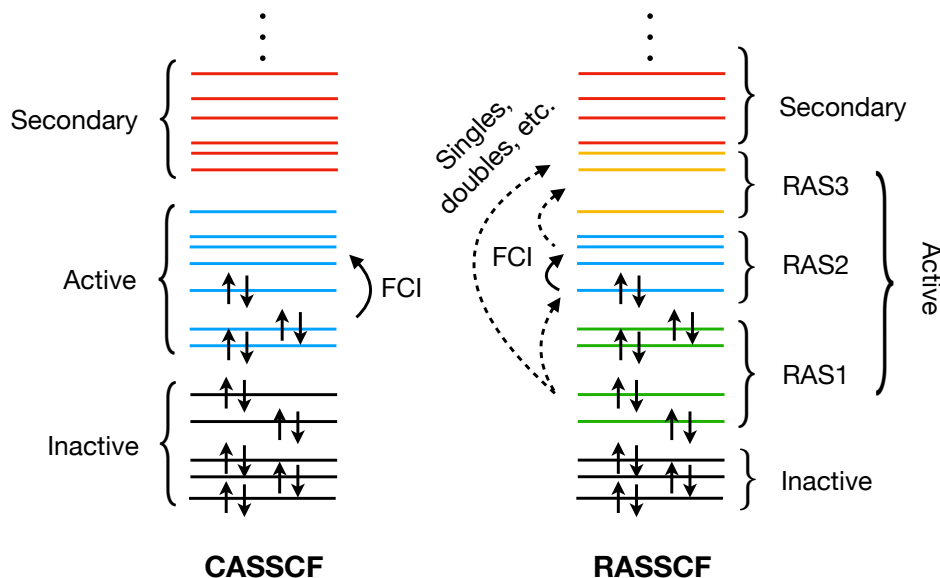
Figure 2.1: CASSCF (*left*) and RASSCF (*right*) schemes. The different configurations are built by moving electrons within the Active space. Solid arrows indicate that all the possible configurations can be built within that space; dashed arrows indicate that only a restricted number of electron configurations are allowed.

vides a more balanced description of the excited states of interest, by considering an averaged set of MOs able to describe equally well all the selected roots, and to guarantee orthogonality of the wanted roots. The ability of describing roots on an equal footing is also important for the calculation of transition properties like transition dipole moments and densities.[3]

2.0.5 CASPT2

Once CASSCF (RASSCF) wave-functions are obtained, second order perturbation theory can be applied to further refine the description of some observables. This procedure, named *Complete Active Space Second-Order Perturbation Theory* (CASPT2[9], or RASPT2[23] when RASSCF type reference wave functions are used), is the multi-configurational counterpart of the Møller-Plesset (MP2) method. The main ingredients of the PT approach are the zeroth order wave-function $|\psi_0\rangle$ (the CASSCF solution) and zeroth order Hamiltonian $\hat{H}_0$ (constructed e.g. as proposed by Andersson, Malmqvist and Roos[24]). The perturbation is computed as $\hat{H}' = \hat{H} - \hat{H}_0$, and the second order corrections to the energy is retained.

---

[3]However, attention should be given in cases where optimal MOs of different wave-functions that enter in the SA procedure differ significantly.

The CASPT2 method is also developed in two different flavors: the *Single State* (SS) and *Multi State* (MS) CASPT2[25]. In the SS-CASPT2 each computed CASSCF wave-function is taken as a reference, and PT2 corrections are performed separately for each state (unfortunately obtaining non-orthogonal SS-CASPT2 wave-functions for different states), while in the MS-CASPT2 the perturbation treatment is applied over two or more reference CASSCF states (obtaining a re-orthogonalization of the states and the reintroduction of the static correlation between them). This is important when one expects strong interaction between different CASSCF wave functions. An effective Hamiltonian is built for a number of CASSCF wave functions obtained in a state-average calculation, containing interaction matrix elements at second order between the different CASSCF states. This Hamiltonian is not symmetric in general, and one usually impose a symmetrization procedure (e.g. considering the average of corresponding off-diagonal elements). It is diagonalized to obtain the final second order energies, together with the new effective zeroth order wave functions, which are linear combinations of the original CASSCF states. This *rotation* possibly leads to states with less mixed configurations, and has to be applied to all the observables of interest (e.g. transition dipole moments and transition densities). In order for the MS-CASPT2 procedure to be applicable, the asymmetric effective Hamiltonian matrix should have small and similar off-diagonal terms. This condition can be achieved, when possible, by enlarging the active space.

The CASPT2 method relies on second order perturbation theory. As such, to be successful, the perturbation should be small. It is therefore of utmost importance that a proper selection of the active space is made in the preceding CASSCF calculation. Attention should be paid to the possible presence of *intruder states*, i.e. configurations with energies close to the reference energy E_0, which can lead to an overestimation or even singularities of the perturbation energy. Such configurations should be included in the preceding CASSCF calculation. In the cases where this is not practicable an imaginary shift (normally 0.1-0.3 a.u. in magnitude) can be applied to the denominator of the second order correction terms.

The typical error in CASSCF/CASPT2 computed excitation energies is in the range 0.0-0.2 eV.

2.0.6 Quantities of interest

Now that we have introduced the method, let us summarize the principal quantities that we are interested to obtain with it:

- **Wave-Function**, which for a generic state m is given by

$$\left|\psi_m^{CAS}\right\rangle = c_0 \left|\bar{\chi}_0\right\rangle + \sum_{r,a} c_a^r \left|\bar{\chi}_a^r\right\rangle + \sum_{rs,ab} c_{ab}^{rs} \left|\bar{\chi}_{ab}^{rs}\right\rangle + \dots \qquad (2.8)$$

where the MOs and the CI coefficients are obtained through the SA-CASSCF procedure. We will in general consider CASSCF/RASSCF wave-functions. Only in few cases, when a strong mixing of configurations is present, we will combine them according to the MS-CASPT2 rotation matrix described above.

- **Energies**, with zero-order contribution obtained from CASSCF/RASSCF estimate and second order correction through CASPT2/RASPT2 (SS in most of the cases, MS when necessary).

$$E_m = \langle\psi_m^{CAS}|\hat{H}|\psi_m^{CAS}\rangle + E_m^{(PT2)} \qquad (2.9)$$

- **Dipole Moments**, defined as

$$\boldsymbol{\mu}_{mn} = e \langle\psi_m^{CAS}|\sum_k^{n_{el}} \hat{\boldsymbol{r}}_k|\psi_n^{CAS}\rangle \qquad (2.10)$$

These quantities (as well as other properties) are obtained using the RASSI[26] (RAS State Interaction) module of Molcas.

- **Transition Densities**, defined as

$$\rho_{mn}\left(\boldsymbol{r}\right) = \langle\psi_m^{CAS}|\delta\left(\boldsymbol{r} - \boldsymbol{r}_1\right)|\psi_n^{CAS}\rangle \qquad (2.11)$$

Transition densities are not provided as output in Molcas. We developed a procedure to extract them, outlined in the Appendix, Section 5.3.

2.0.7 Transition densities: a closer look

The *single particle transition density matrix*, connecting states ψ_m and ψ_n ($m \neq n$) is defined as

$$\begin{aligned}
\rho_{mn}\left(\boldsymbol{r}\right) &= n_{el} \int \psi^*_m\left(\boldsymbol{x}_1 \dots \boldsymbol{x}_{n_{el}}\right)\psi_n\left(\boldsymbol{x}_1 \dots \boldsymbol{x}_{n_{el}}\right) d\boldsymbol{x}_2 \dots d\boldsymbol{x}_{n_{el}} ds_1 = \quad (2.12)\\
&= \langle\psi_m|\delta\left(\boldsymbol{r}_1 - \boldsymbol{r}\right)|\psi_n\rangle
\end{aligned}$$

where the integral is over all the spin variables s, and all the spatial variables except $\boldsymbol{r}_1$.

Consider two generic states ψ_m and ψ_n, expressed as in Eq. (2.8), described by the same set of molecular orbitals (i.e. obtained through the State Average procedure previously outlined). Thus

$$|\psi_n\rangle = c_0 |\bar{\chi}_0\rangle + \sum_{r,a} c_a^r |\bar{\chi}_a^r\rangle + \sum_{rs,ab} c_{ab}^{rs} |\bar{\chi}_{ab}^{rs}\rangle + \ldots \qquad (2.13)$$

$$\langle\psi_m| = h_0^* \langle\bar{\chi}_0| + \sum_{r',a'} h_{a'}^{*r'} \langle\bar{\chi}_{a'}^{r'}| + \sum_{r's',a'b'} h_{a'b'}^{*r's'} \langle\bar{\chi}_{a'b'}^{r's'}| + \ldots \qquad (2.14)$$

We now consider the expectation value $\langle\psi_m| \delta(\boldsymbol{r}_1 - \boldsymbol{r}) |\psi_n\rangle$ by expressing the two states in terms of Eqs. (2.13) and (2.14). Thus

$$\langle\psi_m| \delta(\boldsymbol{r}_1 - \boldsymbol{r}) |\psi_n\rangle = \qquad (2.15)$$

$$= h_0^* \langle\bar{\chi}_0| \delta(\boldsymbol{r}_1 - \boldsymbol{r}) \left\{ c_0 |\bar{\chi}_0\rangle + \sum_{r,a} c_a^r |\bar{\chi}_a^r\rangle + \sum_{rs,ab} c_{ab}^{rs} |\bar{\chi}_{ab}^{rs}\rangle + \ldots \right\} +$$

$$+ \sum_{r',a'} h_{a'}^{*r'} \langle\bar{\chi}_{a'}^{r'}| \delta(\boldsymbol{r}_1 - \boldsymbol{r}) \left\{ c_0 |\bar{\chi}_0\rangle + \sum_{r,a} c_a^r |\bar{\chi}_a^r\rangle + \sum_{rs,ab} c_{ab}^{rs} |\bar{\chi}_{ab}^{rs}\rangle + \ldots \right\} +$$

$$+ \sum_{r's',a'b'} h_{a'b'}^{*r's'} \langle\bar{\chi}_{a'b'}^{r's'}| \delta(\boldsymbol{r}_1 - \boldsymbol{r}) \left\{ c_0 |\bar{\chi}_0\rangle + \sum_{r,a} c_a^r |\bar{\chi}_a^r\rangle + \sum_{rs,ab} c_{ab}^{rs} |\bar{\chi}_{ab}^{rs}\rangle + \ldots \right\} + \ldots$$

In Appendix, Section 5.2, it is shown that the different elements of Eq. (2.15) can be expressed as linear combinations of products of Active Space molecular orbitals pairs. Therefore, the single particle transition density matrix itself can be written as

$$\rho_{mn}(\boldsymbol{r}) = \sum_{a,b} C_{ab}^{mn} \varphi_a^*(\boldsymbol{r}) \varphi_b(\boldsymbol{r}) \qquad (2.16)$$

The coefficients C_{ab}^{mn} summarize the contributions with which each configuration involving a certain pair of (spatial) active orbitals, φ_a and φ_b, participate to the transition of interest. For each pair of states $m - n$ the coefficients C_{ab}^{mn} form a matrix called *transition density matrix*.

Moreover, since every MO is a linear combination of atomic orbitals $A_i(\boldsymbol{r})$ (Eq. (2.5)), the transition density $\rho_{mn}(\boldsymbol{r})$ can be expanded in term of these AOs, as

$$\rho_{mn}(\boldsymbol{r}) = \sum_{a,b} C_{ab}^{mn} \varphi_a^*(\boldsymbol{r}) \varphi_b(\boldsymbol{r}) = \qquad (2.17)$$

$$= \sum_{ij} \underbrace{\sum_{a,b} c_i^{a*} C_{ab}^{mn} c_j^b}_{\tilde{C}_{ij}^{mn}} A_i^*(\boldsymbol{r}) A_j(\boldsymbol{r})$$

and $\tilde{C}_{ij}^{mn}$ is therefore the transition density matrix in atomic basis.

Note that the results of Eqs. (2.16) and (2.17), derived here for transition densities, can be generalized to describe also densities (i.e. $m = n$). In this case, one has to include in the summation of Eq. (2.16) also the orbitals of the inactive space.

The procedure we developed to extract transition densities from Molcas is outlined in Appendix, Section 5.3. From Eq. (2.16) one can see that the fundamental ingredients needed to compute the transition density $\rho_{mn}(\boldsymbol{r})$ are the transition density matrix C_{ab}^{mn} and the active orbitals $\varphi_a(\boldsymbol{r})$. The latter are usually obtained as three dimensional discrete grids of points. The quality of the obtained transition densities is therefore connected to the quality of the computed active orbitals: the grid dimension and density of $\rho_{mn}(\boldsymbol{r})$ is exactly that of the $\varphi_a(\boldsymbol{r})$.

We have designed some tests to check the quality of the computed transition densities. It is known that transition densities should return zero when integrated all over the space, and this property should be accurately reproduced also by our discrete density. Moreover, there are some observables that can be independently computed by the employed quantum chemistry software (e.g. Molcas), and through the obtained transition densities, as the transition dipole moments. We have in fact that

$$
\begin{aligned}
\boldsymbol{\mu}_{mn} &= e \langle \psi_m^{CAS} | \sum_k \boldsymbol{r}_k | \psi_n^{CAS} \rangle \\
&= e n_{el} \langle \psi_m^{CAS} | \boldsymbol{r}_1 | \psi_n^{CAS} \rangle \\
&= e n_{el} \int d\boldsymbol{r} \boldsymbol{r} \langle \psi_m^{CAS} | \delta(\boldsymbol{r} - \boldsymbol{r}_1) | \psi_n^{CAS} \rangle \\
&= e \int d\boldsymbol{r} \rho_{mn}(\boldsymbol{r}) \boldsymbol{r}
\end{aligned}
\tag{2.18}
$$

where the last integral should be performed numerically with the discrete transition density.

In our computations, with default grids, the error of the numerical transition dipoles with respect to the analytical dipoles was always smaller than 1%.

2.1 Computing the Couplings

As we have seen in Chapter 1, the general form of the interaction terms (neglecting overlaps between the chromophores of interest) involves integrals of densities and transition densities (Eq. (1.27)).

In many cases of interest (as we have already pointed out), the most important contributions that have to be calculated are the TRD-TRD interaction terms, given

$$V_{IJ} = \sum_{\alpha\beta} \sum_{\gamma\delta} \tilde{C}_{\alpha\beta} \tilde{C}_{\gamma\delta} \int d\boldsymbol{r} d\boldsymbol{r}' \; A_\alpha^{I*}(\boldsymbol{r}) A_\beta^I(\boldsymbol{r}) \frac{1}{|\boldsymbol{r}-\boldsymbol{r}'|} A_\gamma^{J*}(\boldsymbol{r}') A_\delta^J(\boldsymbol{r}')$$
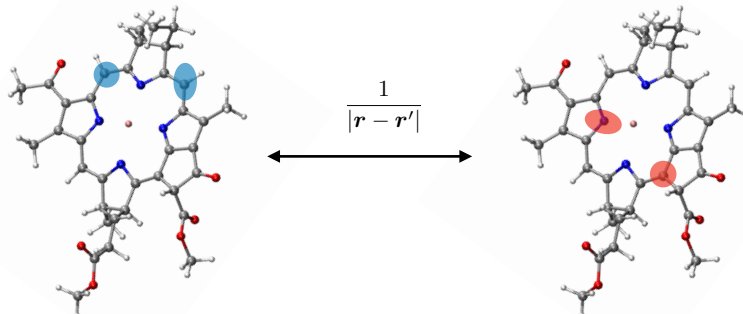
Figure 2.2: Pictorial representation of coupling between Atomic orbitals of different molecules.

by

$$V_{IJ} = \int d\boldsymbol{r} d\boldsymbol{r}' \rho_{ab}^I(\boldsymbol{r}) \frac{1}{|\boldsymbol{r}-\boldsymbol{r}'|} \rho_{cd}^J(\boldsymbol{r}') \tag{2.19}$$

The integration of Eq. (2.19) can be performed either analytically or numerically, and the two different approaches are discussed hereafter.

2.1.1 Analytical method

Transition densities can be expressed in terms of atomic basis functions, as previously shown in Eq. (2.17). The integral of Eq. (2.19) becomes a two electron integral between pairs of basis functions, one belonging to the first chromophore and the other to the second, given by

$$V_{IJ} = \sum_{\alpha\beta} \sum_{\gamma\delta} \tilde{C}_{\alpha\beta} \tilde{C}_{\gamma\delta} \int d\boldsymbol{r} d\boldsymbol{r}' \; A_\alpha^{I*}(\boldsymbol{r}) A_\beta^I(\boldsymbol{r}) \frac{1}{|\boldsymbol{r}-\boldsymbol{r}'|} A_\gamma^{J*}(\boldsymbol{r}') A_\delta^J(\boldsymbol{r}') \tag{2.20}$$

Since the form of this integral is what is routinely computed by quantum chemistry software (e.g., Molcas), and since the transition density matrices in atomic basis coefficients $\tilde{C}$ are also internally used by the software, we have implemented the calculation of the Coulomb coupling between molecules in an in-house modified version of Molcas 8.1. The results were in perfect agreement with the one computed through numerical integration, presented in the following Section.

Similar analytical formulations of the couplings have also been developed and
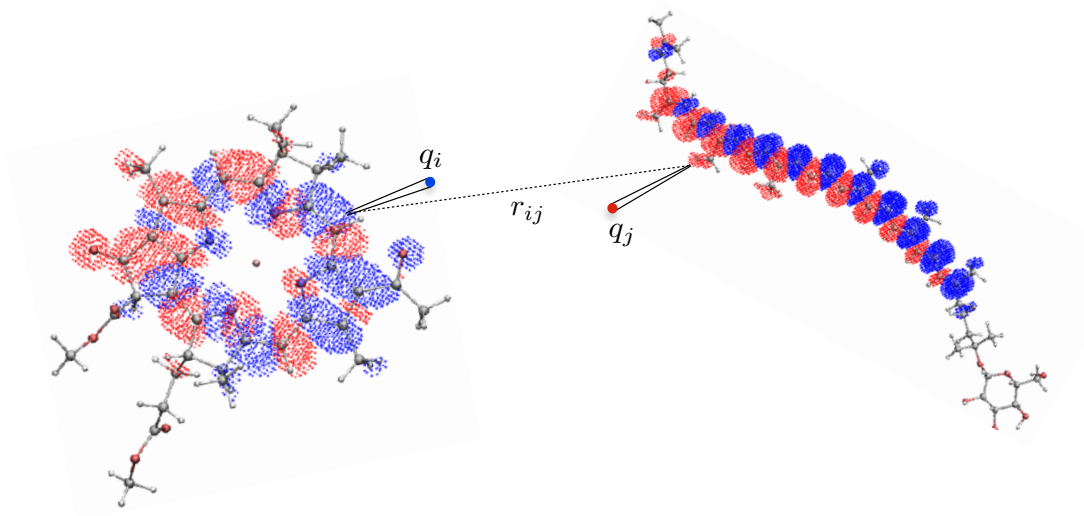
Figure 2.3: Pictorial representation of the coupling between (discrete) reduced transition densities.

used by our collaborators of the Molecolab group of Prof. Benedetta Mennucci at the University of Pisa in their in-house modified version of Gaussian 09, and now available in the last software release, Gaussian 16.

2.1.2 Numerical Method: Transition Density Cube

Discrete densities can be obtained as outlined in Appendix, Section 5.3. These are collections of coordinates (x, y, z) on a 3D grid, to which values $\rho^I(x, y, z)$ are assigned. The use of such discrete functions requires the numerical integration of equations like Eq. (2.19). Every grid point lies in a microscopic volume $d\boldsymbol{r}$, and the product $\rho^I(\boldsymbol{r})d\boldsymbol{r}$ is equal to the charge q_i contained in that volume. By replacing the integrals with discrete sums and the product of densities and integration volumes by charges, one obtains the desired numerical evaluation of Eq. (2.19), as

$$V_{IJ} = \sum_{i \in I} \sum_{i \in J} \frac{q_i q_j}{r_{ij}} \tag{2.21}$$

The sum is performed over all the points of the grids which surround the two molecules, and the numerical coupling obtained. This method is known in the literature as the *transition density cube* method (TDC).[27]

The evaluation of the double sum of Eq. (2.21) can be significantly speeded up by realizing that not all the points of the grid are equally important: the molecule has a non-uniform electron density in the grid volume, so that points close to the edge of the grid boundaries carry very small contributions. We have therefore implemented

a procedure to reduce the number of interaction terms that have to be computed, by discarding all the charges whose absolute value is smaller than a certain threshold value, chosen to be a fraction the absolute value of the largest charge in the grid. We chose the value of the threshold so that the obtained *reduced* transition densities satisfy the same checks previously mentioned (i.e., $\sum_{i \in I} q_i \simeq 0$ and $\boldsymbol{\mu}_{numerical} \simeq \boldsymbol{\mu}_{analytical}$).

Additional attention should be reserved to terms that involve very small distances r_{ij} between the charges q_i and q_j. Due to discretization errors these distances can be artificially small (or even null), leading to divergences of the coupling term. For this reason, a cutoff distance r_c should be set and interaction between charges closer then that distance discarded. Tests to check the cutoff dependence of the results were performed for the couplings computed in this Thesis, and they demonstrated it to be very weak for a large range of reasonable cutoff values.

Finally, we remark that the number of the elements that enter as coupling terms in the off-diagonal sector of the Hamiltonian can be very large, but because they are independent, they can be computed in parallel.

The TDC method presented in this Section has been employed for the calculation of the couplings between the chromophores of the LH2 system, with transition densities at the RASSCF level (see Part III, Chapter 1).

2.1.3 Approximate methods

Molecules that are sufficiently far apart will not be sensitive to the details of the charge distributions of the interacting (transition) densities. It is therefore possible to consider multipolar expansion of $\rho^I(\boldsymbol{r})$, truncated at a certain level. The most commonly employed approximation is obtained by truncating the expansion at the dipole terms, which results in the so-called *Point Dipole Approximation* (PDA). The coupling between transition densities in the PDA then reads

$$V_{IJ}^{PDA} = \frac{\boldsymbol{\mu}_{ab}^I \cdot \boldsymbol{\mu}_{cd}^J}{R_{IJ}^3} - 3 \frac{\left(\boldsymbol{\mu}_{ab}^I \cdot \boldsymbol{R}_{IJ}\right)\left(\boldsymbol{\mu}_{cd}^J \cdot \boldsymbol{R}_{IJ}\right)}{R_{IJ}^5} \qquad (2.22)$$

where $\boldsymbol{\mu}_{ab}^I$ and $\boldsymbol{\mu}_{cd}^J$ are the permanent dipoles (with $a = b$, $c = d$) or the transition dipoles (with $a \neq b$, $c \neq d$) of, respectively, chromophores I and J; R_{IJ} is the distance between the centers of mass of the two chromophores. This approximation can be used as long as R_{IJ} is larger than the spatial extension of the chromophores. While in many cases it is preferable to compute the complete coupling between chromophores, using Eq. (2.19), the PDA approximation provides a simple and easily interpretable (qualitative) picture of the molecular aggregate. Moreover it is
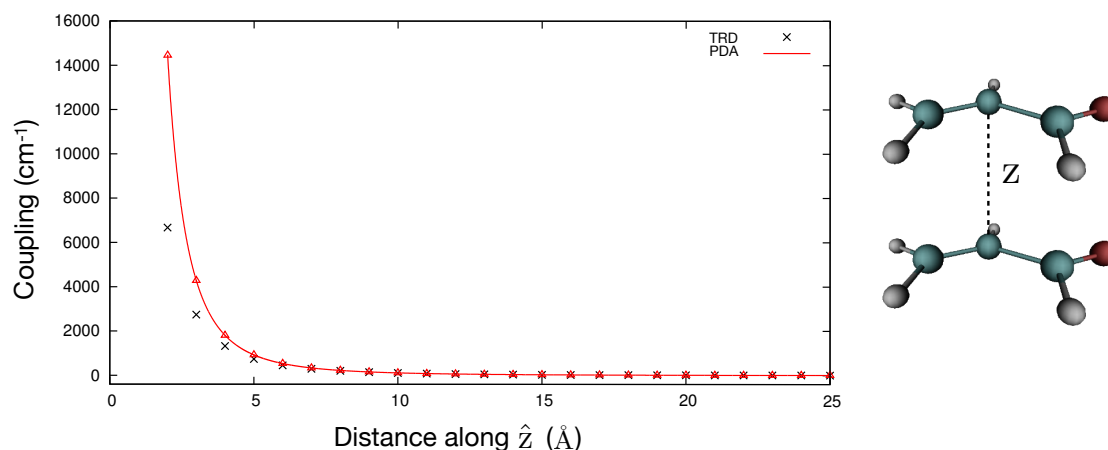
Figure 2.4: Comparison between PDA and full TRD coupling between two identical acrolein molecules, by varying their distance along the z axis.

relatively easy to obtain the transition dipole moments from experiments, so that an estimate of the coupling could be given in principle without a single quantum chemistry computation.

In Figure 3.1 we show the comparison between full TRD-TRD Coulomb couplings and PDA couplings, computed for a dimer of acrolein molecules at different distances. The spatial extension of the acrolein molecule is about $5\overset{\circ}{A}$, and indeed the PDA produces the worst results for distances below this threshold value. Above these value the two methods give the same results.

Coupling to vibrations

Real systems are characterized by the presence of intra- and inter-molecular vibrations, responsible for the fluctuations of the excitation energies. These contributions are fundamental to properly describe the behavior of excited aggregates of molecules: e.g. they drive exciton migration and are responsible for fluctuation and dissipation mechanisms, and thus for the line-shape of recorded spectra. What we have considered so far is just the *system* part of a more complete Hamiltonian, comprising a bath of vibrations coupled to the electronic degrees of freedom. The complete Hamiltonian then reads

$$\hat{H} = \hat{H}_S + \hat{H}_B + \hat{H}_{SB} \tag{3.1}$$

where $\hat{H}_S$ and $\hat{H}_B$ are the system and bath Hamiltonian, and $\hat{H}_{SB}$ is the interaction between the two. In the model that we are going to discuss in this Section, the three terms of Eq. (3.1) are given, respectively, by[28]

$$\hat{H}_S = \sum_i^N \epsilon_i \left| i \right\rangle \left\langle i \right| + \sum_{i \neq j} V_{ij} \left| i \right\rangle \left\langle j \right| \tag{3.2}$$

$$\hat{H}_B = \sum_i^N \sum_{m_i}^{M_i} \frac{1}{2} \left(\hat{P}_{m_i}^2 + \omega_{m_i}^2 \hat{Q}_{m_i}^2 \right) \otimes \hat{\mathbb{1}} \tag{3.3}$$

$$\hat{H}_{SB} = \sum_i^N \sum_{m_i}^{M_i} c_{m_i} \hat{Q}_{m_i} \left| i \right\rangle \left\langle i \right| \tag{3.4}$$

The system-bath interaction is here assumed to have a linear dependence on both the electronic DOFs (the excited state populations $\left| i \right\rangle \left\langle i \right|$) and the bath (mass-
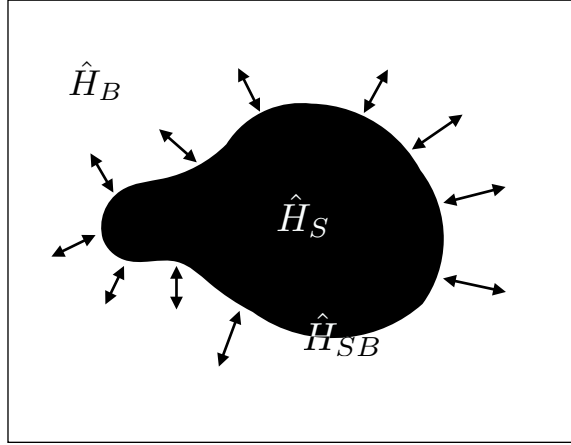
Figure 3.1: Pictorial representation of an open quantum system S interacting with its environment (bath) B.

weighted) coordinates $\boldsymbol{Q}$. Moreover, different modes are supposed to be independent. The bath of each chromophore i is therefore modeled as a collection of *independent harmonic modes*, described by nuclear phase space variables (P_{m_i}, Q_{m_i}), bilinearly coupled to chromophore excitations. The coefficients c_{m_i} control the strength of the interaction of excited chromophore i to the m-th mode of its harmonic bath, whose frequency is ω_{m_i}

The Hamiltonian H can also be rewritten in the exciton basis $(|\alpha\rangle = \sum_i A_{\alpha i} |i\rangle)$ as:

$$\hat{H} = \sum_\alpha^N \epsilon_\alpha |\alpha\rangle \langle\alpha| \tag{3.5}$$

$$+ \sum_i^N \sum_{m_i}^{M_i} \frac{1}{2} \left(\hat{P}_{m_i}^2 + \omega_{m_i}^2 \hat{Q}_{m_i}^2 \right) \otimes \hat{\mathbb{1}} \tag{3.6}$$

$$+ \sum_{\alpha\beta} \left[\sum_i^N \sum_{m_i}^{M_i} A_{\alpha i}^* A_{\beta i} c_{m_i} \hat{Q}_{m_i} \right] |\alpha\rangle \langle\beta| \tag{3.7}$$

We note that the system-bath interaction term $\hat{H}_{SB}$, which was diagonal in the site representation, contributes here also to the off-diagonal sector of the exciton Hamiltonian. We will show how diagonal terms describe the energy fluctuation of the exciton states, while off-diagonal contributions drive the population transfer between excitons.

In the following Sections we introduce a convenient way of representing the coupling to the various modes m, which is the so-called *spectral density* function. This function will enter explicitly in the simulation of the spectroscopy of multi-

chromophoric systems, and will be extensively used in the next Part of the Thesis.

3.1 Spectral density

3.1.1 Definition

The spectral density function *summarizes the properties of the system-bath coupling* described above: the spectral density $J_i(\omega)$ for chromophore i is defined as[29]:

$$J_i(\omega) \equiv \frac{\pi}{2} \sum_{m_i}^{M_i} \frac{c_{m_i}^2}{\omega_{m_i}} \delta(\omega - \omega_{m_i}) \tag{3.8}$$

The frequencies of the modes are denoted as ω_{m_i}, and their coupling strengths to the excited state as c_{m_i}. These are the same parameters which enter in Eqs. (3.2-3.4).

3.1.2 Spectral Density & the Displaced Harmonic Oscillator model

Within the framework of the previously introduced bath of harmonic oscillators linearly coupled to the system degrees of freedom, a simple relation between the ground state (GS) and excited state (ES) Potential Energy Surfaces (PES) properties and the couplings c_{m_i} can be established.

Let us consider, for simplicity, a molecule with a single vibrational normal mode Q[1]. Within the displaced harmonic oscillator (DHO) model, the ground and the electronically excited state PES are harmonic wells along the common bath coordinate Q (and reduced mass m), having the same frequency ω_0 but different equilibrium geometries (Figure 3.2). In the GS the bath mode is assumed to oscillate around d_g (which can be set to zero without any loss of generality), while the ES potential is spatially shifted so that the bath mode oscillates around d_e when the molecule is electronically excited. The assumption of harmonic modes is indeed reasonable for many systems, as generic GS and ES PES can very often be viewed at least as *locally* harmonic[2].

The Hamiltonian of Eq. (3.1), including also the GS explicitly, is here given by:

$$\hat{H} = \hat{T} + \underbrace{\epsilon_g + \frac{1}{2} m \omega_0^2 Q^2}_{V_g(Q)} + \underbrace{\epsilon_e + \frac{1}{2} m \omega_0^2 (Q - d_e)^2}_{V_e(Q)} \tag{3.9}$$

---

[1]The present treatment can be easily extend to an arbitrary number of modes.

[2]Nonetheless we note that here we are not only assuming that GS and ES PES are harmonic, but also that they have the same curvature, which is a stronger assumption.
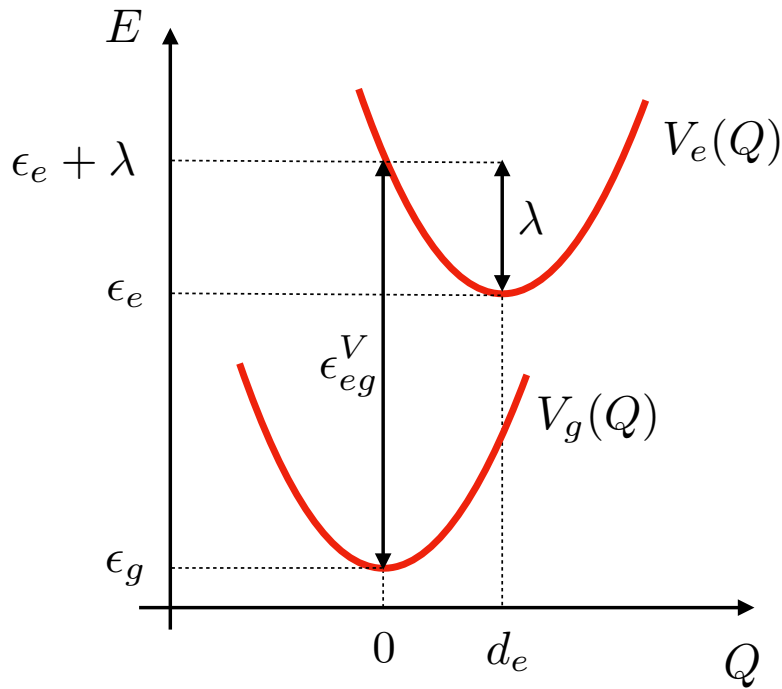
Figure 3.2: Pictorial representation of the DHO model: GS and ES PES (given by the potentials $V_g(Q)$ and $V_e(Q)$, respectively) are described by the same harmonic well displaced along the mode coordinate Q by means of d_e (the equilibrium geometry of the ES). The vertical energy is given by the difference between ϵ_e and ϵ_g plus the reorganization energy λ, which describes the energy that the chromophore loses into the bath by relaxing from the initial (out of equilibrium position) $Q = 0$ to $Q = d_e$.

where $\hat{T}$ is the total kinetic energy, $V_g(Q)$ and $V_e(Q)$ are the GS and ES PES, respectively, and ϵ_g and ϵ_e are the energies of the minima of the two PES. The energy gap between the two curves (as a function of the coordinate Q) can thus be defined by using V_g as a reference:

$$
\begin{aligned}
\delta_{eg}(Q) &= V_e(Q) - V_g(Q) \\
&= \Delta\epsilon_{eg} - m\omega_0^2 d_e Q + \frac{1}{2}m\omega_0^2 d_e^2
\end{aligned}
\tag{3.10}
$$

and $\Delta\epsilon_{eg}$ represents the adiabatic excitation energy of the transition $g \to e$. The last term on the right hand side of Eq. (3.10) is the so-called *reorganization energy* λ:

$$
\lambda = \frac{1}{2}m\omega_0^2 d_e^2
\tag{3.11}
$$

and represents the energy that the chromophore loses to the bath (in this case the unique harmonic oscillator) in relaxing from the Franck-Condon point (located at

$d_g = 0$), a non equilibrium configuration of the bath on the excited-state PES, to the new equilibrium position, determined by the ES PES minimum, d_e (see Figure 3.2).

We can rewrite the reorganization energy by introducing the dimensionless Huang-Rhys factor for the bath mode, S, thus obtaining

$$\lambda = \hbar\omega_0 S \tag{3.12}$$

S represents the number of vibrational quanta, $\hbar\omega_0$, that are equivalent to the amount of energy associated to the reorganization energy of the mode of interest.

By comparing Eq. (3.10) with the Hamiltonian components Eqs. (3.2-3.4) one can identify the connection between the system-bath coupling constant and the parameters of the DHO model, as:

$$c = m\omega_0^2 d_e = \sqrt{\lambda}\omega_0 = \sqrt{\hbar\omega_0 S}\omega_0 \tag{3.13}$$

and

$$\lambda = c^2/(2\omega_0^2) \tag{3.14}$$

When considering M independent modes, one should account for the contributions from M reorganization energies λ_m and M associated Huang-Rhys factors S_m. The total reorganization energy of the considered chromophore i is simply the sum of the individual chromophore bath mode reorganization energies, i.e. $\lambda_i = \sum_{m_i} \lambda_{m_i}$ and $S_i = \sum_{m_i} S_{m_i}$.

The coupling constants c_{m_i} are interpreted in the same simple way as for the single harmonic oscillator, obtaining (in mass-weighted coordinates)

$$|c_{m_i}| = \omega_{m_i}^2 |\left(d_{m_i}^e - d_{m_i}^g\right)| = \sqrt{\lambda_{m_i}}\omega_{m_i} = \sqrt{\hbar\omega_{m_i}S_{m_i}}\omega_{m_i} \tag{3.15}$$

$$\lambda_{m_i} = c_{m_i}^2/2\omega_{m_i}^2 \tag{3.16}$$

The spectral density in Eq. (3.8) can then be rewritten as

$$J_i(\omega) = \pi \sum_{m_i}^{M_i} \omega_{m_i}\lambda_{m_i}\delta\left(\omega - \omega_{m_i}\right) \tag{3.17}$$

and the total reorganization energy for chromophore i can be computed from $J_i(\omega)$ as

$$\lambda_i = \frac{\hbar}{\pi}\int_0^\infty d\omega \frac{J_i(\omega)}{\omega} \tag{3.18}$$

Finally, we note that vertical transition energy ϵ_e^V is obtained as the difference

between the two PESs at the equilibrium geometry of the ground state, i.e. as the sum between the adiabatic energy $\Delta\epsilon_{eg}$ and the reorganization energy λ,

$$\epsilon_{eg}^{V} = \Delta\epsilon_{eg} + \lambda \tag{3.19}$$

3.1.3 Spectral Density & Energy-Gap Fluctuation auto-correlation

As shown in Eq. (3.10), the excitation energy of chromophore i varies linearly as a function of its harmonic bath coordinates, i.e., excluding all constant terms:

$$\delta_{\epsilon_i} = \sum_{m_i} c_{m_i} Q_{m_i} \tag{3.20}$$

For each chromophore i we can define the excitation energy fluctuation auto-correlation function as

$$C_i(t) = \langle \delta_{\epsilon_i}(0)\delta_{\epsilon_i}(t) \rangle = \sum_{m_i} c_{m_i}^2 \langle Q_{m_i}(0)Q_{m_i}(t) \rangle \tag{3.21}$$

where the symbol $\langle \bullet \rangle$ indicates the equilibrium ensemble average over thermal distribution of the states of the harmonic bath.

The average can be performed in the limit of classical harmonic bath, thus obtaining

$$C_i^{cl}(t) = \frac{1}{\beta} \sum_{m_i} \left(\frac{c_{m_i}^2}{\omega_{m_i}^2} \right) \cos(\omega_{m_i}t) \tag{3.22}$$

while for an exact description of the "quantum" bath DOFs we have[3][29]

$$C_i^{qm}(t) = \frac{\hbar}{2} \sum_{m_i} \left(\frac{c_{m_i}^2}{\omega_{m_i}} \right) \left[\coth\left(\frac{\beta\hbar\omega_{m_i}}{2} \right) \cos(\omega_{m_i}t) - i\sin(\omega_{m_i}t) \right] \tag{3.23}$$

The connection between this auto-correlation function and the spectral density is readily obtained as[4]

$$J^{cl}(\omega) = \beta\omega \int_0^\infty dt C^{cl}(t)\cos(\omega t) \tag{3.24}$$

$$J^{qm}(\omega) = \frac{2}{\hbar}\tanh\left(\frac{\beta\hbar\omega}{2} \right) \int_0^\infty dt\,\mathrm{Re}[C^{qm}(t)]\cos(\omega t) \tag{3.25}$$

In the next Section we show how to compute the parameters which enter in the

---

[3]Note that $C_i^{qm}(t) \to C_i^{cl}(t)$ for $\hbar \to 0$, as $\coth(x) \simeq 1/x$ for small values of x.

[4]These results are obtained by multiplying Eqs. (3.22) and (3.23) by $cos(\omega t)$, and using the fact that $\int_{-\infty}^{+\infty} dt e^{i\omega t} = 2\pi\delta(\omega)$.

spectral density function. As stated above, spectral densities are at the core of the simulations of spectroscopic techniques, as they encode the bath induced energy fluctuations and energy transport between exciton states. We will therefore review the role of these functions in the next Part of the Thesis.

3.1.4   Spectral density evaluation: Microscopic Ingredients

The Spectral density of a given chromophore i contains the information of both intra- and inter-molecular vibrations. It is convenient [28, 11] to decompose it into two parts[28]

$$J_i(\omega) = J_i^{intra}(\omega) + J_i^{inter}(\omega) \tag{3.26}$$

where $J_i^{intra}(\omega)$ contains all the intra-chromophore vibrations contributions, and $J_i^{inter}(\omega)$ accounts for all the vibrational contributions caused by the environment. The decomposition is a reliable approximation as energy fluctuations caused by inter- and intra- molecular vibrations (i.e. by short- and long- range interactions) can be considered uncorrelated in many cases of interest.

Within this approximation, the $J_i^{inter}(\omega)$ part of the spectral density can be evaluated from MD trajectories, by the cosine transform of the energy gap fluctuation correlation function along the computed classical path (Eq. (3.24)). The chromophore is kept frozen to avoid double counting of its own frequencies, which will be included in the $J_i^{intra}(\omega)$ term. The intermolecular part of the spectral density usually contains a quasi-continuum of low frequency contributions, and it is often substituted by analytic model functions that mimic its behavior. One of the most commonly employed models is the overdamped Brownian oscillator (OBO)[30, 31], whose spectral density is given by

$$J(\omega) = 2\lambda \frac{\omega/\gamma}{(\omega/\gamma)^2 + 1} \tag{3.27}$$

where λ is the reorganization energy and γ is the damping constant. The inverse of γ gives the bath relaxation time.

The $J_i^{intra}(\omega)$ part of the spectral density is preferably calculated in a different way: there is in fact no guarantee that the force field parameters of MD simulations are accurate enough to reproduce intra-molecular frequencies and reorganization energies[5]. Instead, the needed parameters are calculated by exploiting the simple geometrical ideas introduced for the DHO model, i.e. by computing the frequency of the modes and the displacement of the ES PES with respect to the GS PES through

---

[5]In fact it has been demonstrated that in general they are not[28].
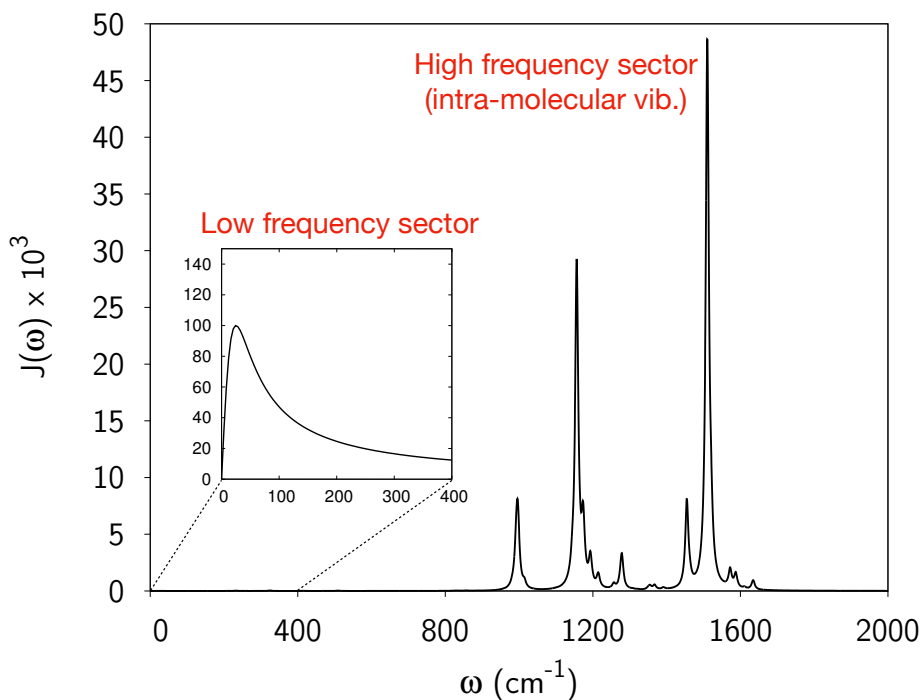
Figure 3.3: Pictorial representation of a spectral density. The low frequency sector displays a OBO with parameters $\gamma = 25$ cm^{-1} and $\lambda = 100$ cm^{-1}. The peaks of the high frequency sector were broadened by means of a weak damping factor γ_d = 5 cm^{-1}. Inter-molecular vibrations fall in the low frequency sector.

accurate quantum chemistry computations. This can be achieved in different ways:

- In the *vertical gradient* approach[11] the structure of e.g. chromophore i is relaxed on its GS (by means of a geometry optimization). Then a normal mode analysis provides the intra-molecular vibration frequencies ω_{m_i} and normal modes $\boldsymbol{Q}_{m_i}$ of the individual chromophore i. Next, the assumption that the same modes and frequencies can describe both the GS and the ES PES is applied, implying that the only difference between the two surfaces is in their vertical and horizontal displacements (by means of the adiabatic excitation energy and the difference in equilibrium positions, respectively). The system bath coupling (as well as the offset between the ground and excited states surfaces) is then obtained by evaluating the gradient to the excited state at the ground state equilibrium geometry:

$$
\begin{aligned}
\nabla_{\boldsymbol{Q}|\boldsymbol{Q}=\boldsymbol{d}_g} V_e(\boldsymbol{Q}) &= \nabla_{\boldsymbol{Q}|\boldsymbol{Q}=\boldsymbol{d}_g} \left[\sum_{m_i} \frac{1}{2} \omega_{m_i} (\boldsymbol{Q}_{m_i} - \boldsymbol{d^e}_{m_i})^2 \right] \\
&= -\sum_{m_i} \omega_{m_i} (\boldsymbol{d}^e_{m_i} - \boldsymbol{d}^g_m) \\
&= -\boldsymbol{c}_{m_i}
\end{aligned}
\tag{3.28}
$$

The vertical gradient approach has been applied in this Thesis for the computation of the spectral densities for the LH2 chromophores (Part III, Chapter 1), and for the spectral densities of some states of the azobenzene molecule (Part III, Chapter 3).

- A different approach to the computation of the coupling is given by the direct evaluation of the two equilibrium geometries $\boldsymbol{d}_g$ and $\boldsymbol{d}_e$, of the GS and ES state PES respectively. A ground state optimization and normal mode analysis are performed, followed by another optimization on the excited state surface: the difference, along each mode, of the GS and ES minima coordinates returns the surfaces displacements, and hence the coupling by means of Eq. (3.15). We note that in this kind of analysis, global translational and rotational DOFs have to be removed prior to computing the difference in Cartesian coordinate. Furthermore, it is paramount that both geometries used to compute $\Delta \boldsymbol{d} = (\boldsymbol{d}_e - \boldsymbol{d}_g)$ have been optimized at the same level of theory in order to avoid spurious contributions to the spectral density.

This second approach is generally more expensive from the computational point of view. Nonetheless, when the mixing between multiple states makes the computations of the vertical gradient unfeasible (e.g. near a conical intersection), it represents a solid alternative. It has been for example applied for the calculations of some of the spectral density parameters in the azobenzene study (see Part III, Section 3.5.6).

The intra-molecular spectral density is generally characterized by high-frequency discrete peaks (Figure 3.3), that can be broadened by gaussian or lorentzian functions to take into account for the finite vibrational life-time and the inhomogeneous distribution of vibrational frequencies.[28]

3.1.5   Summary

Let us summarize the approximations employed in the presented modeling of the system-bath coupling. The bath of vibrations has been introduced as a set of independent harmonic oscillators. The coupling between electronic states and bath modes has been assumed to be linear. The DHO model allows for simple connection between the model parameters of Eqs. (3.2-3.4) and geometrical properties of ground and excited surfaces:

- GS and ES PES are described by harmonic wells;

- They are characterized by the same modes and the same mode frequencies $\boldsymbol{\omega}$;

- They are displaced with respect to each the other by means of $\Delta \boldsymbol{d} = (\boldsymbol{d}_e - \boldsymbol{d}_g)$;

Spectral densities, reorganization energies and Huang-Ryes factors can be rewritten in term of the *geometric* parameters $\boldsymbol{d}$ and normal mode frequencies $\boldsymbol{\omega}$. The bilinear coupling $\boldsymbol{c}$, that controls the strength of the interaction between nuclear and electronic coordinates, can also be rewritten in terms of the DHO quantities as: $c_m = \omega_m^2(d_m^e - d_m^g)$. Some additional consideration and the extension of the presented model to higher lying states are summarized in Appendix, Section 5.4.

In the next Part of the Thesis, when the simulation of spectroscopy will be introduced, we will also assume that certain operators do not depend on the nuclear coordinates. This is for example the case of the dipole operator $\hat{\boldsymbol{\mu}}$, which in the Condon approximation depends just on the considered initial and final electronic states.

Energy Transport theories

The first recorded observation of energy transfer between chemical species is dated 1922: while studying a mixture of mercury and thallium vapor, it was observed [32] that thallium emitted fluorescence when mercury was excited. The concept of energy transfer has since then evolved, but the basic ingredients are the same: a donor (atom, molecule or group of molecules), excited e.g. by an external electromagnetic radiation, *transfers* the absorbed energy to an acceptor (atom, molecule or group of molecules) and this connection is revealed because donor specific absorption results in acceptor-specific spectral signatures (e.g. acceptor emission).

Photosynthetic systems are extremely optimized for transferring absorbed sunlight to reaction centers. The astonishing efficiency with which they exploit excitation energy transfer pathways to funnel the energy throughout the photosynthetic units, even at physiological temperatures, being subjected to the many dissipating processes, has not been fully understood, and it remains an active research topic. Photosynthetic organisms seem to have evolved not only to cope with, but also to take advantage of thermal disorder effects for efficient light-harvesting function. It is still a matter of great interest and dispute in the literature, how prevalent and effectual are purely quantum-mechanical forms of transport under normal conditions (room temperature) for photosynthesis.[33, 34, 35]

The theoretical study of energy transfer in photosynthetic complexes is aimed at shedding new light on the problem, by unraveling the microscopic origin of different EET mechanisms and explaining measured transfer rates.

Energy transport theories are usually grouped according to the relative strength

of inter-molecular and system-bath coupling. Förster theory of energy transfer, e.g., assumes that the system-bath coupling is stronger than that between the molecules. Redfield theory consider the other limit, in which the system is dominated by the coupling between the molecules. In the former case, the excitation is localized on single chromophores, and undergoes incoherent hopping steps to move from localize donor to localized acceptor states. In the latter theory, the strength of inter-molecular coupling is such that the excitation is delocalized on the interacting donor-acceptor pair, and the energy transfer mechanism involves coherent steps, in which the energy is periodically transferred by a traveling wave-packet from one system to the other in a time-dependent fashion. The classification of these mechanisms according to the inter-exciton versus exciton-bath energy criterium, can also be viewed in the time domain: if the transfer time (due to quantum interaction between the molecules) is larger than the typical relaxation time (due to *collisions* with the environment), the localized picture is more adequate; if on the other hand, the transport time is smaller than the typical relaxation time, a coherent transport mechanism, bridged by delocalized states, is likely to occur.

Viewed either in the time or in the energy domain, this classification boils down to the idea that some descriptors of the system are smaller with respect to other, i.e. that some terms of the Hamiltonian can be treated perturbatively. In what follows we consider the global Hamiltonian of the system to be given in the form of Eq. (3.1), and present Förster and Redfield approaches, obtained considering either H_{SB} or the Coulomb coupling between sites to be the perturbative $\hat{H}'$ term, recasting all the other terms in the reference Hamiltonian $\hat{H}_0$.

The state of an open quantum system (e.g., a system which is coupled to a bath of vibrations), is appropriately described by the density matrix operator $\hat{\rho}$. We will make use of it in the following Sections, while extensively reviewing its properties in Part II, Section 2.1.

4.1   Förster energy transport

Within the *Förster Resonant Energy Transfer* (FRET) theory, the Hamiltonian is written as follows:

$$
\begin{aligned}
\hat{H}_0 &= \underbrace{\sum_i \epsilon_i \left| i \right\rangle \left\langle i \right|}_{H_{el}} + \underbrace{\sum_i^N \sum_{m_i}^{M_i} \frac{1}{2}\left(\hat{P}_{m_i}^2 + \omega_{m_i}^2 \hat{Q}_{m_i}^2\right)\mathbb{1}}_{H_B} + \underbrace{\sum_i^N \sum_{m_i}^{M_i} c_{m_i}\hat{Q}_{m_i}\left| i \right\rangle \left\langle i \right|}_{H_{SB}} \\
\hat{H}' &= \underbrace{\sum_{i \neq j} V_{ij} \left| i \right\rangle \left\langle j \right|}_{H_{coul}}
\end{aligned}
\tag{4.1}
$$

In the context of time-dependent perturbation theory, the Fermi Golden Rule gives the probability of the system to migrate from an initial to a final states (given respectively by donor excited with the acceptor in the ground state, and acceptor excited while the donor is in the ground state) via the perturbation $\hat{H}'$.[16]

This leads to the well known Förster rate matrix, which reads:

$$
K_{n,m} = \frac{|V_{mn}|^2}{2\pi}\int_{-\infty}^{+\infty} d\omega\, F_m(\omega)A_n(\omega)
\tag{4.2}
$$

The rate between the donor m and the acceptor n is given by the square of the coupling (a dominant characteristic of FRET) times the so-called *overlap integral*. The overlap integral is related to the optical spectral overlap between the normalized absorption spectrum $A_n(\omega)$ of the acceptor and the normalized fluorescence spectrum $F_m(\omega)$ of the donor. Since the donor-acceptor coupling is assumed to be very small, the spectrum of the donor-acceptor couple is identical to that of the individual non-interacting constituents in the same environment, which is what makes this theory so attractive: the excitation energy transfer (EET) rate is given in terms of easily accessible experimental observables rather than in terms of computed quantities[1]. For molecules sufficiently distant, the coupling can be expressed as a transition-dipole transition-dipole interaction, which results in Förster's famous R^{-6} dependence of FRET rates.[36]

Förster theory can be extended by considering weakly coupled domains of delocalized states (i.e. excitons describing groups of strongly interacting chromophores). This is the so-called *Generalized Förster* theory.

---

[1]Overlap integrals can nonetheless be computed, as so-called *Frank Condon Weighted density of states*, see e.g. [16]

4.2 Redfield energy transport

Within the *Redfield* theory of transport, the Hamiltonian can be written as

$$
\begin{aligned}
\hat{H}_0 &= \underbrace{\sum_i \epsilon_i \left|i\right\rangle\left\langle i\right|}_{H_{el}} + \underbrace{\sum_{i\neq j} V_{ij}\left|i\right\rangle\left\langle j\right|}_{H_{coul}} + \underbrace{\sum_i^N \sum_{m_i}^{M_i} \frac{1}{2}\left(\hat{P}_{m_i}^2 + \omega_{m_i}^2 \hat{Q}_{m_i}^2\right)\hat{\mathbb{1}}}_{H_B} \\
\hat{H}' &= \underbrace{\sum_i^N \sum_{m_i}^{M_i} c_{m_i}\hat{Q}_{m_i}\left|i\right\rangle\left\langle i\right|}_{H_{SB}}
\end{aligned}
\tag{4.3}
$$

It is convenient to rewrite all terms in the exciton basis ($\left|\alpha\right\rangle = \sum_i A_{\alpha i}\left|i\right\rangle$), as in Eqs. (3.7), so that

$$
\hat{H}' = \sum_{\alpha\beta} A_{\alpha i}^* A_{\beta i} \overbrace{\underbrace{\left[\sum_i^N \sum_m^{M_i} c_{m_i}\hat{Q}_{m_i}\right]}_{\delta_{\epsilon_i}(\boldsymbol{Q}_i)}}^{\delta_{\epsilon_{\alpha\beta}}(\boldsymbol{Q})}\left|\alpha\right\rangle\left\langle\beta\right|
\tag{4.4}
$$

As previously noted, the excitonic mixing of localized states give rise to off-diagonal elements in the electron-phonon coupling H_{SB} (Eq. 4.4), which cause relaxation between exciton states.

Using second order cumulant expansion (see next Part of the Thesis), the two-point quantum correlation function between energy gap Hamiltonians in exciton basis is found, and it is linked to the two-point correlation of site energy gap Hamiltonians:

$$
\underbrace{C_{\alpha\beta\gamma\delta}(t)}_{\langle\delta\epsilon_{\alpha\beta}(t)\delta\epsilon_{\gamma\delta}(0)\rangle} = \sum_i A_{\alpha i}^* A_{\beta i} A_{\gamma i}^* A_{\delta i}\ \underbrace{C_i(t)}_{\langle\delta\epsilon_i(t)\delta\epsilon_i(0)\rangle}
\tag{4.5}
$$

$C_i(t)$ was previously introduced in Eq. (3.21), and its connection to the site spectral density established. We can similarly connect $C_{\alpha\beta\gamma\delta}(t)$ to different spectral densities. As an example, for an exciton state α, we have that

$$
C_{\alpha\alpha\alpha\alpha}(t) = \sum_i |A_{\alpha i}|^4\, C_i(t)
\tag{4.6}
$$

so that

$$
J_\alpha(\omega) = \sum_i |A_{\alpha i}|^4\, J_i(\omega)
\tag{4.7}
$$

The electronic part of density matrix is also rewritten in the exciton basis as

$$\rho^{exc} = \mathbf{A}^{\dagger} \rho^{site} \mathbf{A} \tag{4.8}$$

and the Redfield equation is obtained:[37, 16]

$$\frac{\partial}{\partial t} \rho_{ab}^{exc}(t) = -i\omega_{ab}\rho_{ab}^{exc}(t) + \sum_{cd} R_{ab,cd}\rho_{cd}^{exc}(t) \tag{4.9}$$

Eq. (4.9) is valid when H_{SB} is a perturbation and we further assume that the so-called Redfield tensor $R_{ab,cd}$ is time independent, which is true in the Markovian limit. The first term of the equation describes the coherent evolution of the excitons according to H_0, while the second term describes the relaxation dynamics induced by the coupling with bath fluctuations H_{SB}.

The Redfield tensor can be expressed (by Fourier transform) in terms of the spectral densities computed from Eq. (4.5), and different relaxation processes can be distinguished[16]:

- Population relaxation ($R_{aa,aa}$);

- Population transfer ($R_{aa,bb}$, $a \neq b$);

- Coherence dephasing ($R_{ab,ab}$, $a \neq b$);

- Coherence mixing ($R_{ab,cd}$, $a \neq b \neq c \neq d$);

- Population conversion into coherence ($R_{ab,bb}$, $a \neq b$);

- Coherence conversion into population ($R_{aa,bc}$, $a \neq b \neq c$);

In the so-called *secular* approximation to Redfield theory, one retains only terms resonant with ω_{ab}, so that, of the previous list, only population terms $R_{aa,bb}$ (including $a = b$) and coherence dephasing terms $R_{ab,ab}$ survive. This implies that, in the secular approximation, the evolution of populations terms of the density matrix (ρ_{aa}) is decoupled from that of coherences (ρ_{ab}), and also that different coherences evolve independently.

An extension to the Redfield theory is the so-called *modified* Redfield[38, 39], for

which one has the following repartition of the Hamiltonian:

$$
\begin{aligned}
\hat{H}_0 &= \underbrace{\sum_{\alpha} \epsilon_{\alpha} |\alpha\rangle \langle\alpha|}_{H_{exc}} + \underbrace{\sum_{\alpha} \delta_{\alpha\beta}(\mathbf{Q}) |\alpha\rangle \langle\alpha|}_{H_{SB} \text{ diag}} + \underbrace{\sum_{i}^{N} \sum_{m_i}^{M_i} \frac{1}{2} \left(\hat{P}_{m_i}^2 + \omega_{m_i}^2 \hat{Q}_{m_i}^2 \right) \hat{\mathbb{1}}}_{H_B} \\
\hat{H}' &= \underbrace{\sum_{\alpha \neq \beta} \delta_{\alpha\beta}(\mathbf{Q}) |\alpha\rangle \langle\beta|}_{H_{SB} \text{ off}-\text{diag}}
\end{aligned}
\tag{4.10}
$$

The diagonal part of the electron-phonon Hamiltonian is included in the non-perturbative Hamiltonian $\hat{H}_0$: this allows the treatment of the off-diagonal part of the electron-phonon Hamiltonian as a perturbation even when the electron-phonon coupling is not small, providing the spatial overlap of the two exciton wave-functions $(A_{\alpha j}^* A_{\beta j})$ to be small[2].

Modified Redfield introduces the possibility that multiple energy quanta are exchanged between the electronic and vibrational degrees of freedom, and in specific limits it has been shown to behave as Redfield and Förster theories, in the respective regimes of validity of the two methods.[40]

4.3   PLDM dynamics

We briefly outline here the principal ideas behind the *Partial Linearized Density Matrix* (PLDM) method, developed by P. Huo and D. F. Coker[41]. PLDM provides a systematically improvable, accurate, and flexible numerical propagation scheme for treating EET dynamics and simulating, as presented in the next Part of the Thesis, spectroscopy experiments. Among the features, it is nonperturbative, non-Markovian, and does not require any particular form for the system bath interaction.

The method is designed to describe the time evolution of the expectation value of a generic operator, given by

$$
\langle \Psi | \hat{O}(t) | \Psi \rangle = \langle \Psi | e^{-i/\hbar \hat{H} t} \hat{O}(0) e^{i/\hbar \hat{H} t} | \Psi \rangle
\tag{4.11}
$$

where $\hat{H}$ is a general system-bath Hamiltonian (e.g. of the form Eqs. (3.2-3.4)) and the system and bath are prepared in some initial state $|\Psi\rangle$. The forward $(e^{-i/\hbar \hat{H} t})$ and backward $(e^{i/\hbar \hat{H} t})$ propagators can be accurately described using a semiclassical path integral formalism.[42] The central approximation of the method resides in the assumption that for short times, forward and backward nuclear paths should remain

---

[2]This is generally true when the distribution of site energy is large.

close to each other.

In the following Sections we focus on the evolution of the density matrix operator, but the formalism is completely general, and allows to treat generic operators exactly in the same way.

4.3.1 Mapping Representation

Let us consider a density matrix operator which describes a system of nuclei with position R (representing e.g. the protein scaffold, the solvent, and the chromophore vibrations), coupled to a manifold of electronic states, labeled by the quantum number n (usually the diabatic site states of a Frenkel Exciton model).

The time evolution of the density matrix in terms of $|R_t, n_t\rangle$ states is given by:

$$\langle R_t, n_t | \hat{\rho}(t) | R'_t, n'_t \rangle = \langle R_t, n_t | e^{-(i/\hbar)\hat{H}t} \hat{\rho}(0) e^{(i/\hbar)\hat{H}t} | R'_t, n'_t \rangle = \quad (4.12)$$

$$= \sum_{n_0 n'_0} \int dR_0 dR'_0 \langle R_t, n_t | e^{-(i/\hbar)\hat{H}t} | R_0, n_0 \rangle \langle R_0, n_0 | \hat{\rho}(0) | R'_0, n'_0 \rangle \langle R'_0, n'_0 | e^{(i/\hbar)\hat{H}t} | R'_t, n'_t \rangle$$

The total Hamiltonian $\hat{H}$ can be written as the sum of the nuclear kinetic energy term plus a general electronic Hamiltonian in the diabatic representation, as:

$$\hat{H} = \frac{\hat{P}^2}{2M} + \sum_{nn'} |n\rangle \langle n | \hat{h}_{el}(\hat{R}) | n' \rangle \langle n' | \quad (4.13)$$

$\hat{h}_{el}(\hat{R})$ contains the potential energy surfaces for the various states $|n\rangle$ and the coupling between them, and depends on the nuclear configuration R.

To deduce the continuous path integral expression for both the nuclear and electronic degrees of freedom, the Meyer-Miller mapping model is employed: the discrete quantum states of the system (i.e. the electronic DOFs) are exactly mapped onto a set of fictitious harmonic oscillator raising and lowering operators ($|n\rangle \rightarrow \hat{a}_n^\dagger = (\hat{r}_n - i\hat{p}_n)/\sqrt{2}$) and the Hamiltonian of Eq. (4.13) takes the form[43, 44]

$$\hat{H} = \frac{\hat{P}^2}{2M} + \frac{1}{2} \sum_n h_{nn}(\hat{R}) \left(\hat{r}_n^2 + \hat{p}_n^2 - \hbar \right) + \frac{1}{2} \sum_{n' \neq n} h_{nn'}(\hat{R}) \left(\hat{r}_n \hat{r}_{n'} + \hat{p}_n \hat{p}_{n'} \right) \quad (4.14)$$

where $(\hat{r}_n, \hat{p}_n)$ and $(\hat{P}, \hat{R})$ represent the complete sets of *system* and *bath* mapping phase-space DOFs, respectively.

4.3.2 Propagators in the path-integral formalism

The forward propagator of Eq. (4.12) is then written in a discrete phase space path integral form, as

$$\langle R_t n_t | e^{-(i/\hbar)\hat{H}t} | R_0, n_0 \rangle = \int \prod_{k=1}^{N-1} dR_k \frac{dP_k}{2\pi\hbar} \frac{dP_N}{2\pi\hbar} e^{(i/\hbar)S_0} T_{[n_t, n_0]} \tag{4.15}$$

where

$$S_0 = \epsilon \sum_{k=1}^{N} \left[P_k \frac{(R_k - R_{k-1})}{\epsilon} - \frac{P_k^2}{2M} \right] \tag{4.16}$$

is the nuclear kinetic action, ϵ is the nuclear time step, and

$$T_{[n_t, n_0]} = \langle n_t | e^{-(i/\hbar)\epsilon\hat{h}_{el}(R_{N-1})} \dots e^{-(i/\hbar)\epsilon\hat{h}_{el}(R_0)} | n_0 \rangle \tag{4.17}$$

is the quantum transition amplitude associated to the evolution of the electronic (mapping) Hamiltonian of Eq. (4.14) along the discrete path of nuclear configurations $R_0 \dots R_{N-1}$. The Herman-Kluk [45, 46] (or coherent state) semiclassical propagator, with a coherent state width parameter $\gamma = 1/2$, is employed for the system DOFs to rewrite $T_{[n_t, n_0]}$, which then gives

$$T_{[n_t, n_0]} = \int dr_0 dp_0 \frac{1}{2} (r_{n_t} + ip_{n_t})(r_{n_0} - ip_{n_0}) e^{(i/\hbar)S_1(t)}$$
$$e^{-(i/2\hbar)\sum_\alpha (r_{\alpha_t} p_{\alpha_t} - r_{\alpha_0} p_{\alpha_0})} e^{-(1/2\hbar)\sum_\alpha (r_{\alpha_0}^2 + r_{\alpha_0}^2)} \tag{4.18}$$

$S_1(t)$ is the action of the system mapping variables, expressed by

$$S_1(t) = \int_0^t d\tau \left[\sum_\alpha p_\alpha \dot{r}_\alpha - h^{cl}(R) \right] \tag{4.19}$$

where $h^{cl}(R) = \frac{1}{2} \sum_\alpha h_{\alpha\alpha}(R) (r_\alpha^2 + p_\alpha^2) + \frac{1}{2} \sum_{\beta \neq \alpha} h_{\alpha\beta}(R) (r_\alpha r_\beta + p_\alpha p_\beta)$ is the classical equivalent (in the path-integral system variables) of the quantum mapping Hamiltonian of Eq. (4.14).[3]

A similar expression holds for the backward propagator $\langle R_0', n_0' | e^{i/\hbar\hat{H}t} | R_t', n_t' \rangle$,

---

[3]While results are independent of the specific choice of the coherent state width parameter, γ, choosing it as $\gamma = \frac{1}{2}$ has the useful consequence that the coherent state version of the semiclassical van Vleck determinant exactly cancels the troublesome $-\frac{\hbar}{2} \sum_n h_{nn}(R)$ term in Eq. (4.14) [47]. This mitigates the issue of the bath DOFs propagating on an inverted potential energy surface (PES) when the mapping variables sample regions of phase space in which $\hat{r}_\alpha^2 + \hat{p}_\alpha^2 < 1$.

with correspondent terms S_0' and $T_{[n_0',n_t']}$. Eq. (4.12) is then rewritten as:

$$\sum_{n_0 n_0'} \int dR_0 dR_0' \int \prod_{k=1}^{N-1} dR_k \frac{dP_k}{2\pi\hbar} \frac{dP_N}{2\pi\hbar} \int \prod_{k'=1}^{N-1} dR_{k'}' \frac{dP_{k'}'}{2\pi\hbar} \frac{dP_N'}{2\pi\hbar} e^{(i/\hbar)(S_0-S_0')} T_{[n_t,n_0]} T_{[n_0',n_t']}$$

(4.20)

The phases of the path integral expressions for full forward and backward propagators are combined $(e^{-(i/\hbar)(S_0-S_0')}e^{-(i/\hbar)(S_1-S_1')})$ and the bath phase space DOFs are transformed to mean and difference path variables, defined as $\bar{R} = (R + R')/2$ and $Z = R - R'$, respectively, with similar definitions for the corresponding momenta, $\bar{P}$ and Y.

4.3.3   (Partial) Linearization

Until now, we have just rewritten the expression for the density matrix evolution of Eq. (4.12) in a path integral form, and it is still exact. The central approximation of the partial linearized approach comes through a truncation of the functional Taylor series expansion about the mean bath phase space path, $(\bar{R}(t), \bar{P}(t))$, to linear order in the difference path variables, $Z(t)$ and $Y(t)$. This approximation is based on the assumption that forward and backward nuclear paths will remain close to each other for short times.[41]

The difference of forward and backward nuclear and electronic amplitudes, S_0-S_0' and $S_1 - S_1'$, then read[41]

$$(S_0 - S_0') = \bar{P}_N Z_N - \bar{P}_1 Z_0 - \sum_{k=1}^{N-1}(\bar{P}_{k+1} + \bar{P}_k)Z_k - \sum_{k=1}^{N}\left[\frac{\bar{P}_k}{M} - \frac{(\bar{R}_k - \bar{R}_{k-1})}{\epsilon}\right]Y_k$$

(4.21)

and

$$(S_1 - S_1') = \int_0^t d\tau \frac{1}{2}\frac{d}{d\tau}\sum_\alpha\left(r_{\alpha_\tau}p_{\alpha_\tau} - r_{\alpha_\tau}'p_{\alpha_\tau}'\right) +$$
$$\int_0^t d\tau \left[\frac{1}{2}\nabla_R\left(h^{cl}(\bar{R}_\tau, r_\tau, p_\tau) + h^{cl}(\bar{R}_\tau, r_\tau', p_\tau')\right)Z_\tau + \mathcal{O}(Z_\tau^2)\right]$$

(4.22)

where we have expanded and truncated the S_1-S_1' difference at linear order in Z_τ and used the approximation $\sum_\alpha p_\alpha \dot{q}_\alpha - h^{cl}(\bar{R}, p, r) \sim \sum_\alpha p_\alpha \dot{q}_\alpha - h^{cl}(R, p, r) = \frac{1}{2}\frac{d}{d\tau}\left(\sum_\alpha p_\alpha q_\alpha\right)$. Note that the first term of Eq. (4.22) cancels the boundary terms in both $T_{[n_t,n_0]}$ and $T_{[n_0',n_t']}$.

Upon functional integration of this partial linearized approximate result over

bath difference path variables (*i.e.* $Z_0 \dots Z_{N-1}$ and $Y_1 \dots Y_N$)[4], the final expression for the evolution of a generic element of the density matrix operator $\hat{\rho}$ is given by [41]

$$
\begin{aligned}
\left\langle n_t, \bar{R}_N + \frac{Z_N}{2} \middle| \hat{\rho}(t) \middle| n'_t, \bar{R}_N - \frac{Z_N}{2} \right\rangle &= \sum_{n_0, n'_0} \int d\bar{R}_0 dr_0 dp_0 dr'_0 dp'_0 \ G_0 G'_0 \\
&\times \frac{1}{2}(r_{n_t} + ip_{n_t})(r_{n_0} - ip_{n_0}) \frac{1}{2}(r'_{n'_t} - ip'_{n'_t})(r'_{n'_0} + ip'_{n'_0}) \left(\prod_{k=1}^{N-1} \int d\bar{R}_k \frac{d\bar{P}_k}{2\pi} \right) \int \frac{d\bar{P}_N}{2\pi} \\
&\times \rho_W^{n_0 n'_0}(\bar{R}_0, \bar{P}_1) \ e^{(i/\hbar)\bar{P}_N Z_N} \prod_{k=1}^{N-1} \delta\left(\frac{\bar{P}_{k+1} - \bar{P}_k}{\epsilon} - F_k \right) \prod_{k=1}^{N} \delta\left(\frac{\bar{R}_k - \bar{R}_{k-1}}{\epsilon} - \frac{\bar{P}_k}{M} \right)
\end{aligned}
$$

$$(4.23)$$

This equation, which gives the time evolution of a generic expectation value of the density matrix, has the following interpretation:

- Initial (mean) nuclear DOFs are sampled from the probability distribution obtained from the partial Wigner transform of $\hat{\rho}(0)$ with respect to the bath variables, as

$$
\rho_W^{n_0 n'_0}(\bar{R}_0, \bar{P}_1) = \int dZ_0 \langle n_0, \bar{R}_0 + \frac{Z_0}{2} | \hat{\rho} | n'_0, \bar{R}_0 - \frac{Z_0}{2} \rangle e^{-(i/\hbar)\bar{P}_1 Z_0} \tag{4.24}
$$

labeled by initial system states n_0 and n'_0;

- Initial system DOFs (mapping variables) are sampled from the Gaussian functions $G_0 = \exp\left[-\frac{1}{2\hbar} \sum_\alpha (r_{\alpha 0}^2 + p_{\alpha 0}^2) \right]$ and $G'_0 = \exp\left[-\frac{1}{2\hbar} \sum_\alpha (r'^2_{\alpha 0} + p'^2_{\alpha 0}) \right]$;

- The system (mapping) DOFs are evaluated along classical-like trajectories ruled by h^{cl}:

$$
\dot{r}_{n_t} = \frac{\partial h^{cl}(\bar{R}_t)}{\partial p_{n_t}}, \quad \dot{p}_{n_t} = -\frac{\partial h^{cl}(\bar{R}_t)}{\partial r_{n_t}} \tag{4.25}
$$

- The nuclear trajectories are evolved as prescribed by the products of δ-functions, by the effective force

$$
F_k = -\frac{1}{2} \nabla_{\bar{R}_k} \left(h^{cl}(\bar{R}, r, p) + h^{cl}(\bar{R}, r', p') \right) \tag{4.26}
$$

---

[4]The functional integration transforms the $e^{-(i/\hbar)Z}$ and $e^{-(i/\hbar)Y}$ terms in the δ functions which appear in the final expression, Eq. (4.23).
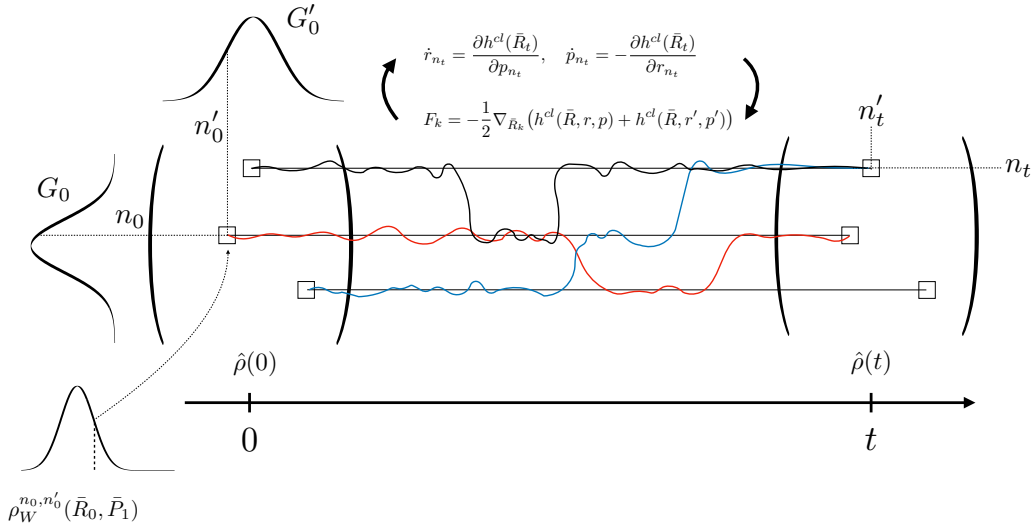
Figure 4.1: Pictorial representation of the central equation of PLDM dynamics, Eq. (4.23). It shows in particular how the coupled bath (nuclear) and system (electronic) dynamics mixes the initially sampled density matrix elements so that they may contribute to the same density matrix element at time t.

which depend on both forward and backward system DOFs ((r, p) and (r', p'), respectively);

- The propagated trajectories, provide a dynamical ensemble over which quantities can be averaged thus performing the following integrals $\sum_{n_0, n_0'} \int d\bar{R}_0 dr_0 dp_0 dr_0' dp_0'$, yielding the desired time evolved density matrix elements.[5]

We note that the necessity of averaging the (often oscillatory) complex phase factors associated with the product of polynomial terms in the mapping variables in Eq. (4.23) can be problematic: it can in fact result in considerable noise in computed averages at longer times, requiring larger ensembles of trajectories to obtain desired convergence. Alternatively, it is possible to treat this algorithm as a short-time propagator, where the linearization approximation is valid, by concatenating many short-time propagations: an accurate evolution of the density matrix for longer times is then obtained. This is the so called *Iterative* PLDM approach[48]. In the limit of infinite time slices, this iterative approach converges to exact quantum mechanical results [48].

---

[5]It should be pointed out that, although the Herman-Kluk propagator is semiclassical, the Meyer-Miller Hamiltonian is at most quadratic in the system mapping variables. Therefore, this semiclassical propagator provides an exact quantum mechanical treatment of the system dynamics for fixed bath variables.

This framework offers a robust and systematically improvable means of computing the time evolution of quantum mechanical operators, which has been demonstrated to provide accurate description of EET dynamics in a wide variety of photosynthetic light harvesting systems.[41, 49]

Appendix

5.1 Off-diagonal entries of the Excitonic Hamiltonian

GS-1st excitation manifold

Here we consider the states $\langle 0_A | \equiv \langle 0_1 0_2 \ldots 0_A \ldots |$ and $|a_A\rangle \equiv |0_1 0_2 \ldots a_A \ldots\rangle$. Then

$$\sum_I \sum_{J \neq I} \langle 0_A | \hat{V}_{IJ} | a_A \rangle \neq 0 \iff \begin{cases} I = A \implies \sum_{J \neq A} \langle 0_A | \hat{V}_{AJ} | a_A \rangle \\ J = A \implies \sum_{I \neq A} \langle 0_A | \hat{V}_{IA} | a_A \rangle \end{cases} \tag{5.1}$$

and since $V_{IJ} = V_{JI}$ the two terms are equal. Moreover we can express the previous result in term of densities and transition densities (Eq. (1.27)), as

$$\int d\boldsymbol{r} \rho_{0a}^A \sum_{I \neq A} \int d\boldsymbol{r}' \frac{\rho_{00}^I(\boldsymbol{r}')}{|\boldsymbol{r} - \boldsymbol{r}'|} + \sum_{i \in I} \frac{Z_i}{|\boldsymbol{r} - \boldsymbol{R}_i'|} \tag{5.2}$$

Therefore, the terms which appear in the *GS-1st excitation manifold* sector of the Hamiltonian are interaction terms between transition densities of the kind $0_A \rightarrow a_A$ and the densities of all the other molecules in their GS.

GS-2nd excitation manifold

Here we consider the states $\langle 0_A 0_B |$ and $|a_A b_B\rangle$, defined similarly as above (i.e. the chromophores which are not explicitly specified are in the GS). Then

$$\sum_I \sum_{J \neq I} \langle 0_A 0_B | \hat{V}_{IJ} | a_A b_B \rangle \neq 0 \iff \begin{cases} I = A, J = B \implies \langle 0_A 0_B | \hat{V}_{AB} | a_A b_B \rangle \\ J = A, I = B \implies \text{similar terms} \end{cases} \tag{5.3}$$

Therefore, in terms of densities, these elements are computed as:

$$\int d\boldsymbol{r} \int d\boldsymbol{r}' \frac{\rho_{0a}^A(\boldsymbol{r}) \rho_{0b}^B(\boldsymbol{r}')}{|\boldsymbol{r} - \boldsymbol{r}'|} \tag{5.4}$$

i.e. this interaction term reduces to the computation of a single TRD-TRD coupling.

1st-2nd

The general interaction term of this manifold is $\sum_I \sum_{J \neq I} \langle a_A | \hat{V}_{IJ} | b_B c_C \rangle$. If $A \neq B \neq C$ this term is zero. We consider two cases for which this term is not zero: $A = B \neq C$, with states $\langle a_A |$ and $| a_A c_C \rangle$ or $| a'_A c_C \rangle$, and the symmetric case given by $A = C \neq B$. Due to the similarity between the two cases we will just consider the first one, i.e.

$$\sum_I \sum_{J \neq I} \langle a_A | \hat{V}_{IJ} | a'_A b_B \rangle \neq 0 \iff \begin{cases} I = A, J = B, a = a' \implies \langle a_A | \hat{V}_{AB} | a_A b_B \rangle \\ I = A, J = B, a \neq a' \implies \langle a_A | \hat{V}_{AB} | a'_A b_B \rangle \\ J = A, I = B \implies \text{sim. terms} \\ I = B, J \neq A \neq B, a = a' \implies \sum_J \langle 0_B | \hat{V}_{BJ} | b_B \rangle \\ J = B, I \neq A \neq B, a = a' \implies \text{sim. terms} \end{cases} \tag{5.5}$$

with terms already discussed before.

2nd-2nd

The general interaction term of this manifold is of the form $\sum_I \sum_{J \neq I} \langle a_A b_B | \hat{V}_{IJ} | c_C d_D \rangle$. Again there are several possible combinations of chromophores and states that make it different from zero. We will study the $A = C$ case, because all the considerations hold also for the symmetric $A = D$. The matrix element of interest is therefore $\langle a_A b_B | \hat{V}_{IJ} | a'_A d_D \rangle$.

- First case: $A = C, B = D$, $a = a', b = b'$ is a diagonal element, already considered above.

- Second case: $A = C, B = D, a = a', b \neq b'$

$$\sum_I \sum_{J \neq I} \langle a_A b_B | \hat{V}_{IJ} | a_A b'_B \rangle \neq 0 \iff \begin{cases} I = A, J = B \implies \langle a_A b_B | \hat{V}_{AB} | a_A b'_B \rangle \\ J = A, I = B \implies \text{similar terms} \\ I = B, J = C \neq A \neq B \implies \sum_C \langle b_B 0_C | \hat{V}_{AB} | b'_B 0_C \rangle \\ I = B, J = C \implies \text{similar terms} \end{cases}$$

$$(5.6)$$

- Third case: $A = C, B = D, a \neq a', b \neq b'$

$$\sum_I \sum_{J \neq I} \langle a_A b_B | \hat{V}_{IJ} | a'_A b'_B \rangle \neq 0 \iff \begin{cases} I = A, J = B \implies \langle a_A b_B | \hat{V}_{AB} | a'_A b'_B \rangle \\ J = A, I = B \implies \text{similar terms} \end{cases}$$

$$(5.7)$$

- Forth case: $A = C, B \neq D, a = a'$

$$\sum_I \sum_{J \neq I} \langle a_A b_B | \hat{V}_{IJ} | a_A d_D \rangle \neq 0 \iff \begin{cases} I = B, J = D \implies \langle b_B 0_D | \hat{V}_{BD} | b'_B d_D \rangle \\ J = B, I = D \implies \text{similar terms} \end{cases}$$

$$(5.8)$$

5.2   Transition density matrix

Consider a Molecular system with N electrons, described by $2K$ (spin) molecular orbitals (and thus only K different spatial wavefunctions $\varphi(\boldsymbol{r})$) given by:

$$|\chi_1\rangle, \ldots |\chi_a\rangle, |\chi_b\rangle, \ldots |\chi_N\rangle, |\chi_{N+1}\rangle, \ldots |\chi_r\rangle, |\chi_s\rangle, \ldots |\chi_{2K}\rangle \qquad (5.9)$$

Slater determinants can be written (in a more compact notation with respect to Eq. (2.4)) as

$$|\bar{\chi}\rangle = \sum_P \text{sign}(P) |\chi_{P_1}(1)\rangle \ldots |\chi_{P_a}(a)\rangle |\chi_{P_b}(b)\rangle \ldots |\chi_{P_N}(N)\rangle \qquad (5.10)$$

where $\sum_P$ is a sum over all possible permutations of the state indexes $1, \ldots a, \ldots b, \ldots N$, described by the vector $P = (P_1, \ldots P_a, \ldots P_b, \ldots P_N)$. The function $\text{sign}(P)$ is equal to $+1$ for even permutations, and -1 for odd permutations. In the simple case of two orbitals, labeled as 1 and 2, P can be either $(1, 2)$ or $(2, 1)$, and thus the sum of Eq. (5.10) is just made of the two terms $|\chi_1(1)\rangle |\chi_2(2)\rangle - |\chi_2(1)\rangle |\chi_1(2)\rangle$.

Following the expression of Eq. 2.8, a generic state $|\psi_m\rangle$ can be written in terms of Slater determinants of the molecular orbitals of Eq. (5.9), so that:

$$|\psi_m\rangle \;=\; c_0 \underbrace{\sum_P \text{sign}(P)\, |\chi_{P_1}(1)\rangle \ldots |\chi_{P_a}(a)\rangle |\chi_{P_b}(b)\rangle \ldots |\chi_{P_N}(N)\rangle}_{|\bar{\chi}_0\rangle} + \qquad (5.11)$$

$$+ \sum_{r,a} c_a^r \underbrace{\sum_P \text{sign}(P)\, |\chi_{P_1}(1)\rangle \ldots |\chi_{P_r}(a)\rangle |\chi_{P_b}(b)\rangle \ldots |\chi_{P_N}(N)\rangle}_{|\bar{\chi}_a^r\rangle} +$$

$$+ \sum_{rs,ab} c_{ab}^{rs} \underbrace{\sum_P \text{sign}(P)\, |\chi_{P_1}(1)\rangle \ldots |\chi_{P_r}(a)\rangle |\chi_{P_s}(b)\rangle \ldots |\chi_{P_N}(N)\rangle}_{|\bar{\chi}_{ab}^{rs}\rangle} + \ldots$$

where the normalization normalization factor $1/N!$ has been absorbed within the coefficients c here). Note that in the second term, the (occupied) molecular orbital $|\chi_a\rangle$ has been removed and substituted by the (virtual) molecular orbital $|\chi_r\rangle$.

Let us consider, term by term, the various pieces of Eq. (2.15). The first term reads

$$\langle \bar{\chi}_0 | \, \delta(\boldsymbol{r}_1 - \boldsymbol{r}) \, |\bar{\chi}_0\rangle = \qquad\qquad (5.12)$$

$$= \sum_Q \text{sign}(Q) \sum_P \text{sign}(P)\, \langle \chi_{Q_1}(1)| \ldots \langle \chi_{Q_a}(a)| \langle \chi_{Q_b}(b)| \ldots \langle \chi_{Q_N}(N)| \, \delta(\boldsymbol{r}_1 - \boldsymbol{r})$$

$$|\chi_{P_1}(1)\rangle \ldots |\chi_{P_a}(a)\rangle |\chi_{P_b}(b)\rangle \ldots |\chi_{P_N}(N)\rangle =$$

$$= \sum_Q \text{sign}(Q) \sum_P \text{sign}(P)\, \langle \chi_{Q_1}(1)| \, \delta(\boldsymbol{r}_1 - \boldsymbol{r}) \, |\chi_{P_1}(1)\rangle \ldots$$

$$\ldots \langle \chi_{Q_a}(a)| \, \chi_{P_a}(a)\rangle \langle \chi_{Q_b}(b)| \, \chi_{P_b}(b)\rangle \ldots \langle \chi_{Q_N}(N)| \, \chi_{P_N}(N)\rangle =$$

$$= \sum_Q \text{sign}(Q) \sum_P \text{sign}(P)\, \langle \varphi_{Q_1}(\boldsymbol{r}_1)| \, \delta(\boldsymbol{r}_1 - \boldsymbol{r}) \, |\varphi_{P_1}(\boldsymbol{r}_1)\rangle \ldots \delta_{Q_a P_a} \delta_{Q_b P_b} \ldots \delta_{Q_N P_N}$$

$$= \mathcal{N} \sum_{i=1}^{N} \int d\boldsymbol{r}_1 \varphi_i^*(\boldsymbol{r}_1) \varphi_i(\boldsymbol{r}_1) \delta(\boldsymbol{r}_1 - \boldsymbol{r})$$

$$= \mathcal{N} \sum_{i=1}^{N} |\varphi_i(\boldsymbol{r})|^2$$

where we have integrated over the spin variables, as the operator $\delta(\boldsymbol{r}_1 - \boldsymbol{r})$ affect only the spatial variable, and we have made use of the orthogonality condition for spatial orbitals, obtaining the sequence of Kronecker deltas $\delta_{Q_a P_a} \delta_{Q_b P_b} \ldots \delta_{Q_N P_N}$. These impose that also $P_1 = Q_1$. $\mathcal{N}$ is a normalization factor (in this case is equal to $(N-1)!)$. In our computations, where one of the two states is the GS and the other is an ES, we assume the pre-factor of this contribution ($h_0^* c_0$) to be very small, and we will neglect this first term.

The second term of Eq. (2.15) reads

$$\langle \bar\chi_0 | \delta(\boldsymbol{r}_1 - \boldsymbol{r}) | \bar\chi_a^r \rangle = \tag{5.13}$$

$$= \sum_Q \mathrm{sign}(Q) \sum_P \mathrm{sign}(P) \langle \chi_{Q_1}(1) | \dots \langle \chi_{Q_a}(a) | \langle \chi_{Q_b}(b) | \dots \langle \chi_{Q_N}(N) | \delta(\boldsymbol{r}_1 - \boldsymbol{r})$$

$$|\chi_{P_1}(1)\rangle \dots |\chi_{P_r}(a)\rangle |\chi_{P_b}(b)\rangle \dots |\chi_{P_N}(N)\rangle =$$

$$= \sum_Q \mathrm{sign}(Q) \sum_P \mathrm{sign}(P) \langle \chi_{Q_1}(1) | \delta(\boldsymbol{r}_1 - \boldsymbol{r}) | \chi_{P_1}(1)\rangle \dots$$

$$\dots \langle \chi_{Q_a}(a) | \chi_{P_r}(a)\rangle \langle \chi_{Q_b}(b) | \chi_{P_b}(b)\rangle \dots \langle \chi_{Q_N}(N) | \chi_{P_N}(N)\rangle =$$

$$= \langle \chi_a(1) | \delta(\boldsymbol{r}_1 - \boldsymbol{r}) | \chi_r(1)\rangle \sum_Q \mathrm{sign}(Q) \sum_P \mathrm{sign}(P) \dots \delta_{Q_b P_b} \dots \delta_{Q_N P_N} =$$

$$= \mathcal{N} \int d\boldsymbol{r}_1 \varphi_a^*(\boldsymbol{r}_1) \varphi_r(\boldsymbol{r}_1) \delta(\boldsymbol{r}_1 - \boldsymbol{r}) =$$

$$= \mathcal{N} \varphi_a^*(\boldsymbol{r}) \varphi_r(\boldsymbol{r})$$

The third term Eq. (2.15) reads

$$\langle \bar\chi_0 | \delta(\boldsymbol{r}_1 - \boldsymbol{r}) | \bar\chi_{ab}^{rs} \rangle = \tag{5.14}$$

$$= \sum_Q \mathrm{sign}(Q) \sum_P \mathrm{sign}(P) \langle \chi_{Q_1}(1) | \dots \langle \chi_{Q_a}(a) | \langle \chi_{Q_b}(b) | \dots \langle \chi_{Q_N}(N) | \delta(\boldsymbol{r}_1 - \boldsymbol{r}) | \chi_{P_1}(1)\rangle$$

$$\dots |\chi_{P_r}(a)\rangle |\chi_{P_s}(b)\rangle \dots |\chi_{P_N}(N)\rangle =$$

$$= \sum_Q \mathrm{sign}(Q) \sum_P \mathrm{sign}(P) \langle \chi_{Q_1}(1) | \delta(\boldsymbol{r}_1 - \boldsymbol{r}) | \chi_{P_1}(1)\rangle \dots$$

$$\dots \langle \chi_{Q_a}(a) | \chi_{P_r}(a)\rangle \langle \chi_{Q_b}(b) | \chi_{P_s}(b)\rangle \dots \langle \chi_{Q_N}(N) | \chi_{P_N}(N)\rangle =$$

$$= \langle \chi_a(1) | \delta(\boldsymbol{r}_1 - \boldsymbol{r}) | \chi_r(1)\rangle \langle \chi_b(a) | \chi_s(a)\rangle + \text{similar terms} =$$

$$= 0$$

because one of the products $\langle \chi_b(a) | \chi_s(a) \rangle$ is always between different states (belonging to the occupied and the virtual orbital subspaces).

The forth term, $\langle \bar\chi_a^r | \delta(\boldsymbol{r}_1 - \boldsymbol{r}) | \bar\chi_0 \rangle$ turns out to be the complex conjugate of $\langle \bar\chi_0 | \delta(\boldsymbol{r}_1 - \boldsymbol{r}) | \bar\chi_a^r \rangle$, thus it is equal to $\mathcal{N} \varphi_r^*(\boldsymbol{r}) \varphi_a(\boldsymbol{r})$.

The fifth term reads

$$\langle \bar\chi_{a'}^{r'} | \delta(\boldsymbol{r}_1 - \boldsymbol{r}) | \bar\chi_a^r \rangle = \tag{5.15}$$

$$= \sum_Q \mathrm{sign}(Q) \sum_P \mathrm{sign}(P) \langle \chi_{Q_1}(1) | \dots \langle \chi_{Q_{r'}}(a) | \langle \chi_{Q_b}(b) | \dots \langle \chi_{Q_N}(N) | \delta(\boldsymbol{r}_1 - \boldsymbol{r})$$

$$|\chi_{P_1}(1)\rangle \dots |\chi_{P_r}(a)\rangle |\chi_{P_b}(b)\rangle \dots |\chi_{P_N}(N)\rangle =$$

$$= \langle \chi_{r'}(1) | \delta(\boldsymbol{r}_1 - \boldsymbol{r}) | \chi_r(1)\rangle \mathcal{N} =$$

$$= \mathcal{N} \varphi_{r'}^*(\boldsymbol{r}) \varphi_r(\boldsymbol{r})$$

The sixth term reads

$$
\begin{aligned}
\langle \bar{\chi}_{a'}^{r'} | \delta(\boldsymbol{r}_1 - \boldsymbol{r}) | \bar{\chi}_{ab}^{rs} \rangle &= \\
&= \sum_Q (-)^Q \sum_P (-)^P \langle \chi_{Q_1}(1) | \dots \langle \chi_{Q_{r'}}(a) | \langle \chi_{Q_{s'}}(b) | \dots \langle \chi_{Q_N}(N) | \delta(\boldsymbol{r}_1 - \boldsymbol{r}) \\
&\quad | \chi_{P_1}(1) \rangle \dots | \chi_{P_r}(a) \rangle | \chi_{P_s}(b) \rangle \dots | \chi_{P_N}(N) \rangle = \\
&= \dots \\
&= \langle \chi_{r'}(1) | \delta(\boldsymbol{r}_1 - \boldsymbol{r}) | \chi_r(1) \rangle \langle \chi_b(a) | \chi_s(a) \rangle + \text{similar terms} + \\
&\quad + \langle \chi_b(1) | \delta(\boldsymbol{r}_1 - \boldsymbol{r}) | \chi_r(1) \rangle \langle \chi_{r'}(a) | \chi_s(a) \rangle = \\
&= \mathcal{N} \varphi_b^*(\boldsymbol{r}) \varphi_r(\boldsymbol{r}) \delta_{r's} + \mathcal{N} \varphi_b^*(\boldsymbol{r}) \varphi_s(\boldsymbol{r}) \delta_{r'r}
\end{aligned}
\tag{5.16}
$$

At this point, it is apparent that all the remaining terms of Eq. (2.15) can also be written as products of active orbitals. Therefore, the single particle transition density matrix can be entirely re-written as a linear combination of products of spatial molecular orbitals of the Active space, i.e.

$$
\rho_{mn}(\boldsymbol{r}) = \sum_{a,b} C_{ab} \varphi_a^*(\boldsymbol{r}) \varphi_b(\boldsymbol{r})
\tag{5.17}
$$

Note that the integral over $\boldsymbol{r}$ of a density/transition density so expressed, is equivalent to the trace of the transition density matrix C_{ab}.

$$
\begin{aligned}
\langle \psi_m | \psi_n \rangle = \int \rho_{mn}(\boldsymbol{r}) \, d\boldsymbol{r} &= \int \sum_{a,b} C_{ab} \varphi_a^*(\boldsymbol{r}) \varphi_b(\boldsymbol{r}) \, d\boldsymbol{r} = \\
&= \sum_{a,b} C_{ab} \int \varphi_a^*(\boldsymbol{r}) \varphi_b(\boldsymbol{r}) \, d\boldsymbol{r} = \\
&= \sum_{a,b} C_{ab} \delta_{ab} = \sum_a C_{aa}
\end{aligned}
\tag{5.18}
$$

5.3 Transition densities: how to obtain them in Molcas

The transition density matrix C_{ab}^{KL} of Eq. (2.16) is routinely produced by quantum chemistry codes (e.g. for the computation of transition dipole moments), and one extracts it through the keyword *TRD1* in the module RASSI[26]. The MOs belonging to the active space are usually produced through the Molcas module *GRID_IT* in the *grid* format (an internal format of Molcas), and are interpreted by the script for the visualization of the orbitals (*gv.exe*). This module allows to define the level of accuracy (density of points) with which these orbitals are printed to file. As an

example, the use of *SPARSE* keyword produces a poorly resolved density, with 1 grid point per a.u., while the *DENSE* keyword produces grids with 10 grid points per a.u. (paying the price of very large output files). The default density of points is set to 3 grid points per a.u., which is the best compromise between accuracy and file dimension. Other parameters that can be chosen are e.g. the grid dimension and grid's axes orientation. As we need to combine these orbitals in the expression given by Eq. (2.16), the more convenient (and more used) *cube* format for the orbitals should be used. The transformation from *grid* to *cube* formats can be performed using the *grid2cube.py* script provided in the Tool folder of Molcas.

The algorithm we designed to obtain the transition densities of interest is here summarized:

1. Perform a SA-CASSCF (SA-RASSCF) computation, including in the SA procedure (at least) all the states of interest.

2. Include in the RASSI section the keyword *TRD1*, which enables to save into a file the transition density matrices for every coupled of states included in the SA procedure.

3. Produce the grid files containing the active orbitals through the *GRID_IT* module, choosing the desired grid density (and grid dimension).

4. The orbitals can be transformed in *cube* format with the grid2cube.py script.

5. Finally, the so produced active orbitals and transition density matrices can be combined according to Eq. (2.16) to obtain the desired transition densities.

5.4 Spectral Density and higher lying states

In this Section we improve the DHO model of Section 3.1.2, by including possible higher lying states. Indeed, this is important for the description of e.g. 2DES spectroscopy, in which a molecule prepared in an excited state e by the first two interactions with the laser field, can be further excited to an higher lying state by the last field interaction.

First of all we note that the displacement d_e with respect to the reference position $d_g = 0$ can assume both positive or negative values (Figure 5.1). This changes the sign of the coupling c, but does not affect the value of neither the reorganization energy (Eq. (3.11)), nor the spectral density (Eq. (3.17)): the displacement d_e
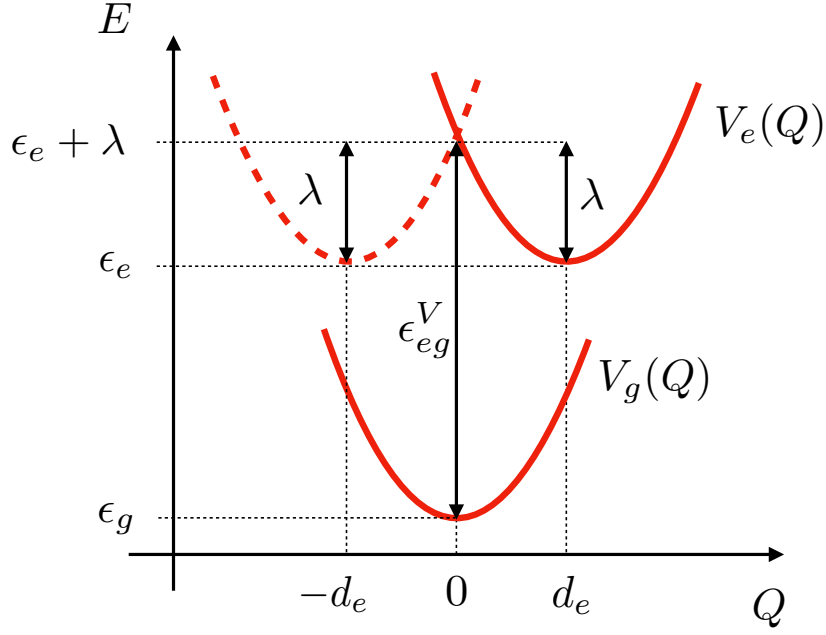
Figure 5.1: Pictorial representation of the DHO model, highlighting the possibility of both positive and negative displacements d_e.

enters in these expressions as a square, which makes them insensitive to its sign.[1]

Let us add another excited state f, with a displacement d_f with respect to the reference $d_g = 0$. This state can for example be reached from e by a light induced transition. The definition of the energy gap between the GS g and the ES e of Eq. (3.10), can be extended to describe the energy gap between the states e and f, as

$$\delta_{fe}(Q) = V_f(Q) - V_e(Q) \tag{5.19}$$

This equation can be further developed, by taking V_g as a reference, so that

$$\delta_{fe}(Q) = (V_f(Q) - V_g(Q)) - (V_e(Q) - V_g(Q)) = \\ = \delta_{fg}(Q) - \delta_{eg}(Q) \tag{5.20}$$

Following the definitions of Section 3.1.3, we compute the energy fluctuation

---

[1]In the next part of the Thesis, we will connect the spectral density to the linear absorption spectrum of a molecular system. The fact that the spectral density is insensitive to the sign of the ES displacements results in identical linear spectra for both $\pm|d_e|$.

auto-correlation function between states e and f as

$$
\begin{aligned}
C_{fefe}(t) = \langle \delta_{fe}(0)\delta_{fe}(t)\rangle = \\
= \langle \delta_{fg}(0)\delta_{fg}(t)\rangle + \langle \delta_{eg}(0)\delta_{eg}(t)\rangle - \langle \delta_{fg}(0)\delta_{eg}(t)\rangle - \langle \delta_{eg}(0)\delta_{fg}(t)\rangle = \quad (5.21) \\
= C_{ff}(t) + C_{ee}(t) - C_{fe}(t) - C_{ef}(t)
\end{aligned}
$$

where the subscript g has been removed from all the expressions, being the common reference to all the obtained results. The first two terms are of the same form of Eq. (3.21), and they still depend on the squares d_f^2 and d_e^2, respectively. At variance, we note a substantial difference in the last two terms, as $C_{fe}(t)$ and $C_{ef}(t)$, which depend on the product $d_e d_f$. This make them sensitive to the sign of the displacements.

In the azobenzene study (see Part III, Chapter 3), we will take care of the sign of the displacements of excited states wells in the parametrization of the spectral densities of the transitions of interest.

Part II

Spectroscopy: experiments vs. modeling

Introduction

The quantum mechanical properties of single molecules and aggregates of interacting molecules have beed discussed in detail in the previous Part of the Thesis. How can we test if any of the obtained information has something to do with the real world? This fundamental question (how can we access the microscopic properties of nature) is common to many research areas, from chemistry to high energy physics. Each of these areas has developed its appropriate tools to enhance the microscopic world to a macroscopic -accessible- scale. The Large Hadron Collider (LHC) in Genève, is an example of such an attempt to probe the invisible world of sub-nuclear physics, achieved through collisions of high-energy particles. The LISA and VIRGO light interferometers, are very large instruments design to capture incredibly small deformations of space(-time) caused by gravitational waves, and reveal where and what has produced them. X-ray radiation allows to determine the atomic positions of crystallized molecules by the diffraction patterns produced upon illumination of the sample. In the field of photochemistry and photophysics, properties of molecules and of aggregates of molecules are probed by studying their response to external light-induced disturbances, in a spectral window which typically range from the ultraviolet (UV), through the visible (VIS) to the infra-red (IR).

The term "spectroscopy" summarizes the conspicuous body of techniques that use radiation to obtain information on the structure and properties of matter.

Spectroscopy allows to study the ability of the primary photoactive molecular entities of light-harvesting (LH) pigment-protein complexes (present in photosynthetic organisms), to absorb light at different wavelengths. The absorbed light is then temporarily harvested in molecular exciton states, which produce energetic funnels from the absorbing molecules to the central powerhouse behind photosynthesis,

the so-called *reaction center*, where this energy is eventually used for function. Advances in non-linear electronic spectroscopy with femtosecond time resolution, such as the two dimensional electronic spectroscopy (2DES), have provided new insight in such energy transfer processes [33, 35, 50, 51]. The possibility of probing the system at selected wave-lengths and time intervals from the primary absorption event, combined with some pre-knowledge of the molecular network, allows to obtain high density of information about system's excitation properties, relaxation pathways, and corresponding photoinduced dynamics (e.g. EET processes).

While experimental results can, in principle, provide important details about the studied system, the complexity of recorded spectra makes a deep understanding of the origin of particular signals a very difficult task: experiments always need to be interpreted. If experimentalists should infer microscopic properties by looking at macroscopic spectral features, theoretical modeling allows to proceed in the opposite direction: microscopic quantum mechanical properties of the system are input parameters for the simulation of spectroscopy, and the matching between simulated and measured spectra confirms the accuracy of the micro-world's description, and allows to precisely identify the microscopic origin of observed signals. As an example, the ability to selectively suppress individual degrees of freedom (DOFs) in computational models of these complex systems, allows for the assignment of measured features, e.g. in congested non-linear maps.[52] The concerted and synergetic theoretical and experimental investigation of nature is the only feasible way to obtain robust understanding of microscopic processes, to foresee new phenomena and to design and control materials having properties of interest.

The outline of this chapter is as follows: first we review some of the most used experimental spectroscopic techniques in photobiology, which include steady-state ground state-absorption and excited-state emission, as well as transient non-linear techniques, like pump-probe and 2DES. Second we outline the key concepts behind the theoretical modeling of these spectroscopic techniques, starting from the field-matter interaction Hamiltonian and developing the system response to external electromagnetic fields, incorporated in the so-called system's *response function*. A large part of the foundational work of this field has been developed by Prof. Shaul Mukamel, and we extensively refer to his book, *Principles of Non-linear optical spectroscopy*.[30] We present the main approximations involved in the perturbative approaches commonly employed for the simulation of non-linear spectroscopy, and we introduce a recently developed semiclassical method (the PLDM-spectroscopy approach) that overcomes many of the issues of these approaches.[53]

The PLDM-spectroscopy approach was implemented in collaboration with the

research group of Prof. David Coker (Boston University, Boston, MA, USA), and offers an exciting starting point from which to explore the development of accurate, yet computationally cheap, methods for computing nonlinear electronic spectroscopy.

CHAPTER 1

Overview of experimental techniques

Optical (absorption and emission) spectroscopy relies on the creation of excited states through the absorption of light. We hereafter briefly review the main ideas behind linear (single interaction between the system and the laser) and non-linear (multiple light-matter interactions) techniques. All these techniques involve the presence of a *source* of electromagnetic radiation, which illuminates a sample containing the system of interest (e.g. some LH complex), and a detector which collects the outgoing radiation. Very generally, the incident light will be absorbed by the molecules of the sample if at least the following two conditions are satisfied:

(a) The photon energy of the incoming radiation matches some (electronic) transitions of the molecular system;

(b) The transitions for which we have such an energy matching condition are *allowed*, i.e. the transition dipole moment matrix element between the starting state and ending state is different from zero.

Spectroscopic techniques can be classified according to the characteristic of the radiation source: in particular we distinguish between steady-state and time-resolved techniques. In steady-state spectroscopy, a sample is continuously irradiated, and excited states are created and eliminated until a steady-state is reached and their concentration remain constant. This provides a high sensitivity, and delivers information about the energetic positions and probabilities of the observed transitions. At variance, time-resolved spectroscopy relies on the irradiation of the sample with
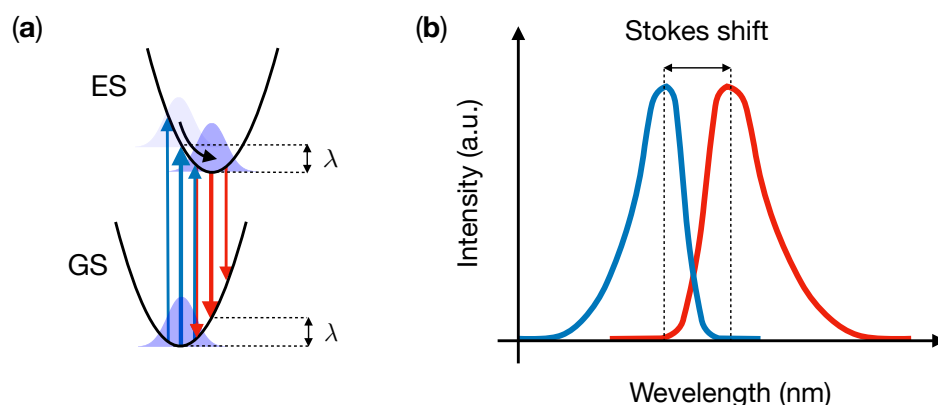
Figure 1.1: Absorption and Emission spectra. (a) Scheme; (b) Spectra. The Stokes shift is highlighted as the distance between absorption and emission maxima. In the harmonic model presented in the previous Part of the Thesis, the Stokes shift is equal to twice the reorganization energy λ (as highlighted in (a)).

a light source whose intensity is modulated as a function of time, and is able to provide kinetic information about the system: pulsed lasers emit flashes of light that create a burst of excited states whose evolution is monitored with a second beam of light as a function of time.

1.1 (Linear) Absorption & Emission techniques

Absorption techniques measure the fraction of light absorbed by a sample irradiated with a continuous-wave beam of light. The absorbed light brings the photoactive species temporarily to an upper excited state, providing information about the energy difference between their ground- and excited-states, and the probability for light absorption to occur, encoded in the recorded absorption spectra (Figure 1.1).

Emission techniques measure the electromagnetic radiation emitted upon deactivation of excited states, providing information about excited-state lifetimes and rate constants. When the emitting excited states are created by the absorption of light, the techniques are referred to as fluorescence and phosphorescence, depending on the nature of the excited state. They are instead referred to as chemiluminescence when the emitting state has been produced through chemical reactions.

The use of polarized light (either linearly or circularly polarized) allows to selectively look at transitions along specific directions, and can give additional information about the nature of the states observed in the spectra.

1.2 Ultrafast time-resolved spectroscopy

The ultrafast photo-induced events which occur in photosynthetic complexes, such as energy migration, electron and/or proton transfer, isomerization, internal conversion, etc., require the use of time-resolved spectroscopy to be studied. In what follows we will focus in the description of *pump-probe* (PP) and *two dimensional Fourier transform* (2DFT) techniques.[1]

1.2.1 Pump-Probe spectroscopy

Pump-probe (PP) spectroscopy is the simplest experimental technique employed to study ultrafast electronic dynamics. In a PP experiment, a fraction of the molecules is promoted by a first (strong) pulse, called *pump* pulse, to an electronic excited state. After a time delay τ, a weaker *probe* pulse is sent to the sample to monitor the pump-induced changes in sample absorption. A difference absorption spectrum (ΔA) is then obtained by subtracting the absorption spectrum of the sample in the ground state from the absorption spectrum of the excited sample. This ΔA spectrum is recorded for a certain number of time delays τ between the two pulses, and the obtained signals are organized along the measured wavelength λ at the given time τ, in $\Delta A(\lambda, \tau)$ maps. The information contained in $\Delta A(\lambda, \tau)$ comes from different processes[54]:

1. *Ground State Bleaching* (GSB) contributions. The fraction of molecules which are in the GS after the first pulse interaction is smaller than the total number of molecules: some of them have in fact been excited by the pump pulse. As a consequence, the ground-state absorption of the excited sample is less than that of the non-excited sample, and a negative signal in the ΔA spectrum is observed in the wavelength region of ground-state absorption.

2. *Stimulated Emission* (SE) contributions. The physical process of stimulated emission is activated when a laser photon induces emission of another photon from an excited molecule, which returns to its ground state. In PP, the molecules that have been excited by the pump pulse can undergo stimulated emission to the ground state when the probe pulse passes through the excited volume. Stimulated emission occurs only for optically allowed transitions and produces a spectral profile that resembles the fluorescence spectrum of the excited chromophore. These signals result in an increase of light intensity at

---

[1]When applied to electronic transitions (VIS, near-IR window), we refer to 2DFT as *two-dimensional electronic spectroscopy* (2DES).
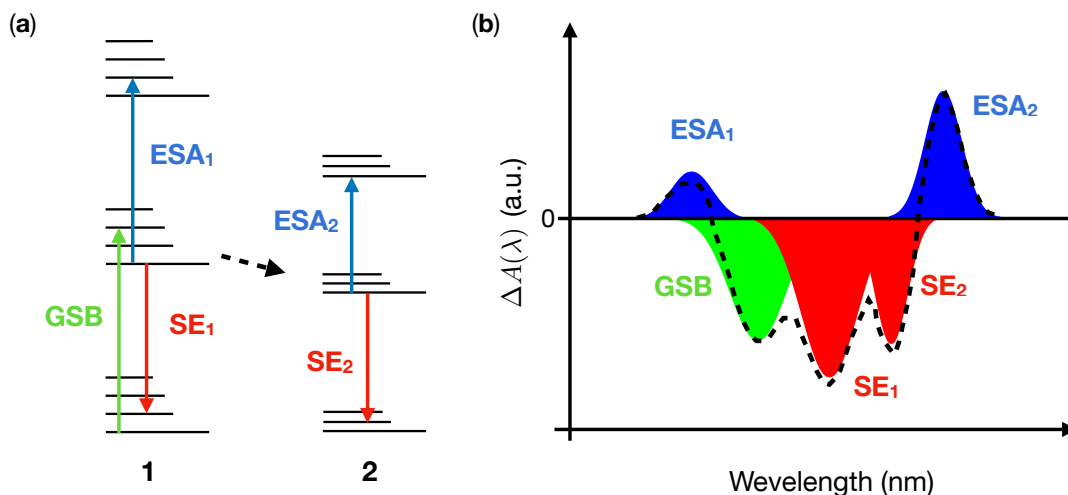
Figure 1.2: (a) Energy level scheme and (b) spectrum of a PP experiment, in which a molecule 1 undergoes energy transfer to a molecule 2. GSB, SE and ESA contributions of both molecules are highlighted in the spectrum as peaks having green, red and blue colors, respectively. The total spectrum is represented by the dashed line.

the detector, corresponding to a negative contribution in ΔA, which sum constructively with the GSB signals. In many chromophores the Stokes shift may be so small that SE and GSB bands merges into one single band.

3. *Excited State Absorption* (ESA) contributions. The molecule's excited states populated by the pump pulse can be themselves excited to optically allowed higher-lying states by the probe pulse. A positive signal in the ΔA spectrum is then observed.

4. *Product Absorption* contributions. These signals appear when the excited molecular states evolve, populating new transient or long-lived (product) molecular states. The probe induced absorption of states which were not present when the pump pulse illuminated the sample, appears as a positive signal in the ΔA spectrum.

The ΔA spectrum is measured in the following way[54]: for every time delay τ, signals of a "pumped" and an "unpumped" sample ($I_{pumped}(\lambda)$ and $I_{unpumped}(\lambda)$ respectively) are recorded, averaging the result over multiple shots to reduce the signal to noise ratio. From the average values of $I_{pumped}(\lambda)$ and $I_{unpumped}(\lambda)$, an absorbance difference spectrum is constructed as

$$\Delta A(\lambda) = -\log\left(I_{pumped}(\lambda)/I_{unpumped}(\lambda)\right) \tag{1.1}$$
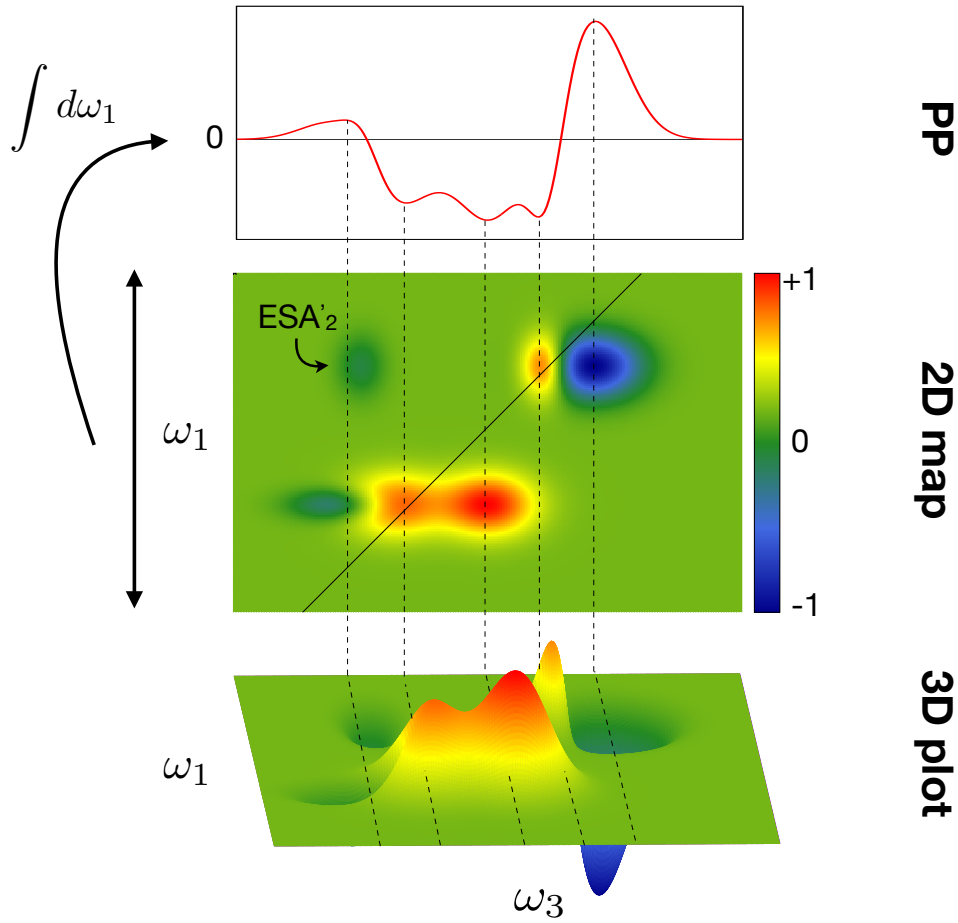
Figure 1.3: Pictorial representation of the relation between PP and 2DES, related to the same energy level scheme displayed in Figure 1.2. Note how the spectral feature labeled as ESA'_2, clearly visible in 2DES, is instead difficult to be discerned in PP, as it overlaps with other signals.

This procedure is repeated for the wanted number of time delays τ, and the entire $\Delta A(\lambda, \tau)$ is collected.

As typical photophysical and photochemical reactions of photosynthetic pigment protein complexes take place on timescales ranging from tens of femtoseconds to a few nanoseconds, the control over the time delay τ between pump and probe pulses and over the pulses duration is of the utmost importance. Experimentally, laser pulses as short as 5 fs have been introduced in transient absorption spectroscopy[55, 56]. Having very short laser pulses allows to follow extremely fast phenomena, but at the cost of a reduced spectral selectivity, as the time-bandwidth product relation $\Delta\nu\Delta t = $ const prohibits the spectral bandwidth $\Delta\nu$ to be arbitrarily small.

Finally, it is possible to control the polarization of the laser beams, which can provide additional information about the exciton migration processes.

1.2.2 Two dimensional Electronic Spectroscopy (2DES)

The two dimensional Fourier transform spectroscopy approach is an extension of the previously presented PP technique: if in PP the evolution of the initially excited sample is monitored over a frequency (detection energy) and a time axis (delay between pump and probe pulses), in 2D spectroscopy one resolves *the same* signal over an additional coordinate, namely the excitation energy. This improvement reveals connections between optical excitations at a given frequency and the signals they create over a wide range of frequencies, untangling possible overlapping signals and eventually giving a direct view of the (potentially) multiple molecular transitions that contribute to a given detected signal.

How can this substantial improvement be obtained?

As we have seen before, the trade-off between time and frequency accuracy (the shorter the pulse the larger the bandwidth) seems to forbid the identification of the initially populated excited states, especially when a high time resolution is required. For instance, a 10-fs gaussian-like pulse with a center wavelength of 800 nm, has a spectral bandwidth of about 100 nm (in this wavelength region) at FWHM (full-width at half maximum), which covers multiple transitions in, e.g., Light Harvesting complexes 2 of several photosynthetic bacteria. This trade-off is circumvented in 2D spectroscopy by introducing an additional *pump* pulse, with a controlled time delay with the other pump pulse, and reconstructing the signal using the Fourier transform methodology.[57] The first pulse excites the molecules having resonant transitions under its bandwidth. This sets in motion the electron charges of these molecules, which then oscillate at their natural (Bohr) frequencies during the time period t_1. The second pulse interacts with the sample exactly after the time delay t_1, and depending on this time delay and the oscillation frequency, it enhances or suppresses the oscillation set in motion by the first pulse (in the same way that a second push of a swing can make it go higher or stop it altogether). This operation is repeated for several pump interpulse delays, and the excitation axis is recovered by Fourier transforming the oscillating signal along the t_1 axis. This explains how the result can have both high temporal and spectral resolution, being therefore limited only by the signal-to-noise ratio.

The radiated signal, obtained as a result of the interaction with the three laser pulses (Figure (1.4)), is a function of the three interpulse time delays, i.e. $E(t_1, t_2, t_3)^2$.

---

[2]Another commonly used notation for denoting these three time intervals is: $\tau \equiv t_1$, $T \equiv t_2$, $t = t_3$.
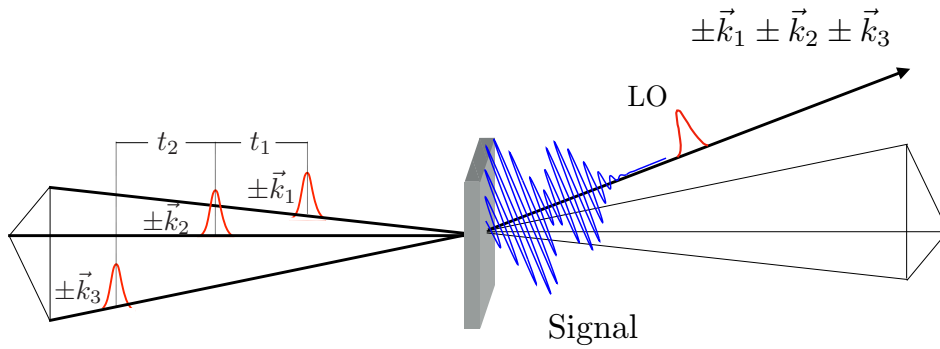
Figure 1.4: Pictorial representation of a third-order nonlinear spectroscopy experiment. The signal is emitted in the direction of the sum of incoming wave vectors. The geometry of the incident pulses can be arranged in different setups: *fully collinear* (all the pulses are in the same direction), *partially noncollinear* (the first two pulses are collinear) and *fully noncollinear* or BOXCARS setup (the one represented here).

The excitation-detection frequency correlation map is calculated by applying, for each time t_2, the Fourier transform along t_1 and t_3, so that $E(t_1, t_2, t_3) \longrightarrow E(\omega_1, t_2, \omega_3)$[3]. In real experiments, only the ω_1 is obtained by an explicit Fourier transform over the scanned time delays t_1, while the detection frequency axis is typically obtained via a heterodyne-detected frequency-domain measurement of the signal, in which the Fourier transform is effectively performed by the spectrometer. In the heterodyne detection mode, the signal field interfere with a local oscillator field which amplifies it and enable the extraction of the complex signal field[58], collecting both phase and intensity information.[4]

Figure 1.4 shows also that the laser pulses approach the sample from (potentially) different directions, as expressed by the fact that each electric field carries a wave-vector ($\boldsymbol{k}_1$, $\boldsymbol{k}_2$ and $\boldsymbol{k}_3$ for, respectively, the first, the second and the third pulses). The signal is therefore observed only in determined directions, the so-called *phase-matching* directions specified by all possible combinations of incident field wave-vectors, $\pm\boldsymbol{k}_1 \pm \boldsymbol{k}_2 \pm \boldsymbol{k}_3$. Two different phase-matched signals are typically recorded in 2DES spectroscopy, along the directions $-\boldsymbol{k}_1 + \boldsymbol{k}_2 + \boldsymbol{k}_3$ and $+\boldsymbol{k}_1 - \boldsymbol{k}_2 + \boldsymbol{k}_3$, called the *rephasing* and *nonrephasing* signals, respectively. *Double-quantum coherence* experiments look instead at the phase-matching direction $+\boldsymbol{k}_1 + \boldsymbol{k}_2 - \boldsymbol{k}_3$. By adding rephasing and non-rephasing signals one obtains absorptive spectra, which gives the maximum information from 2D experiments and facilitates the physical

---

[3]Excitation and detection frequencies are therefore specified by ω_1 and ω_3 axis respectively. We will also use the notation ω_{exc} and ω_{det}.

[4]At variance, in PP experiments it is possible to measure only the signal intensity, thus accessing at a reduced information content of the signal.

interpretation of the measured spectral features[57]. The possibility of looking at different signals in specific phase-matching direction, not only allows to separate them, but also to record signals in background-free conditions (at least in some of the pulses geometries), considerably enhancing the signal-to-noise ratio.

The signals that are measured in 2DES experiments can be summarized in the same categories listed above, i.e., GSB, SE and ESA[5]. The difference here is that no physical switching (on and off) of the pump signal is performed, but rather it is the sequence of the two pump pulses that brings some of the excited molecules back to their ground states in GSB signals. We note that these two approaches are not exactly equal, as possible dephasing and intra-molecular vibration can take place during the time t_1, inducing dynamical features in the 2DES measured GSB signals. We also note that the convention of the signs of the various contributions in 2DES is usually the opposite of that of Pump-Probe experiments: GSB and SE signals are positive, ESA (and product absorption) are negative.

We note here that PP experiment can be obtained from 2DFT measurements through the integration of the obtained signal along the ω_1 coordinate (Figure 1.3). This correspond to a situation in which the time delay t_1 between the first two interactions is set to zero. The projection-slice theorem of multidimensional Fourier analysis[57] gives the needed mathematical expressions to extract 1D time-resolved experiments (e.g., pump-probe) from 2DFT measurements.

1.2.3   2DES: information content

How should 2DES maps be interpreted?

For every given time t_2 a two dimensional plot having excitation and detection frequencies (or wavelengths) axes is examined, as shown in Figure (1.5). Two types of peaks are distinguished: diagonal peaks at ($\omega_{exc} = \omega_{det}$), that mirror the linear absorption spectrum and thus highlight the transitions between the ground-state and the states of the first excitation manifold; and cross-peaks ($\omega_{exc} \neq \omega_{det}$), lying outside the diagonal, which can have different origin and disclose different processes.

At $t_2 = 0$, cross-peaks give valuable information about excitonic coupling between transitions, while they reveal energy transfer pathways when growing along increasing waiting times ($t_2 > 0$) (24). Negative peaks (on both diagonal or off-diagonal positions) can demonstrate the presence of ESA signals, and the appearance of new negative features at increasing waiting-time t_2 can indicate the production of new states through, e.g., energy transfer or internal conversion. Recorded oscil-

---

[5]Product absorption signals can be included in the ESA category.
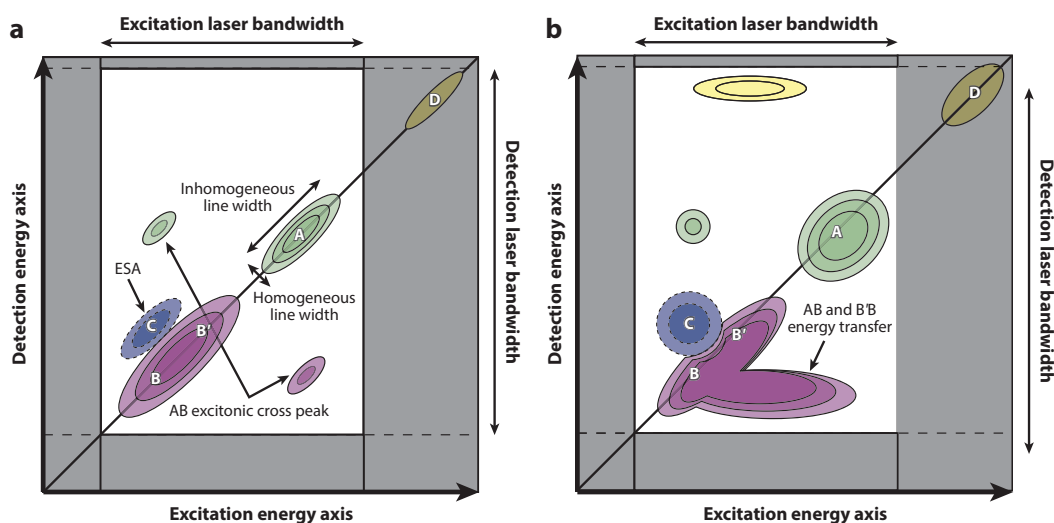
Figure 1.5: Schematic illustration of the information contained in absorptive 2DES. The shaded regions are outside the excitation and detection pulse bandwidth. (a) The $t_2 = 0$ map reveals excitonic coupling, ESA features, together with homogeneous and inhomogeneous line widths. (b) At $t_2 > 0$, the progressive broadening of peaks in the antidiagonal direction reflects spectral diffusion. Growing of cross peaks indicates energy transfer, while the appearance of entirely new peaks at later waiting times, such as the yellow cross-peak in panel b, represents the formation of a new product species D, populated upon excitation of B'. Figure taken from ref. 59.

lations of the diagonal and cross-peaks along t_2 reflect electronic, vibrational and vibronic coherences. The interpretation of the physical origin of such oscillations and their possible importance for photosynthetic energy and charge transfer is currently subject of intense debate.[35, 60, 61]

The line-shapes of the measured transitions contain information about the interaction of the electronic states with the surrounding environment: the ratio of the diagonal to anti-diagonal widths is known to reflect the degree of inhomogeneous versus homogeneous broadening (see Appendix, Section 4.1).[62, 57] At longer t_2 delays, the so-called spectral diffusion of inhomogeneously broadened transitions is observed, as the system-bath interaction erases the memory (correlation) of the initial excitation frequency. The initially diagonal elongation of these peaks is gradually lost, and the timescale of this memory loss provides microscopic understanding of e.g. liquid dynamics and solvation[62, 63].

2DFT techniques can also be applied with polarized pulses, adding transition selectivity and providing additional information. Among the possible refinements and frontier pursuit by 2D spectroscopy we mention: its application in the UV window, promising new structural probes of conformational dynamics, energy and

charge transfer in biological systems[64]; the advent of chiral 2D, employing chiral control of the pulses[65]; the development of mixed-frequency techniques that combine pump and probe pulses at different windows of the electromagnetic radiation; the development of single-molecule 2D spectroscopy.

Despite the high density of information contained in 2DES maps, the overlap of spectral features originating from many different processes make their interpretation highly non-trivial: the analysis requires some pre-knowledge of the system components and relaxation dynamics, and this can lead to strongly biased understanding of the observed data. It is therefore necessary to support experimental measurements with theoretical modeling.

Theoretical Methods for Spectroscopy

Theoretical methods are an effective tool to achieve a microscopic understanding of the processes activated when light impinges on a system of light-sensitive molecules. From a purely theoretical point of view, the problem is summarized within the field-matter Hamiltonian

$$\hat{H} = \hat{H}_0 + \hat{H}'(t) \tag{2.1}$$

where $\hat{H}_0$ is the *matter* or *molecular* Hamiltonian, described in the previous Part of this Thesis, and $\hat{H}'$ represent the interaction term between the external electromagnetic field and the system of molecules. The semiclassical treatment of the molecular coupling to the radiation field is usually employed, for which the quantum molecular system interacts with a classical field:

$$\hat{H}'(t) = -\hat{\boldsymbol{\mu}} \cdot \boldsymbol{E}(\boldsymbol{r}, t) \tag{2.2}$$

In the previous equation $\hat{\boldsymbol{\mu}}$ is the dipole operator of the QM system, and $\boldsymbol{E}(\boldsymbol{r}, t)$ is the incoming field.

Solving the time-dependent Schrödinger driven by the Hamiltonian of Eq. (2.1) would in principle return all the properties of the field-matter interaction problem. The various types of spectroscopy experiments would then be obtained by computing the macroscopic polarization induced in the sample by the external field, which is the source of the radiated signal. This brute-force approach is generally unaffordable.

Therefore, time-dependent perturbation theory is usually applied to tackle this

problem, where the n-th order perturbative expansion in terms of $H'(t)$ represents a situation in which the electromagnetic field $\boldsymbol{E}(t)$ has interacted n times with the sample. Different orders of the perturbative expansion then give rise to different kinds of signals, and we will focus on first- and third-order signals.

A density matrix approach is usually preferred to a wave-function based approach[1] for the description of the system, since it is the natural formulation of open quantum system problems. Indeed, in the density matrix formalism it is possible to include the fluctuations and dissipations processes that occur due to the interaction between the system and the environment. The needed microscopic inputs for a minimal modeling of system spectroscopy are: the manifold of states and the transition dipole moments between them, together with a phenomenological description of the bath induced perturbations. Again, this zero-th order picture can be refined by considering intra- and inter-molecular vibrations (i.e. the system's spectral density), which are responsible for the relaxation and transport processes observed in the spectra.

2.1   Density matrix

Consider a dimer of strongly interacting molecules immersed in a fluctuating environment. The system is excited, and a delocalized exciton is formed. With time, the interaction between the molecules and the environment tends to destroy the coherent relation between the two, and to localize the excitation on either one or the other chromophore. This final state of the system, in which the excitation can be on either sites with a certain probability, cannot be described by a wave function, and therefore calls for a more advanced description, a *density matrix* description.

For an isolated quantum system, a *pure state* containing all the information about it can be defined, e.g. through a wave-function $|\psi\rangle$. An equivalent way of describing it, is through its density matrix, defined as

$$\hat{\rho}(t) = |\psi(t)\rangle \langle\psi(t)| = \sum_{ab} c_b^*(t) c_a(t) |a\rangle \langle b| \tag{2.3}$$

where the set of $|a\rangle$ states represents an arbitrary basis on which the wave-function $|\psi(t)\rangle$ is expanded.

For statistical ensembles of states, or non-isolated systems, it is impossible to define a pure state, i.e. a state that completely incorporates all the knowledge about the system, but rather one deals with a set of states $|\psi_k\rangle$ with probability p_k

---

[1] For a wave-function treatment of the field-matter interaction, see e.g. ref. 66.

$(\sum_k p_k = 1)$ to be observed. The density operator of this *mixture* of states reads

$$\hat{\rho}(t) = \sum_k p_k \left|\psi_k(t)\right\rangle \left\langle\psi_k(t)\right| \tag{2.4}$$

which in the basis set $\{|a\rangle\}$ can be written

$$\hat{\rho} = \sum_{ab} \rho_{ab} \left|a\right\rangle \left\langle b\right| \tag{2.5}$$

Diagonal elements ρ_{aa} are real quantities called *populations*, and give the probability of occupying a quantum state $|a\rangle$; off-diagonal elements ρ_{ab} ($a \neq b$), called *coherences*, are complex numbers and have a time dependent phase factor that describe the evolution of coherent superpositions of states.

The name density matrix, derives from the observation that it plays the role of a probability density. Indeed, the expectation value of a given operator $\hat{A}$ can be expressed in terms of the density matrix as

$$\langle A \rangle = Tr[\hat{\rho}\hat{A}] \tag{2.6}$$

The density matrix operator satisfies the following properties:

- $\hat{\rho}^\dagger = \hat{\rho}$ (hermiticity);

- $\hat{\rho}_{aa} \geq 0 \,\forall\, n$, as it describes the probability of being in the state $|a\rangle$;

- $Tr[\hat{\rho}] = 1$ (normalization);

- $Tr[\hat{\rho}^2] \leq 1$ (in general), and it is exactly equal to 1 only for pure states.

If the dynamical equation for the evolution of a wave-function is the Schrödinger equation, the time evolution of density matrix operator is described by the *Liouville-von Neumann* equation, given by

$$i\hbar\frac{d\hat{\rho}}{dt} = \left[\hat{H}, \hat{\rho}\right] \tag{2.7}$$

If $\hat{H}$ is time independent, the formal solution of this equation is given by

$$\hat{\rho}(t) = e^{-\frac{i}{\hbar}\hat{H}t}\hat{\rho}(0)e^{\frac{i}{\hbar}\hat{H}t} \tag{2.8}$$

and by expanding this solution in terms of the Hamiltonian's eigenstates, one obtains constant populations and coherences oscillating at the characteristic Bohr frequencies $\omega_{ab} = (E_a - E_b)/\hbar$.

The quantum state of an ensemble of optically driven molecular aggregates in their environment, is conveniently defined by the density matrix of Eq. (2.5).

2.2 Field-Matter interaction

Consider the field-matter Hamiltonian of Eq. (2.1): assuming the interaction with the external electromagnetic field to be much weaker than that of the internal fields of the molecular system, one can treat the interaction term perturbatively.

The formal integration of the Liouville-von Neumann equation (Eq. (2.7)) leads to[2]

$$\rho(t) = \rho(t_0) - \frac{i}{\hbar} \int_{t_0}^{t} d\tau \, [H(\tau), \rho(\tau)] \tag{2.9}$$

We can solve this equation iteratively, by plugging it into itself:

$$\begin{aligned} \rho(t) &= \rho(t_0) + \sum_{n=1}^{\infty} \left(-\frac{i}{\hbar} \right)^n \int_{t_0}^{t} d\tau_n \int_{t_0}^{\tau_n} d\tau_{n-1} \cdots \int_{t_0}^{\tau_2} d\tau_1 \\ & \quad [H(\tau_n), [H(\tau_{n-1}), \ldots [H(\tau_1), \rho(t_0)] \ldots]] \end{aligned} \tag{2.10}$$

Since H is not generally small, it is not possible to truncate the expansion and all the order should be retained for the computation of $\rho(t)$. What it is small is actually the interaction term $H'(t)$, and we would like to be able to write a similar expression as that of Eq. (2.10) in terms of $H'(t)$ only. To do that, we introduce the *interaction picture representation*[3] of the density matrix and of the perturbative term of the Hamiltonian as

$$\rho_I(t) = e^{\frac{i}{\hbar} H_0 t} \rho(t) e^{-\frac{i}{\hbar} H_0 t} = \mathbb{G}^*(t) \rho(t) \tag{2.11}$$

$$H'_I(t) = e^{\frac{i}{\hbar} H_0 t} H'(t) e^{-\frac{i}{\hbar} H_0 t} = \mathbb{G}^*(t) H'(t) \tag{2.12}$$

where the superoperator $\mathbb{G}(t)$ is defined as $\mathbb{G}(t) \bullet = e^{-\frac{i}{\hbar} H_0 t} \bullet e^{\frac{i}{\hbar} H_0 t}$, and H_0 is here the non perturbative part of the field-matter Hamiltonian, i.e. the molecular Hamiltonian.

In terms of these newly defined operators, the dynamical Eq. (2.9) can be rewritten as

$$i\hbar \frac{d\rho_I}{dt} = [H'_I, \rho_I] \tag{2.13}$$

which is formally equivalent to original Liouville-von Neumann equation. Therefore,

---

[2]To simplify the notation, we will from now on discard the hat $\hat{\bullet}$ on the top of operators.

[3]See e.g. ref. 66.

the expansion presented in Eq. (2.10) holds also for $\rho \longrightarrow \rho^I$ and $H \longrightarrow H^I$, and it reads

$$
\begin{aligned}
\rho_I(t) \;=\; & \rho_I(t_0) + \sum_{n=1}^{\infty} \left(-\frac{i}{\hbar}\right)^n \int_{t_0}^{t} d\tau_n \int_{t_0}^{\tau_n} d\tau_{n-1} \cdots \int_{t_0}^{\tau_2} d\tau_1 \\
& [H_I'(\tau_n), [H_I'(\tau_{n-1}), \dots [H_I'(\tau_1), \rho_I(t_0)] \dots]]
\end{aligned}
\tag{2.14}
$$

The density matrix at time t_0, $\rho(t_0)$, is the equilibrium density matrix prior to any field interaction, and we can safely assume that it does not evolve in time when subject to the system Hamiltonian H_0. By applying the superoperator $\mathbb{G}$ on both sides of the equation, this expression is then rewritten as

$$
\begin{aligned}
\rho(t) \;=\; & \mathbb{G}(t)\rho_I(t_0) + \sum_{n=1}^{\infty} \left(-\frac{i}{\hbar}\right)^n \int_{t_0}^{t} d\tau_n \int_{t_0}^{\tau_n} d\tau_{n-1} \cdots \int_{t_0}^{\tau_2} d\tau_1 \\
& [\mathbb{G}(t-\tau_n)H'(\tau_n), [\mathbb{G}(\tau_n-\tau_{n-1})H'(\tau_{n-1}), \dots [\mathbb{G}(\tau_1)H'(\tau_1), \rho(t_0)] \dots]]
\end{aligned}
\tag{2.15}
$$

The Hamiltonian $H'(t)$ is a perturbation, and we can therefore truncate the series of integrals, obtaining the perturbative order by order expansion of the density matrix. The density matrix to the n-th order in the external field perturbation reads

$$
\rho(t) = \rho^{(0)}(t_0) + \rho^{(1)}(t) + \rho^{(2)}(t) + \cdots + \rho^{(n)}(t)
\tag{2.16}
$$

and $\rho^{(n)}(t)$ is given by

$$
\begin{aligned}
\rho^{(n)}(t) \;=\; & \left(-\frac{i}{\hbar}\right)^n \int_{t_0}^{t} d\tau_n \int_{t_0}^{\tau_n} d\tau_{n-1} \cdots \int_{t_0}^{\tau_2} d\tau_1 \\
& [\mathbb{G}(t-\tau_n)H'(\tau_n), [\mathbb{G}(\tau_n-\tau_{n-1})H'(\tau_{n-1}), \dots [\mathbb{G}(\tau_1)H'(\tau_1), \rho(t_0)] \dots]]
\end{aligned}
\tag{2.17}
$$

By sending $t_0 \to -\infty$, Eq. (2.16) becomes

$$
\rho(t) = \rho^{(0)}(-\infty) + \sum_{n=0}^{\infty} \rho^{(n)}(t)
\tag{2.18}
$$

2.3 The (Mukamelian) Response Function Approach

When an external electromagnetic field impinges on a sample of light-sensitive molecules, the charges of these molecules start to vibrate with characteristic (Bohr) frequencies, i.e. the field produces a time-dependent polarization of the sample. This time dependent polarization is the source of new field, which may interfere with the incident field and give rise to the measured signal of spectroscopic experi-

ments. The induced polarization of the considered ensemble of molecules is therefore the quantity of interest for the simulation of spectroscopy. The n-th order polarization induced by the perturbing field is given by the expectation value of the dipole operator, as

$$\boldsymbol{P}^{(n)}(t) = Tr\left[\boldsymbol{\mu}\rho^{(n)}(t)\right] \tag{2.19}$$

Combining Eq. (2.19) with Eq. (2.17) and specifying the form of the perturbation as in Eq. (2.2), i.e. $H' = -\boldsymbol{\mu} \cdot \boldsymbol{E}(t)$, we obtain

$$\begin{aligned}
\boldsymbol{P}^{(n)}(t) = \left(-\frac{i}{\hbar}\right)^n \int_0^\infty dt_n \int_0^\infty dt_{n-1} \cdots \int_0^\infty dt_1 \\
E(t - t_n)E(t - t_n - t_{n-1})\dots E(t - t_n - t_{n-1} - \cdots - t_1) \\
Tr\left[\hat{\boldsymbol{\mu}}\mathbb{G}(t_n)\mu^\times\mathbb{G}(t_{n-1})\mu^\times \dots \mu^\times\mathbb{G}(t_1)\mu^\times\rho_0\right]
\end{aligned} \tag{2.20}$$

where ρ_0 is the equilibrium density matrix, $\mu^\times \bullet \equiv [\hat{\mu}, \bullet]$ is the dipole super-operator, and we have changed variables.[4]

2.3.1 Linear Polarization

The linear (first-oder) polarization is connected to the incident radiation field through the linear relation

$$\boldsymbol{P}^{(1)}(\boldsymbol{r}, t) = \int_0^\infty dt_1 R^{(1)}(t_1)E(\boldsymbol{r}, t - t_1) \tag{2.21}$$

$R^{(1)}(t_1)$ is the so-called (first-oder) system *response function* and contains the information of the first-order perturbed system. According to Eq. (2.19) and Eq. (2.21), together with the definition of $\rho^{(n)}$ from Eq. (2.17), $R^{(1)}(t_1)$ can be written as[30]

$$R^{(1)}(t_1) = \left(\frac{i}{\hbar}\right) Tr\left[\hat{\boldsymbol{\mu}}\mathbb{G}(t_1)\mu^\times\hat{\rho}_0\right] \tag{2.22}$$

where $\hat{\rho}_0$ is the equilibrium density matrix (i.e. the density matrix prior to any field interaction). This equation reads in the following way:

1. Start from the the equilibrium density matrix ρ_0;

2. Interact once with the laser via the dipole superoperator $\mu^\times$;

---

[4] $\tau_1 = 0$, $t_1 = \tau_2 - \tau_1$, $t_2 = \tau_3 - \tau_2$, ..., $t_n = t - \tau_n$. We can choose $\tau_1 = 0$ since the time-zero point is arbitrary.

3. Evolve the perturbed density matrix[5] according to the field-free molecular hamiltonian H_0 for a time t_1;

4. With this perturbed and evolved density matrix, compute the first order macroscopic polarization;

The expression for the linear polarization given in Eq. (2.21) will be connected to the ground-state absorption spectroscopy in the following Sections.

2.3.2 Third-order Polarization

Similarly, the third-order polarization reads

$$
\boldsymbol{P}^{(3)}(\boldsymbol{r},t) = \int_0^\infty dt_3 \int_0^\infty dt_2 \int_0^\infty dt_1 R^{(3)}(t_3,t_2,t_1) \times
$$
$$
E(\boldsymbol{r},t-t_3)E(\boldsymbol{r},t-t_3-t_2)E(\boldsymbol{r},t-t_3-t_2-t_1) \qquad (2.23)
$$

where the third-order response function, $R^{(3)}(t_3,t_2,t_1)$, is given by[30]

$$
R^{(3)}(t_3,t_2,t_1) = \left(\frac{i}{\hbar}\right)^3 Tr\left[\hat{\boldsymbol{\mu}}\mathbb{G}(t_3)\mu^\times\mathbb{G}(t_2)\mu^\times\mathbb{G}(t_1)\mu^\times\hat{\rho}_0\right] \qquad (2.24)
$$

The interpretation of Eq. (2.24) follows from that presented for $R^{(1)}(t_1)$: three interactions (denoted by $\mu^\times$) with the incoming laser field, three field-free propagations by means of $\mathbb{G}(t)$, and the signal generation described by the last dipole $\hat{\boldsymbol{\mu}}$. The third-order induced polarization is obtained by combining the computed response function with the incoming laser fields, specified by

$$
\boldsymbol{E}\left(\boldsymbol{r},t\right) = \sum_j \sum_{u_j=\pm 1} \mathbb{E}_j^{u_j}\left(t-\tau\right)\exp\left[iu_j\left(\boldsymbol{k_j}\boldsymbol{r}-\omega_j\left(t-\tau\right)\right)\right] \qquad (2.25)
$$

where $\mathbb{E}_j^{u_j}\left(t-\tau\right)$ is the complex envelope of the pulse, centered at time τ, and the fields have carrier frequency ω and wavevectors $\boldsymbol{k}$. The positive and negative frequency components of the fields are specified by $u=+1$ and $u=-1$ respectively, and $\left[\mathbb{E}_j^-\right] = \left[\mathbb{E}_j^+\right]^*$.

Some sensible considerations allow to simplify Eq. (2.24), untangling many different contributions:

---

[5]In is important to notice that the dipole operated density matrix, i.e. $[\hat{\boldsymbol{\mu}},\hat{\rho}_0]$ is no more a density matrix, as it does not satisfy some of its fundamental properties, e.g. $Tr[\rho]=1$. The complete time-evolved density matrix (unperturbed plus first order perturbed) is actually given by $\mathbb{G}(t_1)\hat{\rho}_0 + \mathbb{G}(t_1)\mathbb{V}\hat{\rho}_0$. Since $Tr[\hat{\boldsymbol{\mu}}\mathbb{G}(t_1)\hat{\rho}_0]=0$, the result obtained by including or excluding this piece is the same, which implies that evolving the complete density matrix or only its first order perturbation gives here the same result.

- *Time-ordering*: we assume that the pulses are temporally well separated, i.e. that they are shorter than the time delay between them, and they do not overlap. This allows to reduce the number of terms that enter in the third-order response, as the first interaction will occur due to the field with wave-vector $\boldsymbol{k}_1$, followed by an interaction with the $\boldsymbol{k}_2$ field, and finally with the field specified by $\boldsymbol{k}_3$;

- *Semi-impulsive limit*: it is often assumed that the laser pulses are short compared to any time scale of the system, but long compared to the oscillation period of the light field. The pulses envelopes can then be approximated by delta functions in time[6];

- *Rotating Wave Approximation (RWA)*: molecular frequencies ω_{eg} which appear in the response function are combined with field frequencies $\pm\omega_j$. The rotating-wave approximation retains only low-frequency terms, i.e. $\omega_{eg} - \omega_j$. The high frequency contributions $\omega_{eg} + \omega_j$, which add very small corrections, are neglected;

- *Phase-matching*: the wave vectors of the three incident fields combine, so that the generated field propagates in the directions $\pm\boldsymbol{k}_1 \pm\boldsymbol{k}_2 \pm\boldsymbol{k}_3$, and a detector in the experiments can resolve the various contributions by recording the signal in a chosen direction. There are four independent combinations of the wave-vectors $\boldsymbol{k}$, which represent four independent third-order techniques:

$$
\begin{aligned}
\boldsymbol{k}_I &= -\boldsymbol{k}_1 + \boldsymbol{k}_2 + \boldsymbol{k}_3 & (u_1, u_2, u_3) &= (-1, 1, 1) \\
\boldsymbol{k}_{II} &= +\boldsymbol{k}_1 - \boldsymbol{k}_2 + \boldsymbol{k}_3 & (u_1, u_2, u_3) &= (1, -1, 1) \\
\boldsymbol{k}_{III} &= +\boldsymbol{k}_1 + \boldsymbol{k}_2 - \boldsymbol{k}_3 & (u_1, u_2, u_3) &= (1, 1, -1) \\
\boldsymbol{k}_{IV} &= +\boldsymbol{k}_1 + \boldsymbol{k}_2 + \boldsymbol{k}_3 & (u_1, u_2, u_3) &= (1, 1, 1)
\end{aligned}
$$

---

[6]In Part III, Chapters 1 and 3, it is shown that it can be important to remove this approximation when comparing simulated spectra to experiments performed using realistic (band-width limited) pulses.

Let us rewrite Eq. (2.24) by explicitly developing all the commutators, obtaining:

$$Tr\left[\hat{\boldsymbol{\mu}}\mathbb{G}(t_3)\mu^\times\mathbb{G}(t_2)\mu^\times\mathbb{G}(t_1)\mu^\times\hat{\rho}_0\right] =$$

$$+Tr\left[\hat{\boldsymbol{\mu}}\mathbb{G}(t_3)\hat{\boldsymbol{\mu}}\mathbb{G}(t_2)\hat{\boldsymbol{\mu}}\mathbb{G}(t_1)\hat{\boldsymbol{\mu}}\rho_0\right] \qquad \Rightarrow R_4$$

$$-Tr\left[\hat{\boldsymbol{\mu}}\mathbb{G}(t_3)\hat{\boldsymbol{\mu}}\mathbb{G}(t_2)\hat{\boldsymbol{\mu}}\mathbb{G}(t_1)\rho_0\hat{\boldsymbol{\mu}}\right] \qquad \Rightarrow R_1^*$$

$$-Tr\left[\hat{\boldsymbol{\mu}}\mathbb{G}(t_3)\hat{\boldsymbol{\mu}}\mathbb{G}(t_2)\mathbb{G}(t_1)\hat{\boldsymbol{\mu}}\rho_0\hat{\boldsymbol{\mu}}\right] \qquad \Rightarrow R_2^*$$

$$+Tr\left[\hat{\boldsymbol{\mu}}\mathbb{G}(t_3)\hat{\boldsymbol{\mu}}\mathbb{G}(t_2)\mathbb{G}(t_1)\rho_0\hat{\boldsymbol{\mu}}\hat{\boldsymbol{\mu}}\right] \qquad \Rightarrow R_3$$

$$-Tr\left[\hat{\boldsymbol{\mu}}\mathbb{G}(t_3)\mathbb{G}(t_2)\hat{\boldsymbol{\mu}}\mathbb{G}(t_1)\hat{\boldsymbol{\mu}}\rho_0\hat{\boldsymbol{\mu}}\right] \qquad \Rightarrow R_3^*$$

$$+Tr\left[\hat{\boldsymbol{\mu}}\mathbb{G}(t_3)\mathbb{G}(t_2)\hat{\boldsymbol{\mu}}\mathbb{G}(t_1)\rho_0\hat{\boldsymbol{\mu}}\hat{\boldsymbol{\mu}}\right] \qquad \Rightarrow R_2$$

$$+Tr\left[\hat{\boldsymbol{\mu}}\mathbb{G}(t_3)\mathbb{G}(t_2)\mathbb{G}(t_1)\hat{\boldsymbol{\mu}}\rho_0\hat{\boldsymbol{\mu}}\hat{\boldsymbol{\mu}}\right] \qquad \Rightarrow R_1$$

$$-Tr\left[\hat{\boldsymbol{\mu}}\mathbb{G}(t_3)\mathbb{G}(t_2)\mathbb{G}(t_1)\rho_0\hat{\boldsymbol{\mu}}\hat{\boldsymbol{\mu}}\hat{\boldsymbol{\mu}}\right] \qquad \Rightarrow R_4^* \qquad (2.26)$$

The terms R_1^*, R_2^*, R_3^*, R_4^* are the complex conjugate of R_1, R_2, R_3, R_4. We can further develop the various terms of Eq. (2.26) in a simple model in which H_0 is just the system part of a generic system-bath Hamiltonian (Part I, Eq. 3.1). We assume the system to be described by a ground-state g, the first excitation manifold of states labeled by e, and the second exciton manifold of states f (Part II, Figure 2.1). The manifolds are connected by the dipole operator $\boldsymbol{\mu}$, and we assume that only transition between $g \to e$ and $e \to f$ can occur. Therefore, by considering $\rho_0 = |g\rangle\langle g|$ and inserting the completeness relation $\mathbb{1} = \sum_a |a\rangle\langle a|$ (where a runs over all the states of the system) in between the various operators, the term R_4 of Eq. (2.26), taken here as an example, can be rewritten as

$$Tr\left[\hat{\boldsymbol{\mu}}\mathbb{G}(t_3)\hat{\boldsymbol{\mu}}\mathbb{G}(t_2)\hat{\boldsymbol{\mu}}\mathbb{G}(t_1)\hat{\boldsymbol{\mu}}\rho_0\right] =$$

$$= \sum_{abcd} \langle d|\,\hat{\boldsymbol{\mu}}\,|c\rangle \langle c|\, e^{-iHt_3}\hat{\boldsymbol{\mu}}\,|b\rangle \langle b|\, e^{-iHt_2}\hat{\boldsymbol{\mu}}\,|a\rangle \langle a|\, e^{-iHt_1}\hat{\boldsymbol{\mu}}\,|g\rangle \langle g|\, e^{+iH(t_1+t_2+t_3)}\,|d\rangle =$$

$$= \sum_{abcd} \hat{\boldsymbol{\mu}}_{dc}e^{-iH_c t_3}\hat{\boldsymbol{\mu}}_{cb}e^{-iH_b t_2}\hat{\boldsymbol{\mu}}_{ba}e^{-iH_a t_1}\hat{\boldsymbol{\mu}}_{ag}e^{+iH_g(t_1+t_2+t_3)}\,\langle g|d\rangle =$$

$$= \sum_{ee'b} \boldsymbol{\mu}_{ge'}\boldsymbol{\mu}_{e'b}\boldsymbol{\mu}_{be}\boldsymbol{\mu}_{eg}e^{-i\omega_{e'g}t_3}e^{-i\omega_{bg}t_2}e^{-i\omega_{eg}t_1} \qquad (2.27)$$

where we have also made use of the fact that $\boldsymbol{\mu}_{gf} = 0$ (only transitions between $g \to e$ and $e \to f$ are allowed). Under the time-ordering hypothesis and by applying the RWA, we obtain that

1. The only term of the summation over the index b which survives the RWA is
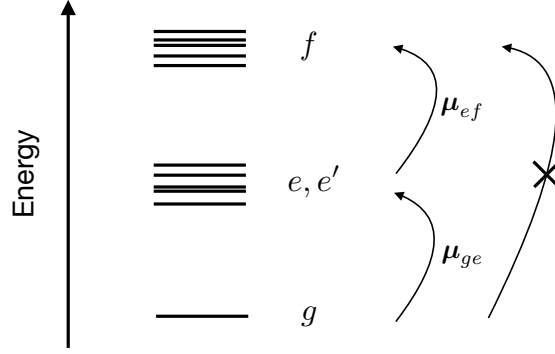
Figure 2.1: Energy level scheme of a generic system, given by the ground state g, the first excitation manifold of states e, e' and the second excitation manifold of states f. The transitions between g and f are forbidden.

$b = g$, and Eq. (2.27) becomes

$$\sum_{ee'} \boldsymbol{\mu}_{ge'} \boldsymbol{\mu}_{e'g} \boldsymbol{\mu}_{ge} \boldsymbol{\mu}_{eg} e^{-i\omega_{e'g}t_3} e^{-i\omega_{eg}t_1} \qquad (2.28)$$

2. Only some components of the fields (Eq. (2.25)) will produce non null results, and precisely that specified by wave-vectors $+\boldsymbol{k}_1$ and $+\boldsymbol{k}_3$. This implies that this signal will be detected only in that specific phase-matching direction, which in this particular case is the non-rephasing direction.

Similar derivations follows for all the terms of Eq. (2.26), and we can group them (in the time-ordering hypothesis, under the RWA) in specific phase-matching directions: the wave-vector dependent response function $R^{(3)}_{\boldsymbol{k}_s}(t_3, t_2, t_1)$ will contain all the signals produced in the $\boldsymbol{k}_s$ direction, with $\boldsymbol{k}_s = u_1\boldsymbol{k}_1 + u_2\boldsymbol{k}_2 + u_3\boldsymbol{k}_3$ (the signal wave-vector).

We focus hereafter on two of the four possible independent choices of u_j, namely the techniques specified by $\boldsymbol{k}_I$ and $\boldsymbol{k}_{II}$, which correspond to *rephasing* and *non-rephasing* signals. Similar considerations also apply for the double quantum technique $\boldsymbol{k}_{III}$, while $\boldsymbol{k}_{IV}$ signals vanishes within the RWA.

2.3.3   Feynman Diagrams

When looking at the specific rephasing and non-rephasing phase-matching directions, one realizes that the RWA acts as a filter for the eight terms of Eq. (2.26): only three of the eight terms survives in both the techniques, and these represent different physical processes (GSB, SE and ESA) that can occur when the sequence
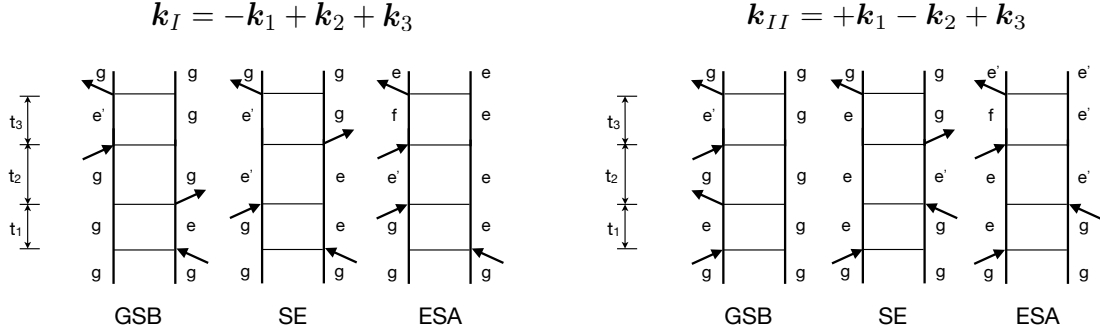
$$\boldsymbol{k}_I = -\boldsymbol{k}_1 + \boldsymbol{k}_2 + \boldsymbol{k}_3 \qquad\qquad \boldsymbol{k}_{II} = +\boldsymbol{k}_1 - \boldsymbol{k}_2 + \boldsymbol{k}_3$$

Figure 2.2: Feynman diagrams for rephasing (*left*) and nonrephasing (*right*) phase matching directions. Ground-state bleaching (GSB), stimulated emission (SE) and excited state absorption (ESA) diagrams are distinguished (applying the time-ordering prescription and rotating wave approximations).

of laser pulses impinge on the system. These resonant terms of the third-order response function are usually interpreted using Feynman diagrams, showed in Figure 2.2. Feynman diagrams are simple schematic representations of selected terms of the third-order response function, and they manifest in a pictorial way the physical processes which lie behind the equations.

Given a Feynman diagram, it is possible to built the corresponding response function (e.g., $R_{\boldsymbol{k}_I}^{ESA}$) following the rules that translate diagrams into equations:[67]

1. The two vertical lines represent the time evolution of the ket (left) and bra (right) of the density matrix. Time flows from the bottom to the top. The system is assumed to start from the equilibrium density matrix, given by $\hat{\rho}_0 = |g\rangle \langle g|$.

2. Interactions with the field are represented by arrows, acting either on the left or on the right, which change the state of the corresponding density matrix element (ket or bra, respectively).

3. An arrow pointing to the right represents the positive frequency field component $e^{-i\omega t + i\boldsymbol{k}\boldsymbol{r}}$, while an arrow pointing to the left represents the negative frequency field component $e^{+i\omega t - i\boldsymbol{k}\boldsymbol{r}}$. The emitted light (represented by the last outgoing arrow), has frequency and wavevector determined by the sum of the input frequencies and wavevectors (considering the appropriate signs).

4. Each diagram carries a sign $(-1)^n$, where n is the number of interactions from the right. This comes from the fact that each time an interaction occurs from the right, the negative term of the commutator $\mu^\times$ is being considered. Since

the last interaction is not part of the commutator, it is not counted in this sign-rule. By following these rules, one realizes that GSB and SE diagrams have a positive sign, while ESA diagram have a negative sign.

5. Arrows pointing towards the system represent a photon absorption, accompanied by a molecular transition to a higher energy state of the corresponding side of the density matrix; arrows pointing away represent a photon emission and a transition to a lower-energy state. This rule follows from the employed RWA. Since the last interaction corresponds to an emission of light, it always points away from the system.

6. The last interaction must end in a population state (as the final trace operation filters only diagonal terms).

During the intervals between the interactions (t_1, t_2 and t_3), the density matrix evolves freely, i.e. according to the molecular Hamiltonian H_0. During t_1 and t_3 the system is in a coherence state, while during t_2 it is in a population state. In absence of transport, the density matrix elements can only change by interacting with the field. We will remove this restriction towards the end of the chapter, by introducing response function terms (and correspondent Feynman diagrams) in presence of exciton transport.

What was introduced in the experimental spectroscopy Chapter (Chapter 1), is here understood in terms of the microscopic description of the interaction between the incident field and the density matrix of the considered ensemble of optically driven molecules.

2.3.4 $R^{(1)}$ & Spectroscopy: Phenomenological Dephasing

Here we connect the linear absorption spectrum with the first-order response function of Eq. (2.22). For simplicity we consider the molecular Hamiltonian $\hat{H}_0$ to be given by only the system (electronic) part, while adding the effect of vibrations phenomenologically, as a source of signal dephasing.[7]

$R^{(1)}(t_1)$ can then be expanded in the eigenstate (exciton) basis, resulting in

$$R^{(1)}(t_1) = \left(\frac{i}{\hbar}\right) \sum_e \boldsymbol{\mu}_{ge} \boldsymbol{\mu}_{eg} e^{-i\omega_{eg}t - \gamma_{eg}t} + c.c. \tag{2.29}$$

---

[7]This phenomenological dephasing term can be introduced as a dissipative term in the Liouville von Neumann equation (Eq. 2.7), which describes the decaying of signal coherence as an effect of the interaction with the environment.
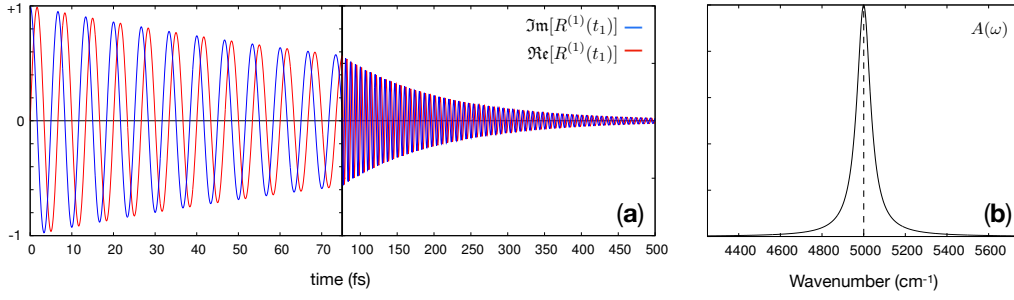
Figure 2.3: (a) Response function $R^{(1)}(t_1)$ and (b) absorption spectrum $A(\omega)$ in the case of phenomenological dephasing. $\omega_{eg} = 5000cm^{-1}$, $\gamma_{eg} = 40cm^{-1}$. Note that the Lorenzian shape of the peak in (b), symmetric with respect to ω_{eg}.

where we assume the equilibrium density matrix $\hat{\rho}_0$ (the state of the system prior to any field interaction) to be in the ground state population $|g\rangle \langle g|$, $\omega_{eg} \equiv (\epsilon_e - \epsilon_g)/\hbar$, and the exponential rate γ_{eg} to be the phenomenological dephasing constant.

In the ground-state absorption, the transmission of the incident laser beam is measured. The detector reveals the net optical field, which is the result of the interference between the incident field, E_0, and the field produced by first order polarization induced in the sample, $E^{(1)}$. The intensity of absorption is given, by the attenuation of the incident field intensity I_0 while traveling through a sample of thickness L (the Beer-Lambert law), as

$$I = I_0 \exp(-A(\omega)L) \tag{2.30}$$

We can rewrite the ratio I/I_0 by exploiting the fact that the intensity of an electromagnetic radiation is proportional to the square of the electric field, so that

$$\frac{I}{I_0} = \frac{\left|E_0(\omega) + E^{(1)}(\omega)\right|^2}{|E_0(\omega)|^2} \simeq 1 + \frac{2\Re\mathfrak{e}\left(E_0(\omega)E^{(1)}(\omega)\right)}{|E_0(\omega)|^2} \tag{2.31}$$

where we have discarded the $\left|E^{(1)}(\omega)\right|^2$ term since it is much smaller than the incident field E_0. The absorption spectrum $A(\omega)$ is the logarithm of this expression (Eq. (2.30)), which in the small signal limit gives[8]

$$A(\omega) \propto -\frac{2\Re\mathfrak{e}\left(E_0(\omega)E^{(1)}(\omega)\right)}{|E_0(\omega)|^2} \propto -2\Re\mathfrak{e}\left(E^{(1)}(\omega)\right) \tag{2.32}$$

In the last step we have made use of the fact that the laser pulse is a δ-like function, whose Fourier transform is constant in frequency. Since $E^{(1)}(\omega) = -iP^{(1)}(\omega)$

---

[8]$\log(1 + x) \sim x$ for small values of x.

we obtain

$$A(\omega) \propto 2\Im\mathfrak{m}\left(P^{(1)}(\omega)\right) = \sum_e |\boldsymbol{\mu}_{eg}|^2 \frac{\gamma_{eg}}{(\omega - \omega_{eg})^2 + \gamma_{eg}^2} \tag{2.33}$$

The absorption-spectrum is then a sum of transitions centered at ω_{eg}, having Lorenzian line-shapes whose widths are governed by the phenomenological dephasing coefficients γ_{eg}.

2.3.5 $R^{(3)}$ & Spectroscopy: Phenomenological Dephasing

Similarly, the third-order signals are obtained from the third-order induced polarization. In the heterodyne detection mode, the field exciting the sample is mixed with a local oscillator field, and the signal is thus obtained as:

$$
\begin{aligned}
S_{\boldsymbol{k}_s}^{(3)}(t_3, t_2, t_1) &= \int_{-\infty}^{+\infty} dt P_{\boldsymbol{k}_s}(t) \, \mathbb{E}_s^*(t - \tau_s) \, e^{i\omega_s(t-\tau_s)} = \\
&= \int_{-\infty}^{+\infty} dt P_{\boldsymbol{k}_s}(t + \tau_s) \, \mathbb{E}_s^*(t) \, e^{i\omega_s t}
\end{aligned}
\tag{2.34}
$$

and it depends parametrically on the time intervals $t_3 = \tau_s - \tau_3$, $t_2 = \tau_3 - \tau_2$ and $t_1 = \tau_2 - \tau_1$. $\mathbb{E}_s^*(t)$ is the local oscillator field envelope used for heterodyne detection.

Let us consider the signal produced by, e.g., the stimulated emission in the non-rephasing direction. In the semi-impulsive limit $S_{\boldsymbol{k}_s}^{(3)}(t_3, t_2, t_1) = R_{\boldsymbol{k}_s}^{(3)}(t_3, t_2, t_1)$[9], and for the non-rephasing SE diagram we have:

$$
\begin{aligned}
S_{\boldsymbol{k}_{II}}^{SE}(t_3, t_2, t_1) &= \left(\frac{i}{\hbar}\right)^3 \sum_{ee'} \boldsymbol{\mu}_{ge'}\boldsymbol{\mu}_{eg}\boldsymbol{\mu}_{e'g}\boldsymbol{\mu}_{ge} \times \\
&\exp\left(-i\omega_{eg}t_1 - i\omega_{e'e}t_2 - i\omega_{e'g}t_3 - \gamma_{eg}t_1 - \gamma_{e'e}t_2 - \gamma_{e'g}t_3\right)
\end{aligned}
\tag{2.35}
$$

Focusing for simplicity on $t_2 = 0$, and on the pathway $e = e'$, we perform the Fourier transform along t_1 and t_3. The FT along t_1 ($\int_0^\infty dt_1 e^{i\omega_1 t_1} e^{-i\omega_{eg}t_1} e^{-\gamma_{eg}t_1}$) gives

$$S_{\boldsymbol{k}_{II}}^{SE}(t_3, t_2, \omega_1) \propto i \left[\frac{\gamma_{eg} - i(\omega_{eg} - \omega_1)}{\gamma_{eg}^2 + (\omega_{eg} - \omega_1)^2} \right] e^{-\omega_{eg}t_3} e^{-t_3 \gamma_{eg}} \tag{2.36}$$

---

[9]This result is obtained by using δ-functions pulse envelopes in Eq. (2.34) and Eq. (2.23).
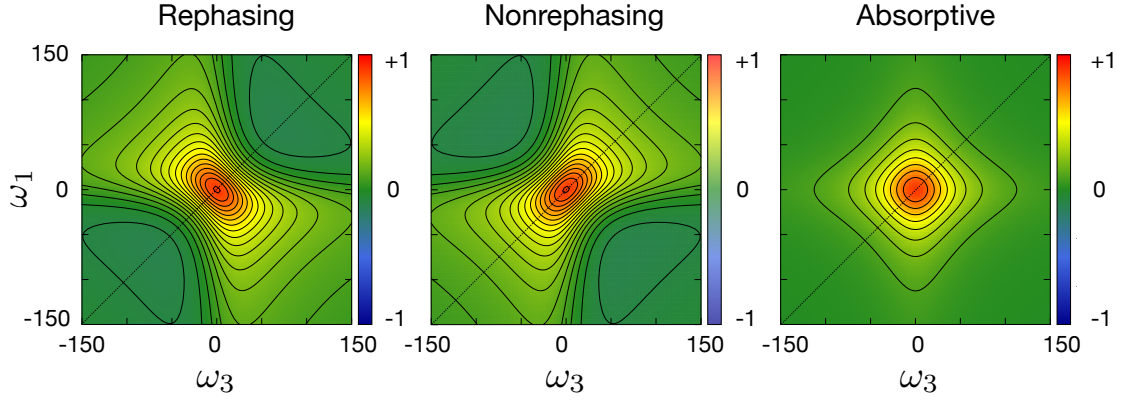
Figure 2.4: Rephasing ($\boldsymbol{k}_I$), Nonrephasing ($\boldsymbol{k}_{II}$) and Absorptive ($\boldsymbol{k}_I + \boldsymbol{k}_{II}$) maps at $t_2 = 0$, obtained as contour plots of the functions specified by Eq. (2.38) and Eq. (2.39).

and that along t_3 returns

$$
\begin{aligned}
S^{SE}_{\boldsymbol{k}_{II}}(\omega_3, t_2, \omega_1) &\propto i \left[\frac{\gamma_{eg} - i\left(\omega_{eg} - \omega_1\right)}{\gamma_{eg}^2 + \left(\omega_{eg} - \omega_1\right)^2} \right] \left[\frac{\gamma_{eg} - i\left(\omega_{eg} - \omega_3\right)}{\gamma_{eg}^2 + \left(\omega_{eg} - \omega_3\right)^2} \right] \\
&\propto i \left[\frac{\gamma_{eg}^2 - \left(\omega_{eg} - \omega_1\right)\left(\omega_{eg} - \omega_3\right)}{\left[\gamma_{eg}^2 + \left(\omega_{eg} - \omega_1\right)^2\right]\left[\gamma_{eg}^2 + \left(\omega_{eg} - \omega_3\right)^2\right]} + i \ldots \right] \quad (2.37)
\end{aligned}
$$

The measured signal has both $\mathfrak{Re}$ and $\mathfrak{Im}$ parts (which is, as we have already said, one of the strength of the 2D in heterodyne detection mode). Considering the $\mathfrak{Im}$ part of $S^{SE}_{\boldsymbol{k}_{II}}(\omega_3, t_2, \omega_1)$ we have

$$
\mathfrak{Im}\left[S^{SE}_{\boldsymbol{k}_{II}}(\omega_3, t_2, \omega_1) \right] \propto \frac{\gamma_{eg}^2 - \left(\omega_{eg} - \omega_1\right)\left(\omega_{eg} - \omega_3\right)}{\left[\gamma_{eg}^2 + \left(\omega_{eg} - \omega_1\right)^2\right]\left[\gamma_{eg}^2 + \left(\omega_{eg} - \omega_3\right)^2\right]} \quad (2.38)
$$

We note that this expression can be both positive or negative according to the values (ω_1, ω_3) and the strength of the phenomenological dephasing parameter γ_{eg}, as both absorptive and dispersive contributions are present.[67]

Something similar happens for the rephasing SE signal, whose imaginary part then reads:

$$
\mathfrak{Im}\left[S^{SE}_{\boldsymbol{k}_I}(\omega_3, t_2, \omega_1) \right] \propto \frac{\gamma_{eg}^2 + \left(\omega_{eg} + \omega_1\right)\left(\omega_{eg} - \omega_3\right)}{\left[\gamma_{eg}^2 + \left(\omega_{eg} + \omega_1\right)^2\right]\left[\gamma_{eg}^2 + \left(\omega_{eg} - \omega_3\right)^2\right]} \quad (2.39)
$$

We note that the sign of ω_1 is the opposite of that of the corresponding non-rephasing signal, since the coherence during t_1 is reversed. This contribution can also assume both positive and negative values. The different sign of ω_1 produces a

different phase twist for $S_{\boldsymbol{k}_{II}}^{(3)}$ and $S_{\boldsymbol{k}_I}^{(3)}$, as shown in Figure 2.4.[67]

By summing rephasing and nonrephasing contributions, and inverting the sign of the ω_1-coordinate of the former, one obtains (quasi-)absorptive spectra through cancelation of the dispersive components[10], which gives the highest frequency resolution and allows for a simpler physical understanding of the signals of 2D experiments.[67]

2.3.6 $R^{(1)}$ & Spectroscopy: Line-shape functions

The role of the environment in the simulation of spectroscopy has been introduced in the previous Section as a source of signal dephasing, which causes an exponential attenuation of the coherence over time. The microscopic model of the bath of vibrations coupled to the electronic states of the studied system have been introduced in the previous Part of the Thesis (Part I, Eqs. (3.2-3.4)). In particular the spectral density was presented as a key quantity for summarizing the properties of the system-bath coupling. Here we develop the cumulant expansion of gaussian fluctuations (CGF) as a mean to describe the effect of the environment on the transition line-shapes, beyond the phenomenological treatment.

We first of all note that $R^{(1)}(t_1)$ can be rewritten as

$$
\begin{aligned}
R^{(1)}(t_1) &= \left(\frac{i}{\hbar}\right) Tr\left[\hat{\boldsymbol{\mu}}\mathbb{G}(t_1)\mu^{\times}\hat{\rho}_0\right] \\
&= \left(\frac{i}{\hbar}\right) Tr\left[\hat{\boldsymbol{\mu}}\exp\left(-\frac{i}{\hbar}Ht_1\right)(\hat{\boldsymbol{\mu}}\hat{\rho}_0 - \hat{\rho}_0\hat{\boldsymbol{\mu}})\exp\left(\frac{i}{\hbar}Ht_1\right)\right] \\
&= \left(\frac{i}{\hbar}\right) Tr\left[\exp\left(\frac{i}{\hbar}Ht_1\right)\hat{\boldsymbol{\mu}}\exp\left(-\frac{i}{\hbar}Ht_1\right)(\hat{\boldsymbol{\mu}}\hat{\rho}_0 - \hat{\rho}_0\hat{\boldsymbol{\mu}})\right] \\
&= \left(\frac{i}{\hbar}\right) Tr\left[\hat{\boldsymbol{\mu}}(t)\hat{\boldsymbol{\mu}}(0)\hat{\rho}_0 - \hat{\boldsymbol{\mu}}(0)\hat{\boldsymbol{\mu}}(t)\hat{\rho}_0\right] \\
&= \left(\frac{i}{\hbar}\right) \left[\mathbb{J}(t_1) - \mathbb{J}^{*}(t_1)\right]
\end{aligned}
\tag{2.40}
$$

where $\mu(t)$ is the dipole operator in the interaction picture, $\mathbb{J}(t) = Tr\left[\hat{\boldsymbol{\mu}}(t)\hat{\boldsymbol{\mu}}(0)\hat{\rho}_0\right] = \langle\hat{\boldsymbol{\mu}}(t)\hat{\boldsymbol{\mu}}(0)\rangle$ is the *two-point dipole correlation function*, and the symbol $\langle\bullet\rangle$ indicates the equilibrium statistical averaging over the bath[11]. Note also that $\mathbb{J}(-t) = \mathbb{J}^{*}(t)$.

Let us consider the simple case of a single molecule with two electronic states, namely the ground state $|g\rangle$ and the excited state $|e\rangle$ which are coupled to nuclear coordinates $\boldsymbol{Q}$. The (adiabatic) Hamiltonian of the complete system can be written

---

[10]Purely absorptive maps are obtained for uncoupled states, while for coupled systems only a partial cancellation of the dispersive contribution is reached.

[11]In the derivation we have made use of the property $Tr\left[ABC\right] = Tr\left[CAB\right] = Tr\left[BCA\right]$.

as

$$\hat{H} = H_g(\boldsymbol{Q}) |g\rangle \langle g| + H_e(\boldsymbol{Q}) |e\rangle \langle e| \tag{2.41}$$

where $H_g(\boldsymbol{Q}) = \mathcal{E}_g + V_g(\boldsymbol{Q})$ and $H_e(\boldsymbol{Q}) = \mathcal{E}_e + V_e(\boldsymbol{Q})$. One can for simplicity think of the previously introduced displaced harmonic oscillator model, but the form of $V_g(\boldsymbol{Q})$ and $V_e(\boldsymbol{Q})$ is completely general. We assume here that the full (nuclear and electronic) initial density matrix $\hat{\rho}_0$ can be factorized in system and bath components, so that $\hat{\rho}_0 = |g\rangle \rho_g \langle g|$. The electronic part of $\hat{\rho}_0$ is given by the ground-state population $|g\rangle \langle g|$, while ρ_g is the nuclear density operator, which at thermal equilibrium, reads:

$$\rho_g = \frac{\exp\left(-\beta V_g\right)}{Tr_B \exp\left(-\beta V_g\right)} \tag{2.42}$$

In the Condon approximation the dipole operator $\hat{\mu}$ does not depend on the coordinates $\boldsymbol{Q}$, so that it can be factored out the averaging procedure. We can thus rewrite $\mathbb{J}$ as:

$$\begin{aligned}
\mathbb{J}(t) &= |\hat{\mu}_{ge}|^2 \left\langle \exp\left(\frac{i}{\hbar} H_g t\right) \exp\left(-\frac{i}{\hbar} H_e t\right) \rho_g \right\rangle \\
&= |\hat{\mu}_{ge}|^2 \exp\left(-i\omega_{eg}t\right) \left\langle \exp\left(\frac{i}{\hbar} V_g t\right) \exp\left(-\frac{i}{\hbar} V_e t\right) \rho_g \right\rangle
\end{aligned} \tag{2.43}$$

where $\hbar\omega_{eg} = \mathcal{E}_e - \mathcal{E}_g$, and the angular brackets represent the average over the bath DOFs. The trace can be calculated by employing a complete set of GS vibrational states ($|v\rangle$), obtaining

$$\begin{aligned}
\mathbb{J}(t) &= |\hat{\mu}_{eg}|^2 e^{-i\omega_{eg}t} \sum_v \mathcal{P}(\epsilon_v) \exp\left(\frac{i}{\hbar} \epsilon_v t\right) \langle v| \exp\left(-\frac{i}{\hbar} V_e t\right) |v\rangle \\
&= |\hat{\mu}_{eg}|^2 e^{-i\omega_{eg}t} \sum_v \mathcal{P}(\epsilon_v) \exp\left(\frac{i}{\hbar} \epsilon_v t\right) \langle v|v(t)\rangle
\end{aligned} \tag{2.44}$$

where $\mathcal{P}(\epsilon_v)$ is the Boltzmann probability for the bath to stay in state $|v\rangle$, ϵ_v is the (vibrational) energy of $|v\rangle$, and $\langle v|v(t)\rangle$ is the time dependent overlap between the wave-packet $\langle v|$ on the GS and the wave-paket $|v(t)\rangle$, moving on the ES surface, as schematically depicted in Figure 2.5.

Instead of describing the time-dependent overlap of Eq. (2.44) in term of the ES hamiltonian H_e, it is convenient to take the ground state PES as a energy reference, and rewrite the state propagator $\exp\left(-\frac{i}{\hbar} V_e t\right)$ in terms of the energy gap fluctuations. The connection with the spectral density will become apparent soon.
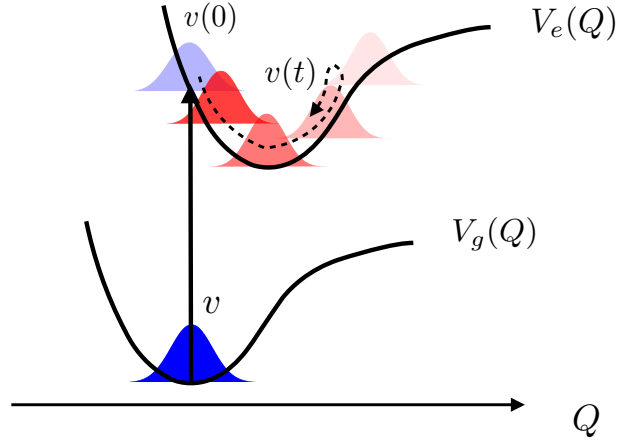
Figure 2.5: Pictorial representation of the evolution of the wavepacket $|v\rangle$ on the ES PES. Note that at $t = 0$, after the field interaction, the wavepacket $|v(0)\rangle$ has unitary overlap with the wavepacket in the GS (the Condon approximation).

Let us define the energy gap between the two PES as

$$\delta_e = V_e - V_g \Longrightarrow V_e = \delta_e + V_g \qquad (2.45)$$

Since we want to take V_g as a reference, we express the evolution of δ_e under the ground state dynamics as

$$\delta_e(t) = e^{iV_g t} \delta_e e^{-iV_g t} \qquad (2.46)$$

Making use of the time ordered exponential we have[12]

$$\exp\left(-\frac{i}{\hbar} V_e t\right) = \exp\left(-\frac{i}{\hbar} V_g t\right) \exp_+\left(-\frac{i}{\hbar} \int_0^t dt' \delta_e(t')\right) \qquad (2.47)$$

and $\mathbb{J}(t)$ becomes (in the Condon approximation)

$$\begin{aligned} \mathbb{J}(t) &= e^{-iw_{eg}t} |\hat{\mu}_{eg}|^2 \left\langle \exp_+\left[-\frac{i}{\hbar} \int_0^t dt' \delta_e(t')\right]\right\rangle \\ &= e^{-iw_{eg}t} |\hat{\mu}_{eg}|^2 D(t) \end{aligned} \qquad (2.48)$$

---

[12]The time-ordered exponential of $\delta_e(t)$ is defined as

$$\exp_+\left(-\frac{i}{\hbar} \int_0^t dt' \delta_e(t')\right) = \sum_{n=0}^{\infty} \left(\frac{-i}{\hbar}\right)^n \int_0^t d\tau_n \int_0^{\tau_n} d\tau_{n-1} \cdots \int_0^{\tau_1} d\tau_1 \delta_e(\tau_n) \delta_e(\tau_{n-1}) \dots \delta_e(\tau_1)$$

The expression presented in Eq. (2.47) can be understood by noticing that: first, given two operators $\hat{A}$ and $\hat{B}$, the property $\exp(\hat{A} + \hat{B}) = \exp(\hat{A})\exp(\hat{B})$ does not hold in general, but only in the case $[\hat{A}, \hat{B}] = 0$. Second, Eq. (2.47) can be proven if one consider, order by order, the result of applying the derivative $\frac{d^n}{dt^n}\big|_{t=0} \bullet$ both the left and right-hand side of the equation, making use of the property $\frac{d}{dt}\exp_+\left(-\frac{i}{\hbar} \int_0^t dt' \delta_e(t')\right) = \delta_e(t) \exp_+\left(-\frac{i}{\hbar} \int_0^t dt' \delta_e(t')\right)$.
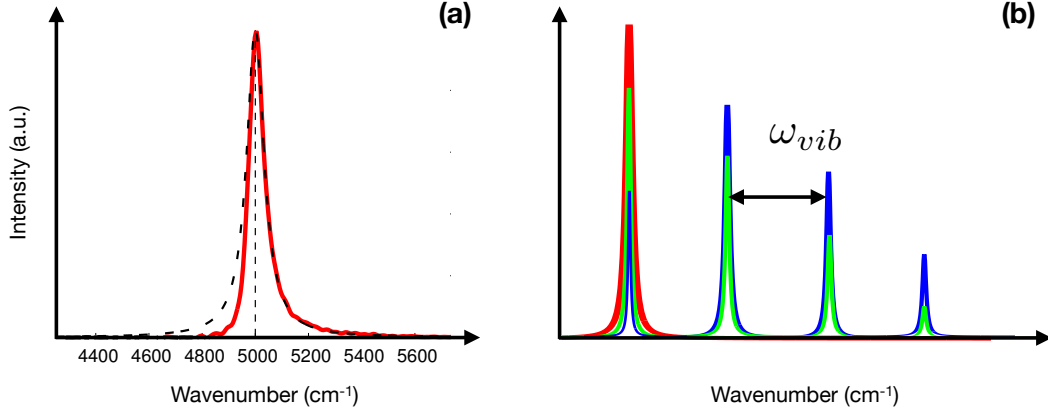
Figure 2.6: (a) Comparison of absorption spectra obtained with: (red) lineshape functions for an overdamped brownian oscillator model (Part I, Eq. 3.27), and (dashed black) employing a phenomenological dephasing model (same parameters of Figure 2.3). Note that the OBO model allows to describe asymmetric peak shapes. (b) Vibronic spectra obtained within the lineshape function approach. This allows to describe high frequency vibrations and strong system bath coupling. Different curves refer to the same mode with frequency ω_{vib} but different coupling to the electronic transition (i.e. different Huang Ryes factor S): $S = 0$ is represented by the red curve, $S < 1$ by the green curve, and $S > 1$ by the blue curve.

Now we make a step forward by expanding $D(t)$ in orders of δ_e, performing the so-called *cumulant expansion*.

$$D(t) \simeq \exp \left[-\frac{i}{\hbar} \int_0^t d\tau_1 \langle \delta_e(\tau_1) \rangle - \frac{1}{\hbar^2} \int_0^t d\tau_1 \int_0^{\tau_1} d\tau_2 \langle \delta_e(\tau_1) \delta_e(\tau_2) \rangle \ldots \right] \quad (2.49)$$

The first order term can be set to zero without loss of generality. The expansion is usually truncated at the second order, which is an exact result for baths characterized by gaussian fluctuations[30].

We define $C(t)$ as

$$C(t) = \frac{1}{\hbar^2} \langle \delta_e(t) \delta_e(0) \rangle \quad (2.50)$$

and $g(t)$ as

$$g(t) = \int_0^t d\tau_2 \int_0^{\tau_2} d\tau_1 C(\tau_1) \quad (2.51)$$

which is the second term of Eq. (2.49).

The connection between Eq. (2.50) and the spectral density defined in the previous Part of the Thesis is now apparent. We can finally rewrite $\mathbb{J}(t)$ as

$$\mathbb{J}(t) = |\hat{\mu}_{eg}|^2 \, e^{-iw_{eg}t - g(t)} \quad (2.52)$$

which leads to a higher level description of the absorption spectrum (with respect to that obtained by employing the phenomenological dephasing parameter γ, Eq. (2.33)) given by:

$$A(\omega) \propto \mathfrak{Re} \int_0^\infty dt\, e^{i(\omega - \omega_{eg})t - g(t)} \tag{2.53}$$

The function $g(t)$ is called *line-shape* function and it takes into account the effects of the bath on the system. The absorption spectrum obtained employing the phenomenological dephasing (with its characteristic Lorenzian shape of the transitions) can be recovered here in the limit $g(t) = \gamma t$.[13]

The line-shape function here introduced for a simple two-level system, can be generalized for an arbitrary system of interacting molecules. The derivation follows the one presented above, but two important differences should be underlined

1. The system is conveniently described by exciton states. This implies that quantity previously derived in term of site basis (e.g. the correlation function of Eq. (2.50)) should be rewritten in the exciton basis. As an example, the energy fluctuation of an exciton $|\alpha\rangle = \sum_i A_{\alpha i} |i\rangle$, is connected to the site energy fluctuations as

$$C_\alpha(t) = \frac{1}{\hbar^2} \langle \delta_{\epsilon_\alpha}(t) \delta_{\epsilon_\alpha}(0) \rangle = \frac{1}{\hbar^2} \sum_i |c_{\alpha i}|^4 \langle \delta_i(t) \delta_i(0) \rangle \tag{2.54}$$

which connects exciton (diagonal) fluctuations with site fluctuations.

2. The system-bath coupling part of the Hamiltonian in the exciton basis is non diagonal, which implies that not only the diagonal (energy fluctuations) terms of Eq. (2.54) should be considered, but also the additional off-diagonal terms. These terms are responsible for the bath induced transport between excitons, and we will describe their effect in the next Sections.

2.3.7 $R^{(3)}$ & Spectroscopy: Line-shape functions

We can similarly introduce line shape functions for the third-order responses. First of all, the four-point dipole correlation function is introduced as[68]

$$F(\tau_4, \tau_3, \tau_2, \tau_1) = \langle \hat{\boldsymbol{\mu}}(\tau_4) \hat{\boldsymbol{\mu}}(\tau_3) \hat{\boldsymbol{\mu}}(\tau_2) \hat{\boldsymbol{\mu}}(\tau_1) \rangle \tag{2.55}$$

---

[13]For bath with gaussian statistics this expression for $\mathbb{J}(t)$ is exact.

Expansion in the exciton eigenstates of F leads to

$$F(\tau_4, \tau_3, \tau_2, \tau_1) = \sum_{abcd} \rho_a \boldsymbol{\mu}_{ad} \boldsymbol{\mu}_{dc} \boldsymbol{\mu}_{cb} \boldsymbol{\mu}_{ba} \exp\left[-i(\omega_{da}\tau_{43} + \omega_{ca}\tau_{32} + \omega_{ba}\tau_{21}) + \phi_{dcba}(\tau_4, \tau_3, \tau_2, \tau_1)\right]$$

(2.56)

where $\tau_{ij} = \tau_i - \tau_j$ and ρ_a is the equilibrium population of state a. The function $\phi_{dcba}(\tau_4, \tau_3, \tau_2, \tau_1)$ is a four-point line-shape function, which takes into account the effects of inter- and intra-molecular nuclear dynamics. By employing the previously introduced cumulant expansion, and in the case of harmonic bath models, the expression of ϕ can be further developed in terms of the lineshape functions $g_{ab}(t)$, yielding[68]

$$
\begin{aligned}
\phi_{cbag}(\tau_4, \tau_3, \tau_2, \tau_1) = \ & -g_{cc}(\tau_{43}) - g_{bb}(\tau_{32}) - g_{aa}(\tau_{21}) \\
& -g_{cb}(\tau_{42}) + g_{cb}(\tau_{43}) + g_{cb}(\tau_{32}) \\
& -g_{ca}(\tau_{41}) + g_{ca}(\tau_{42}) + g_{ca}(\tau_{31}) \\
& -g_{ca}(\tau_{32}) - g_{ba}(\tau_{31}) + g_{ba}(\tau_{32}) + g_{ba}(\tau_{31})
\end{aligned}
$$

(2.57)

The third-order response can be recast by using the four-point dipole correlation function F as

$$
\begin{aligned}
R^{(3)}(t_3, t_2, t_1) = \ & \left(\frac{i}{\hbar}\right)^3 [F(t_1, t_1 + t_2, t_1 + t_2 + t_3, 0) + \\
& + \ F(0, t_1 + t_2, t_1 + t_2 + t_3, t_1) + \\
& + \ F(0, t_1, t_1 + t_2 + t_3, t_1 + t_2) + \\
& + \ F(t_1 + t_2 + t_3, t_1 + t_2, t_1, 0)] + c.c.
\end{aligned}
$$

(2.58)

and for each given Feynman-diagram it is therefore possible to specify the appropriate combination of line-shape functions. For example, the non-rephasing GSB is given by:

$$
\begin{aligned}
R^{(GSB)}_{\mathbf{k}_{II}}(t_3, t_2, t_1) = \ & \left(\frac{i}{\hbar}\right)^3 \sum_{ee'} \boldsymbol{\mu}_{ge'} \boldsymbol{\mu}_{e'g} \boldsymbol{\mu}_{ge} \boldsymbol{\mu}_{eg} \times \\
& \exp\left[-i\omega_{e'g}t_3 - i\omega_{eg}t_1 + \phi_{e'geg}(t_1 + t_2 + t_3, t_1 + t_2, t_1, 0)\right]
\end{aligned}
$$

(2.59)

Finally, we note that the terms $g_{ab}(t)$ (with $a \neq b$) of Eq. (2.57), involve products of displacements $d_a d_b$. This means that, as pointed out in Part I, Section 5.4, the sign of the displacements has to be considered for the proper description of the lineshape of simulated spectra (see e.g., the azobenzene study, Part III, Chapter 3).

2.3.8   Summary

From the computational point of view, the necessary ingredients to simulate spectroscopic experiments at the level of the theory here presented, are:

- The energies of the system manifold of states;

- The transition dipoles between the states[14];

- The spectral density associated to the various transitions.

The major approximations made to develop the line-shape function treatment of system's fluctuations through the spectral density are:

- The factorization of the initial density matrix in system and bath components.

- The truncation at the second-order cumulant in the expansion of energy gap fluctuations. This is not an approximation when considering bath with gaussian statistics.

- The Condon approximation, for which we assume that the dipole operator $\boldsymbol{\mu}$ is not affected by the nuclear coordinates.

- The description of diagonal (energy) bath-induced fluctuations only, neglecting bath-assisted transport processes caused by off-diagonal fluctuations.

In the next Section we discuss some approximate methods to include transport between exciton states as an effect of intra- and inter-molecular vibrations.

2.4   Transport

Population relaxation has been so far neglected. It can be reintroduced approximately at various level of sophistication. The zero-order approach assumes bath fluctuation timescale to be faster than that of all the other processes (bath correlation time $\tau_c \to 0$), and the Markovian approximation is then applied. More advanced approaches allow fluctuations to occur in a broad range of timescales.

---

[14]At least between those resonant within the observed spectral window.

2.4.1   Fast-timescale bath fluctuations

The simplest approach to include transport is that of secular Redfield theory, which consider the bath fluctuations to be faster than both transport and coherence-dephasing time. The Markovian approximation is applied to the bath fluctuations for all the time intervals t_1, t_2 and t_3, and the secular approximation disentangles the evolution of populations from that of coherences. The time evolution of density matrix elements is described by

- A Pauli rate equation for populations, which reads

$$\frac{d\rho_{ee}(t)}{dt} = -\sum_{e'} K_{ee,e'e'} \rho_{e'e'}(t) \tag{2.60}$$

  whose formal solution is given by

$$\rho_{e'e'}(t) = \sum_{e} \mathbb{G}^{N}_{e'e',ee}(t)\rho_{ee}(0) \tag{2.61}$$

  $K_{ee,e'e'}$ is the population transfer rate from state e' into e, and $\mathbb{G}^{(N)}_{e'e',ee} \equiv [\exp{(-Kt)}]_{e'e',ee}$ is the population Green's function, which describes the probability of a bath assisted transition $e \to e'$ during time t.

- An exponential suppression of coherences governed by the lifetime of the states, given by

$$\frac{d\rho_{e'e}(t)}{dt} = [-i\omega_{e'e} - \Gamma_{e'e}]\,\rho_{e'e}(t),\ e \neq e' \tag{2.62}$$

  with solutions

$$\rho_{e'e}(t) = \exp{(-i\omega_{e'e}t - \Gamma_{e'e}t)} \tag{2.63}$$

  where $\Gamma_{e'e} = \frac{1}{2}\left(K_{ee,ee} + K_{e'e',e'e'}\right) + \gamma_{e'e}$. The first two terms represent population relaxation, while the last term represent the pure dephasing rate, which accounts for all the bath-induced dephasing mechanisms beside the transport. We note that the secular approximation also implies that coherences evolve separately, never mixing with each other.

The tensor $K_{ee,e'e'}$ satisfies the following properties, that ensure thermal equilibrium is reached at long times:

- $K_{ee,ee} > 0$;

- $K_{ee,e'e'} < 0$ when $e \neq e'$;

- $\sum_e K_{ee,e'e'} = 0$ (probability conservation);

- $K_{e_2e_2,e_1e_1}/K_{e_1e_1,e_2e_2} = \exp\left(-\hbar\omega_{e_2e_1}/(\mathrm{k_B T})\right)$ (detailed balance)

New Feynman diagrams are introduced for describing exciton relaxation processes, shown in Figure (2.7). Dashed lines indicate that during t_2, density matrix populations are allowed to mix with each other according to Eq. (2.60).

$$\boldsymbol{k_I = -k_1 + k_2 + k_3} \qquad \boldsymbol{k_{II} = +k_1 - k_2 + k_3}$$
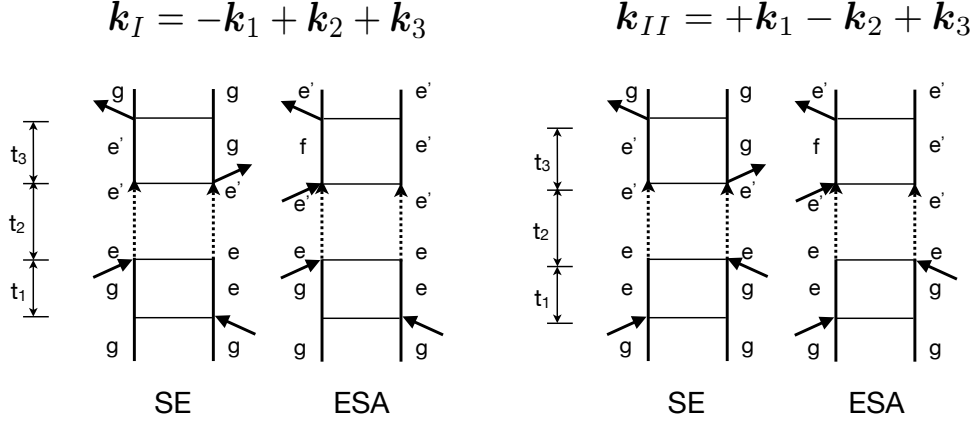
Figure 2.7: Feynman diagrams for rephasing (*left*) and nonrephasing (*right*) phase matching directions, that extend the corresponding diagrams of Figure 2.2 by including population transport (highlighted as dashed line along time t_2).

From Eq. (2.63) one can see that the finite state life-time provides an additional suppression of coherences, i.e., contributing to the homogeneous broadening of the signals in the spectra. In the context of secular Redfield theory, closed expressions are given for both relaxation rates and pure dephasing terms $\gamma_{ee'}$.[68] We note that in this model, dephasing and energy-transfer processes enter as simple exponential decays, so that the computed spectra have Lorenzian line-shape.

2.4.2 Intermediate-timescale bath fluctuations

Here we make a step forward: considering processes for which $t_1, t_3 \ll t_2$, the bath fluctuations are assumed to be fast compared to the transport, but slow (or comparable) with respect to the coherence-dephasing time. We still apply the secular approximation, so that transport can occur only between populations (i.e. during t_2 in $\boldsymbol{k_I}$ and $\boldsymbol{k_{II}}$), and dephasing occurs during the delay times t_1 and t_3.

The response function is factorized in the *doorway-window* form, given by[68]

$$R^{(3)}(t_3, t_2, t_1) = \left(\frac{i}{\hbar}\right)^3 Tr\left[\mathbb{W}(t_3)\mathbb{G}(t_2)\mathbb{D}(t_1)\right] \tag{2.64}$$

where $\mathbb{D}(t_1) \equiv \mathbb{V}G(t_1)\mathbb{V}\rho_0$ is the *doorway* exciton wavepacket, prepared by the first two pulses, $\mathbb{G}(t_2)$ describe the propagation along t_2 and $\mathbb{W}(t_3) \equiv \hat{\boldsymbol{\mu}}G(t_3)\mathbb{V}$, is the *window* wavepacket, which represents the detection.

$R^{(3)}$ is further partitioned (secular approximation) in two terms:

$$R^{(3)}(t_3, t_2, t_1) = R^{(3)}_{(C)}(t_3, t_2, t_1) + R^{(3)}_{(P)}(t_3, t_2, t_1) \qquad (2.65)$$

where $R^{(3)}_{(C)}(t_3, t_2, t_1)$ collects all the terms that are always described by coherences (also during t_2), and $R^{(3)}_{(P)}(t_3, t_2, t_1)$ collects all the terms that during t_2 are in a population. Population response functions (for both SE and ESA) are weighted by the solutions of the Pauli master equation Eq. (2.60), which prescribes the pathways and the rates with which an exciton migrates through the various exciton states.

Since the timescale of coherence-dephasing is faster than that of bath correlation, diagonal fluctuations are treated exactly for the $R^{(3)}_{(C)}(t_3, t_2, t_1)$ pathways, and off-diagonal contributions are included (in the Markovian approximation, i.e. according to Eqs. (2.60-2.62)) only to compute the life-time broadening of these signals. These diagrams maintain the correlated bath dynamics over all the time intervals t_1, t_2 and t_3. Pathways containing populations during t_2, i.e. $R^{(3)}_{(P)}(t_3, t_2, t_1)$, ignore bath fluctuation correlations between the different propagation intervals: diagonal fluctuations are treated exactly during t_1 and t_3 (via cumulant expansion), and life-time broadening is added as provided by Eq. (2.62). During t_2, the memory is erased, and second order Markovian perturbation theory is performed for the coupling with all the bath coordinates (leading to Eq. (2.60)). This implies that line-shape functions for (P) diagrams do not explicitly contain the time t_2, and that correlation between times t_1 and t_3 is neglected for these pathways.[68]

This model allows the consideration of finite bath timescale and arbitrary line shapes (as opposed to the Lorenzian line shape of the zero-order approach of the previous Section). However, the complete factorization into the doorway and window functions produces the loss of memory during the t_2 time interval, so that correlations between fluctuations during intervals t_1 and t_3 are neglected in population diagrams.

2.4.3 Slow diagonal fluctuations

Baths with both fast and slow modes (along all the three time intervals t_1, t_2 and t_3) can be approximately treated[69]. The Markovian approximation is applied only to the fast modes (denoted by a generic bath coordinate $\boldsymbol{Q}^{(F)}$): during t_1 and t_3, these cause homogeneous line broadening (diagonal bath fluctuations), while during t_2 they induce population relaxation (off-diagonal bath fluctuations) described by

the Pauli master equation Eq. (2.60). The slow bath modes (denoted by a generic bath coordinate $\mathbf{Q}^{(S)}$) are instead responsible for spectral diffusion during t_1, t_2, and t_3, causing correlations during all the three time intervals.

The response function is again recast as in Eq. (2.65), and the various contributions (GSB, SE and ESA) are split in Population and Coherence contributions.

The population contributions then read:

$$
\begin{aligned}
R_{(P)}^{(ESA)}(t_3, t_2, t_1) &= i \sum_{ee'} \sum_f \mu_{fe'}^2 \mu_{ge}^2 \mathbb{G}_{e'e'ee}^{(N)}(t_2) \\
&\times \left[\delta_{ee'} \mathcal{F}_{efe}^{(C)*}(t_1, t_1 + t_2, t_1 + t_2 + t_3, 0) \right. \\
&+ \left. \zeta_{ee'} \mathcal{F}_{fe'e'e}^{(I)*}(t_3, t_2, t_1) \right] \quad (2.66) \\
R_{(P)}^{(SE)}(t_3, t_2, t_1) &= -i \sum_{ee'} \mu_{ge}^2 \mu_{ge'}^2 \mathbb{G}_{e'e'ee}^{(N)}(t_2) \\
&\times \left[\delta_{ee'} \mathcal{F}_{ege}^{(C)}(0, t_1 + t_2, t_1 + t_2 + t_3, t_1) \right. \\
&+ \left. \zeta_{ee'} \mathcal{F}_{e'ge'e}^{(I)*}(t_3, t_2, t_1) \right] \quad (2.67) \\
R_{(P)}^{(GSB)}(t_3, t_2, t_1) &= -i \sum_{ee'} \mu_{ge}^2 \mu_{ge'}^2 \mathbb{G}_{e'e'ee}^{(N)}(t_2) \\
&\times \mathcal{F}_{ege'}^{(C)}(0, t_1, t_1 + t_2 + t_3, t_1 + t_2) \quad (2.68)
\end{aligned}
$$

The Coherence contributions read:

$$
\begin{aligned}
R_{(C)}^{(ESA)}(t_3, t_2, t_1) &= i \sum_{e \neq e'} \sum_f \mu_{fe'} \mu_{fe} \mu_{ge'} \mu_{ge} \\
&\times \mathcal{F}_{e'fe}^{(C)*}(t_1, t_1 + t_2, t_1 + t_2 + t_3, 0) \quad (2.69) \\
R_{(C)}^{(SE)}(t_3, t_2, t_1) &= -i \sum_{e \neq e'} \mu_{ge}^2 \mu_{ge'}^2 \\
&\times \mathcal{F}_{ege'}^{(C)}(0, t_1 + t_2, t_1 + t_2 + t_3, t_1) \quad (2.70)
\end{aligned}
$$

where $R_{(C)}^{(GSB)}(t_3, t_2, t_1) = 0$, $\zeta_{ab} = 1 - \delta_{ab}$. The population contributions (P), contain two terms: a coherent, population-conserving term $\mathcal{F}^{(C)}$, when populations during t_2 do not change ($e = e'$), weighted by the probability of remaining in the same state during t_2 ($\mathbb{G}_{eeee}^{(N)}(t_2)$) and the population-transfer term, $\mathcal{F}^{(I)}$, where populations hop from state e into e'.

$\mathcal{F}^{(C)}$ contains line-shape functions obtained by cumulant expansion over all the modes, specified by Eq. (2.57). $\mathcal{F}^{(I)}$ is developed by including the diagonal fluctuations of slow bath modes $\mathbf{Q}^{(S)}$ also along t_2.[69] New line-shape functions are obtained for $\mathcal{F}^{(I)}$, and differently to the doorway-window approach, they depend on

all three time intervals.[69] This level of theory can reproduce some signatures of population transport during t_2, such as time-dependent Stokes shift.[68, 69]

From the computational point of view, spectral densities are again the key quantities: on one side they are used to describe the diagonal (energy) fluctuations through the computation of line-shape functions; on the other side they are input quantities for the transport theories that provides the elements of the rate matrix K.

We note that we have not removed the secular approximation, which decouples populations from coherences. In the next Section we will present a different approach which overcomes many of the employed approximations, by introducing our recently developed model for describing 2DES spectroscopy through the accurate quantum dissipative PLDM dynamics.

2.5   Summary

In the previous Sections we have developed the response function formalism for the computation of linear and non-linear spectroscopy: we summarize here the main information obtained and the approximations made throughout the derivation.

- We started from the field-matter Hamiltonian given by $\hat{H} = \hat{H}_0 + \hat{H}'(t)$, and described the system in terms of its density matrix, which is the natural formulation in the context of open quantum system.

- The interacting term, $H'(t)$, of the field-matter Hamiltonian is treated perturbatively, and an order-by-order expansion of the density matrix is obtained.

- The n-th order induced polarizability is the quantity of interest in spectroscopy, being the source of the measured signal. In particular we focused on linear and third-order polarizabilities, connected, e.g., to ground-state absorption and 2DES techniques, respectively. These are conveniently written by separating the response of the system and the incident electromagnetic field as:

$$R^{(1)}(t_1) = \left(\frac{i}{\hbar}\right) Tr\left[\hat{\boldsymbol{\mu}}\mathbb{G}(t_1)\mu^{\times}\hat{\rho}_0\right] \tag{2.71}$$

and

$$R^{(3)}(t_3, t_2, t_1) = \left(\frac{i}{\hbar}\right)^3 Tr\left[\hat{\boldsymbol{\mu}}\mathbb{G}(t_3)\mu^{\times}\mathbb{G}(t_2)\mu^{\times}\mathbb{G}(t_1)\mu^{\times}\hat{\rho}_0\right] \tag{2.72}$$

The functions $R^{(1)}$ and $R^{(3)}$ contain all the information about the system dynamics which follows the interaction with light.

- For third-order response, we partitioned the response function according to the different physical processes taking place when multiple laser pulses interact with the sample: GSB, SE and ESA. Feynman diagrams were introduced, and the connection between diagrams, equations and underlying physical processes established.

- The role of the environment was unraveled by connecting the microscopic system fluctuations to line-shape functions for both linear and non-linear techniques. The spectral density plays a central role. This model is exact providing the absence of transport between excitons.

- Approximate strategies for introducing transport were presented.

All the concepts introduced in this Chapter have been extensively used for the simulation of spectroscopies in Part III of this Thesis: linear and non-linear spectra are computed by means of Eq. (2.71) and Eq. (2.72), respectively. Lineshape functions (Eq. (2.57)), obtained through computed spectral densities, are employed to describe the effect of both inter- and intra- molecular vibrations on the spectra. Exciton transport is also considered, as described in the advanced model of Section 2.4.3, always relying on the secular approximation.

PLDM approach to Spectroscopy

The method outlined in this Chapter has been developed in collaboration with the research group of Prof. David F. Coker (Boston University, Boston, MA, USA) and a related paper has been published in the *Journal of Chemical Theory and Computation*, ref. 53.

The reliability of the simulation of spectroscopic experiments is significantly affected not only by the microscopic input of the Frenkel Exciton model, but also by the quantum dissipative dynamics employed to describe the system evolution. PLDM dynamics proved to be an effective method for computing the evolution of the density matrix of a quantum system coupled to a fluctuating environment, through a non-perturbative, non-Markovian, non-secular semiclassical path integral approach, that explicitly treats all DOFs [41, 48].

We have recently developed a method to exploit the accuracy of PLDM in the simulation of spectroscopy.

At the core of the method there is a simple generalization of PLDM to the evolution of generic operators (and not just of the density matrix). Eq. (2.22) and (2.24) furnish the recipe to be followed to compute the response function: interact with the external laser, propagate the system, interact, propagate, *etc.* This approach inherits from PLDM the absence of many of the standard approximations of the existing methods used to simulate spectroscopy: no perturbative treatment of system-bath coupling, no dynamical approximations about time scales of different processes (e.g., no Markovian limit), no secular approximation (all the density matrix elements can in principle mix with each other). No assumptions are made

about the nature of intra-system couplings or the form of the spectral density. The PLDM approach to spectroscopy therefore provides a way of accurately treating the coupled electronic, vibrational and vibronic dynamics at the heart of the nonlinear optical response. Moreover it is based on propagating classical-like trajectories that include effects such as quantum transitions and the decay of an initially prepared coherent superposition of system quantum states in the presence of coupling to the environment. The independent trajectory nature of the approach makes for a highly efficient implementation for computing nonlinear responses, even if it is more expensive than standard perturbative approaches, and as such it is in general applicable to smaller system.

In what follows we show how the PLDM framework has been utilized to compute linear and non-linear response functions, and hence simulate linear and non-linear spectroscopy.

Both $R^{(1)}(t_1)$ and $R^{(3)}(t_3, t_2, t_1)$ can be written in terms of multi-point dipole correlation functions as[1]:

$$R^{(1)}(t_1) = \left(\frac{i}{\hbar} \right) \langle \hat{\mu}(t_1) \; \hat{\mu}^{\times}(0) \rangle \tag{3.1}$$

and

$$R^{(3)}(t_3, t_2, t_1) = \left(\frac{i}{\hbar} \right)^3 \langle \hat{\mu}(t_3 + t_2 + t_1) \; \hat{\mu}^{\times}(t_2 + t_1) \; \hat{\mu}^{\times}(t_1) \; \hat{\mu}^{\times}(0) \rangle \tag{3.2}$$

The PLDM framework has been shown to be capable of accurately reproducing quantum autocorrelation functions [70, 71] and we employ it here to compute the third-order optical spectroscopy response function according to the following expression ($\hbar = 1$):

---

[1]This is nothing but a simple reorganization of the terms of equations Eq. (2.22) and Eq. (2.24): there we employed a Schrödinger like representations, here instead we rewrite the terms in the Interaction representation.

$$R^{(3)}(t_3, t_2, t_1) = (i)^3 \sum_{n_{t_3}} \left(\prod_{k=N_2+N_1+1}^{N_3+N_2+N_1} \int d\bar{R}_k \frac{d\bar{P}_k}{2\pi} \right) \sum_{n_{t_2}, n'_{t_2}} \int d\bar{R}_{N_2+N_1} \frac{d\bar{P}_{N_2+N_1}}{2\pi} dx_{t_2} dp_{t_2} dx'_{t_2} dp'_{t_2} \ G_{t_2} G'_{t_2}$$

$$\times \left(\mu \rho^{(3)} \right)_{n_{t_3} n_{t_3}} \prod_{k=N_2+N_1+1}^{N_3+N_2+N_1-1} \delta \left(\frac{\bar{P}_{k+1} - \bar{P}_k}{\epsilon} - F_k \right) \prod_{k=N_2+N_1+1}^{N_3+N_2+N_1} \delta \left(\frac{\bar{R}_k - \bar{R}_{k-1}}{\epsilon} - \frac{\bar{P}_k}{M} \right) \delta \left(\bar{P}_{N_2+N_1+1} - \bar{P}_{N_2+N_1} \right)$$

$$\times \delta \left(\frac{\bar{R}_{N_2+N_1} - \bar{R}_{N_2+N_1-1}}{\epsilon} - \frac{\bar{P}_{N_2+N_1}}{M} \right) \left(\prod_{k=N_1+1}^{N_2+N_1-1} \int d\bar{R}_k \frac{d\bar{P}_k}{2\pi} \right) \sum_{n_{t_1}, n'_{t_1}} \int d\bar{R}_{N_1} \frac{d\bar{P}_{N_1}}{2\pi} dx_{t_1} dp_{t_1} dx'_{t_1} dp'_{t_1} \ G_{t_1} G'_{t_1}$$

$$\times \left(\mu^\times \rho^{(2)} \right)_{n_{t_2} n'_{t_2}} \prod_{k=N_1+1}^{N_2+N_1-1} \delta \left(\frac{\bar{P}_{k+1} - \bar{P}_k}{\epsilon} - F_k \right) \prod_{k=N_1+1}^{N_2+N_1} \delta \left(\frac{\bar{R}_k - \bar{R}_{k-1}}{\epsilon} - \frac{\bar{P}_k}{M} \right) \delta \left(\bar{P}_{N_1+1} - \bar{P}_{N_1} \right)$$

$$\times \delta \left(\frac{\bar{R}_{N_1} - \bar{R}_{N_1-1}}{\epsilon} - \frac{\bar{P}_{N_1}}{M} \right) \left(\prod_{k=1}^{N_1-1} \int d\bar{R}_k \frac{d\bar{P}_k}{2\pi} \right) \sum_{n_0, n'_0} \int d\bar{R}_0 dx_0 dp_0 dx'_0 dp'_0 \ G_{t_0} G'_{t_0}$$

$$\times \left(\mu^\times \rho^{(1)} \right)_{n_{t_1} n'_{t_1}} \prod_{k=1}^{N_1-1} \delta \left(\frac{\bar{P}_{k+1} - \bar{P}_k}{\epsilon} - F_k \right) \prod_{k=1}^{N_1} \delta \left(\frac{\bar{R}_k - \bar{R}_{k-1}}{\epsilon} - \frac{\bar{P}_k}{M} \right) \left(\mu^\times \rho^{(0)} \right)_W^{n_0 n'_0} (\bar{R}_0, \bar{P}_1)$$

$$(3.3)$$

Eq. (3.3) follows from the central equation of PLDM dynamics (Part I, Eq. 4.23), applied here for describing the evolution of the operator $(\hat{\mu}^\times \hat{\rho})$. The third-order response function is obtained by repeatedly nesting this time evolution as described in Eq. (3.2), and tracing the result over all the DOFs. The derivation of this equation is reported in the Appendix (Section 4.2).

Here $(\hat{\mu}\hat{\rho}^{(j)})_{n_{t_j} n'_{t_j}}$ are the matrix elements of the product of the transition dipole operator and the evolved density operator after the jth field interaction. From Eq. (4.23) of Part I, the elements of $\hat{\rho}^{(j)}$ are computed from the time evolved mapping variables as $\hat{\rho}^{(j)}_{k_{t_j} l_{t_j}} = \frac{1}{2}(x_{k_{t_j}} + ip_{k_{t_j}})(x_{n_{t_{j-1}}} - ip_{n_{t_{j-1}}})\frac{1}{2}(x'_{l_{t_j}} - ip'_{l_{t_j}})(x'_{n'_{t_{j-1}}} + ip'_{n'_{t_{j-1}}})$. The initial distribution of mapping variables for the $(j+1)^{\text{th}}$ time interval is provided by the functions $G_{t_j} = \exp[-\frac{1}{2}\sum_\alpha (x_{\alpha_{t_j}}^2 + p_{\alpha_{t_j}}^2)]$ and G'_{t_j}.[2]

Due to the state-collapsing nature of the dipole operator, each time it is applied it projects the evolving operator onto a different subspace of the global Hilbert space (see Figure 3.1). Therefore, after a dipole interaction, each matrix element can potentially give rise to a large number of new matrix elements that need to be propagated. From Eq. (3.3) the sums over the starting state indices at each of the interaction times have the potential to dramatically increase the number of terms that must be evolved, and each, in principle, require propagating many independently sampled trajectories. This suggests that the complete treatment of realistic systems will be very computationally demanding with a brute-force implementation.

---

[2]Note: The k indices labeling the terms in the products in Eq.(3.3) apply only to the quantities immediately to the right of the product.

$$\text{Tr } \hat{\mu} \begin{pmatrix} \begin{array}{|c|c|c|} \hline & \blacksquare & \\ \hline \blacksquare & & \blacksquare \\ \hline & \blacksquare & \\ \hline \end{array} \end{pmatrix} \leftarrow \hat{\mu}^{\times} \begin{pmatrix} \begin{array}{|c|c|c|} \hline \blacksquare & & \blacksquare \\ \hline & \blacksquare & \\ \hline & \blacksquare & \\ \hline \end{array} \end{pmatrix} \leftarrow \hat{\mu}^{\times} \begin{pmatrix} \begin{array}{|c|c|c|} \hline & \blacksquare & \\ \hline \blacksquare & & \\ \hline & & \\ \hline \end{array} \end{pmatrix} \leftarrow \hat{\mu}^{\times} \begin{pmatrix} \begin{array}{|c|c|c|} \hline \blacksquare & & \\ \hline & & \\ \hline & & \\ \hline \end{array} \end{pmatrix}$$

$$\hat{\rho}^{(3)}(t_1 + t_2 + t_3) \qquad \hat{\rho}^{(2)}(t_1 + t_2) \qquad \hat{\rho}^{(1)}(t_1) \qquad \hat{\rho}^{(0)}(0)$$

with label over the last matrix: $|g\rangle|e_i\rangle|e_j\rangle|f\rangle$
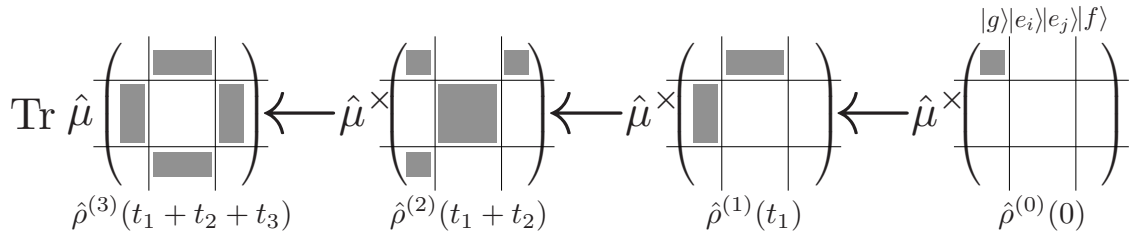
Figure 3.1: Pictorial representation of the effect of the subsequent dipole interactions on the evolving operator, represented as a matrix in which filled grey sectors correspond to non-zero elements of selected subspaces of the global Hilbert space. The arrows indicate time propagation.

To mitigate this problem, a Monte-Carlo importance sampling procedure is employed to treat the intermediate state sums for the interactions at t_1 and t_2 by selecting the "most important" matrix element as the sole initially-occupied state for subsequent propagation. Also, the intermediate mapping variable integrals are evaluated using a "steepest descent" approximation. This method, termed "focusing" (the basic ingredients of which have already been presented in the literature [72]), drastically reduces the computational effort needed to compute multi-point correlation functions in the PLDM framework.[3]

3.1   Implementation

This algorithm can be summarized for a general n-state system as follows:

1. At t=0, the dipole commutator prepares the system in a coherence between the ground and single exciton manifold (e.g., $|e\rangle\langle g|$) and initial system mapping variables are sampled from Gaussian distributions as indicated in Eq. (3.3). Assuming the bath DOFs are unaffected by the electronic dipole operator (the Condon approximation), these variables are sampled from their equilibrium distribution on the ground electronic state. An ensemble of trajectories, originating from these system and bath initial conditions is then initiated.

2. The system DOFs are propagated for a time t_1 using classical trajectories that satisfy Hamilton's equations obtained from the mapping Hamiltonian in Part I, Eq. (4.14). The bath DOFs are propagated simultaneously according to the effective forces which depend on (both forward and backward) system mapping variables, as outlined in Part I, Eq. (4.26).

---

[3]When evaluating linear response functions this focusing procedure is unnecessary because there is only a single time interval.

3. At $t = t_1$, the dipole commutator is applied again and the system is projected into a new set of states, while the bath DOFs remain continuous through the operation of the dipole. For each state of the projected subspace, mapping variables are re-sampled from gaussian distributions.

· If "focusing" is applied then the "most important" matrix element is selected as the new initial condition for subsequent propagation, according to the following steps:

a) The elements of the dipole operated density matrix are written, in polar coordinates, as:

$$(\mu\rho^{(1)})_{n_{t_1} n'_{t_1}} \rightarrow r_{n_{t_1}} r_{n'_{t_1}} e^{i(\theta_{n_{t_1}} - \theta_{n'_{t_1}})} \tag{3.4}$$

and a normalized probability density function, $m_{n_{t_1} n'_{t_1}}$, is constructed according to:

$$m_{n_{t_1} n'_{t_1}} = \frac{r_{n_{t_1}} r_{n'_{t_1}}}{N_{t_1}} \; ; \; N_{t_1} = \sum_{n_{t_1} n'_{t_1}} r_{n_{t_1}} r_{n'_{t_1}} \tag{3.5}$$

b) A uniform random number $\xi \in (0,1]$ is extracted, and the probability density $m_{n_{t_1} n'_{t_1}}$ uniformly sampled (Appendix, Section 4.3), selecting the "most important" matrix element $(n^o_{t_1}, n'^o_{t_1})$ as the new (occupied) initial system density matrix element for the next time interval propagation

c) A trajectory dependent weight $\Omega_{t_1} = N_{t_1} e^{i(\theta_{n^o_{t_1}} - \theta_{n'^o_{t_1}})}$ is saved.

d) The "steepest descent" approximation is used to evaluate the integrals over the mapping variables resulting in the following:

$$(n_{t_1}, n'_{t_1}) = (\delta_{n_{t_1}, n^o_{t_1}}, \delta_{n'_{t_1}, n'^o_{t_1}}) \tag{3.6}$$

where δ_{ab} is the Kronecker delta function.

4. For each given t_1, steps 2-3 are repeated for a desired number of t_2 values (*i.e.* replacing t_1 by t_2 in these steps).

5. For each combination of t_1, t_2 the system and bath are propagated for a time delay t_3, after which the expectation value of the third-order polarization is computed by averaging over all trajectories.
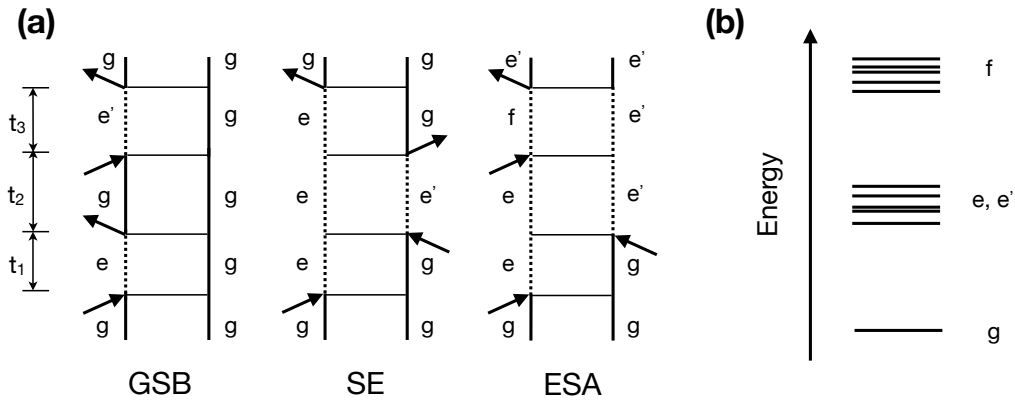
Figure 3.2: (a) Double-sided Feynman diagrams that represent nonrephasing interaction schemes. For conciseness, only diagrams that survive the rotating wave approximation are shown. The vertical lines represent time evolution, with dashed lines indicating time periods where the corresponding wave function can mix into a linear combination of eigenstates. Note that, in this methodology, mixing is also allowed when the system is in a coherence, not just when it is in a population. (b) Pictorial representation of the excitation manifolds involved in the Feynman diagrams depicted in (a).

· If "focusing" is used, the appropriate Monte-Carlo weights are accumulated and applied when computing the contribution of each trajectory to the final response.

By applying the RWA one can produce Feynman diagrams which look very similar to those introduced previously. The difference here is that, by avoiding the use of the secular approximation and the assumption that energy transfer occurs only when the system is in a population state, there are more time intervals in which the density matrix elements are allowed to mix. These are identified as dashed lines in Figure 3.2. Furthermore, dephasing of coherences and energy transfer are here described beyond the simple exponential picture of the previously presented approximated techniques.

We demonstrate the accuracy of the proposed approach in the limit of slow bath relaxation times, for which standard implementations of the theory employing assumptions on the bath timescales proved to fail.

3.2   Example I

In our first test of the methodology, the 2DES of a coupled dimer is computed. In this model we assume a pair of coupled sites, each of which has two levels, *i.e.*

each site has a significant gap between its first, and all the other excited states. The manifold of coupled dimer states probed during a third-order nonlinear spectroscopy experiment is completely described by the site basis states, $|ij\rangle$, so that a general time dependent state has the form:

$$|\psi(t)\rangle = \sum_{i,j=0}^{1} C_{ij}(t)|ij\rangle \tag{3.7}$$

where i and j represent the electronic state of each site. The Hamiltonian in this representation becomes

$$\hat{H} = \sum_{i,j=0}^{1} \epsilon_{ij} |ij\rangle\langle ij| + \sum_{ij\in 01,10} J_{ij,ji} |ij\rangle\langle ji|$$
$$+ \sum_{ij\in 01,10,11} \sum_{m=1}^{M} c_{ij}^{m}\hat{Q}_m |ij\rangle\langle ij| + \sum_{m=1}^{M} \frac{1}{2}\left(\hat{P}_m^2 + \omega_m^2\hat{Q}_m^2\right)\hat{\mathbb{1}} \tag{3.8}$$

where $\boldsymbol{c}$ is the strength of the linear system-bath coupling, with $\boldsymbol{c}_{11} = \boldsymbol{c}_{10} + \boldsymbol{c}_{01}$, and $\epsilon_{11} = \epsilon_{10} + \epsilon_{01}$. The spectral density that determines the bath mode frequencies and the frequency dependent system-bath coupling constants is the overdamped brownian oscillator form, $J(\omega) = 2\lambda\frac{\omega/\gamma_c}{(1+(\omega/\gamma_c)^2)}$ (Part I, Eq. (3.27)). In the calculations carried out here, each site was coupled to its own independent identical set of $M = 100$ bath oscillators sampled from this distribution.[73]

To demonstrate the applicability of the PLDM 2DES approach in parameter regimes where perturbation theory-based methods can become inaccurate, we considered a dimer system coupled to a bath with a slow relaxation time ($\gamma_c^{-1} = 300$ fs). In the limit of slow bath relaxation, the Markovian approximation can become unphysical. In Figure 3.3 the 2DES results computed with the PLDM approach are seen to reproduce those obtained from numerically exact hierarchical equations of motion (HEOM) calculations with surprising accuracy, even when the results are averaged over a limited number of trajectories. The "SPEC" results reported in Figure 3.3 were computed using the SPECTRON software package [68], employing line-shape functions obtained from the spectral density to account for all dephasing mechanisms in the absence of transport, and then using secular Redfield theory to describe transport. It is well known that Redfield theory can provide inaccurate transport dynamics in certain model parameter regimes, and we have already noticed that the use of the secular approximation not only decouples populations from coherences, but also prohibits the mixing between coherences. This means that a density matrix element initiated in $|e\rangle\langle g|$ will evolve according to its own equation
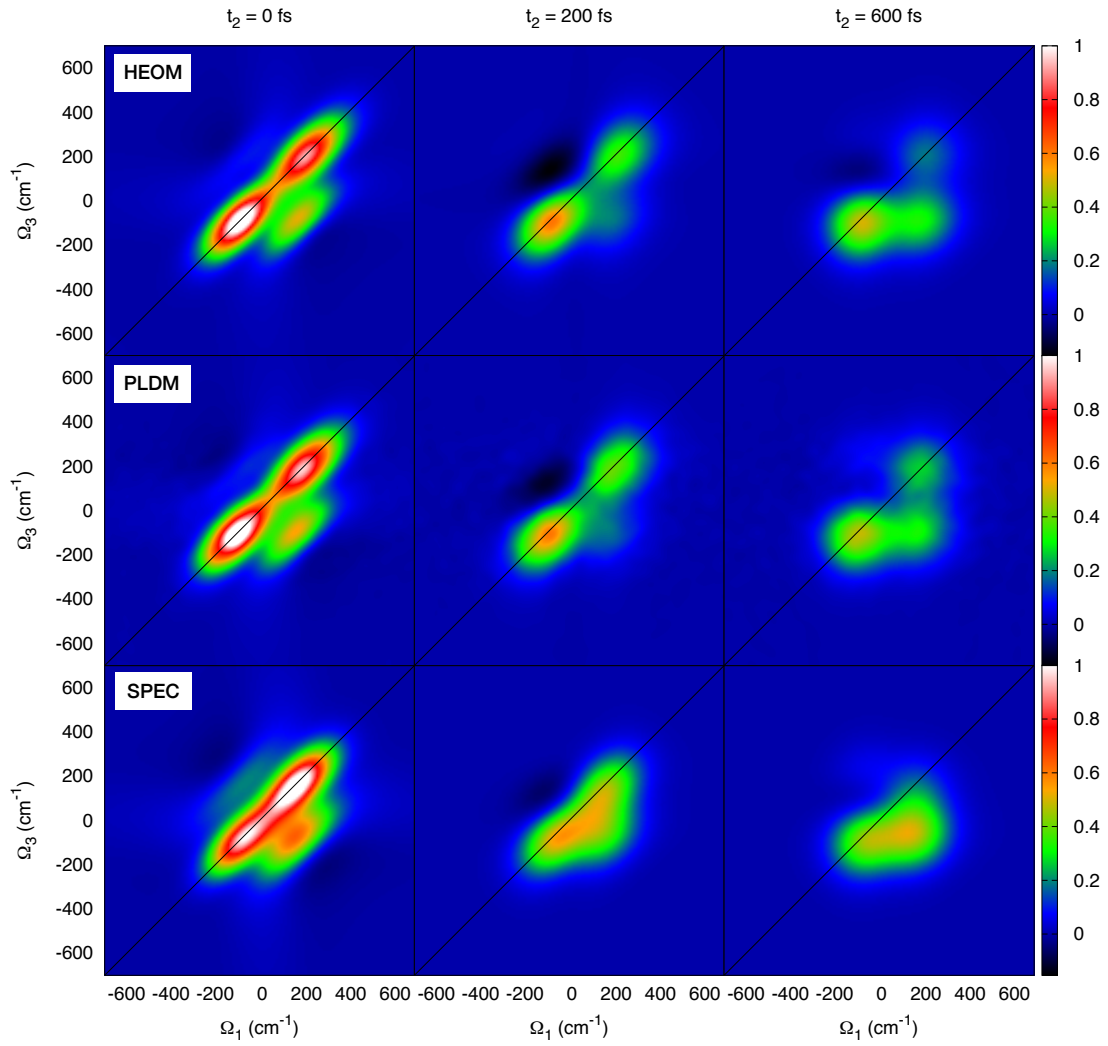
Figure 3.3: Comparison of HEOM, PLDM, and SPECTRON 2DES at different t_2 times for a coupled dimer at 300 K with $\epsilon_{10} - \epsilon_{01} = 100$ cm^{-1}, $\Delta_{01,10} = 100$ cm^{-1}, and $\mu_{00,01}/\mu_{00,10} = -0.2$. The bath has a cutoff frequency of $\gamma_c = 18$ cm^{-1} and a reorganization energy of $\lambda = 50$ cm^{-1}. The PLDM calculation presented here is averaged over only 60,000 trajectories initialized from each element of $\left(\mu^{\times}\rho^{(0)}\right)$ with nonzero amplitude. Note: The color range has been scaled to highlight the midrange features as detailed in the Appendix, Section 4.4

of motion, without coupling with any other $|e'\rangle\langle g|$ term. These approximations lead to qualitatively inaccurate results, even for $t_2 = 0$ fs, where this approach predicts inverted relative intensities of features corresponding to the two exciton states. In recent work it was demonstrated that this coupled dimer model also exhibits the complete breakdown of the second-order time-convolutionless master equation for this range of parameters.[74].

3.3 Example II

In many systems-of-interest, there can be higher frequency nuclear vibrational modes that are strongly coupled to the electronic transitions [75]. In this case, the nuclear vibration are preferentially treated as inherently quantum mechanical. In order to track the dynamics of particular *vibronic* states, a repartitioning of the system-bath Hamiltonian is required. For illustrative purposes, we consider a simple vibronic monomer including one discrete harmonic vibrational mode and a single electronic excited state interacting with a continuum of M_c more weakly coupled bath modes described by a Hamiltonian of the following form:

$$\hat{H} = \sum_{n_u=0}^{\infty} \epsilon_g^{(n_u)} |g_{n_u}\rangle\langle g_{n_u}| + \sum_{n_s=0}^{\infty} \epsilon_e^{(n_s)} |e_{n_s}\rangle\langle e_{n_s}| + \sum_{n_s=0}^{\infty}\sum_{m=1}^{M_c} c_m \hat{Q}_m |e_{n_s}\rangle\langle e_{n_s}|$$
$$+ \sum_{m=1}^{M_c} \frac{1}{2}\left(\hat{P}_m^2 + \omega_m^2 \hat{Q}_m^2\right)\hat{\mathbb{1}} \tag{3.9}$$

where $|g_{n_u}\rangle$ is the electronic ground state dressed with the state of the discrete vibrational mode with frequency Ω_d and in energy level n_u centered in coordinate space about the ground electronic state's unshifted ("u") equilibrium position, $|e_{n_s}\rangle$ is the electronic excited state dressed with the discrete vibrational mode in energy level n_s centered in coordinate space about the excited electronic state's shifted ("s") equilibrium position, and $\epsilon_g^{(n_u)} = \epsilon_g + \left(n_u + \frac{1}{2}\right)\Omega_d$ are the energies of the electronic ground state manifold. In a similar fashion, $\epsilon_e^{(n_s)} = \epsilon_e - \lambda_d + \left(n_s + \frac{1}{2}\right)\Omega_d$ is the excitation energy at the Franck-Condon point minus the reorganization energy, $\lambda_d = \frac{c_d^2}{2\Omega_d^2}$, dressed with the discrete mode (see Figure 3.4).

In the vibronic basis, elements of the electronic dipole matrix are modulated by the overlap of shifted vibrational wavefunctions. The magnitude of the overlap is dictated by Huang-Rhys factor, $S = \lambda_d/\Omega_d$, which indicates the relative shift between ground and excited state PESs.

$$\langle e_{n_s}|\hat{\mu}|g_{m_u}\rangle = \mu_{eg}\langle n_s|m_u\rangle$$
$$= \mu_{eg}\int dx\ \langle n|x - c/\Omega_d^2\rangle\langle x|m\rangle \tag{3.10}$$

In the calculation presented here, only vibrational energy levels 0 and 1 of the strongly coupled discrete mode were included due to the rapid fall-off of vibrational overlap for transitions between $|g_0\rangle \rightarrow |e_{n_s}\rangle$ for increasing Huang-Rhys factors. [76]

Figure 3.4 presents 2DES results for the vibronic system at various values of t_2.
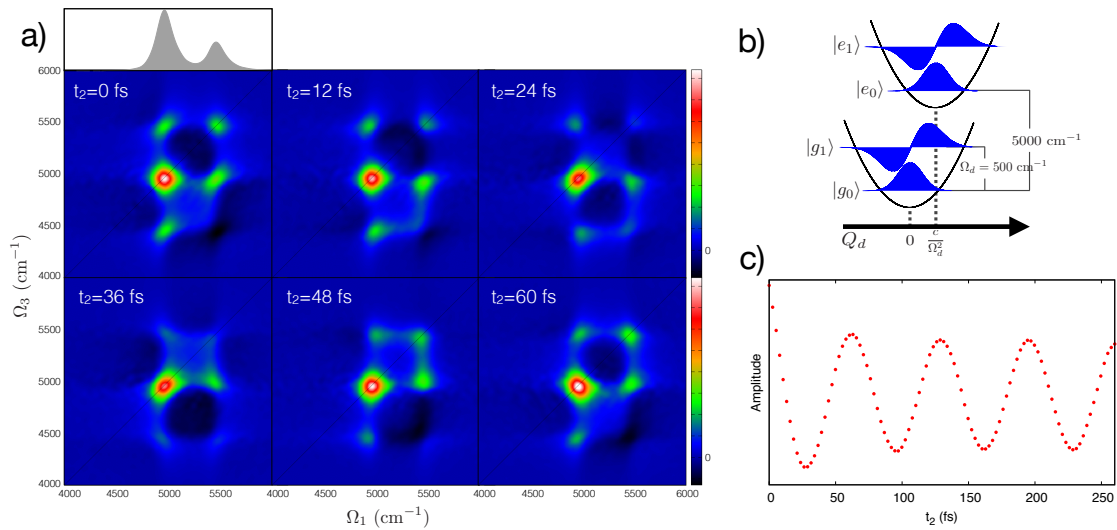
Figure 3.4: Summary of Vibronic Monomer study at 300 K. The electronic system-bath coupling model spectral density is a OBO with $\lambda = 50$ cm^{-1} and $\gamma_c = 200$ cm^{-1}. The additional discrete mode in the vibronic monomer model studied here has a frequency of $\Omega_d = 500$ cm^{-1} and Huang-Rhys factor $S = 0.45$. The $|g_n\rangle$ to $|e_n\rangle$ energy gap is 5000 cm^{-1}. In this study the initial system density operator is a population on the total ground state $|g_0\rangle$. Panel a) shows the linear absorption spectrum as well as the corresponding 2DES spectra for various values of t_2. Panel b) presents a pictorial representation of the model system Hamiltonian used in this study. Panel c) shows the evolution of the off-diagonal peak located at $(\Omega_1, \Omega_3) = (5000, 5500)$ cm^{-1} as a function of the t_2 delay time.

The evolution of the diagonal peaks and cross-peaks is modulated with a period of $66.7\ fs$, corresponding to the 500 cm^{-1} frequency of the discrete mode. These signal modulations can be easily misinterpreted in experiments as a signature of electronic coherence between different sites. For example, in Figure 3.4 it is shown that off-diagonal features associated with pure vibrational coherence can exhibit oscillatory modulation reminiscent of peaks associated with electronic coherence. The accuracy of the dynamics method presented in this work allows us to reproduce, and correctly interpret all kinds of signal oscillations.

3.4 Summary

To summarize this Chapter, we have presented a semiclassical path integral method for computing nonlinear optical response functions in non-Markovian open quantum systems. It combines a detailed description of the non-equilibrium dynamics responsible for energy transfer after photo-excitation in molecular aggregates (through the PLDM methodology) with response function theory of field-matter interactions, al-

lowing for the direct connection between theory and experiment.

We have demonstrated that the method presented here is capable of producing accurate results in parameter regimes where perturbation theory-based methods breakdown significantly. [74] If perturbation theory-based methodologies remain the only feasible way of treating system with a very large number of interacting chromophores, while paying the price of using approximations which limit their validity to certain parameters regimes, the methodology introduced here avoids this drawback by making no assumption about the form or strength of intra-system or system-bath couplings, even if it is generally more expensive. This method is not restricted to harmonic baths, although its accuracy in computing nonlinear spectra for anharmonic systems has yet to be studied. We also note that, being trajectory based, it scales linearly in a parallel computation environment.

This semiclassical path integral method offers an exciting starting point from which to explore the development of accurate, yet computationally economical, methods for computing nonlinear electronic spectroscopy. It can be used to study *e.g.* systems of coupled vibronic sites (to clarify the influence of coherent phenomena in energy transfer) and to describe the effects of finite bandwidth pulse shapes in the spectra.

Appendix

4.1   Homogeneous and inhomogeneous broadening

Experimental spectra have always a finite, non-null, line-width. There are various phenomena that contribute to this broadening, and they are usually grouped in two main sets: homogeneous and inhomogeneous broadening.

- *Homogeneous* broadening: The absorption lineshape is dynamically broadened by rapid variations in the energy gap ω_{eg} (e.g. due to nuclear motion) and for the finite state lifetime. This effects contribute to an exponential decay of coherences.

- *Inhomogeneous* broadening: In this limit, the lineshape reflects a static distribution of resonance frequencies, which arises from different local configurations of the environment. The width of the line therefore represents the distribution of frequencies.

If in ground-state absorption homogeneous and inhomogeneous broadening are in general both present and difficult to distinguish, in 2DES (as we have pointed out in Section 1.2.3) these two contributions split, giving rise to, respectively, off-diagonal and diagonal elongations of the peaks.

4.2 PLDM expression for the third-order response function

We here derive Eq. (3.3) for a single contribution to the overall third-order response, given by

$$
\begin{aligned}
R_+^{(3)}(t_3, t_2, t_1) &= \left(\frac{i}{\hbar}\right)^3 \langle \hat{\mu}(t_3 + t_2 + t_1)\, \hat{\mu}(t_2 + t_1)\, \hat{\mu}(t_1)\, \hat{\mu}(0) \rangle \\
&= \left(\frac{i}{\hbar}\right)^3 \mathrm{Tr}\left[\hat{\mu} e^{-iHt_3} \hat{\mu} e^{-iHt_2} \hat{\mu} e^{-iHt_1} \hat{\mu} \hat{\rho}_0 e^{iH(t_1 + t_2 + t_3)} \right]
\end{aligned}
\tag{4.1}
$$

which is the contribution that includes only the positive terms of the commutators $\mu^\times$. Upon insertion of complete sets of states, Eq. (4.1) becomes

$$
\begin{aligned}
R_+^{(3)}(t_3, t_2, t_1) = \left(\frac{i}{\hbar}\right)^3 \sum_{n_{t_3}} \sum_{n_{t_2}, n'_{t_2}} \sum_{n_{t_1}, n'_{t_1}} \sum_{n_0, n'_0} \int &\, dR_{N_3+N_2+N_1} dR_{N_2+N_1} dR'_{N_2+N_1} dR_{N_1} dR'_{N_1} dR_0 dR'_0 \\
&\langle n_{t_3}, R_{N_3+N_2+N_1} | \hat{\mu} e^{-iHt_3} | n_{t_2}, R_{N_2+N_1} \rangle \langle n_{t_2}, R_{N_2+N_1} | \hat{\mu} e^{-iHt_2} | n_{t_1}, R_{N_1} \rangle \\
&\langle n_{t_1}, R_{N_1} | \hat{\mu} e^{-iHt_1} | n_0, R_0 \rangle \langle n_0, R_0 | \hat{\mu} \hat{\rho}^{(0)} | n'_0, R'_0 \rangle \langle n'_0, R'_0 | e^{iHt_1} | n'_{t_1}, R'_{N_1} \rangle \\
&\langle n'_{t_1}, R'_{N_1} | e^{iHt_2} | n'_{t_2}, R'_{N_2+N_1} \rangle \langle n'_{t_2}, R'_{N_2+N_1} | e^{iHt_3} | n_{t_3}, R_{N_3+N_2+N_1} \rangle
\end{aligned}
\tag{4.2}
$$

Within the Condon approximation this result can be further decomposed by inserting system complete sets of states, leading to

$$
\begin{aligned}
R_+^{(3)}(t_3, t_2, t_1) = \left(\frac{i}{\hbar}\right)^3 \sum_{n_{t_3}} \sum_{n_{t_2}, n'_{t_2}} \sum_{n_{t_1}, n'_{t_1}} \sum_{n_0, n'_0} \sum_{m_{t_1}, m_{t_2}, m_{t_3}} \int &\, dR_{N_3+N_2+N_1} dR_{N_2+N_1} dR'_{N_2+N_1} dR_{N_1} dR'_{N_1} dR_0 dR'_0 \\
&\langle n_{t_3} | \hat{\mu} | m_{t_3} \rangle \langle m_{t_3}, R_{N_3+N_2+N_1} | e^{-iHt_3} | n_{t_2}, R_{N_2+N_1} \rangle \langle n_{t_2} | \hat{\mu} | m_{t_2} \rangle \langle m_{t_2}, R_{N_2+N_1} | e^{-iHt_2} | n_{t_1}, R_{N_1} \rangle \\
&\langle n_{t_1} | \hat{\mu} | m_{t_1} \rangle \langle m_{t_1}, R_{N_1} | e^{-iHt_1} | n_0, R_0 \rangle \langle n_0, R_0 | \hat{\mu} \hat{\rho}^{(0)} | n'_0, R'_0 \rangle \langle n'_0, R'_0 | e^{iHt_1} | n'_{t_1}, R'_{N_1} \rangle \\
&\langle n'_{t_1}, R'_{N_1} | e^{iHt_2} | n'_{t_2}, R'_{N_2+N_1} \rangle \langle n'_{t_2}, R'_{N_2+N_1} | e^{iHt_3} | n_{t_3}, R_{N_3+N_2+N_1} \rangle
\end{aligned}
\tag{4.3}
$$

The connection with the PLDM algorithm is readily obtained, by recognizing that the term

$$
\sum_{n_0, n'_0} \int dR_0 dR'_0 \langle m_{t_1}, R_{N_1} | e^{-iHt_1} | n_0, R_0 \rangle \langle n_0, R_0 | \hat{\mu} \hat{\rho}^{(0)} | n'_0, R'_0 \rangle \langle n'_0, R'_0 | e^{iHt_1} | n'_{t_1}, R'_{N_1} \rangle
\tag{4.4}
$$

can be rewritten in the PLDM formalism as

$$\sum_{n_0, n_0'} \int d\bar{R}_0 dr_0 dp_0 dr_0' dp_0' \; G_0 G_0' \frac{1}{2}(r_{m_{t_1}} + ip_{m_{t_1}})(x_{n_0} - ip_{n_0})\frac{1}{2}(r_{n_{t_1}'}' - ip_{n_{t_1}'}')(r_{n_0'}' + ip_{n_0'}')$$

$$\times \left(\prod_{k=1}^{N_1-1} \int d\bar{R}_k \frac{d\bar{P}_k}{2\pi} \right) \int \frac{d\bar{P}_{N_1}}{2\pi} (\mu\rho)_W^{n_0 n_0'}(\bar{R}_0, \bar{P}_1) \; e^{i\bar{P}_{N_1} Z_{N_1}} \prod_{k=1}^{N_1-1} \delta\left(\frac{\bar{P}_{k+1} - \bar{P}_k}{\epsilon} - F_k \right) \quad (4.5)$$

$$\times \prod_{k=1}^{N_1} \delta\left(\frac{\bar{R}_k - \bar{R}_{k-1}}{\epsilon} - \frac{\bar{P}_k}{M} \right)$$

Upon summation over m_{t_1} we have the necessary matrix elements that define the initial conditions for subsequent propagation. The Condon approximation implies that bath DOFs are unaffected by the application of the dipole operator, and therefore propagate continuously after the various dipole interactions. The initial momentum distribution for the subsequent propagation is provided by the integral over Z_{N_1} of $O_W^{n_{t_1} n_{t_1}'}(\bar{R}_{N_1}, \bar{P}_{N_1+1}) = \int dZ_{N_1} \langle n_{t_1}, \bar{R}_{N_1} + \frac{Z_{N_1}}{2} | \hat{O} | n_{t_1}', \bar{R}_{N_1} - \frac{Z_{N_1}}{2} \rangle e^{-i\bar{P}_{N_1+1} Z_{N_1}}$, which gives $\delta(\bar{P}_{N_1+1} - \bar{P}_{N_1})$. The integration over $\bar{R}_{N_1}$ can be evaluated analytically according to $\delta(\bar{P}_{N_1+1}/M - (\bar{R}_{N_1+1} - \bar{R}_{N_1})/\epsilon)$.

This scheme is continued until all propagations and dipole operations have been performed, at which point the result is traced, leading to the expression in Eq. (3.3).

4.3 Focusing - uniform sampling

The intermediate sums in Eq. (3.3) are conveniently rewritten in a form that is amenable to a uniform random sampling as:

$$\sum_{n_{t_i} n_{t_i}'} r_{n_{t_i}} r_{n_{t_i}'} e^{i(\theta_{n_{t_i}} - \theta_{n_{t_i}'})} \rightarrow \mathcal{N}_{t_i} \sum_{n_{t_i} n_{t_i}'} m_{n_{t_i} n_{t_i}'} e^{i(\theta_{n_{t_i}} - \theta_{n_{t_i}'})} \quad (4.6)$$

Where $\mathcal{N}_{t_i} = \sum_{n_{t_i} n_{t_i}'} r_{n_{t_i}} r_{n_{t_i}'}$ and $m_{n_{t_i} n_{t_i}'} = \frac{r_{n_{t_i}} r_{n_{t_i}'}}{\mathcal{N}_{t_i}}$ defines the normalized probability density function that will be directly sampled using a uniform random number, $\xi \in (0, 1]$. This sampling procedure selects (on average) the matrix element of $(\hat{\mu}\hat{\rho}^{(i)})_{n_{t_i} n_{t_i}'}$ that has the largest instantaneous magnitude. The selected element is assigned as the sole initially occupied "state", $(n_{t_i}^o, n_{t_i}'^o)$, for subsequent propagation. Figure 4.1 contains a pictorial representation of the importance sampling scheme.
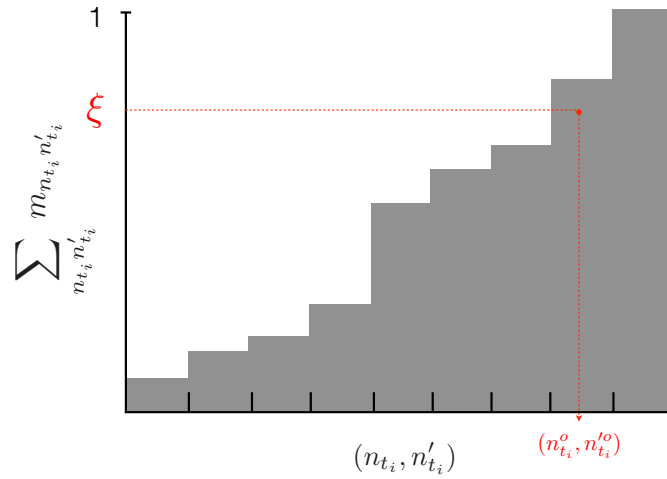
Figure 4.1: Pictorial representation of the Monte-Carlo importance sampling scheme.

4.4 Color range of Figure 3.3

In order to highlight the difference between mid-range features at longer times, the color scale has been enhanced in this region. To achieve an adequate coloring scheme, the maximum of the color range (white) was set as $0.85*\max\{\tilde{R}\}$ while the minimum of the color range (black) was set as $0.425*\min\{\tilde{R}\}$ where $\tilde{R}$ refers to the entire Fourier transformed response function (*i.e.* $\tilde{R} = \tilde{R}(\Omega_3^{min} : \Omega_3^{max}, t_2^{min} : t_2^{max}, \Omega_1^{min} : \Omega_1^{max})$). Imposing these boundaries on the color range makes it so all $\tilde{R}(\Omega_3, t_2, \Omega_1) \geq 0.85*\max\{\tilde{R}\}$ are represented as white and all $\tilde{R}(\Omega_3, t_2, \Omega_1) \leq 0.425*\min\{\tilde{R}\}$ are represented as black.

Part III

Results

Introduction

Here we make use of the concepts previously introduced to study some real systems. Three examples are proposed: the study of the Light Harvesting complex 2 (LH2) of the photosynthetic bacterium *rodopseudomonas acidophila*, the study of the energy transfer between carotenoid and retinal in the *xanthorhodopsin* protein, and the photoisomerization of the *azobenzene* molecule. Comparison with experiments has been carried out in all the three cases, and it is shown how an integration between theory and measurements is mandatory to clarify the origin of the observed spectral features and shed light on the EET mechanisms employed by nature.

In the first study, a first-principles approach is presented that combines accurate quantum chemical descriptions with state-of-the-art models for the environment through the use of atomistic and polarizable embeddings. Slow and fast bath dynamics, along with exciton transport between the pigments, are included. This approach is applied to the 2DES spectroscopy of the Light-Harvesting 2 (LH2) complex of purple bacteria. Simulations are extended, for the first time, over the entire visible-near-infrared spectral region to cover both carotenoid and bacteriochlorophyll signals. Our results provide an accurate description of excitonic properties and relaxation pathways, and give an unprecedented insight into the interpretation of the spectral signatures of the measured 2D signals.

In the second example, by comparing two-dimensional electronic spectroscopy (2DES) measurements on xanthorhodopsin (XR) and reduced-xanthorhodopsin (RXR) complexes, the ultrafast carotenoid-to-retinal energy transfer pathway is directly revealed by an excess of signal amplitude at the associated cross-peak. We show that the remarkable velocity of this transfer, despite the non-negligible energy separation between the two chromophores, points toward a crucial role of molecular vibra-

tions in assisting the energy transfer process. The combination of measured 2DES spectroscopic data with theoretical modeling, allows for a clear identification of the main experimental signals and for a comprehensive interpretation of their origin and dynamics.

Finally, in the third example, we combine sub-20-fs transient absorption spectroscopy in the UV range with state-of-the-art computational tools to study the ultrafast photoinduced dynamics of *trans*-azobenzene (*trans*-AB). The 1DPP experiment allows to resolve the evolution of the principal states involved, by exploiting the presence of state-specific ESA signals: the lifetime of the $\pi\pi^*$ state, the build-up of the $n\pi^*$ population and the following coherent oscillatory dynamics. The simulations reproduce with remarkable accuracy the positions of all ESA bands and reveal a non-reactive decay channel on the $n\pi^*$ state, accessible after excitation of the $\pi\pi^*$ state through a planar conical intersection, which allows the decay to the ground state on a sub-ps timescale, and accounts for the violation of the Kasha rule observed in AB.

CHAPTER 1

A Quantum Chemical Interpretation of Two-Dimensional Electronic Spectroscopy of Light-Harvesting Complexes

---

The work presented in this chapter has been done in collaboration with the *Molecolab* group of Prof. Benedetta Mennucci (Università di Pisa, Pisa, IT), and published in F. Segatta *et al.*, ref. 52.

1.1 Introduction

Advances in electronic spectroscopy with femtosecond time resolution, such as the *two dimensional electronic spectroscopy* (2DES), have provided new insight into the energy transfer processes in the light-harvesting (LH) pigment-protein complexes present in photosynthetic organisms.[50, 51, 77, 78] The high complexity of these systems, where multiple interacting pigments are embedded in a protein matrix, leads to extremely intricate energy landscapes due to the interplay of excitonic, vibronic and, eventually, charge-transfer states. By spreading signals along two frequency axes and following the dynamics of excitation with very high time resolution, the 2DES technique allows to disentangle the overlapping transient spectra. As a result, a high density of information is obtained, but to objectively disentangle all these features and reach a detailed and reliable map of the energy transfer network is still a challenge. A possible strategy to solve the latter issue is to integrate the measurements with theoretical models: this has been successfully done by combining calculations, data extracted from experiments, and tunable parameters.[79, 80, 81, 82] Attempts to apply more sophisticated quantum chemical approaches to the simula-

tion of 2DES were conducted for the Fenna-Matthews-Olson complex,[83] however these rely on semiempirical calculations of key quantities.

Here we present an accurate quantum-chemistry based multiscale approach to simulate 2DES spectra of multichromophoric systems in complex environments for a direct comparison with experiments. By combining two different levels of quantum chemistry (Density Functional Theory and multireference perturbative RASSCF/ RASPT2) with two classical embedding schemes (electrostatic and polarizable) to account for the environment, we calculate all quantities needed to build up the exciton-phonon model with a unified theoretical framework able to incorporate slow and fast bath dynamics, along with exciton transport between the pigments. Because of its *ab initio* character, our approach represents an unambiguous strategy to achieve a clear interpretation of the spectra even when many different pigments are involved and a large range of wavelengths has to be explored. By switching on and off selected interactions among pigments, a detailed molecular-level analysis of the intricate network of couplings between the multiple electronic processes and the intra/intermolecular nuclear degrees of freedom can be achieved.

We demonstrate the potential of our approach by simulating the 2DES spectroscopy at low (77 K) and room temperature of one of the most challenging system, namely the main LH complex of purple bacteria, the Light-Harvesting 2 (LH2) of *rps. acidophila*. Since the determination of its high-resolution structural model reported in 1995 by Cogdell and co-workers [84], LH2 has been extensively studied with different experimental techniques (see ref. 85 for a recent exhaustive review). Many theoretical studies have also been performed;[80, 82, 86, 87, 88, 89, 90, 91, 92, 93, 94] however, the accurate interpretation of the excitonic properties of this highly symmetric system is still disputed, mostly owing to the different coupling regimes, which are active at the same time.

The LH2 complex is characterized by a cylindrical C_9 structure, containing 27 bacteriochlorophylls *a* (BChl) and 9 carotenoids (Car) as absorbing pigments.[95] The BChls are organized in two rings, a closely packed ring (B850) containing 18 BChls whose molecular plane is perpendicular to the cylinder radius, and a more loosely packed ring (B800) that contains 9 BChls, whose molecular plane is perpendicular to the C_9 axis (see Figure 1.1). The backbone of the Car molecules (Rhodopin Glucoside) encompasses the whole polypeptide chain and bridges the two BChl rings.

Due to this unique structural arrangement, the bright Q_y excitations of the B850 BChls are strongly coupled, whereas those of the B800 BChls are more weakly coupled; the coupling between the two rings is also not negligible. This is reflected
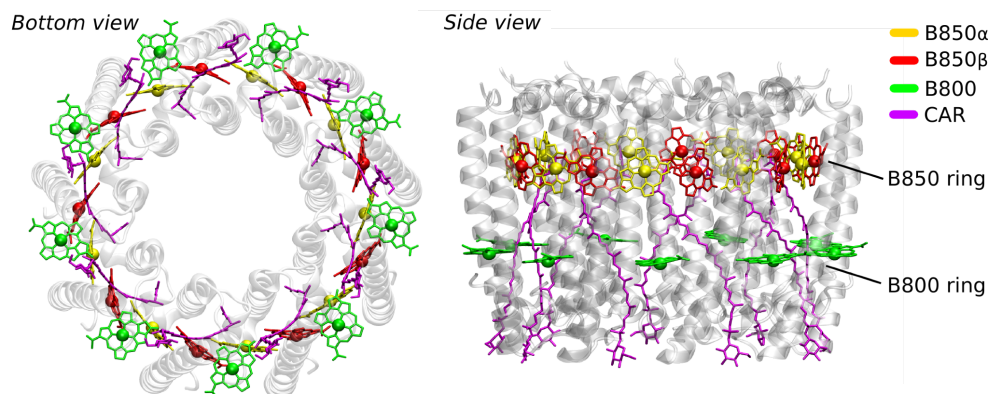
Figure 1.1: Molecular structure of LH2. Pigments are highlighted using the following color code: yellow for BChl B850α, red for B850β, green for B800, purple for the Carotenoid.

in the near IR characteristic signal arising from delocalized Q_y excitons. When we move to the region where the Q_x transition of the BChls and/or the bright state of the carotenoids are excited, the couplings decrease significantly in both rings as well as between the BChl rings and the connecting Cars.

For the first time, the present simulation is extended over the entire Car-Q_x plus Q_y visible-near-infrared (VIS-NIR) region. Due to the very different coupling regimes, the exciton model is combined with Redfield and Modified Redfield theories[38, 39, 40, 96] to describe exciton relaxation within delocalized states of the Q_y region, and the Förster theory within the Car-Q_x region.

Our results are compared with recently published experimental 2DES data,[97, 98] showing the importance of previously unaddressed aspects of the modeling and revealing new aspects of the recorded signals.

Focusing on the Q_y region, the good agreement between experimental and theoretical maps, obtained when the Coulomb interaction of the full transition densities and the polarization effects of the environment are included, points to the importance of a proper evaluation of the intra and inter-ring couplings. Moreover, we show that the simulations must include the excitation and detection pulse envelopes in order to achieve a quantitative agreement of the simulated intensities of B800 and B850 bands with experimentally recorded 2D maps.

Moving to the Car-Q_x region of the 2D map, the calculations clearly identify the signals due to the combined effect of the vibronic progression of the Car's bright S_2 state and BChl's Q_x transition, respectively. This is particularly important for those off-diagonal peaks that were used to reveal the presence of a previously postulated carotenoid dark state of the same symmetry of S_2,[99] which lies in between S_2 and Q_x states. The comparison between simulated and measured spectra reveals which
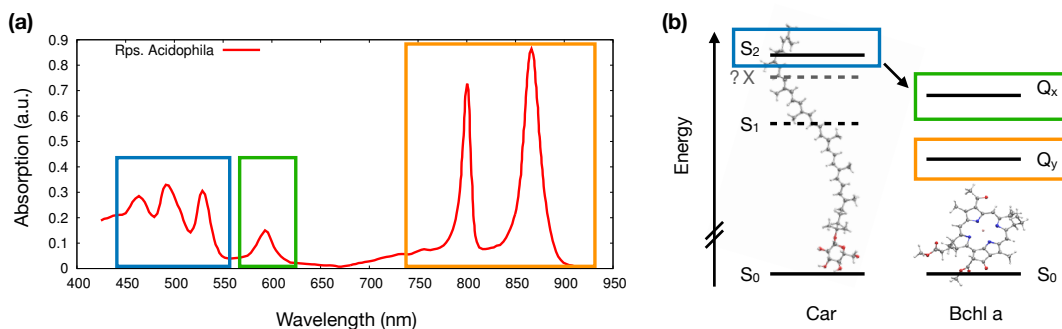
Figure 1.2: (a) Experimental linear absorption of LH2 complex[100] and (b) Energy level scheme of the states of interest for both Car and BChls. The different transitions are highlighted with different colors: blue for the S_2 state of the Carotenoid, green for the Q_x state of the BChls, and orange for the Q_y state of the BChls.

signals are due to vibronic progression of BChl Q_x, which can be labeled as pure vibrational progressions of the bright Car S_2 state, and which should indeed be recognized as Car signatures coming from states other than S_2.

1.2   Structure and Methods

We used the crystal structure of LH2 (PDB code: 1NKZ) resolved at 2.0 Å.[101] To ensure a C_9 symmetry, we considered a single monomer, which was replicated over the symmetry axis. All the details regarding the structure preparation are reported in Appendix, Section 1.5.1.

The multichromophoric system is described in terms of an exciton Hamiltonian

$$\hat{H} = \sum_i \epsilon_i \, |i\rangle \, \langle i| + \sum_{ij} V_{ij} \, |i\rangle \, \langle j| \tag{1.1}$$

where ϵ_i is the excited-state energy of the i-th chromophore, and V_{ij} is the electronic coupling between chromophores i and j. We considered separate Hamiltonians for (i) the near-infrared region of the spectrum, which includes the Q_y transitions of BChls, and (ii) the visible region, which contains contributions from the bright (S_2) states of Cars and the Q_x states of BChls.

The elements of the exciton Hamiltonian were computed using a hybrid QM/MM model to account for the effect of the protein environment. In particular, we employed two levels of QM theory, i.e. Time-Dependent Density Functional Theory (TD-DFT) with the CAM-B3LYP functional,[102] and the RASSCF/RASPT2 methodology [8, 23], with different Active Spaces (AS) and State Average (SA) set-

tings in the two different regions of the spectrum (Appendix, Section 1.5.5). The TD-DFT based calculations were performed within both an electrostatic (MM) and a polarizable embedding (MMPol). In the latter model, the environment is described as a set of atomic point charges and isotropic atomic polarizabilities[103]. The RAS calculations were performed within the electrostatic embedding of fixed point charges. Higashi *et al.* showed CAM-B3LYP to be inaccurate for the description of solvatochromic shifts when coupled with an electrostatic embedding, and proposed to tune the range-separation parameter.[104, 105] However, the exciton structure obtained in ref. 93 with CAM-B3LYP/MMPol well reproduced the exciton splitting of the B850 ring, therefore CAM-B3LYP is appropriate for describing excitation with a polarizable embedding. Further details on the quantum chemical calculations are reported in Appendix, Section 1.5.2.

The electronic couplings in the TD-DFT/MMPol scheme were computed as the Coulomb interaction between the transition densities of the interacting moieties.[106] Note that the polarizable environment adds an explicit screening term to the Coulomb coupling.[103] In the RASSCF/RASPT2/MM approach, the Coulomb couplings were computed with the transition density cube (TDC) method[27], where no explicit screening is included. It has been shown, both theoretically[93] and experimentally, [107] that the nearest-neighbor Q_y couplings in the B850 ring are reduced with increasing temperature; for this reason, in order to reproduce the room-temperature properties, we used the exciton Hamiltonian calculated along a classical molecular dynamics (MD) trajectory.[93]

The full set of excitonic parameters (site energies and couplings) used is reported in Appendix, Sections 1.5.7 and 1.5.9.

In order to describe exciton-phonon couplings, the spectral densities (SD) of the different transitions were modeled as a sum of one overdamped Brownian oscillator (Part I, Eq. (3.27)) and M discrete contributions. The discrete part of the SD, which accounts for the intramolecular vibrations of the various molecules, was determined using the vertical gradient approach (Part I, Section 3.1.4), from a normal mode analysis of the pigments in the crystal structure, and typical values[80] were adapted for the continuous part. Different spectral densities were explicitly used for the Q_y transitions of B850 α, B850 β and B800 molecules, but we used an average spectral density for all Q_x transitions. All details and parameters are reported in Appendix, Section 1.5.4.

To describe spectra and dynamics within the Q_y region, we employed the disordered exciton model with both standard Redfield (sR) and modified Redfield (mR) theories.[38, 96] This choice is natural if one considers the strongly coupled B850

pigments; moreover, mR theory has shown to compare well against nonperturbative hierarchical equations for the simulation of the linear spectra of the B800 ring.[89] Spectra and dynamics within the Car-Q_x region were described by Förster theory. This is justified by the large reorganization energy of the Cars and by the considerable energy gap between Cars and Q_x states. Static disorder in the transition energies of the various pigments (chosen to reproduce the broadening of the linear absorption peaks, as detailed in Appendix, Section 1.5.4) was taken into account by averaging the optical properties on a Gaussian distribution of site energies. Further details about the choice of the exciton dynamics theory are reported in Appendix, Section 1.5.3.

2DES pump-probe (rephasing plus non-rephasing) spectra were simulated within the approach outlined in Part II, Chapter 2, as implemented in the Spectron 2.7 code[68] using site energies, couplings and transition dipole moments either from TD-DFT or RAS based computations, and accounting for different experimental set-ups in the different spectral regions investigated. We adopted a spectral line shape model that incorporates slow and fast bath dynamics, together with exciton transport between the chromophores, as described in Part II, Section 2.4.3.[68, 69] Unless otherwise specified, the 2DES maps are calculated at $t_2 = 0$ fs. We considered only those double excitations that are associated with combinations of electronic states in the single-exciton manifold, while all the higher lying states of a single chromophores were not included in the simulation. We further refined the spectra by including proper pulse envelopes and polarizations (Appendix, Sections 1.5.3 and 1.5.8).

All TD-DFT and RAS calculations as well as all spectra simulations have been performed using an in-house modified version of Gaussian G09[108], MOLCAS 8.1[10] and Spectron 2.7[68], respectively.

1.3   Results and Discussion

For clarity, the presentation of the results is divided into two Sections, one referring to the Q_y region, for which standard and modified Redfield theories were used, and the other focused on the the Car-Q_x region, for which the Förster theory was employed.

1.3.1   The Q_y Region

The exciton Hamiltonians for the Q_y region calculated with alternative strategies (namely RASSCF/RASPT2/MM, TD-DFT/MM, and TD-DFT/MMPol) are de-

tailed in Appendix, Table 1.5. The values of the site energies obtained for the crystal structure with the two different QM levels (RASSCF/RASPT2 and TD-DFT) are generally quite similar (within 600 cm^{-1}) when the same electrostatic embedding model is used (MM). The introduction of a more refined polarizable embedding (MMPol) leads to a significant red-shift, due to the inductive effects of the protein residues surrounding the pigments.[109] Some differences between the QM levels are instead found in the relative ordering of the site energies for the different BChls: in particular, TD-DFT models give B800 as the most blue-shifted, while in the RASSCF/RASPT2 calculations B800 is found between B850 α and β. This different behavior, which is not due to the embedding model, as both TD-DFT/MM and TD-DFT/MMPol give the same trend, is related to the different electronic description by the two QM levels at slightly different internal geometries of the BChls.

The specific embedding model has a significant effect on the couplings: for example, the inverted behavior and the different magnitude of the $V_{\alpha\beta}^1$ and the $V_{\alpha\beta}^2$ coupling values (Appendix, Table 1.5) in the two different levels of QM theory can safely be attributed to the screening effect,[93] included only in the TD-DFT/MMPol calculations through the polarizable embedding. As expected, this screening plays a significant role in determining the coupling between BChls within the B850 ring where the BChls are closely packed.

By using the three different Hamiltonians, the linear spectra generated as described in Methods Section are reported in Figure 1.3. Due to differences in the site energies in the different QM methods, the computed spectra were shifted individually by a different amount, in order to compare with experiment. As expected, RASSCF/RASPT2 level of QM description gives a more accurate estimation of the site energies, and the corresponding spectrum requires only a small (120 cm^{-1}) shift to the blue to match the experimental B800 peak. A much larger blue-shift is necessary at the TD-DFT level. However, in spite of the larger offset in the absolute energies, the TD-DFT/MMPol approach better reproduces the band splitting between the two peaks at 800 and 850 nm, due to a more balanced description of site energy differences and couplings. The latter, in fact, correctly accounts for the possible screening effects as a polarizable embedding (MMPol) has been used. For this reason, we employed TD-DFT/MMPol data to model the 2DES maps.[1]

In Figure 1.4 we report the simulated 2DES maps at zero population time and temperatures 77 K (d) and 300 K (e), along with the experimental map (f) of the bacterium *Rps. palustris*[98] in the same spectral region, acquired at zero population

---

[1]We note, however, that RASSCF/RASPT2/MM data produce 2DES spectra which fully preserve all the features discussed here for the TD-DFT/MMPol spectra.
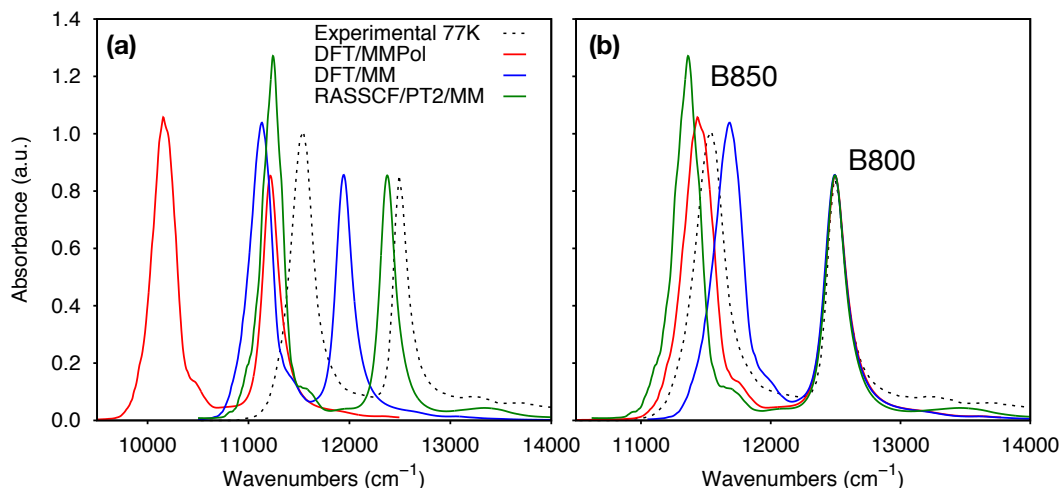
Figure 1.3: Comparison of linear absorption spectra of the Q_y region computed at 77 K, using modified Redfield theory, at different levels of QM theory and/or embedding models. The experimental spectrum is also reported (dashed line).[100] (a) Spectra as obtained from the computations; (b) Spectra shifted to match the experimental peak at 800 nm. The TD-DFT/MMPol, TD-DFT/MM and RASSCF/RASPT2/MM spectra have been shifted by 1280, 550, and 120 cm^{-1}, respectively.

time and 300 K. The 77 K 2DES map was computed using the TD-DFT/MMPol Hamiltonian calculated on the crystal structure, whereas for the 300 K map we employed the MD Hamiltonian from ref. 93. The pulse shapes were designed in order to resemble the experimental pulse envelopes (approximately the same overlap with the various bands as it appears in the experimental spectrum).

The simulated maps at the two temperatures show a similar positioning of peaks and cross-peaks, but, as expected, the 77 K map is dominated by the site energy static disorder (peaks extended along the diagonal), while the 300 K map shows much broader peaks. We observe a considerable similarity between simulated and experimental maps at 300 K especially in the relative position, shape and intensity of the positive and negative B850 signals. In this regard, it has been shown by Fleming et al.[110] that the positioning of these positive and negative B850 related features can be used as a coarse-grained probe for structural insights on the studied system. Symmetrically, when the structure is already known (such as for the LH2 of *Rps. acidophila*), the correct reproduction of positioning, shapes and relative intensities of these features supplies an indirect proof of the accuracy of both the underlying quantum chemical method and the spectra simulation protocols used. With regard to B800 signals, strong excited state absorption (ESA) signals on both sides of the main diagonal are present in the experiment, whereas the same signals appear to be
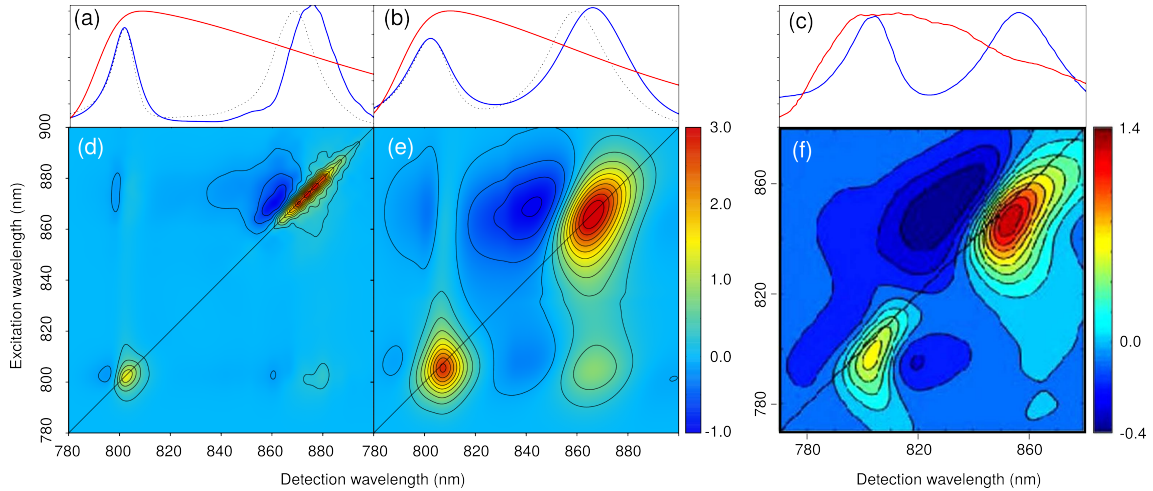
Figure 1.4: Comparison of 2DES pump-probe maps at zero population time. Simulated maps at 77 K (d) were computed for the TD-DFT/MMPol Hamiltonian. Simulated maps at 300 K (e) were computed for the MD Hamiltonian.[93] In both cases the modified Redfield theory of transport was employed. All simulated maps were shifted to match the experimental peak at 800 nm. The experimental map at 300 K (f) refers to the LH2 of *Rps. palustris*.[98] The corresponding linear absorptions (blue) and pulse shapes (red), along with the relative experimental linear spectra (dashed line),[100] are reported in (a), (b) and (c), respectively. Simulated maps are normalized between their minimum and maximum values. By convention, bleach and stimulated emission contributions appear as positive (red) signals, excited state absorption appears as negative (blue) peaks. The experimental map has been adapted from ref. 98.

weaker in the computed maps. We note that our simulated ESA signals only arise from combinations of electronic states in the single-exciton manifold; thus, we did not include ESA signals related to the excitation of the higher lying Soret bands from the Q_y transition. As the frequency of such excitations is compatible with these negative ESA signals on both sides of the positive bleaching, it is possible that $Q_y \rightarrow$ Soret excitations contribute to the negative signals around the diagonal B800 peak. Furthermore, it should also be noted that calculations and experiments refer to different bacteria even if they present a high similarity in both the linear absorption and circular dichroism spectra.[100]

A good agreement between experimental and theoretical maps can be found also in the off-diagonal regions, with similar positive and negative features in both sides of the maps. The presence of these off-diagonal signals in the spectra reflects the weak but still non-negligible coupling between the excitons of the two rings, which is accurately taken into account in our model. In fact, these off-diagonal signals are present also in the rephasing maps measured by Harel and Engel for the LH2 of *Rb. Sphaeroides*.[111] We reported the simulated rephasing 2DES map for the LH2 of the *Rps. acidophila* in Appendix, Figure 1.19: the calculated map clearly shows two

	Modified Redfield (mR)		Redfield (sR)	
	77 K	300 K	77 K	300 K
B800 → B800	321 (81)	196 (60)	317 (100)	168 (64)
B800 → B850	1045 (85)	630 (79)	1032 (79)	670 (65)
B850 → B850	244 (36)	137 (25)	244 (26)	142 (19)

Table 1.1: Average transfer times (in fs) of the LH2 ring, computed over 10 000 realizations of site energy static disorder. Numbers in parentheses refer to the average of maximum rates taken within every realization. Different columns refer to different temperatures. The 300 K rates were computed on the MD Hamiltonian.[93] Only downhill rates have been considered in this analysis.

off-diagonal signals, which originate from both ground state bleaching and excited state absorption pathways and reveal the exciton coupling between the B800 and B850 rings.

Interestingly, even if all the relevant excited states are properly included in the 2DES simulations, one should also take into account the proper shape of excitation and detection pulses, as implemented here. This refinement is mandatory if, for example, one is interested in comparing the intensities of B800 and B850 bands in simulated and experimentally recorded 2D maps (Appendix, Figure 2.7).

The downhill relaxation rates among the Q_y excitons were analyzed for over 10 000 realizations of static disorder of the site energy (gaussian) distributions, at 77 K and room temperature. For each realization of the disorder, the exciton states were assigned to the B800(B850) ring on the basis of the participation of the B800(B850) pigments to the exciton state. The average relaxation times over 10 000 system realizations of all the rates in each of the three channels (B800 → B800, B800 → B850, and B850 → B850) as well as those obtained averaging just the maximal rate of each channel, are shown in Table 1.1.

Calculated B800 → B850 transfer times are around 0.6–1 ps, in line with several experimental findings.[112, 113, 114, 85, 95] The calculated rates depend on temperature, with the mR 300 K rates being 66% faster than the 77 K rates. This is in agreement with the temperature dependence of the B800 → B850 energy transfer in *Rps. acidophila* determined by pump-probe spectroscopy, where the 300 K rate is ∼60% faster than the 77 K rate.[112] Similar measurements on the LH2 of *Rb. spheroides* show the same behavior for the inter-ring transfer times.[115] The good reproduction of the temperature dependence of the rates shows the importance of a detailed calculation of the excitonic Hamiltonian for the complex under different conditions.

The intra-B800 relaxation rates are much harder to determine experimentally;
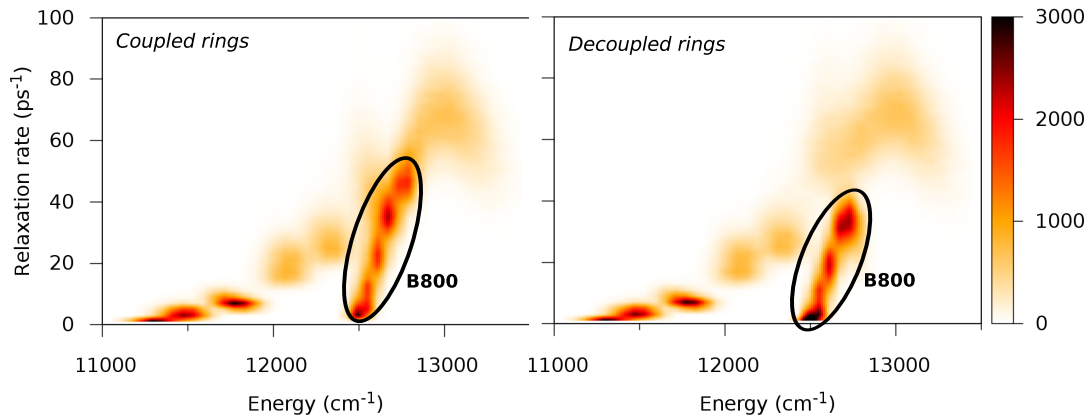
Figure 1.5: Two-dimensional histogram plots of exciton relaxation rates versus exciton energies (modified Redfield theory using the TD-DFT/MMPol exciton Hamiltonian at 77 K). The histograms show the distribution of energy and relaxation rates over 10 000 realizations of the site energy static disorder. The color range indicates the number of occurrences. The contribution of the B800 states is highlighted with a circle. Left: complete Hamiltonian with coupled rings; right: Hamiltonian with the B800 ring decoupled from the B850 ring.

anisotropy decay spectroscopy at different temperatures on *Rps. acidophila* shows that the intra-B800 transfer occurs on a 400–800 fs time scale at room temperature,[112] also in agreement with three-pulse photon echo studies.[116] Our intra-B800 300 K transfer rates are faster, indicating the limits of modified Redfield theory in describing the intra-B800 dynamics. Conversely, at 77 K, the calculated rates are much closer to the experiment (240 fs),[112] suggesting that the energy transfer mechanism is different at low and room temperature.

The results also show a weak dependence of the transfer rates on the excitation transfer theory adopted. The main difference between sR and mR theories is that in mR multiple quanta of energy can be exchanged between excitons and phonons, even though sR exciton transfer rates can be larger than mR rates.[40] Modified Redfield reduces to standard Redfield when the site energies approach degeneracy. [40, 96] Our results point to a small influence of multiphonon relaxation, for the average relaxation pathways, within our combination of exciton Hamiltonian and energetic fluctuations.

Further insight into the rate analysis can be obtained by investigating the energy dependence of the relaxation rates. In Figure 1.5 we report two-dimensional histogram plots of the exciton relaxation rate vs. exciton energy at 77 K. Notably, the exciton relaxation rates strongly depend on the exciton energy. In the low-energy B850 region (< 12400 cm^{-1}) the exciton relaxation rate rises with the energy; a region with slow relaxation rates can be found around 12500 cm^{-1}, due to

the low-energy end of the B800 band. At the blue edge of the B850 band we notice excitons with a very fast relaxation rate (tens of femtoseconds). We also compared the relaxation rates of the full Q_y sector of the LH2 system with a Hamiltonian where the B800 ring is decoupled from the B850 ring. The comparison with the artificially decoupled system shows that coupling to the B850 states shortens the lifetime (enhances the relaxation rate) of the B800 states. Finally, as the B850 states in this energy region are optically dark, their lifetime can only be measured if these states are mixed with the B800 states. In the B800 region the exciton lifetime generally decreases at higher energies. This is in agreement with polarized pump-probe measurements and rate calculations on the LH2 of *Rs. molischianum* at 77 K.[117] Although our computed exciton lifetimes are shorter than the measured polarization relaxation times, it is important to notice that exciton relaxation rates also include processes that may not change the polarization of the transition.[118]

A detailed statistics of delocalization length, dipole strength, and transfer rates in the three lowest exciton states of LH2, which belong to the B850 ring, is reported in Appendix, Figure 1.18.

1.3.2   The Carotenoid-Q_x Region

The Car-Qx linear spectra at both 77 K and 300 K were simulated as described in the Methods Section using the site energies and couplings reported in Appendix, Table 1.7. Due to the multiexcitation nature of the Car states, only the RASSCF/RASPT2/MM level has been used for the excitonic Hamiltonian in this spectral region, relying on the less expensive TD-DFT computations for the description of the chromophores vibrations (within the spectral densities). The results at both temperatures, together with the experimental spectra, are reported in Figure 1.6.

The computed spectra, at both 77 K and room temperature, compare well with experiment, showing a similar shape, position and intensity of the absorption bands. Nonetheless, the slight offset in the relative intensities of the Car vibronic peak seems to point to a possible underestimation of the Huang-Rhys factors for the S_2 state, which leads to a general overestimation of the 0-0 transition intensity. A non-negligible blu-shift of the Car vibronic peaks is also observed, possibly related to the level at which the Car structure was optimized (B3LYP/6-31G(d)).

Differently from the Q_y region, available experimental 2D maps in the Car-Q_x region refer exactly to the same photosynthetic organism, namely the *Rps. acidophila*.[97]

In Figure 1.7, we interpret the origin of experimental signals by artificially disentangling the Car- and BChl-related regions. For such an analysis, we refer to
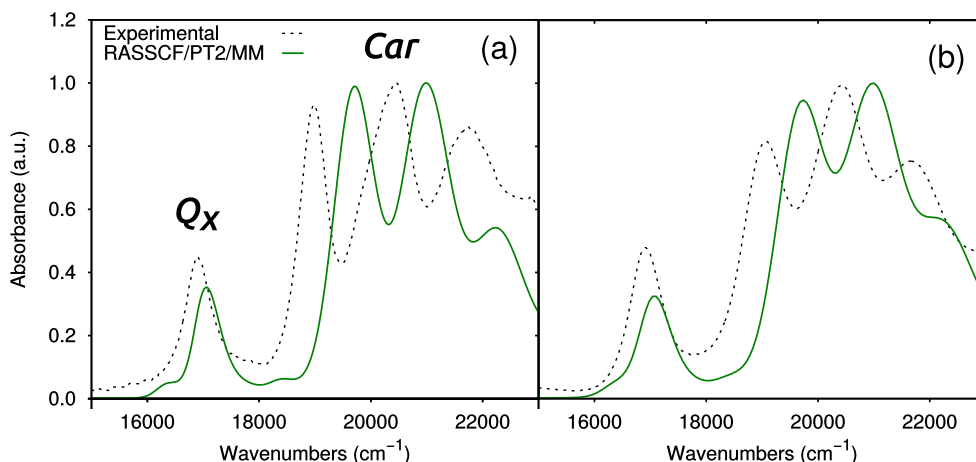
Figure 1.6: Linear absorption spectra for the Car-Q_x region computed at 77 K (a) and 300 K (b) using Förster transport, at the RASSCF/RASPT2/MM level of theory. The experimental spectra are also reported (dashed line), taken from ref. 100. All the spectra have been normalized with respect to the maximum peak. Calculated spectra have not been shifted.

the extrapolated map (corresponding to $t_2 \to 0$) obtained by Ostroumov et al.[97] through a global target analysis of the measured 2D data.

From the (experimental) target analysis, the three main diagonal contributions were assigned to ground state bleaching (and stimulated emission) signals from Car S_2 state (full triangle of Figure 1.7b), BChl Q_x state (empty triangle), and an additional X state of Car (empty circle), located in between the S_2 and Q_x transitions. The positive off-diagonal peaks were interpreted as additional signatures suggesting the presence of this elusive Car X state: the strong below-diagonal cross-peak (full diamond) was attributed to an ultrafast $S_2 \to X$ energy transfer, whereas for the above-diagonal cross-peak (empty square) the origin was associated with a ground state bleaching arising from mixed excitation of coupled Q_x and Car X states.

We compare these experimental data with our simulated maps consisting, respectively, of purely Car S_2 state signals (Figure 1.7a), and purely BChl Q_x state contributions (Figure 1.7c). On the diagonal of the two simulated maps, we observe the bleaching signals of the Car S_2 (full triangle in (a)) and BChl Q_x (empty triangle in (c)) states. We also note that the broad Car S_2 signal has significant contributions along the diagonal towards larger wavelengths, and that an additional diagonal peak around 550 nm (open circle in (c)) is present in the BChl Q_x map. This peak has to be attributed to the direct excitation of the first vibrational state of the 1300-1400 cm^{-1} sequence of modes of the Q_x state, especially the very intense one at 1300 cm^{-1} (see the spectral density reported in Appendix, Figure 1.10(a)),
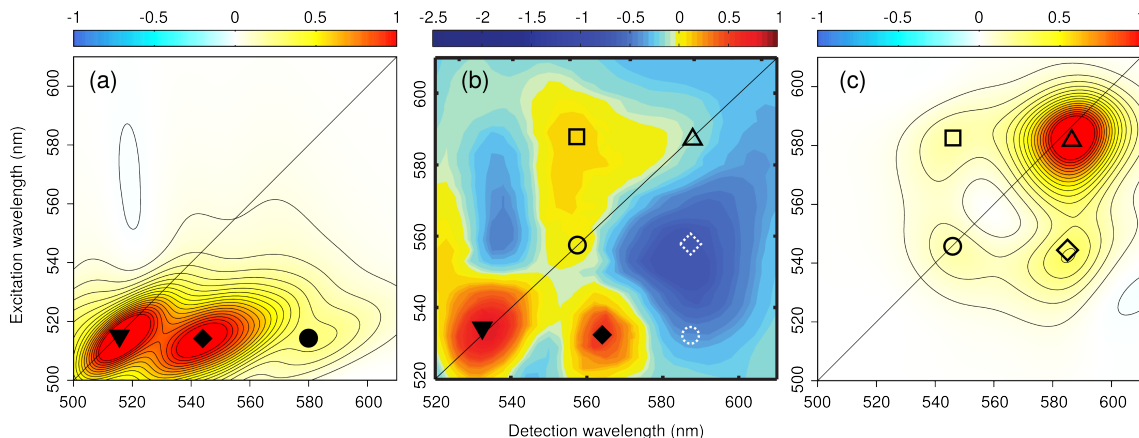
Figure 1.7: Calculated 2DES pump-probe maps at $t_2 = 0$ obtained by separately computing Car (a) and BChl (c) contributions. (b) Short t_2 component of the 2D evolutionary-associated spectra obtained through a global target analysis of the experimental 2D data.[97] The effect of the pulse shape has been taken into account in the simulated maps. Simulated maps are normalized to their maximum. By convention bleach and stimulated emission contributions appear as positive (red) signals, excited state absorption appear as negative (blue) peaks. Full (referring to Cars) and empty (referring to BChls) geometric symbols are used to indicate correlations between calculated and measured signals.

whose intensity is enhanced by the pulse shape envelopes. A quantification of the effect of this mode on the 2DES map is reported in Appendix, Figure 1.21. Our calculations therefore reveal a significant contribution on the diagonal, at the X position, deriving from both the broad S_2 bleaching and the Q_x vibronic state, which can in principle explain the observed positive peak.

Moreover, we observe off-diagonal features that can be correlated to experimental signatures, but providing a different interpretation for their origin: the sequence of off-diagonal peaks that appear pumping the Car and probing at larger wavelengths has to be assigned to the S_2 stimulated emission (the full diamond and circle in (a)), and the positive elongations of the experimental Q_x transition, at smaller excitation and detection wavelengths with respect to the bleaching, originate from the vibronic progression of the Q_x (the empty square and diamond in (c)).

The calculated spectra explain the main features of the extrapolated map in terms of the Car bright (S_2) state combined with the Q_x vibronic progression of BChls. We must note, however, that the present theoretical analysis is limited to early t_2 population times without exploiting all the wealth of additional information present at later times to definitely check the validity of the suggested interpretation. Nonetheless, our analysis suggests that it is necessary to review the interpretation of some of the observed signals, clearly indicating the importance of previously unaddressed features, such as the Car S_2 stimulated emission signals and the BChl

Q_x vibronic signatures. The signals on and below the diagonal at the 560 nm excitation wavelength cannot be unambiguously assigned to Car or BChl due to overlaps of the S_2 and Q_x related signatures, indicating the difficulties present in using these peaks for a definitive proof of the Car X state. Instead, the peak above the diagonal (indicated with the empty square in Figure 1.7b) is not significantly affected by any S_2-related signal. The oscillations of this off-diagonal peak have been recently investigated using a global target analysis of the absorptive 2D signals.[119] The resulting vibration-associated spectra (2DVAS) have been compared to those of the isolated Car and the observed similarity has been used to confirm the Car origin of the signal.

To unify all these theoretical and experimental findings it seems to be necessary to invoke the presence of a Car dark state, either an additional electronic state (the X state) or a very hot vibrational level of the low-lying S_1 state. The RASSCF/RASPT2 calculations give an electronic state with the same symmetry as S_2 but lying well above S_2; however, previous multireference DFT calculations[120] have shown that the relative position of the electronic states in Cars strongly depend on the geometry through variations in the bond length alternation. It is thus possible that geometrical fluctuations and/or distortions can bring the X state down below the bright one.

Having analyzed the contributions of the two pigments separately, in Figure 1.8 we report a comparison between the computed Car-Q_x coupled map and the experimental spectrum at early t_2 time ($t_2 = 22$ fs).

At this short time, the Car region is expected to be dominated by the S_2 state and higher-energy states reached from it. However, some features due to the dark S_1 state cannot be excluded, as assuming an internal conversion process 100-150 fs long, S_1 can still be populated from S_2. Indeed, we note that the negative signals at the red side of the S_2 bleaching, absent in the $t_2 \to 0$ extrapolated map, and rapidly increasing at larger t_2 times, are likely due to the ESA from both S_2 and S_1. As in our calculations the internal conversion to S_1 is not allowed and both $S_{1 \to n}$ and $S_{2 \to n}$ ESA signals are not included, these negative signals are completely absent. Because these negative signals lower the intensity and modify the shape of the positive S_2 SE, a much more intense and less red-shifted signal is present in the calculated map (see Figure 1.8). We also observe that the negative signal at increasing excitation wavelengths also contains pure S_2 contributions, since a similar feature also appears in the Car-only simulated map (Figure 1.7a).

As previously commented for the linear spectra, the relative intensity of the Q_x band with respect to the Car S_2 is weaker in the computed maps compared to the
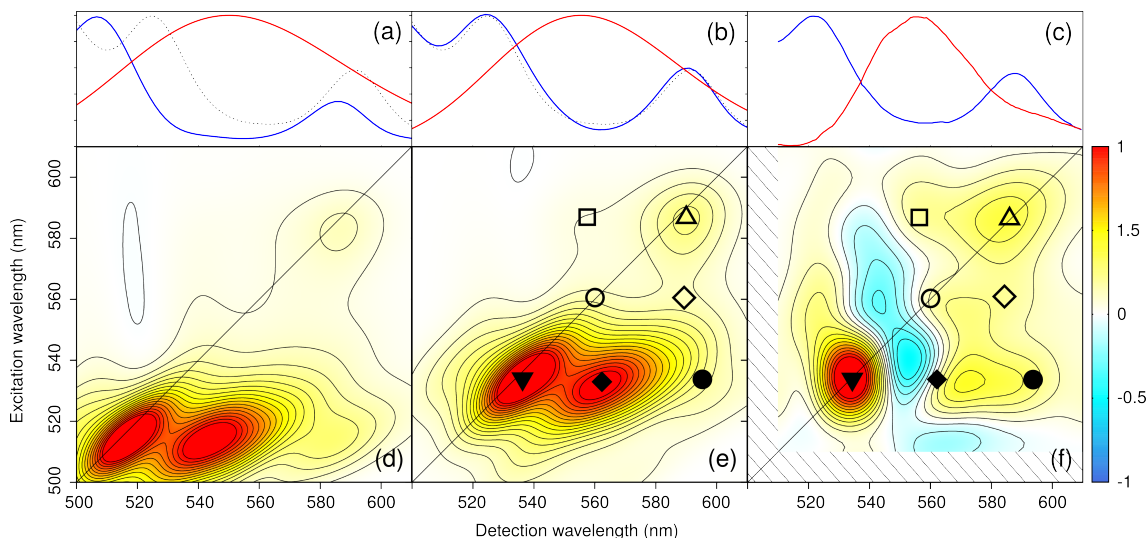
Figure 1.8: Comparison of simulated (d,e) and experimental[97] (f) 2DES pump-probe maps of *Rps. acidophila* at 300 K and waiting time $t_2 = 22$ fs. The corresponding linear absorptions (blue) and pulse shapes (red), along with the relative experimental linear spectra (dashed line),[97] are reported in (a), (b) and (c), respectively. In the calculated maps the pulse shape was adapted to have the same overlap between pulses and absorption bands as the one reported in the experiments. Panel (e) refers to a calculated map where Car S_2 site energies and Q_x transition dipoles have been scaled to match the position and the intensities measured in the linear spectrum. Simulated maps are normalized to their maximum. By convention, bleach and stimulated emission contributions appear as positive (red) signals, excited state absorption appears as negative (blue) peaks. The geometric symbols represent the same peaks as in Figure 1.7.

experiment. This difference is even more pronounced in the 2D (Figure 1.8d) due to the multiple interactions between light and the transition dipole moments of the molecules, which characterize this technique. Moreover, the calculated gap between S_2 and Q_x states is slightly too large, leading to a too small spectral overlap between these two signals. To check the effects of these deviations, we have recalculated the 2D map by introducing two corrections: (i) we have introduced a scaling of the Q_x transition dipoles so to match the relative absorption intensities of the experimental linear spectrum and (ii) we have separately red-shifted the Car S_2 and the BChl Q_x site energies so to match the corresponding measured peaks in the linear spectrum (see the linear spectra reported in Figure 1.8).

The comparison between the corrected (Figure 1.8e) and the original calculated 2D maps shows that the main features are fully preserved, telling us that the method used provides a robust description. This is further confirmed by the analysis of the calculated rates of $S_2 \rightarrow Q_x$ energy transfer, obtained applying the Förster theory. These transfers can be separated into three channels, that is, from Car to

B800, B850α, and B850β, respectively. The fastest energy transfer occurs to the Q$_x$ state of BChl B850α, which is the most strongly coupled to S_2 (175 cm^{-1} from our calculations).[27] Its EET rate is predicted to be around 140 fs^{-1} (or 110 fs^{-1} if we use the corrected energies). We predict slower EET rates to B800 and B850β, around 1 ps^{-1}. The resulting S_2 depopulation time for EET to Q$_x$ states is ~120 fs (or 90 fs with the corrected energies). Assuming that the $S_2 \rightarrow S_1$ internal conversion rate of the Car is 130 fs^{-1},[121, 122] we estimate a 59% efficiency of energy transfer from the Car to the Q$_x$ states, and a 48% efficiency of EET to B850α alone. These results are in good agreement with several experiments,[121, 123] and in particular with the rates estimated from fluorescence upconversion and coupling calculations.[124] Our calculations predict that the Q$_x$ state of B850α is the main energy acceptor from S_2.

1.4   Conclusions

Numerous quantum chemical approaches have been employed to describe LH complexes through excitonic models (for a recent review see ref. 125). However, the majority of these theoretical investigations concerned linear absorption spectra with very rare extensions to 2DES spectra.[83, 82] Furthermore, due to the large size of the multichromophoric aggregate of LH complexes, and the very heterogeneous composition of the embedding, rather approximate QM methods (mostly of semiempirical nature) and/or simplified descriptions of the environment have been generally used. Indeed, the application of ab initio methods have been mostly limited to benchmark studies on the electronic properties of single pigments.[91]

Here, for the first time, the simulation of linear and 2DES spectra of LH2 over the entire Car-Q$_x$ plus Q$_y$ VIS-NIR region has been presented by integrating quantum-chemistry and electron-phonon exciton models. Single and multireference QM methods have been combined with electrostatic and polarizable classical embeddings to properly account for the effect of the protein in all the steps of the simulation. On the one hand, TD-DFT/MMPol computations have been proved to achieve a refined description of the effect of the environment in the Q$_y$ region via a precise reproduction of the B800-B850 bands splitting. On the other hand, the multiconfigurational multireference RASSCF/RASPT2/MM approach provides an accurate description of the Car-Q$_x$ region. All these data were used as input parameters for the construction of exciton Hamiltonians able to describe the manifold of states of the LH2 complex.

In particular, we have shown that, in addition to the molecular components and

the accurate description of the environment effects, the modeling of 2D maps must include the pulse envelopes in order to achieve a reliable and complete comparison with experiment. Most importantly, the possibility of artificially switching on and off interactions among the different components of the multichromophoric systems, provides a unique tool for interpreting the origin of the different signals which overlap in the highly congested experimental spectrum. This analysis is especially effective in the Car-Q_x region, where we have given a possible interpretation of the main features of the very-short time 2DES spectrum in terms of the bright S_2 and Q_x vibronic progression of Car and BChl, respectively. By combining these results with those obtained from a global target analysis applied to 2DES data,[119] we have reviewed several observed signals and reinforced the hypothesis that a contribution coming from a dark state of the carotenoid lying in between the S_2 and the Q_x is likely to be present; if this is an additional electronic state (the previously suggested X state) or a high-energy vibrational level of the S_1 is still an open question that calls for further investigation.

We have further shown that the integration of multiscale models and experiments is crucial: only by combining the "independent" results from accurate quantum chemical based methods and detailed 2DES experiments, the complex network of energy transfer routes in LH2 (and in other LH systems) can be definitely revealed. To do that, however, two important improvements are still needed in the theoretical strategy. The ESA signals of Cars, in particular those from S_1, which become increasingly important for longer waiting time, have to be explicitly included to follow the system evolution and simulate time resolved 2D maps. Moreover, a detailed account of possible geometrical distortions of the pigments (especially the Cars) due to temperature-dependent fluctuations of the protein is necessary, as this mechanism could affect the relative energy and the nature of the excited states involved in the excitons and in the energy transfer processes.

1.5   Appendix - LH2

1.5.1   Structure preparation

For all calculations, we employed the crystal structure of LH2 (PDB code: 1NKZ) resolved at 2.0 Å[101]. This structure only contains a third of the whole complex, and the three monomeric units explicitly contained in the PDB file are not identical. To ensure a C_9 symmetry, we considered only one monomer, which was replicated over the symmetry axis.

Hydrogen atoms were added by using the *LeAP* module of AmberTools,[126] considering all the titrable residues in their standard protonation state. All Histidine residues were kept in the ϵ configuration except the ones axially coordinated with the B850 BChls. The positions of the hydrogen atoms were then relaxed at MM level using Amber14.[126] In all calculations, the phytyl tail of the BChl molecule was truncated at the CAA–CBA bond, and assigned to the classical part. The crystal structure of the Car molecule was refined optimizing the bond lengths at the B3LYP/6-31G(d) level.

1.5.2   Exciton Model

The multichomophoric system is described in terms of an exciton Hamiltonian, as described in the main text. The approximation made by separating the LH2 Hamiltonian into two blocks for the Q_y region and the carotenoid/Q_x region is justified by the large energy difference between the two excited state manifolds.

We used the following charges for QM/MM calculations: the Amber ff99SB[127] force field for the protein, literature parameters for BChls,[128] and for the Cars an approach recently developed in our group using a TD-DFT based strategy [129]. For the QM/MMPol calculations, isotropic polarizabilities and charges of the protein were taken from the literature.[130] For the pigments, atomic MMPol charges were fitted self consistently with the atomic polarizabilities according to the dipole interaction model adopted.[131] A cutoff of 12 Å from the atoms of the QM pigment was used to define the polarizable MM region.

Site energies and couplings were computed in the environment of GS charges (and also polarizabilities in QM/MMPol calculations) of both the protein and the other molecules. The use of GS charges for all the terms of the exciton hamiltonian is here justified as the GS and ES permanent dipoles of the states of interest have been found to be very similar.

As stated in the main text, we also made use of the exciton Hamiltonian obtained

along a molecular dynamics trajectory in order to calculate the spectra at 300 K temperature. We have previously shown[93] that the exciton Hamiltonian of LH2 depends on temperature, in particular as regards the nearest-neighbor B850 exciton couplings, in agreement with excitation anisotropy data.[107]

1.5.3   Linear and non-linear spectra

The two spectral regions investigated in this work contain contributions from transitions of different nature. The near-IR characteristic signal arises from the excitonic nature of Q_y states. It is well established that the B850 BChls are strongly coupled, whereas the B800 BChls are more weakly coupled. There is a non negligible interaction between the two rings.

We employed the disordered exciton model with both sR and mR theories to describe exciton relaxation within the Q_y band. The applicability of second-order transport theories to light-harvesting antennae has been questioned. The state-of-the-art hierarchical equations of motion (HEOM) method should properly describe the exciton dynamics regardless of the relative strength of exciton coupling and exciton-phonon coupling. However, for systems with large number of states, like the LH2 manifold of 27 Q_y states, the HEOM approach is too computationally expensive. Redfield theory, which describes the strong exciton coupling limit, is suitable for the strongly coupled excitations within the B850 ring, but the B800 ring calls for more caution. A benchmark study of a disordered B800 ring (in C_8 symmetry), conducted by Novoderezhkin and Van Grondelle, showed that the modified Redfield results agree with the numerically exact HEOM method,[89] at least in the description of linear spectra. The disordered exciton method with modified Redfield (mR) theory has also been successfully employed to describe spectra and dynamics of the B850 ring.[132, 133] More recently, the whole Q_y sector of the LH2 system has been studied with standard Redfield (sR) theory to describe the temperature dependence of 2DES spectra at zero population time.[80] The short-time dynamics needed for these maps justified the use of Redfield theory.

Static disorder was modeled by allowing random Gaussian uncorrelated fluctuations of the site energies (See Table 1.2). Spectra were averaged over the static disorder by increasing the number of samples N until convergence of the spectral features. In particular N was set to 500(1000) for T=77 K Q_y 2D maps(linear spectra), 250(1000) for room temperature Q_y 2D maps(linear spectra). For each realization of the disorder, the Exciton Hamiltonian of Eq (1.1) is diagonalized, obtaining exciton energies E_n and exciton coefficients C_j^n for every state $|n\rangle$. The intra and inter-band downhill relaxation rates were analyzed along the disorder realizations

by assigning the exciton states to either the B800 or the B850 ring on the basis of the wavefunction amplitude $|C_j^n|^2$.

The Car-Q_x manifold of states comprises the S_2 bright states of 9 Car molecules, plus the Q_x states of the 27 BChls. An analysis of the energy scales in play in this manifold shows that the excitations should be rather localized in this manifold: in fact, Car-Car couplings ($\lesssim 60$ cm^{-1}, see Table 1.7) are much smaller than the Car's reorganization energy (~ 1700 cm^{-1}, Table 1.2), and the Car/Q_x site energy difference ($\gtrsim 3000$ cm^{-1}) prevents the delocalization between Car and Q_x states. The dynamics within the Car-Q_x region was described by Förster theory, taking into account the presence of static disorder by averaging the optical properties over a Gaussian distribution of site energies.[134] For every realization of the static disorder (see Table 1.2) a different spectral overlap is obtained for every pair of pigments. We stress the fact that a different relative positioning of the computed transitions (the S_2 for the Car and the Q_x for the BChls), with respect to the experimental ones, may result in a different magnitude of the computed and experimental rates. The total relaxation rate for every pigment contributes to the homogeneous broadening of linear and non-linear spectra. 2DES maps were computed at room temperature from an average of 200 realizations (maps converge after 100 realizations).

Unless otherwise noted, we report the real (absorptive) part of 2DES simulated maps; by convention, bleach and stimulated emission contributions appear as positive (red) signals, excited state absorptions appear as negative (blue) peaks.

For all simulations we used a non-chiral $xxxx$ pulse polarization sequence. We have accounted for the real shapes (finite frequency width and fixed center position) of the laser pulses by weighting the calculated 2D maps with experimental-like laser spectrum envelopes. These envelopes were reproduced with a skewed Gaussian function. The calculated third-order response in the frequency domain was multiplied by the (real) laser pulse shape envelope $\mathbb{E}(\omega)$ along the ω_1 and ω_3 axes in order to simulate the detected signal, as

$$S_{PS}^{(3)}(\omega_3, t_2, \omega_1) = S^{(3)}(\omega_3, t_2, \omega_1)\mathbb{E}(\omega_1)\mathbb{E}(\omega_3) \tag{1.2}$$

1.5.4 Spectral densities and static disorder

Spectral densities of the exciton-phonon coupling have usually been computed with the vertical gradient approach of ref. 28 (Part I, Section 3.1.4), described in previous parts of the Thesis.

The spectral densities (SD) of the different transitions were modeled as a sum

of one overdamped Brownian oscillator[30] and M discrete contributions:

$$C_j(\omega) = 2\lambda_{c,j} \frac{\omega/\gamma_{c,j}}{(\omega/\gamma_{c,j})^2 + 1} + \sum_{m=0}^{M} S_{m,j}\,\omega_{m,j}\,\frac{\omega\gamma_{m,j}}{(\omega - \omega_{m,j})^2 + \gamma_d^2} \qquad (1.3)$$

where j indicates the transition of interest (BChl B800, B850α, B850β, or Car), m runs on the vibrational modes of the pigment, λ_c is the continuous contribution to the reorganization energy, and γ_c is the damping parameter of the overdamped Brownian oscillator. Finally, $\omega_{m,j}$ and $S_{m,j}$ are the frequency and Huang-Rhys factor of mode m and transition j. γ_d is the damping parameter for discrete modes, which was set to 5 cm^{-1}. The total reorganization energy is then given by:

$$\lambda_j = \int_0^\infty \frac{C_j(\omega)}{\pi\omega}\,\mathrm{d}\omega = \lambda_{c,j} + \sum_{m=0}^{M} S_{m,j}\,\omega_{m,j} \qquad (1.4)$$

| Pigment (Tr.) | λ_d | T = 77 K | | | | T = 300 K | | | |
		σ	γ_c	λ_c	λ_{tot}	σ	γ_c	λ_c	λ_{tot}
B850α (Q$_\text{y}$)	143	250	100	80	223	250	100	280	423
B850β (Q$_\text{y}$)	165	250	100	80	245	250	100	280	445
B800 (Q$_\text{y}$)	139	60	100	80	219	40	100	50	189
BChl (Q$_\text{x}$)	331	150	100	120	451	50	100	120	451
RGT (S$_2$)	1430	300	25	300	1730	220	25	300	1730

Table 1.2: Parameters of the static and dynamic disorder used in this work. Parameter λ_d is the (calculated) discrete contribution to the reorganization energy (second term of the rhs of Eq. 1.4), λ_{tot} is the total reorganization energy. The standard deviation of the static disorder on site energies is denoted as σ. All values are in cm^{-1}.

The discrete part of the SD was determined from a normal mode analysis[28] of the pigments in the crystal structure, employing the following procedure: the geometry of every pigment was first relaxed to the ground state minimum using a QM/MM ONIOM scheme[135] with frozen MM environment, followed by frequency calculations. The Huang-Rhys factor $S_{m,j}$ of each mode m was computed by projecting the gradient of the excited state j on the ground-state normal mode m.[28] All calculations were performed at the (TD)B3LYP/6-31G(d):AMBER level of theory.

The reorganization energies for the discrete and continuous parts of the spectral densities are reported in Table 1.2. The spectral densities used in this work for all chromophores are shown in Figure 1.9 and 1.10.

The width of static disorder for the Q$_\text{y}$ region was taken from ref. 80 and adapted to the calculated exciton Hamiltonian, which is clearly different from that of ref. 80.
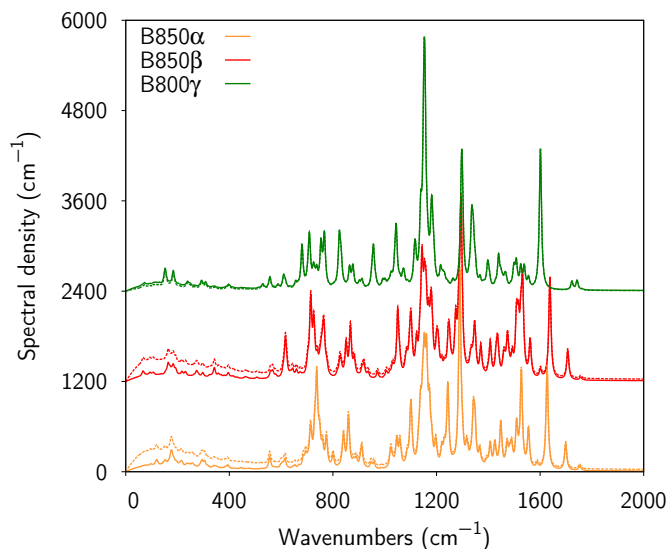
Figure 1.9: Spectral densities of the BChl's Q_y transitions. Different colors refer to different BChls. The solid lines refer to the spectral densities used for 77 K simulations, whereas the dashed lines refer to the 300 K ones.

The parameters were adapted to reproduce the broadening of the linear absorption peaks. These parameters are also similar to those used by Scholes and Fleming within Generalized Förster theory.[136]

We note that the whole Hamiltonian is temperature-dependent,[93] and our disorder parameters should be differently tuned for the 77 K and 300 K spectra. The continuous part of the spectral density is not constrained to be independent of temperature, as this part represents the many anharmonic, low-frequency modes of the protein and the solvent, which can depend on temperature. Indeed, this possibility was previously invoked in order to model 2DES spectra of LH2 at different temperatures.[80]

1.5.5   RASSCF/RASPT2 details

RASSCF calculations were performed within a State Average (SA) approach followed by Single State (SS) or Multi State (MS) RASPT2 perturbative corrections. An IPEA shift of 0.0 a.u.[137] and an imaginary shift of 0.2 a.u.[138] were used. The environment was included as an electrostatic embedding of fixed point charges, as outlined in the main text. All these quantum-mechanical calculations were carried out with software package MOLCAS version 8.1.[10]. All calculations employed a 6-31G* basis set.

A similar multi-configurational multi-reference quantum chemical approach, which make use of a SA-RASSCF/RASPT2 computational scheme, was recently proposed
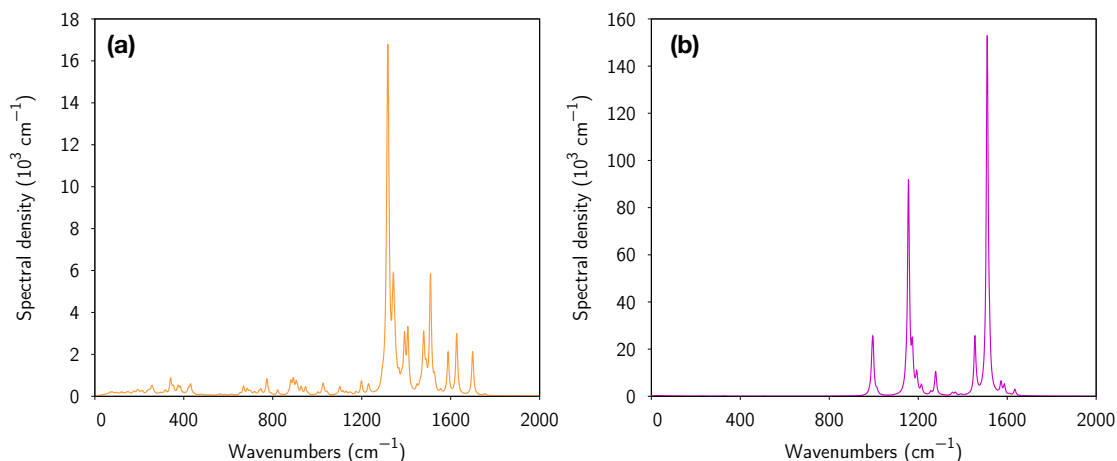
Figure 1.10: (a) Spectral density of the Q_x transition of BChl B850α; (b) Spectral density of the Car's S2 transition.

by De Vico et al.[91] In the Q_y region we used a SA-2 RASSCF$(2, 11|4, 4|2, 9)$/MS-RASPT2 approach, with an AS composed by all the π orbitals of the macrocycle ring. We observed that MS-RASPT2 computations introduce negligible corrections with respect to SS-RASPT2 for these two roots.

In the Car-Q_x region we used a SA-15 RASSCF$(2, 10|4, 4|2, 10)$/SS-RASPT2 approach for the Car, and a SA-5 RASSCF$(2, 11|4, 4|2, 9)$/MS-RASPT2 approach for the BChls. BChls RASSCF roots 3 and 4 appear heavily mixed (e.g., 29% of H $\rightarrow$ L+1 and 34% of 2H $\rightarrow$ 2L for root 3 and 26% of H $\rightarrow$ L+1 and 29% of 2H $\rightarrow$ 2L for root 4 in B850α). Therefore, a MS-RASPT2 procedure was used on these roots to produce correct energy values and compute corresponding transition dipoles and transition densities. Since BChls SA-5 RASSCF/SS-RASPT2 roots 1 and 2 returns the same energy values we found for SA-2 (MS- and SS-RASPT2, see discussion above for the Q_y region) we did not include them in the MS-PT2 procedure.

The transition densities (needed for the computation of the couplings between the chromophores) were computed combining the cubes of the Active Orbitals, $\varphi_i(\boldsymbol{r})$, with the transition density matrices of the RAS orbitals, $C_{ij}(\boldsymbol{r})$, and both quantities were obtained using Molcas 8.1 as outlined in Part I of the Thesis.

Table 1.3 and Table 1.4 summarize the properties of low lying excited states in BChls and CAR.

Table 1.3: Q_y Region: properties of BChls ground and first excited state (Q_y) by the SA-2 RASSCF$(2, 11|4, 4|2, 9)$/MS-RASPT2 calculations in the chromophores electrostatic embedding. Only configurations with weight larger than 5% were included.

Chromophore	Root (State)	ΔE^a_{RASPT2}	f^b_{0-1}	Configuration[a]	Weight[a]
B850α	*Root* 1 (GS)	0	-	SCF-GS	65.7%
	Root 2 (Q_y)	12533	0.38	H $\rightarrow$ L	59.2%
				H-1 $\rightarrow$ L+1	8.4%
B850β	*Root* 1 (GS)	0	-	SCF-GS	51.8%
				H $\rightarrow$ L	23.6%
	Root 2 (Q_y)	12279	0.45	SCF-GS	22.9%
				H $\rightarrow$ L	51.8%
B800	*Root* 1 (GS)	0	-	SCF-GS	59.1%
				H $\rightarrow$ L	13.2%
	Root 2 (Q_y)	12503	0.40	SCF-GS	12.6%
				H $\rightarrow$ L	55.4%
				H-1 $\rightarrow$ L+1	5.5%

[a] From MS-RASPT2 computations (energies are in cm^{-1});

[b] f_{0-1} oscillator strengths are obtained by use of RASPT2 energies;

Table 1.4: Car-Q_x Region: properties of the BChls and Cars lowest excited states by, respectively, the SA-5 RASSCF$(2, 11|4, 4|2, 9)$/MS-RASPT2 and SA-15 RASSCF$(2, 10|4, 4|2, 10)$/SS-RASPT2 calculations in the chromophores electrostatic embedding. Only configurations with weight larger than 5% were included.

Chromophore	Root (State)	ΔE^a_{RASPT2}	f^b_{0-n}	Configuration[c]	Weight[c]
B850α	Root 1 (GS)	0	-	SCF-GS	68.3%
	Root 2 (Q_y)	12366	0.40	H → L	61.2%
				H-1 → L+1	8.4%
	Root 3 (Q_x)	17300	0.12	H → L+1	11.8%
				H-1 → L	53.3%
	Root 4	20795	0.00	2H → 2L	59%
B850β	Root 1 (GS)	0	-	SCF-GS	52.4%
				H → L	20.2%
	Root 2 (Q_y)	12577	0.39	SCF-GS	17.9%
				H → L	51.1%
	Root 3 (Q_x)	16699	0.03	H → L+1	18.3%
				H-1 → L	24.6%
				2H → 2L	23.9%
	Root 4	20967	0.09	H-1 → L	20%
				2H → 2L	38%
B800	Root 1 (GS)	0	-	SCF-GS	69.1%
	Root 2 (Q_y)	12104	0.41	H → L	61.3%
				H-1 → L+1	6.7%
	Root 3 (Q_x)	17432	0.13	H → L+1	6.6%
				H-1 → L	51.8%
				H-1,H → L	11.3%
	Root 4	19204	0.00	2H → 2L	59%
CAR	Root 1 (GS)	0	-	SCF-GS	65.3%
	Root 2 (S1)	21112	0.00	H → L+1	13.8%
				H-1 → L	17.6%
				2H → 2L	29.1%
	Root 3 (S2)	21039	2.77	H → L	65.4%

[a] E_{RASPT2} energies (in cm^{-1}) are SS-RASPT2 for roots 1 and 2 and MS-RASPT2 for roots 3 and 4;

[b] f_{0-1} oscillator strengths are obtained by use of RASPT2 energies;

[c] Roots 1 and 2 from SS-RASPT2 computations, while roots 3 and 4 from MS-RASPT2.

We hereafter report a plot of the orbitals included in the Active Space for the SA-2 B850α and for the CAR. The B850β and B800 Active Space orbitals (both with SA-2 and SA-5) are similar.
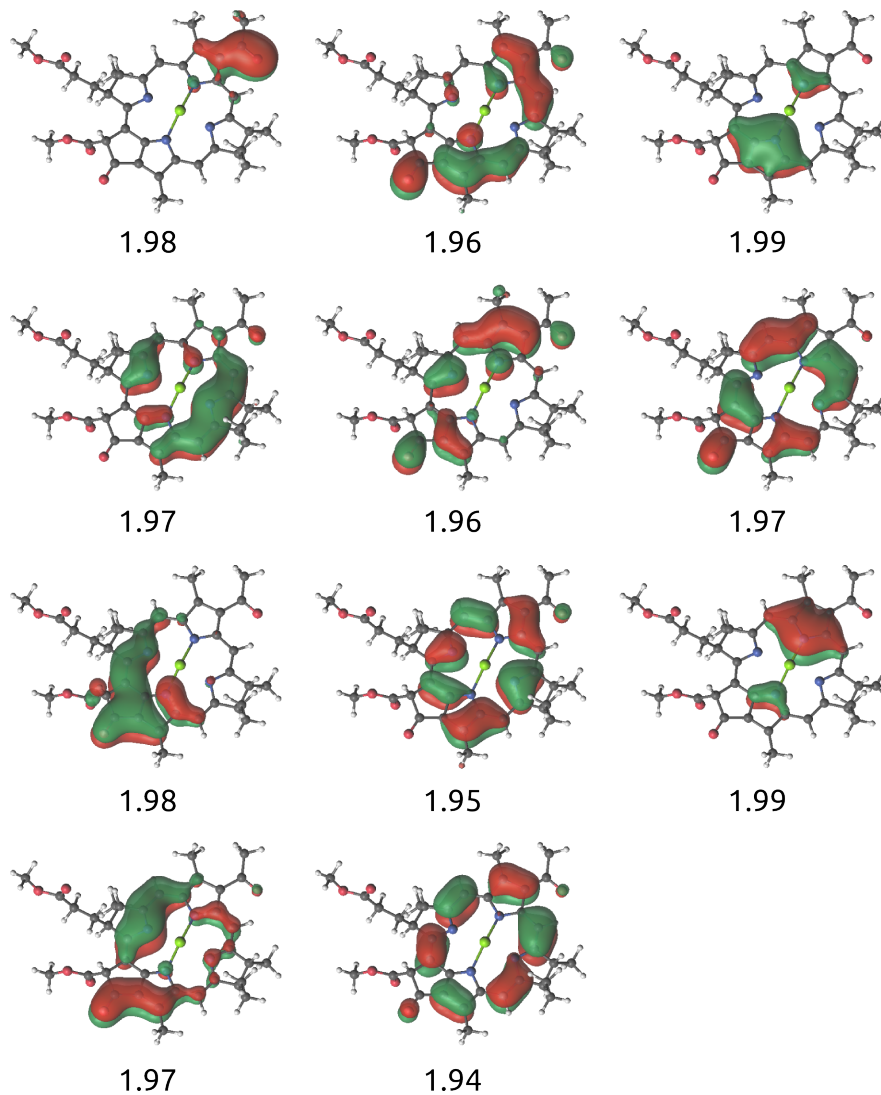
Figure 1.11: RAS1 of BChl α. Average occupancy is reported below each orbital.
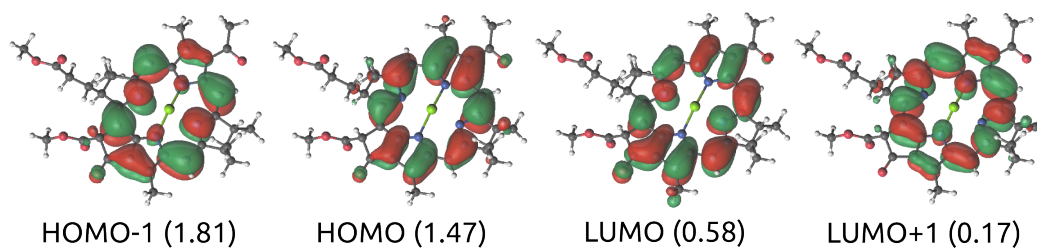
Figure 1.12: RAS2 of BChl α. Average occupancy is reported below each orbital.
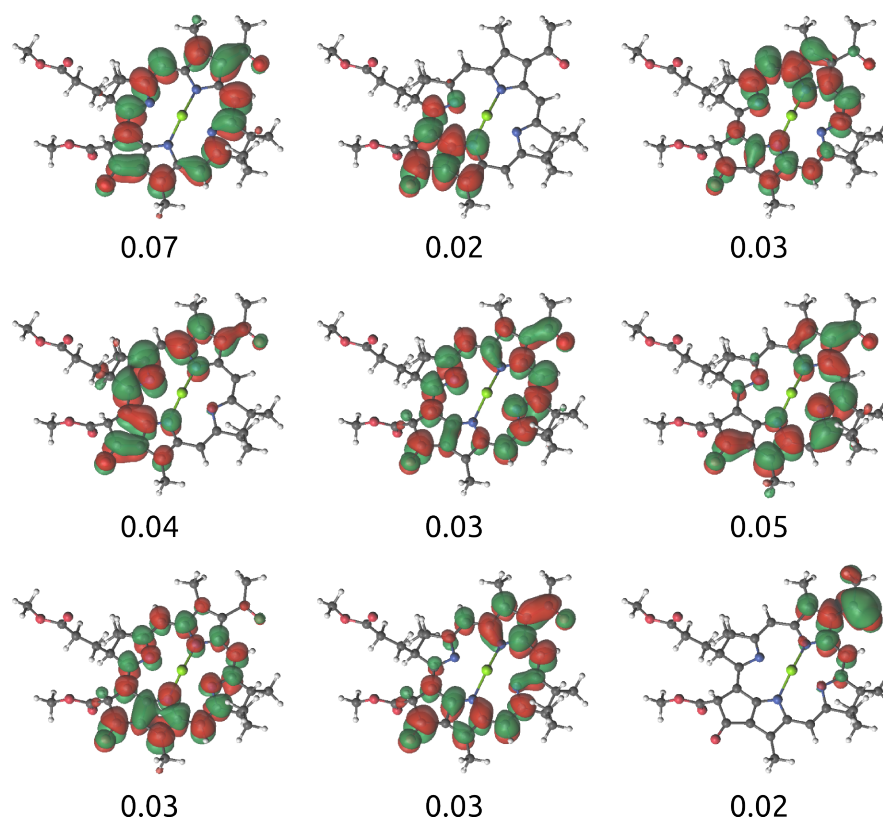
Figure 1.13: RAS3 of BChl α. Average occupancy is reported below each orbital.
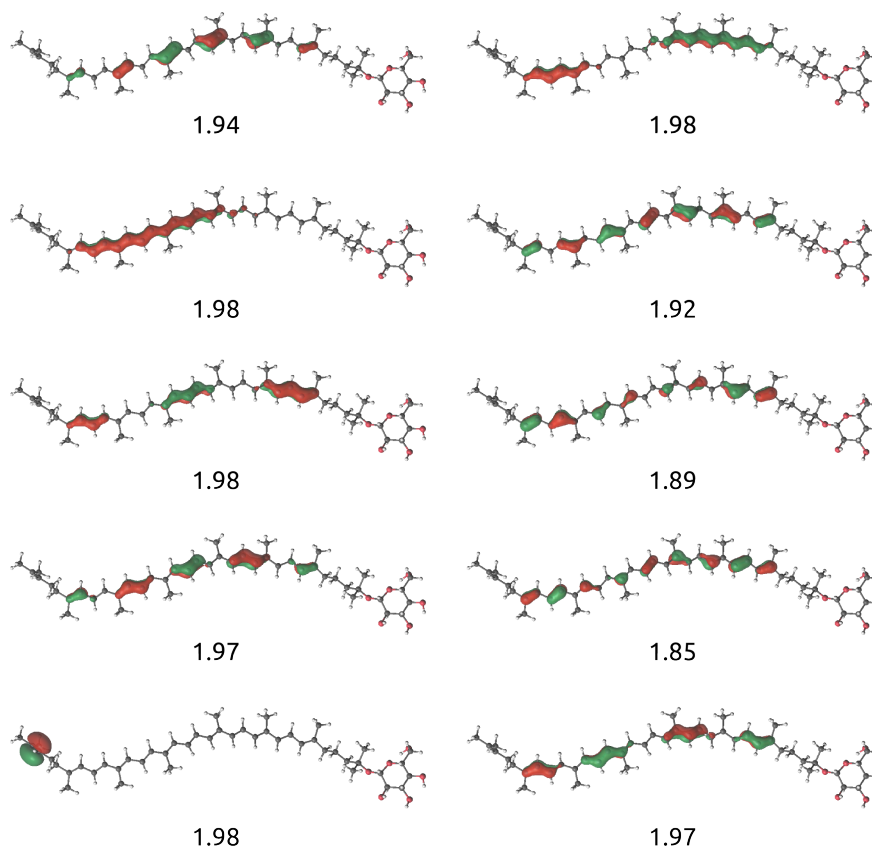
Figure 1.14: RAS1 of Car. Average occupancy is reported below each orbital.
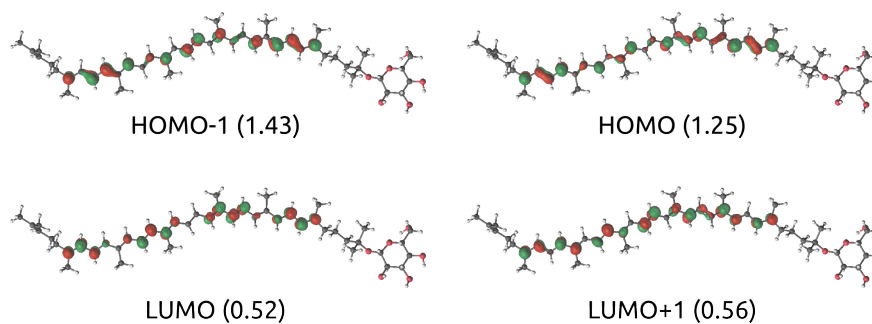
Figure 1.15: RAS2 of Car. Average occupancy is reported below each orbital.

0.14

0.10

0.03

0.07

0.04

0.03

0.02

0.02

0.02

0.02
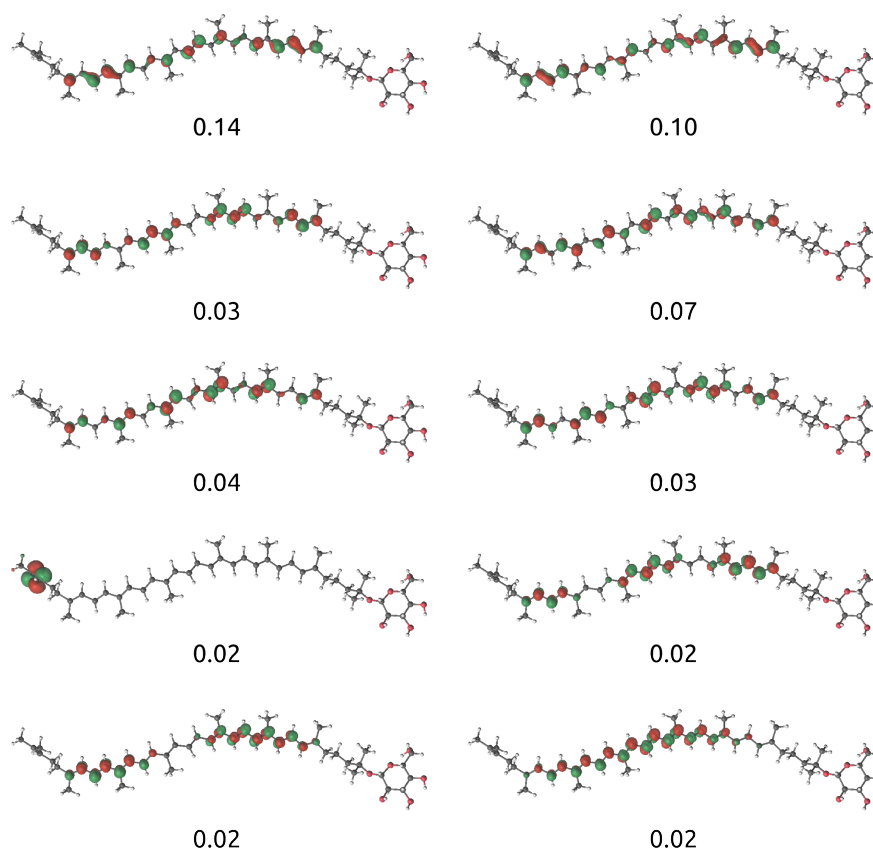
Figure 1.16: RAS3 of Car. Average occupancy is reported below each orbital.

1.5.6   Definition of couplings

In Figure 1.17 we define the main couplings across the LH2 system.
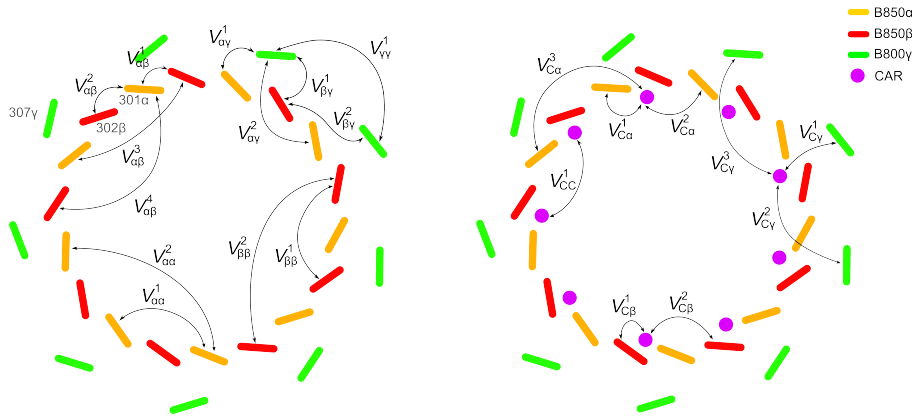
Figure 1.17: Electronic coupling definition. BChls are highlighted using the following color code: yellow for B850-α, red for B850-β, green for B800-γ. The Car is highlighted in purple. The superscript ranks proximity according to center–center distance. Note that the system has a C9 symmetry and the labels for equivalent coupling terms are reported only once. Couplings smaller than 5 cm^{-1} are not indicated. Left: couplings involving BChls only. Right: couplings involving the Car.

1.5.7   Q$_y$ region

The exciton Hamiltonians for the Q$_y$ region calculated with the two alternative strategies (namely RASSCF combined with an electrostatic embedding and TD-DFT combined with a polarizable embedding) is detailed in Table 1.5. Here we only show couplings larger than 5 cm^{-1}, even though all couplings were considered in spectra calculations. The couplings are defined in Figure 1.17.

Relaxation rates   The downhill relaxation rates among the Q$_y$ region excitons of LH2 were analyzed for over 10 000 realizations of static disorder site energy distributions, for the full LH2 Q$_y$ Hamiltonian and for a Hamiltonian in which the inter-ring couplings are all set to zero. For each realization of the disorder, the exciton states were assigned to the B800(B850) ring on the basis of the participation of the B800(B850) pigments to the exciton state. The average of 10 000 realizations is shown in Table 1.6 as a relaxation time. We show the average of all B800 $\rightarrow$ B800, B800 $\rightarrow$ B850, and B850 $\rightarrow$ B850 transfer rates, along with the average of the maximal rates taken within every realization. Notably, assignment of states is exact when the two rings are completely decoupled, but, in the general case, the excitons could be partially delocalized over the two rings.

Table 1.5: Site energies and couplings (in cm^{-1}) for the Q$_y$ region computed at the three different levels of theory, including the values computed on a MD trajectory at room temperature. [93] The couplings are defined according to Figure 1.17.

		TDDFT MMPol	RASSCF/PT2 MM	TDDFT MM	TDDFT (MD,300K) MMPol
Site energy	B850α	11163	12533	11963	12799
	B850β	11030	12279	11900	12806
	B800γ	11351	12503	12074	13021
Intra-B850	$V^1_{\alpha\beta}$	409	474	288	317
	$V^2_{\alpha\beta}$	362	563	336	339
	$V^3_{\alpha\beta}$	25	26	24	20
	$V^4_{\alpha\beta}$	24	22	23	18
	$V^1_{\alpha\alpha}$	-87	-83	-91	-66
	$V^2_{\alpha\alpha}$	-14	-10	-11	-10
	$V^1_{\beta\beta}$	-59	-69	-63	-51
	$V^2_{\beta\beta}$	<5	8	8	<5
B850-B800	$V^1_{\alpha\gamma}$	59	46	44	42
	$V^2_{\alpha\gamma}$	-20	-22	-19	-16
	$V^1_{\beta\gamma}$	-12	-9	-8	-10
	$V^2_{\beta\gamma}$	-6	-11	-11	-3
Intra-B800	$V^1_{\gamma\gamma}$	-50	-46	-47	-32

The calculated average transfer rates as obtained from the sR and mR models are shown in Table 1.6.

Figure 1.18 shows the statistics of delocalization length, dipole strength, and transfer rates in the three lowest exciton states of LH2, which belong to the B850 ring. The lowest exciton state has a dipole strength that is larger on average than the isolated BChl, and becomes darker the more this state delocalizes over many BChls. The delocalization length, $\sim$8 on average, has a very spread distribution, but remains always larger than 2. The delocalization of the lowest state also gives rise to a larger transfer rate from the second state. The second and third states, which roughly correspond to the $\pm$1 states of a perfect ring, are responsible for the 850 nm absorption peak, showing a dipole strength that is $\sim$6.5 times the single BChl. The relaxation rate between these states is rather low, as expected from the low wavefunction overlap,[132, 133] and lower than the relaxation rate from the fourth state.

	Coupled		Decoupled	
	77 K	300 K	77 K	300 K
Modified Redfield				
B800 → B800	321 (81)	196 (60)	239 (65)	175 (53)
B850 → B850	244 (36)	137 (25)	220 (31)	123 (23)
B800 → B850	1045 (85)	630 (79)	n.a.	n.a.
Redfield				
B800 → B800	317 (100)	168 (64)	227 (73)	142 (56)
B850 → B850	244 (26)	142 (19)	219 (23)	130 (18)
B800 → B850	1032 (79)	670 (65)	n.a.	n.a.

Table 1.6: Average transfer times (in fs) of the LH2 ring. Numbers in parentheses refer to the average of maximum rates taken within every realization. Different columns refer to different Hamiltonians, which can include (Coupled) or not (Decoupled) the inter-ring couplings. The 300 K rates were computed on the Hamiltonian taken from molecular dynamics simulations.[93] Only downhill rates have been considered in this analysis.
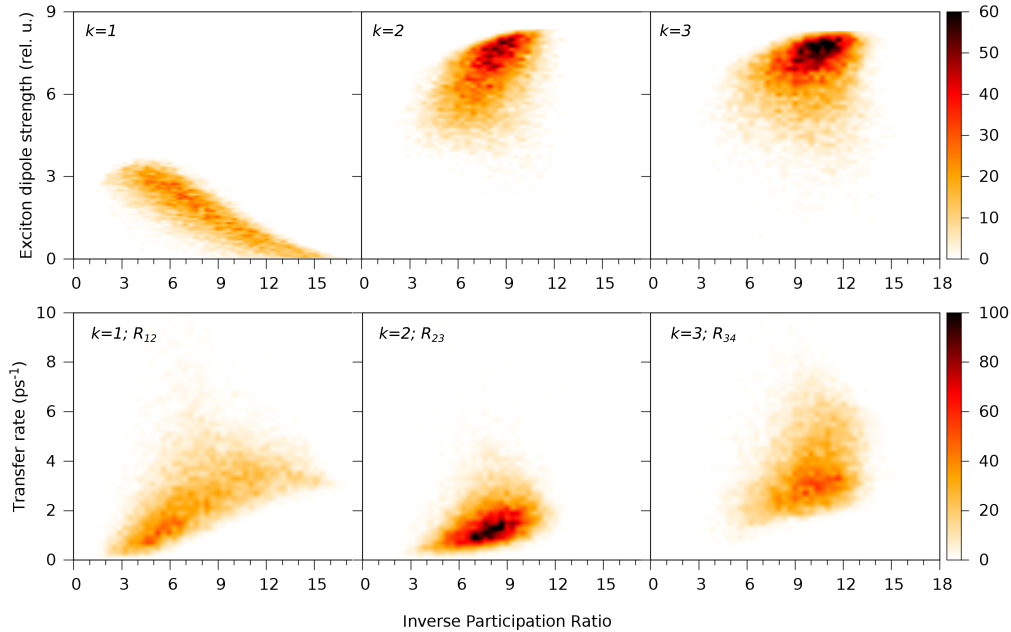
Figure 1.18: Two-dimensional histogram plots of dipole strength and downhill relaxation rate versus the delocalization length measured as inverse participation ratio (IPR). The three lowest exciton states are considered; these states are delocalized across the B850 ring. The top panel depicts the relationship between dipole strength of state k (relative to a single BChl) and the IPR of the same state. The bottom panel depicts the relationship between the downhill transfer rate between two successive states ($R_{k,k+1}$) and the IPR of the lower state k. Results obtained at the TD-DFT level of theory.

Rephasing 2DES Map   We report in Figure 1.19 the calculated absolute value of the rephasing 2DES map of the Q_y region, for comparison with the one measured for *Rb. Sphaeroides.*[111]
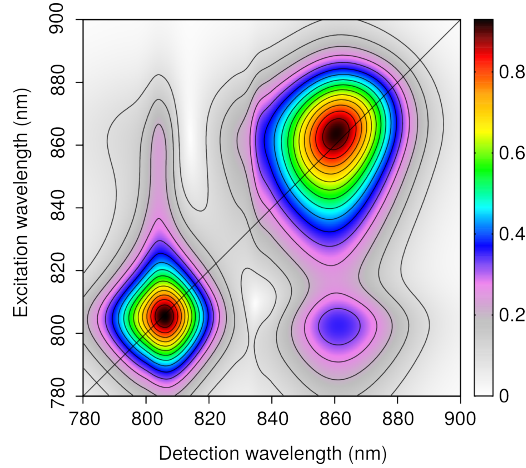
Figure 1.19: Absolute value of the Rephasing 2DES map of the Q_y region, calculated at 300 K and $t_2 = 0$. The color map is adapted for comparison to Ref. 111. The calculated map accounts for the shape of the excitation pulse.[111]

1.5.8   Effect of the pulse shape

In Figure 2.7 we report a comparison between the same map obtained including or not the proper pulse shape.
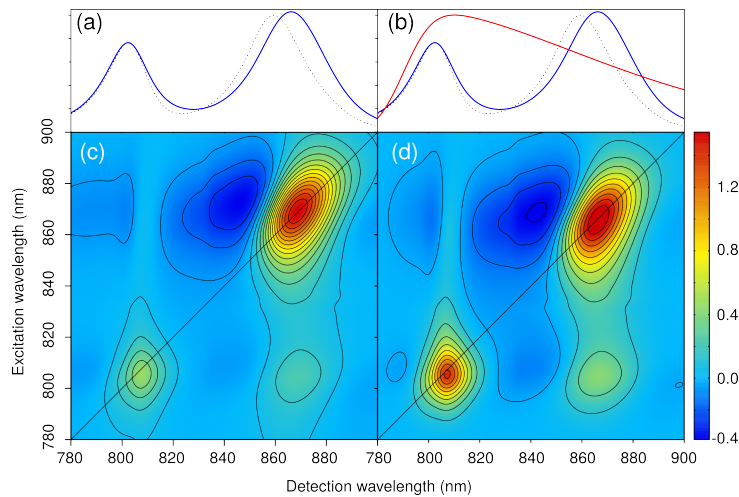
Figure 1.20: Comparison between the simulated 2DES pump-probe maps with (d) and without (c) including the pulse shape. The maps are referred to the Q_y region and they are calculated at zero population time at 300 K using the modified Redfield theory of transport. The corresponding linear absorptions (blue) and pulse shapes (red) are also reported in panels (a) and (b). The color map convention corresponds to the one reported in Figure 3.

1.5.9 Carotenoid-Q_x region

Excitonic Hamiltonian The site energies for the Car-Q_x region, which are computed at the RASSCF/RASPT2/MM level of theory, together with the relevant (non-negligible) couplings, are detailed in 1.7.

Table 1.7: Site energies and couplings (in cm^{-1}) for the Car-Q_x region computed at RASSCF/RASPT2/MM level of theory. The couplings are defined according to Figure 1.17.

		RASSCF/RASPT2/MM
Site energy	Car	21039
	B850α	17300
	B850β	16700
	B800γ	17432
Intra-B850	$V_{\alpha\beta}^1$	26
	$V_{\alpha\beta}^2$	90
	$V_{\alpha\alpha}^1$	14
B850-B800	$V_{\alpha\gamma}^1$	11
	$V_{\alpha\gamma}^2$	7
Intra-B800	$V_{\gamma\gamma}^1$	7
CAR-BChl	$V_{C\alpha}^1$	175
	$V_{C\alpha}^2$	-15
	$V_{C\alpha}^3$	10
	$V_{C\beta}^1$	-24
	$V_{C\beta}^2$	54
	$V_{C\gamma}^1$	63
	$V_{C\gamma}^2$	-42
	$V_{C\gamma}^3$	15
CAR-CAR	V_{CC}^1	57

Analysis of the Q_x 2DES map In Figure 1.21 we report the comparison of 2DES maps obtained for the Q_x region, using the spectral density of Figure S2, and a modified one, in which we have switched off the strong 1300 cm^{-1} mode. The strong quenching of Q_x vibronic signatures in the map, and complete disappearance of the diagonal positive peak after the removal of this mode can be clearly seen.
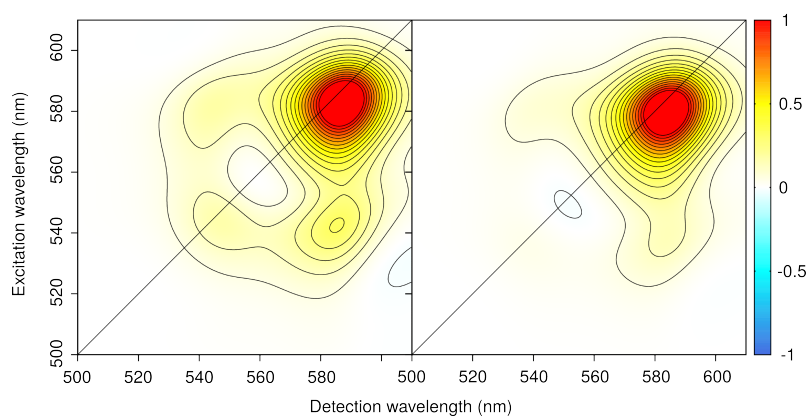
Figure 1.21: Comparison of the Q_x 2DES map including and excluding the normal mode around 1300 cm^{-1}. (a) same map as Figure 6c. (b) 2DES map with modified spectral density, where the intense mode around 1300 cm^{-1} is removed and consequently the Q_x vibronic contributions are suppressed.

Two-dimensional Electronic Spectroscopy provides Direct Evidence of Ultrafast Carotenoid to Retinal Energy Transfer in Xanthorhodopsin

The work presented in this Chapter, performed in collaboration with the experimental group of Prof. Giulio Cerullo (Politecnico di Milano, Milano, IT), is in preparation for submission.

2.1 Introduction

Xanthorhodopsin (XR) of the extremely halophilic eubacterium *salinibacter ruber*[139], is a light-driven transmembrane proton pump with two chromophores: an all-trans-retinal (RET), which is responsible for the proton transport function, and a C40 carotenoid (CAR) salinixanthin[140], which acts as a light harvesting antenna. It represents one of the simplest photosynthetic protein complexes for the study of excitation energy transfer: a perfect donor-acceptor pair, with the carotenoid bound to the protein in a 1:1 ratio. The complex excited state structure of the salinixanthin includes the bright S_2 state, responsible for the strong absorption in the blue-green spectral region, and a dark state, S_1, lower in energy and populated via S_2-to-S_1 internal conversion (IC) on a sub-picosecond timescale. The existence of additional dark states (e.g. the so-called S^* state), located between the S_1 and S_2 states, has also been proposed in previous studies.[141, 142] In the protein-bound retinal, the reactive S_1 state is known to undergo an ultrafast isomerization from all-trans to
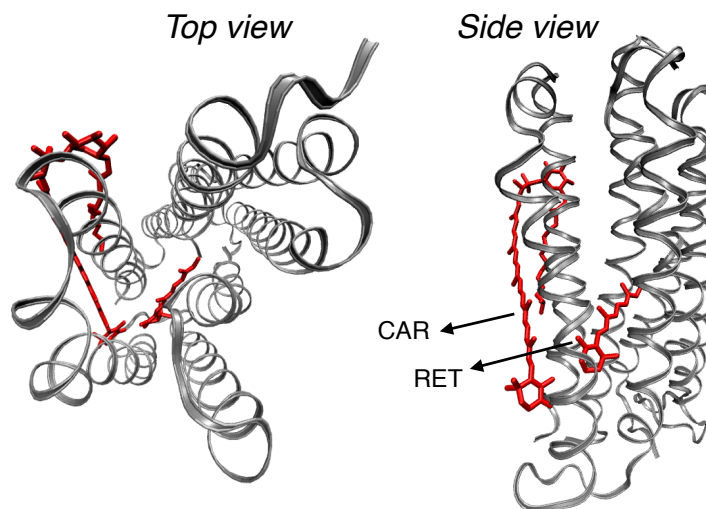
Figure 2.1: Crystal structure of XR (PDB code: 3DDL) resolved at 1.9 Å[144]. Pigments are highlighted in red.

13-cis (see energy level scheme depicted in Figure 2.5a).[143]

The resolved XR crystal structure[144] (Figure 2.1) reveals a 46° angle between the two chromophore molecular axes, and a center to center distance of 11.7 Å. Steady-state spectroscopic studies [145] were performed on both XR system and $NaBH_4$-treated XR, so-called reduced-xanthorhodopsin (RXR). The $NaBH_4$ treatment blue-shifts the absorption energy of the RET, due to hydrogenation of the retinal Schiff base double bond, and prevents energy transfer without perturbing the CAR binding site. In both samples, well-resolved vibronic absorption bands of salinixanthin bound to XR are observed[146] (see Figure 2.2). Action spectra[1] for proton transport[146, 147] as well as fluorescence excitation spectra of the retinal chromophore[145] showed that light absorbed not only by the retinal but also by the carotenoid is employed for function. Quantum yields of emissions and energetic positioning of the chromophore states, indicate that the EET route should proceed from the extremely short-lived CAR S_2 state to the reactive retinal S_1. The efficiency of this process was estimated to be between 30% and 50%,[146, 147, 145] suggesting an ultrafast EET process able to compete with the sub-picosecond CAR $S_2 \rightarrow S_1$ IC. Femtosecond transient absorption (1DPP) studies[148, 149] have been employed to directly investigate the dynamics of CAR $\rightarrow$ RET EET and CAR $S_2 \rightarrow S_1$ IC in XR. These studies provide a further support to the postulated EET pathway as well as an estimate of its rate $((192\pm30 \text{ fs})^{-1}$ [148], $(165\pm25 \text{ fs})^{-1}$ [149],

---

[1]An *action spectrum* correlate the rate of a given process to the wavelength of light that have produced it.

to be compared with the IC rate of $(66 \text{ fs})^{-1}$ [149]). However, overlapping signals from the single chromophoric species (RET and CAR), that further superimpose with the EET signals, lead to congested spectra whose interpretation is not always straightforward.

By spreading the signals along two frequency axes, time resolved two-dimensional electronic spectroscopy (2DES) is the elective technique to both decongest spectra and follow the direct signal of an EET process. This will appear as a cross peak between the two interacting chromophores, whose shape and evolution in time allows to directly probe its dynamics. Support by theoretical modeling is also mandatory to interpret the signals and disentangle the different components observed, specifically when spectrally congested regions persist.

In the present study, we compare experimental two-dimensional electronic spectroscopy of XR and RXR system with simulated CAR maps, aimed at revealing direct signatures of CAR $\rightarrow$ RET EET. We demonstrate that the clear increase of the signal at early times at the CAR-RET cross-peak, is indeed a signature of the EET route from the bright S_2 state of the CAR to the S_1 of the RET. By accounting for all the signals observed, we unravel the different processes that take place after excitation of the CAR moiety, and explain their dynamics. Eventually, and most remarkably, we provide evidence for a vibrationally driven $S_2 \rightarrow S_1$ EET process whose efficiency is controlled and promoted by CAR ground-state vibrational modes.

2.2   Theoretical Modeling

The electronic structure parameters of the S_2 state of the salinixanthin (CAR) moiety in both XR and RXR, were tuned to fit the red side of the experimental RXR absorption spectrum (less affected by the presence of the reduced retinal absorption). The main ingredients of the model include vertical excitation energy, transition dipole moment, and the strong intra-molecular C-C and C=C stretching modes (centered at $1155 cm^{-1}$ and $1520 cm^{-1}$, respectively, in accordance with the Fourier analysis of XR spectral modulations[148]), responsible for the pronounced vibronic structure observed in the linear spectra (Figure 2.2). The lifetime of the Car S_2 state was accounted for, and set to 120 fs in the RXR (matching the $S_2 \rightarrow S_1$ internal conversion rate experimentally observed[149]) and to 60 fs in the XR (assuming a 50% efficiency for both S_2-to-S_1 IC rate and carotenoid-to-retinal EET rate, as suggested by recent pump-probe experiments[149]). Higher energy carotenoid excited states were also included in the model to reproduce the measured excited state absorption (ESA) signals ($S_1 \rightarrow S_{1n}$ and $S^* \rightarrow S_n^*$ transitions), and their parameters
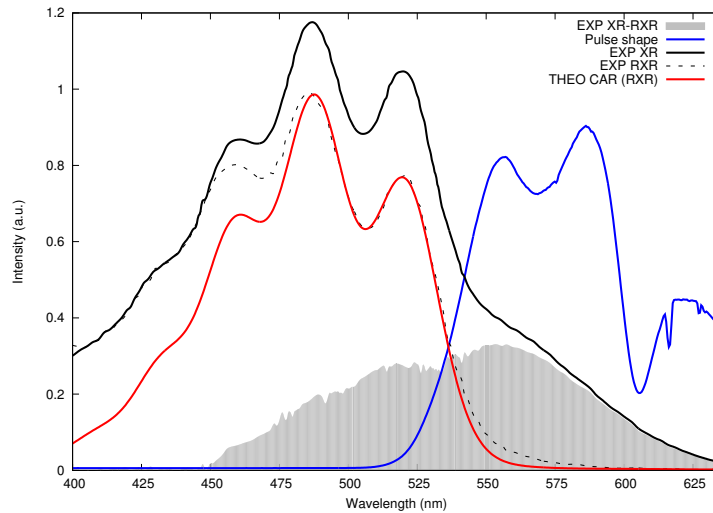
Figure 2.2: Experimental absorption spectra of XR (black solid line) and RXR (dashed line), together with their difference (gray filled curve), which reveals the RET absorption. The theoretical RXR absorption (red solid line) does not contain the reduced retinal contribution in the blue side of the window. The pulse shape (measured upstream of the sample) is also reported (blue solid line). The experimental spectra were adapted from ref. 145.

were fine-tuned to reproduce 2DES cuts at early times. All the model parameters are summarized in Appendix, Tables 2.1 and 2.2. The coupling of all the transitions to the continuum bath was modeled through a spectral density (adapted from ref. 150), and the static disorder of the S_2 excitation energy was introduced. In the simulation of 2DES maps, we have accounted for the finite time duration of the pulses by convoluting the maps (along t_2) with a gaussian function, whose width was determined as the time-width of the pulses (Appendix, Section 2.4.3). A Stokes shift of 240 cm^{-1} for the RXR-CAR and 270 cm^{-1} for the XR-CAR, was applied to the simulated Stimulated Emission (SE) signals, to reproduce the 2DES cuts at early times.

The comparison between experimental absorption spectra of XR and RXR and the theoretical CAR (salinixanthin) curve are shown in Figure 2.2. As previously reported[149, 145], the reduction of the retinal chromophore after treatment with NaBH$_4$, produces a quenching in the absorption from 450 nm to the red side of the spectrum, accompanied by an increase of the absorption below 450 nm. The difference between the XR and the RXR curves (grey filled area of Figure 2.2) therefore reveals, in this region of the spectrum, the retinal contribution to the overall XR absorption. The theoretical RXR absorption spectrum matches the experimental one in the red side of the considered window, while it is considerable less intense in the blue side, where reduced retinal contributions (not accounted for in the model)
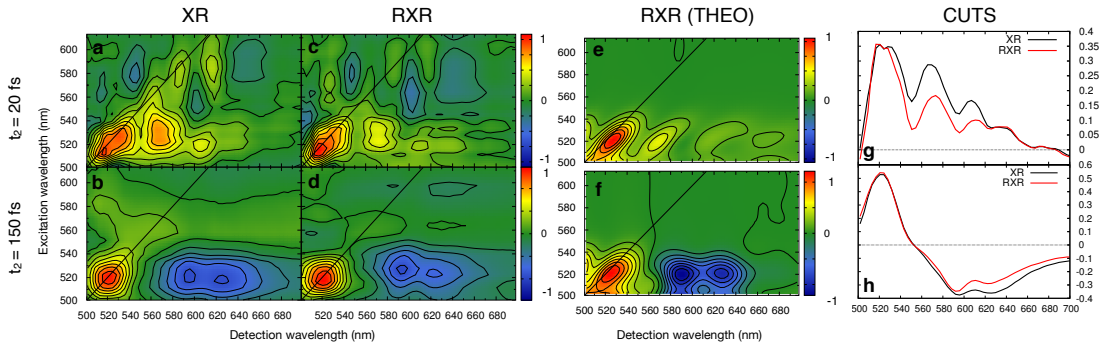
Figure 2.3: Experimental 2DES XR maps (a-b), experimental 2DES RXR maps (c-d), simulated RXR maps (e-f) and cuts of these maps (g-h) at different waiting times. The experimental maps were normalized to a common maximum value at every selected t_2 time. Theoretical maps were also normalized to the max at every t_2. The 2D-cuts (experimental) were taken averaging the signal in the pump rage 515-530 nm.

are present. Note also that the negligible shift of the CAR transitions in XR and RXR indicates that CAR and RET are not forming delocalized exciton states, as they maintain their individuality in both samples. Figure 2.2 also shows the experimental pulse shape employed in the PP measurements, which overlaps only with the tail of the CAR S_2 transition: the impact on the spectra of the finite pulse shape bandwidth is summarized in Appendix, Section 2.4.3.

In Figure 2.3, a sequence of experimental 2DES spectra at different waiting times t_2 for the XR and the RXR samples, together with simulated RXR spectra and 2D cuts comparison of the various maps is presented. In the experiments, the XR and RXR samples concentration was adjusted to have the same absorption at 490 nm. At $t_2 = 20$ fs (first row of Figure 2.3) the main detected signals in both samples are the positive GSB (diagonal peak) and SE (sequence of peaks from the diagonal to the red side of the spectrum) of the salinixanthin S_2 state, as further confirmed by the simulated map (which contains only CAR contributions); the XR sample shows an excess of signal amplitude with respect to the RXR at the Car-Ret cross-peak, directly revealing the presence of the underlying EET.

At t_2 times around $100 - 200$ fs (bottom row in Figure 2.3) we observe the positive salinixanthin S_2 GSB band, which becomes more symmetric, from the initially elongated form, due to spectral diffusion, and the negative salinixanthin S_1 (and S^*) ESA signals, in the interval 550-750 nm, which dominate and cover the carotenoid-retinal cross-peak. The comparison of the 2D cuts (Figure 2.3h) shows an unexpected similarity of the ESA signals intensity in the two samples, even though the RXR salinixanthin S_1 (and S^*) state should have been populated more than the salinixanthin S_1 (and S^*) state in XR, being the IC the unique deactivation

channel in the former system. The apparent contradiction can be explained if one considers that, in XR, hot vibrational states of the salinixanthin GS are populated in the EET process: the subsequent absorption from this vibrationally hot ground state will result in a negative signal that appears red-shifted with respect to the original *cold* salinixanthin ground state absorption (Figure 2.5). This signal superimposes constructively with the negative S_1 ESA, and explains the enhanced intensity of XR features in that spectral region. This mechanism can also explain why we do not observe a decreasing of the carotenoid GSB signal concurrent to EET, which should happen when the original (cold) CAR GS is recovered. The involvement of vibrationally excited GS in salinixanthin, reached from the S_2 state with shorter jumps in energy (and higher probability, due to an increased overlap between nuclear wave-functions in the two PES), can explain the ultrafast nature of the carotenoid-to-retinal EET route in terms of the improved resonant condition between donor and acceptor molecules.[151] The EET mechanism here proposed is a Förster-like transport between localized states. This can also be inferred by the previously mentioned absence of any significant shift of the S_2 bands (clearly shown in Figure 4b of ref. 145[2]) between XR and RXR samples, which implies negligible delocalization and electronic overlap between the two chromophores.

At longer times ($t_2 > 1ps$, Figure 2.6, Appendix) we still observe the carotene S_2 GSB signal on the diagonal and the S_1 (S^*) ESA cross peak, narrowed and blue-shifted due to S_1 vibrational cooling. In the XR complex we expect to see also the (negative) absorption signals of the J (and early populated K) photoproduct state of RET as previously suggested by Polivka et al.[149], which is indeed revealed by the clear increase of signal in the XR cut.

In Figure 2.4, we present a comparison between experimental and theoretical differences of XR and RXR 2D cuts (obtained by averaging the signals in the pump wavelength interval 515-530 nm). We show that the prediction of a model which excludes both direct and indirect retinal contributions at pump wavelength corresponding to salinixanthin S_2 excitation (red dashed curve in Figure 2.4(c)), is qualitatively different with respect to experimental measurements. On the contrary, the addition of a retinal-like GSB/SE contribution (that is modeled via a gaussian function centered around the retinal absorption maximum, the grey filled curve of Figure 2.4(c)), turns out to reproduce the main features of the XR/RXR difference. We assign the EET related signal to the excess of signal amplitude observed at the (520nm,560nm) cross-peak in the XR sample. To support this assignment, we dis-

---

[2]The figure shows the comparison of second derivatives of the ground-state absorption spectra of XR and RXR, which perfectly overlap in the CAR region.
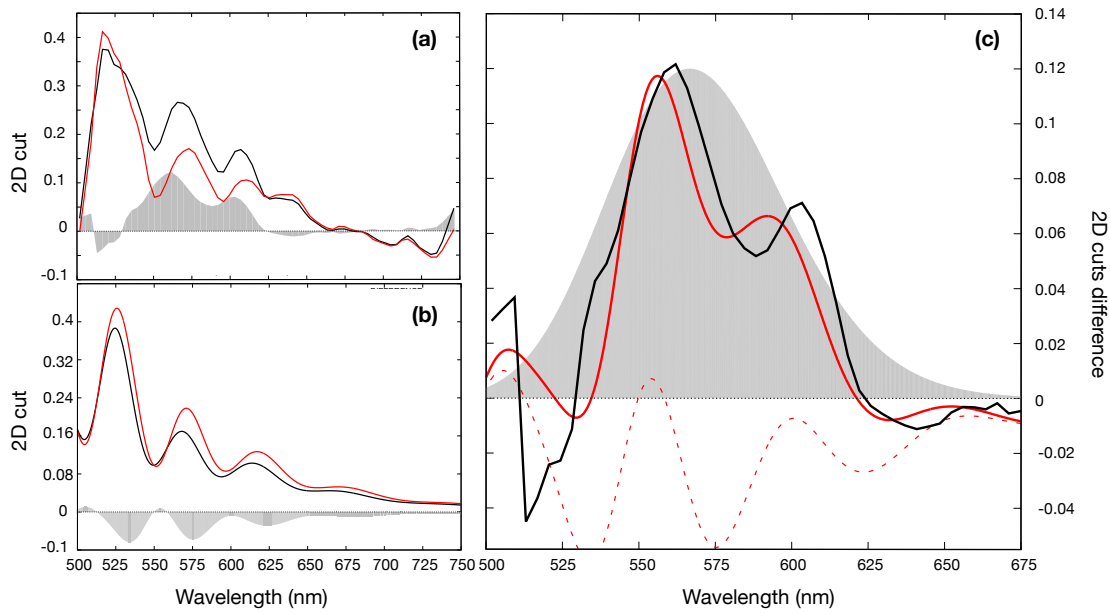
Figure 2.4: Differences of XR and RXR 2D cuts selected by pump wavelengths in the 515-530 nm interval at $t_2 = 20fs$. Experimental (a) and Theoretical (b) XR and RXR cuts (red and black solid line respectively) together with their differences (grey filled curves). Since in the theoretical maps we are not considering RET contributions, the differences between the two curves are only given by the different S_2 state lifetimes (which rule the S_2 SE disappearance, and produce the lifetime broadening of the transitions). Panel (c): experimental difference (black solid line) and theoretical difference, before (red dashed line) and after (red solid line) the sum with the retinal emission component (grey filled curve).

cuss in detail the origin of all the signals which could in principle contribute to this spectral region, i.e. when pumping the carotene chromophore (between 510-530 nm) and probing in the 500-650nm region at early times.

The presence of possible carotene $S_2 \rightarrow S_{2n}$ ESA signals cannot be excluded, but to the best of our knowledge it has never been reported in studies of similar carotenoid systems in this spectral region. We exclude CAR $S_1 \rightarrow S_{1n}$ (and corresponding $S^* \rightarrow S_n^*$) ESA signals, which are known to appear only at later times. Contributions from direct retinal excitation (which has a non-negligible absorption at 520 nm) are also of minor importance: direct retinal contributions are barely detected, in 2DES maps, at the maximum of the retinal absorption (a very weak signal is measured on the diagonal around 560 nm), being therefore even weaker for wavelengths around 520 nm, where the retinal is known to absorb less. At variance, indirect RET signals (i.e. signals coming from RET populated via EET from the CAR S_2) are much more intense, as they are weighted with the CAR S_2 dipole strength, as explained in Appendix, Section 2.4.4. One could expect to observe, due to the presence of a finite carotenoid-retinal coupling, cross-peaks in the carotenoid-
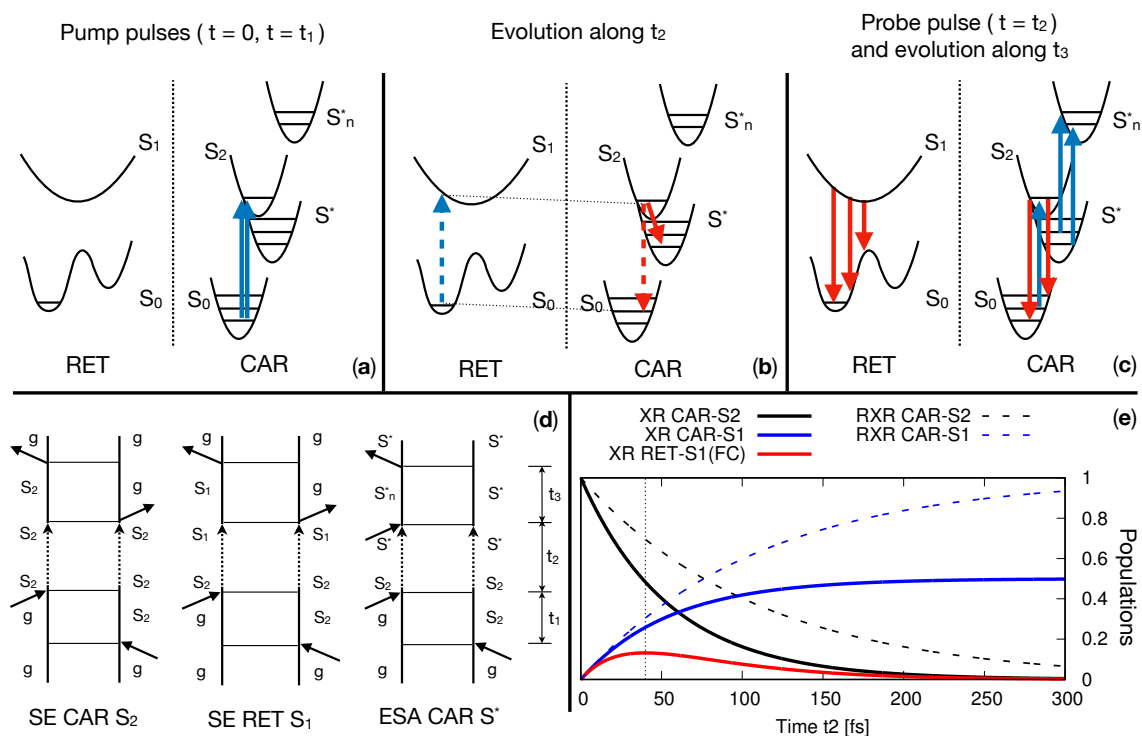
Figure 2.5: (a-c) Energy level scheme depicting the main transitions occurring during the times t_1, t_2 and t_3: (a) excitation of the salinixanthin S_2 state, (b) IC and EET processes activated after excitation of salinixanthin in xanthorhodopsin (the energy matching condition for EET occurs when hot CAR GS vibrations are populated: this is the scenario most likely involved in the CAR $\rightarrow$ RET EET process), (c) main SE (both in CAR S_2 and in RET S_1) and ESA signals ($S^* \rightarrow S_n^*$); blue arrows underline absorption, while red arrows emission; only the S^* state is shown for clarity (similar schemes hold for CAR S_1), and for the same reason only one effective mode in the PES is depicted; (d) (Rephasing) Feynman diagrams of the possible processes activated after population of CAR S_2 (a population preserving diagram, giving rise to S_2 SE, and two population changing diagrams, giving rise to EET related SE and IC related ESA); similar considerations hold for non-rephasing diagrams. (e) Population dynamics of the spectroscopic relevant states in XR (solid lines) and RXR (dashed lines), for a model in which both IC and EET have 50% efficiency.

retinal off-diagonal regions, both above and below diagonal. We do not observe any signal in the above diagonal region, and we can exclude possible contributions also in the region of interest: due to the negligible delocalization of the excitation on the two chromophores we expect GSB and ESA signals (coming from diagrams which involve both CAR S_2 and RET S_1) to cancel each other.

It is worth noting that a fast disappearance of the XR-RXR differential signal at this cross-peak is also observed. This can be easily accounted for considering the underlying fast evolution of the retinal chromophore when promoted to its S_1 state by the EET process: in fact, if at short times the retinal emission (appearing during

the carotene-to-retinal EET process) should be similar to the retinal absorption, it very quickly undergoes a pronounced red-shift, disappearing from the probed window, as previously observed for other rhodopsin system.[152, 153] Moreover, negative contributions from the salinixanthin S_1 (S^*) ESA will progressively gain intensity at increasing t_2 times, thus masking the positive EET related cross peak (the evolution of the state populations are reported in Figure 2.5(e)).

All that considered, the most likely explanation of the observed signals (over a range of times and wavelengths) involves the presence of retinal that has been indirectly excited through an ultrafast EET process from the carotene moiety, directly excited by light.

A comprehensive scheme of the states involved and of the transitions between these states which occur in a 2DES experiment, is depicted in Figure 2.5, and it summarizes some of the obtained results:

- Figures 2.5(b) shows that the resonant donor-acceptor condition is fulfilled thanks to GS vibrations of the donor (salinixanthin).

- Figures 2.5(c) shows both the red-shifting of the RET emission over time, the $S^* \rightarrow S_n^*$ ($S_1 \rightarrow S_{1n}$) ESA following IC, and the "hot" CAR ground-state absorption following EET.

- Figure 2.5(e) summarizes the evolution of state populations in both XR and RXR, as obtained within a simple rate equation model. The model includes the ultra-short lifetime of the Franck-Condon S_1 state of the retinal, set to 30 fs (following the arguments of ref. 152). The fast evolution of the RET on its PES, together with the emerging CAR S_1 (and S^*) ESA signals, explains the fast disappearance of EET related RET signals around 560 nm in the 2D maps.

2.3 Conclusions and perspectives

We have compared 2DES measurements performed on both xanthorhodopsin and reduced-xanthorhodopsin systems. The identification and interpretation of the recorded signals, supported by a theoretical analysis, allowed us to provide direct evidence of the ultrafast carotene-to-retinal EET process at very early population times t_2. Interestingly, our analysis uncovers the importance of hot vibrational levels in the carotenoid ground electronic states in assisting the ultrafast CAR $\rightarrow$ RET EET process: they provide improved energy matching and increased transition probability. This model is supported by the fact that the CAR S_2 GSB signal does not decay

during the EET process (as one should expect as a result of the EET related recovery of the original CAR GS) and by the presence in XR of an additional negative signal at the red side of the CAR S_2 bleaching, here interpreted as the absorption from these excited vibrational levels to the CAR S_2.

Despite the simplicity of the system (a donor-acceptor couple), the measured 2DES maps are highly congested by overlapping spectral features. In this perspective, the presented theoretical modeling allows for a clearer identification of the signals origin. Nonetheless, some important improvements are necessary: first of all, we are currently working on an ab-initio modeling of the presented systems, as a means to objectively disentangle the various contributions and to obtain an independent confirmation of the proposed mechanisms. Secondly, an advanced simulation protocol (as the PLDM approach to spectroscopy, Part II, Chapter 3) is needed to describe more accurately the population dynamics which follows excitation of the salinixanthin, and the subtle effects introduced by the finite pulses band-width.

2.4   Appendix - XR

2.4.1   Experimental details

The 2DES experiment was performed in a VVHH[3] configuration of the pulses polarization, which minimizes the pump scattering. The pulses have a sub-10-fs duration ($\sim$8 fs), and as such at 20 fs (the first map analyzed e.g. in Figure 2.3a) they are not overlapping.

2.4.2   Comparison of XR and RXR maps at $t_2 = 2ps$
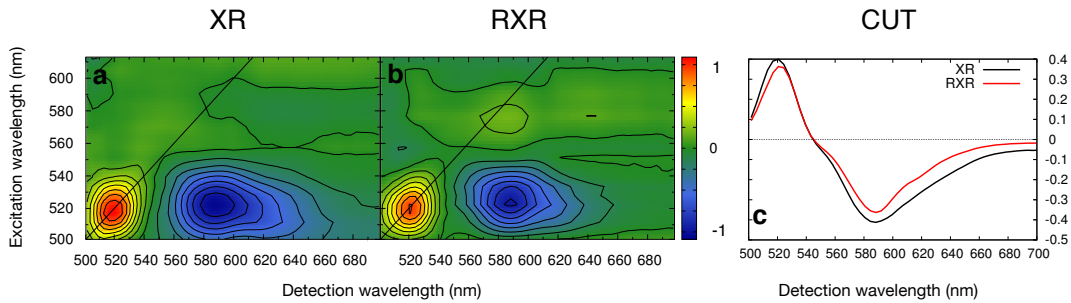
Figure 2.6: Experimental 2DES XR map (a), experimental 2DES RXR map (b) and cut of these maps (d) at $t_2 = 2ps$. The experimental maps are normalized to a common maximum value. The 2D-cut is taken averaging the signal in the pump rage 515-530 nm.

2.4.3   Pulse Shape

Figure 2.7 shows the envelope of the pump and probe pulses used in the 2DES experiment. We note that they overlap only with the tail of the CAR $S_0 \rightarrow S_2$ transition, so that they will populate only the vibrational ground state of the CAR S_2 state. Let us describe the consequences of this particular pulse shape setup:

- The strong displacement of GS and ES PES implies that the highest Frank-Condon factor (i.e. the highest transition probability) is not the one of the $0 \rightarrow 0$ transition, but that of the $0 \rightarrow 1$ transition. Nonetheless, the shape of the pulses allows only the $0 \rightarrow 0$ transition.

- The proper theoretical description of the $S_0 \rightarrow S_2$ transition therefore require to explicitly account for the vibrational states of the various electronic states.

---

[3]VVHH stands for vertical-vertical-horizontal-horizontal pulses polarizations.

This was not implemented in the current simulations of 2DES maps. As a consequence, theoretical maps present a different (more pronounced) dynamics of the peaks, due to the motion of the wave-packet in the S_2 PES.

- Another important difference between the theoretical and experimental maps, is related to the unexpected behavior of the diagonal CAR S_2 peak evolution: the expected behavior is reported in Figure 2.8(a), and shows a very fast increase of the signal up to a maximum (in which S_2 SE and GSB sum constructively), followed by a decrease of the signal concurrent to the disappearance of the SE (as S_2 undergoes population transfer via IC and EET), and by a stabilization to a plateau (the sole GSB signal). What is instead observed (Figure 2.8(a)) is a constant increase of the signal until the reach of the plateau. There are different reasons that can explain this discrepancy:

  1. Possible $S_2 \rightarrow S_{2n}$ ESA signal can superimpose to the $S_0 \rightarrow S_2$ transition. This has for example been reported in studies of similar carotenoid system, as the β-carotene.[150]

  2. The relaxation of the populated S_2 can be very quick, causing an ultrafast Stokes-shift that displaces the CAR S_2 SE signal to the red. The SE will still partially overlap with the CAR S_2 GSB, therefore this mechanism can only partially explain the observed behavior.

  3. Another possible explanation involves the shape of the pulses: following the diagrams of Figure 2.8(b-c), the first pulse selectively populate only the GS vibrational level of the S_2 excited states, the second pulse send the
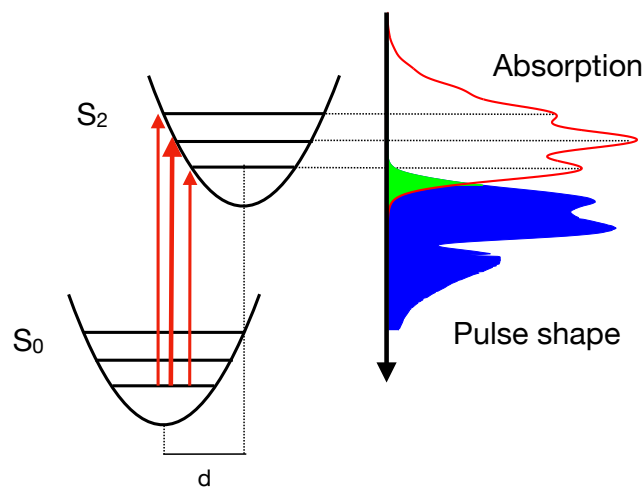
Figure 2.7: The pulse shape filters the possible arrival (vibrational) states of CAR S_2. The green area is the overlap between absorption and pulse shape. d is the displacements between the S_0 and S_2 PES.
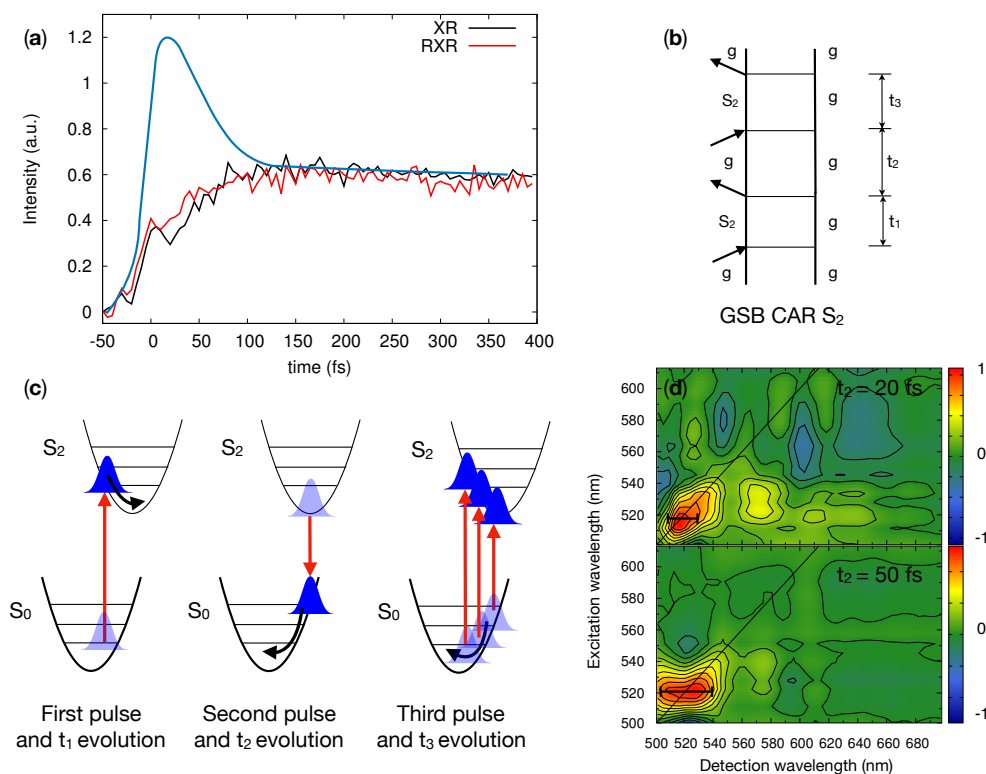
Figure 2.8: (a) Time evolution of the diagonal at 520 nm: the expected behavior is depicted in blue, the measured values for XR and RXR are the black and red lines, respectively. (b) Feynman diagram for the non-rephasing GSB of the CAR S_2 state. (c) Evolution of the wave-packet along GS and S_2 PES of the CAR chromophore, which explains the broadening along the detection wavelength. (d) 2DES maps showing the elongation of the diagonal signals in the detection wavelength at various times.

wave-packed back to the GS, and since it is not in an equilibrium position it will start to oscillate; when the third pulse arrives, the moving wave-packet on the GS will broaden the transition along ω_3, spreading the GSB signal over a larger frequency interval and thus reducing its intensity. The elongation of the peaks in the detection frequency axis in the experimental maps (see Figure 2.8(d)) seems to confirm this interpretation.

2.4.4 Dipole argument against direct RET excitation at 520nm

One can argue that the signal observed at the cross-peak (520 nm,560 nm) is not EET related, but it follows from direct RET excitation: indeed, at 520 nm, the principal absorber is the CAR moiety, but there are also non-negligible RET contributions (as shown in Figure 2.2). In the main text we observed that direct RET GSB and SE signatures are barely detected in 2DES maps at the maximum RET absorption, at the diagonal position 560 nm. Here we further develop this argument.
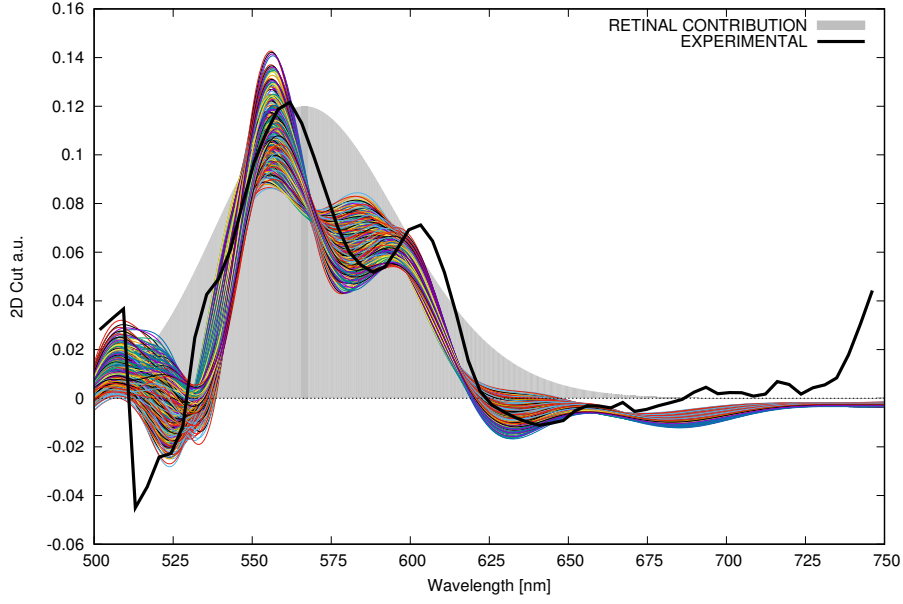
Figure 2.9: Experimental *(black)* and theoretical *(multi-colors)* difference of XR-RXR cuts of 2DES maps, averaging over the Pump interval $510 - 530$ nm, together with the RET-like gaussian contribution centered at 567 nm as grey filled curve. The theoretical curves have been obtained by combining different sets of parameters for the pulse width in time, the pulse center and the Stokes shift of XR and RXR Stimulated emission, and then added to the gaussian contribution.

Figure 2.5(d) shows the Feynman diagrams of the possible processes occurring after population of CAR S_2. Following the rules of Feynman diagrams, the RET SE diagram is weighted by the dipole factor $\langle \left(\boldsymbol{\mu}_{CAR-S_2} \cdot \hat{E}_1 \right)^2 \left(\boldsymbol{\mu}_{RET-S_1} \cdot \hat{E}_2 \right)^2 \rangle$, where $\hat{E}_1$, $\hat{E}_2$ are the polarization of the pump and probe pulses, and $\langle \bullet \rangle$ is the average over all the possible orientation of the XR protein. Similarly, direct retinal diagrams are weighted by $\langle \left(\boldsymbol{\mu}_{RET-S_1} \cdot \hat{E}_1 \right)^2 \left(\boldsymbol{\mu}_{RET-S_1} \cdot \hat{E}_2 \right)^2 \rangle$. By recalling that the experimental pulse polarization was set to VVHH (which implies $\hat{E}_1 = \hat{x}$ and $\hat{E}_2 = \hat{y}$), and that the angle between $\boldsymbol{\mu}_{RET-S_1}$ and $\boldsymbol{\mu}_{CAR-S_2}$ is 46°, one can show that the ratio between these two pre-factors gives:

$$\frac{\langle \left(\boldsymbol{\mu}_{RET-S_1} \cdot \hat{x} \right)^2 \left(\boldsymbol{\mu}_{RET-S_1} \cdot \hat{y} \right)^2 \rangle}{\langle \left(\boldsymbol{\mu}_{CAR-S_2} \cdot \hat{x} \right)^2 \left(\boldsymbol{\mu}_{RET-S_1} \cdot \hat{y} \right)^2 \rangle} = \frac{|\boldsymbol{\mu}_{RET-S_1}|^2}{|\boldsymbol{\mu}_{CAR-S_2}|^2} \frac{9}{15} \ll 1 \qquad (2.1)$$

because $|\boldsymbol{\mu}_{RET-S_1}|^2 < |\boldsymbol{\mu}_{CAR-S_2}|^2$.

Finally, we note also that since the lifetime of CAR S_2 is $\tau_{CAR} \simeq 60$ fs, while the lifetime of the Franck-Condon RET S_1 is $\tau_{RET-FC} \simeq 30$ fs, direct retinal signals are more broadened than the indirect ones.

2.4.5   Robustness of theoretical prediction

We tested a range of parameters of the theoretical model to access the robustness of the proposed picture. In particular we vary the pulse shape width (FWHM) from 16.5 to 23.5 fs, the pulse center from $t_2 = 18$ fs to $t_2 = 26$fs, and the Stokes Shift in the range 230-270 cm^{-1} for the XR-CAR SE and 270-370 cm^{-1} for the RXR-CAR SE. We thus produce a large number of curves combining all the possible choices of parameters, added them to the same gaussian contribution previously introduced, obtaining a picture which preserve the qualitative agreement with the experimental cuts difference (Figure 2.9).

2.4.6   Tables of parameters

The energies and transition dipoles of the principal electronic transitions involved in the model were tuned in order to reproduce the ground-state absorption spectrum of RXR, and the 2DES maps at early times. The choice of the model parameters for S_1 and S^* cannot be unique, due to the limited amount of information that can be extracted from the sole experimental 2DES cuts.[150]

	$\epsilon_{vertical}$ (cm^{-1})	ϵ_{0-0} (cm^{-1})	$|\boldsymbol{\mu}|$
$S_0 \to S_2$	20920	18830	1
$S_1 \to S_{1n}$	16900	15600	1.2
$S^* \to S_n^*$	17620	16680	1.2

Table 2.1: Energies and transition dipoles of the Electronic Transitions involved in the Model. In the first column we report the vertical transition energy, while the second gives the adiabatic energy of the pure electronic transition. The last column gives the module of the transition dipole moments normalized to that of the $S_0 \to S_2$ transition.

The form of the spectral density was adapted from ref. 150, and the parameters tuned with the same rationale explained above.

For the CAR S_2 transition, a (diagonal) static disorder of $\sigma = 220$ cm^{-1} was employed. The maps were obtained by averaging the results over 300 realizations of the static disorder. The rate $S_2 \to S_1$ was set to $(270$ fs$)^{-1}$, while the rate $S_2 \to S^*$ was set to $(217$ fs$)^{-1}$. In this way, the lifetime of S_2 is exactly equal to 120 fs.

$J(S_0 \to S_2)$	τ (ps)	λ (cm^{-1})	ω_c (cm^{-1})
gauss	0.020	125	—
exp$_1$	0.080	120	—
exp$_2$	5.0	155	—
Vib$_1$	2.2	890	1150
Vib$_2$	2.2	800	1520
$J(S_1 \to S_{1n})$	τ (fs)	λ (cm^{-1})	ω_c (cm^{-1})
gauss	0.020	125	—
exp$_1$	0.080	120	—
exp$_2$	5.0	155	—
Vib$_1$	2.2	500	1150
Vib$_2$	2.2	400	1520
$J(S^* \to S_n^*)$	τ (fs)	λ (cm^{-1})	ω_c (cm^{-1})
gauss	0.020	125	—
exp$_1$	0.080	120	—
exp$_2$	5.0	155	—
Vib$_1$	2.2	270	1150
Vib$_2$	2.2	270	1520

Table 2.2: Parameters for the Spectral Densities of the transitions involved in the model involved in the Model. In the table, τ denotes the relaxation time, and λ the reorganization energy of the specific part of the spectral density. For the two intra-molecular vibrations, the central frequency ω_c is given.

Sub-20-fs Pump-Probe Spectroscopy of Coherent Excited-state Dynamics of *trans*-Azobenzene

The work presented in this Chapter has been done in collaboration with the experimental group of Prof. Giulio Cerullo (Politecnico di Milano, Milano, IT). My contribution was mainly focused on the simulation of the transient absorption (TA) spectra. This work has been published in the *Journal of Physical Chemistry Letters*, ref. 154.

3.1   Introduction

Photochromism is at the heart of light-powered nanomachines, also known as molecular photoswitches or optical switches, which can be reversibly switched between two or more stable configurations by exposure to light.[155] Over the years the technological potential of optical switches has been demonstrated in various applications like optical storage devices[156], triggers for peptide folding[157, 158, 159], light-gated ion channel control or nonlinear optical materials[160] to name a few. Azobenzene (AB) based compounds are prominent photoswitches that undergo an ultrafast (picosecond) *trans-cis* photoisomerization associated with changing the conformation of the central N=N double bond (Figure 3.1). AB has attracted attention due to its favorable photochromic properties, such as a significant change in geometry of the molecule upon isomerization, photoactivity even under strong constraints[161, 162, 163, 164] and discrete absorption bands allowing to selectively address either the *trans* or *cis* configurations. It is therefore not surprising that considerable effort has
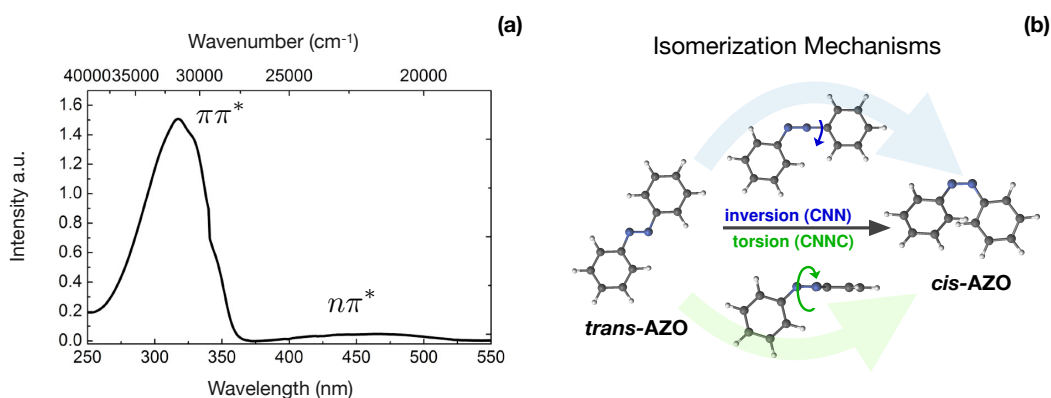
Figure 3.1: (a) Linear absorption spectrum of *trans*-AB; (b) Reversible *trans*-*cis* isomerization of AB and mechanisms.

been put into scrutinizing its photoactivity[165]. However, despite the vast amount of experimental[161, 166, 167, 168, 169, 170, 171, 172, 173, 174, 175, 176, 177] and theoretical works[174, 177, 178, 179, 180, 181, 182, 183, 184, 185, 186, 187, 188, 189, 190, 191], there is still a controversy over two key aspects of the photoisomerization: the isomerization mechanism itself and the wavelength dependence of the quantum yield (QY) of *trans*-AB.

In the 80s Lueddecke and co-workers postulated that *trans*-AB should undergo different isomerization pathways upon excitation of either the $n\pi^*$ (broad absorption band at $\sim$440 nm) or the $\pi\pi^*$ (peaked at 315 nm) state (Figure 3.1), in order to account for the violation of Kasha rule[161]. This view was supported by an early theoretical (single-excitation configuration interaction) work by Monti *et al.*[178] reporting high energetic barriers along the torsional coordinate opposite to absent barriers along the inversion coordinate.

In the 90s, Lednev *et al.* reported femtosecond transient absorption measurements for *trans*-AB[166, 167]. These studies revealed an ultrafast ($<$ 200 fs) decay component under excitation of the $\pi\pi^*$ state, which was attributed to motion along the torsional coordinate, and a 2.5-ps lifetime for the $n\pi^*$ state, assigned to motion along the inversion coordinate. Later on, in a series of femtosecond TA spectroscopy, time-resolved fluorescence and Raman experiments[168, 169, 170], Fujino *et al.* dismissed the hypothesis of different pathways: according to their interpretation, the entire $\pi\pi^*$ population relaxes on a sub-100 femtosecond (fs) timescale, presumably with AB still in a planar geometry, to the $n\pi^*$ state. Isomerization was found to take place from the $n\pi^*$ state with time constants of $\sim$1 ps and $\sim$17 ps. Broadband TA by Braun and co-workers[171] noted the similarity in the decay associated spectra (DAS) of $n\pi^*$- and $\pi\pi^*$-initiated dynamics while resolving an additional shorter life-

time of 0.2-0.4 ps associated with the decay of the $\pi\pi^*$ population (also documented in works of Zinth, Wachtveitl and colleagues[172, 173]), thus supporting Fujino's interpretation that the isomerization should occur on the $n\pi^*$ surface. Time-resolved photoelectron spectroscopy experiments further supported this theory[174]. By then it was largely accepted that both $n\pi^*$ and $\pi\pi^*$ decay to the ground state (GS) via the inversion mechanism (which was therefore recognized as the main isomerization channel), based on the computational results of Monti[178] and the Raman studies by Fujino[168]. The latter demonstrated that the frequency of the N=N stretch vibration does not change substantially during the isomerization, therefore ruling out the torsional pathway, which should instead imply a double bond breaking, together with the change of the N=N stretching frequency.

The application of multiconfigurational methods (multi-reference single and double excitation configuration interaction (MR-SDCI)) to AB by Ishikawa *et al.*[179] offered new insights which challenged the inversion mechanism. The dynamically correlated description of the $n\pi^*$ potential energy surface (PES) revealed that the torsional pathway offers a vanishing barrier, while a huge barrier was predicted for the in-plane inversion. These results have been confirmed at the level of the complete active space self-consistent field (CASSCF) augmented with multiconfigurational second order perturbation theory (CASPT2)[180, 181]. In a notable contribution Taketsugu and colleagues demonstrated through CASPT2 frequencies computed along the torsional and inversion pathways that the N=N stretching mode is insensitive to the mechanism, thus mitigating the main argument in favor of the inversion path.[182] In a recent joint experimental (jet-cooled multiphoton ionization) / time-dependent density functional theory (TDDFT) work Buma, Zerbetto et al. revealed a ~2 kcal/mol barrier along the $n\pi^*$ isomerization path[183], consistent with the torsional path. Nevertheless, the active modes observed in the excitation spectrum contain a significant amount of CNN bending character, prompting the authors to describe the mechanism as "inversion-assisted torsion". Molecular dynamics simulations in gas-phase (semi-classical CASSCF-[184] and TDDFT- based[185]) and in solution (tailored classical force fields[186]) upon $n\pi^*$ excitation support this idea, indicating that the decay to the GS does not require a complete 90°-torsion around the N-N bond but rather occurs in a broad area of the CNNC-torsion / CNN-bending sub-space. Notably, decay through pure in-plane inversion upon $n\pi^*$ excitation has not been observed in these studies.

Based on the studies above, the most plausible scenario for the decay to the GS upon $n\pi^*$ excitation of *trans*-AB involves an extended conical intersection (CI) seam reached through both CNNC-torsion and CNN-bending (inversion-assisted torsion

channel, Figure 3.2b). Recently, the lifetimes associated with the decay (0.35 ps and 2.7 ps[171, 172, 173]) have been challenged by Kovalenko *et al.* who first recorded broadband TA covering the ground state bleach (GSB) spectral window (280-340 nm)[177]. They reported a 15-ps time constant for the GSB recovery, deducing the possibility of an intermediate non-planar stable configuration along the $n\pi^*$ potential energy surface introducing a 8 kcal/mol barrier to the CI region.

The second open question concerns the wavelength dependence of the isomerization QY, which shows a 50% decrease upon excitation of *trans*-AB with UV light (where the $\pi\pi^*$ state absorbs). The view of a pathway common to $\pi\pi^*$- and $n\pi^*$-excitation is supported by the similar time constants obtained by fitting the excited state absorption (ESA) decay in TA studies upon $n\pi^*$ (0.35 ps, 2.7 ps, 12 ps) and $\pi\pi^*$ (0.4 ps, 2.9 ps, 12 ps) excitation[171, 172, 173, 177, 178]. Braun noted the differences in the relative intensities of the DAS for the sub-ps lifetimes, with the amplitude for the 0.4 ps component being strongly enhanced after $\pi\pi^*$-excitation, suggesting a different branching ratio on the $n\pi^*$ potential energy surface with a large amount of molecules leaving the electronic excited state (ES) via a non-reactive path on a sub-ps time scale[171]. Through normalization of the TA spectra Kovalenko et al. quantified this amount to 50%[177]. Furthermore, and very notably, they reported a GSB recovery time constant of 1 ps, not observed after $n\pi^*$ excitation. Kovalenko questioned Fujino's interpretation that the $\pi\pi^*$ population relaxes to the same Franck-Condon (FC) region on the $n\pi^*$ state accessed after $n\pi^*$ excitation, noting the possibility that either a region inaccessible upon $n\pi^*$ excitation is visited upon initial $\pi\pi^*$ absorption (labeled the "hot channel" in Figure 3.2a) or that not the entire $\pi\pi^*$ population decays to the $n\pi^*$ state. The latter view was shared by Conti *et al.*[180], who, based on CASSCF optimized geometries and CASPT2 corrected energetics, postulated the involvement of higher lying "dark" states (Figure 3.2a, the "phantom state channel") that funnel part of the population into non-reactive channels and reduce the QY. Semi-classical dynamics seem to support this mechanism, although not always agreeing on the nature of the states involved[174, 185]. On the contrary, Buma et al. did not see indications of the involvement of other states[183].

In a nutshell, several open questions on the photoisomerization mechanism of *trans*-AB remain yet to be answered. To date, the temporal resolution of transient experiments has not permitted one to determine the lifetime of the $\pi\pi^*$ state ($?_1$ in Figure 3.2a). To the best of our knowledge a value of 110 fs[177] is the shortest lifetime reported in the literature, which is comparable to the used instrumental response function (see Figure 3.2c for a literature survey of $\pi\pi^*$ and $n\pi^*$ lifetimes). It is evident that a significant part of the population is involved in the ultrafast
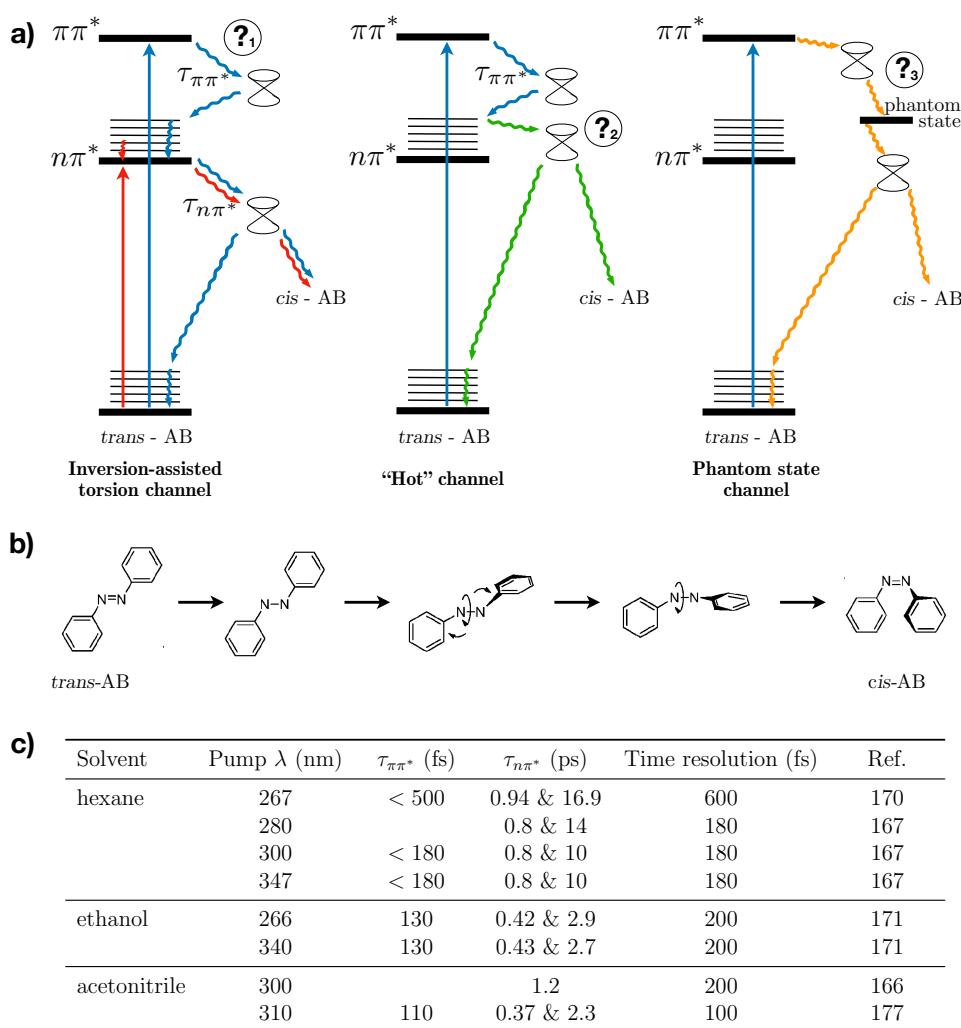
Figure 3.2: (a) Energy diagrams of the relaxation channels in the *trans*-AB after nπ^* and $\pi\pi^*$ excitation, proposed in the literature; (b) The *trans*→*cis* mechanism of inversion-assisted torsion; (c) Literature survey of the $\pi\pi^*$ and nπ^* lifetimes.

relaxation dynamics ($\sim$ 0.4 ps) associated with the decrease of the ESA signals. However, it is still unclear what is the nature of the molecular motion associated to this ultrafast spectral dynamics, and whether this relaxation channel is reactive (i.e., leading to *cis*-AB) or non-reactive and whether it can be made responsible for the QY decrease. Related to this, the involvement of "dark" states remains yet to be definitely confirmed or disproved.

We address the above questions by combining high time resolution TA spectroscopy and multiconfigurational wavefunction techniques. TA measurements were performed utilizing sub-20 fs pump pulses at 320 nm and broadband probe pulses ranging from the visible (350-700 nm) to the ultraviolet (250-380 nm), which:

(a) Allow to resolve the dynamics in the $\pi\pi^*$ state prior to its ultrafast (sub-100 fs) decay;

(b) Resolve coherent ESA oscillations of the $n\pi^* \to$ higher lying states transitions;

(c) Explore the deep UV window (250-280 nm), rich with spectroscopic fingerprints of reactant and photoproducts.

Our calculations show that the $\pi\pi^*/n\pi^*$ CI resides in a strongly out-of-equilibrium region of the $n\pi^*$ PES, and that the transferred (*hot*) population accumulates a large amount of vibrational energy in four CNN-bending modes. This energy allows to reach a high lying region of the $n\pi^*/GS$ CI seam, documented in the computational study of Casellas *et al.*[181], and shown to be accessible through pronounced CNN-bending deformations. Interestingly enough, the direct excitation of the $n\pi^*$ state create a *cold* population, which has not enough energy to access that high lying $n\pi^*/GS$ CI seam. We argue that this channel is non-reactive and, thus, the prime reason for the violation of the Kasha rule and the reduction of QY upon $\pi\pi^*$ excitation.

Ab initio molecular dynamics simulations (not covered in this Thesis, even if discussed in the published paper) within the CASPT2 framework utilizing a full-π active space, directly demonstrate that relaxation routes from the FC point on the $\pi\pi^*$ state to the GS, thereby confirming ultrafast $\pi\pi^* \to n\pi^*$ decay.

Combining high-level electronic structure calculations with nonlinear spectroscopy techniques we simulate TA spectra, thereby explicitly incorporating the, so far, theoretically elusive ESA features, as well as their vibrational lineshape properties. By uncovering the nature of the coherent oscillations observed in the experiment we establish a direct link to the experimental observables.

3.2   Theoretical Methods

The 1DPP signal was obtained by computing the third-order response function, and setting $t_1 = 0$. In the semi-impulsive limit, the signal is thus produced by Fourier transforming $R^{(3)}(0, t_2, t_3)$ over t_3, obtaining a function of probe wavelength ω_3 and pump-probe delay t_2 which can be compared to the measured data. The non-linear response can be expressed within the framework of cumulant expansion of Gaussian fluctuations (CGF) presented in Part II, Section 2.3.7, accounting for population transfer by means of the method described in Part II, Section 2.4.3. The spectral density was partitioned in a) a part responsible for the vibrational progression

in the spectra, described through the multidimensional uncoupled displaced harmonic oscillator (DHO) model; b) a part describing the homogeneous broadening due to coupling to a continuum of low-frequency modes represented by the lineshape function of the overdamped Brownian oscillator (OBO). In this work the OBO parameters were chosen so to reproduce the $\pi\pi^*$ bandwidth in the linear absorption spectrum at room temperature (see Figure 3.12 in the Appendix). In the lineshape functions of population transfer diagrams (P), which describes the jump from the $\pi\pi^*$ to the $n\pi^*$ surfaces, correlations between t_1 and t_2 were removed, while those between t_2 and t_3 were maintained. We assume the transition dipole moments $\boldsymbol{\mu}_{ij}$ to be coordinate-independent (the Condon approximation). The parameters of the DHO model can be obtained from electronic structure computations at few selected geometries. These parameters were computed for:

(a) the $\pi\pi^*$, $n\pi^*$ and hot ground state (GS*) involved in the population dynamics;

(b) the higher lying ESs probed out of the $\pi\pi^*$ state at early times;

(c) the higher lying ESs probed out of the $n\pi^*$ state at later times.

Energies, gradients and transition dipole moments were computed at CASPT2 level, the relative displacements d_{ij} were obtained through the vertical gradient approach[28], utilizing MP2 and CASSCF normal modes and frequencies. The protocol for obtaining the parameters is outlined in detail in Part I, Section 3.1.4. Spectra simulations were performed with a development version of Spectron 2.7[68].

Adiabatic molecular dynamics simulations (not covered in this Thesis) following Newton's equations of motion for the nuclei and utilizing numerical CASPT2 gradients were performed in the $\pi\pi^*$ and $n\pi^*$ states without initial kinetic energy (so called 0 K trajectories). The simulations were carried out using the molecular dynamics code COBRAMM interfaced with the ab initio software package Molcas[10] with an integrated scheme for obtaining numerical gradients and non-adiabatic couplings at CASPT2/RASPT2 level[23]. Geometries and velocities were propagated with the Velocity-Verlet algorithm with a time step of 0.5 fs. Further details are provided in the published paper. Utilizing the outcome of the molecular dynamics simulations performed in this study, the current experimental data and the findings of previous TA experiments, we elaborated a "quasi-sequential" model that describes the population decay following excitation of the bright $\pi\pi^*$ state (See Appendix, Section 3.5.3).

3.3   Results and Discussion

The sample was pumped with 16-fs UV pulses at a central wavelength of 330 nm, resonant with the $\pi\pi^*$ state, and probed over a broad wavelength range. Figure 3.3(a) shows the TA spectra in the visible (VIS) between 360-700 nm for the first 500 fs. In agreement with previous studies[167, 170, 171, 177], at early times (<100 fs) we observe two photoinduced absorption (PA) bands: a broad intense band ranging from 550 nm to 700 nm (PA1) and a narrower band between 450 nm and 500 nm (PA2). A global fit of the data[192, 193] reveals that PA1 and PA2 decay with a lifetime of $\sim$50 fs (Figure 3.3(c)), giving rise to a new PA band (PA3) peaking around 400 nm. Considering their ultrafast decay and their absence in the spectra when the $n\pi^*$ state is selectively excited, PA1 and PA2 have been previously assigned as fingerprints of the $\pi\pi^*$ state[171, 177, 178]. PA3, on the other hand, is a fingerprint of the $n\pi^*$ state[171, 172, 173, 177, 178]. It shows oscillatory behavior with a period of 170 fs (195 cm^{-1}), an indication of coherent dynamics damped after about 2 ps. Note, that similar oscillatory patterns are observed also along the 600 nm and 670 nm traces after the initial fast intensity decay. Measurements at longer timescale show that the PA3 decay is best described by the sum of three exponentials with time constants 0.45 ps, 2.5 ps and 11 ps, in agreement with previous studies[171, 172, 173, 177]. Figure 3.3(b) depicts the simulated TA map in the same temporal and spectral windows. Despite the notable blue-shift of the computed signals with respect to experiment (that fall within the accuracy of the computational approach) the agreement is excellent. These results allow us to identify the nature of the underlying transitions. The rapidly decaying PA1 and PA2 features are fingerprints of the $\pi\pi^*$ state, which arise due to the spectral overlap of ESA bands associated with several electronic transitions. In particular, the 550-700 nm ESA (PA1) has contributions from three higher lying states which are bright from the $\pi\pi^*$ state and have a pronounced multiconfigurational nature and significant weights of doubly excited configuration state functions (Appendix, roots 5,6,7, Table 3.1). The same holds true also for the 450 nm band (PA2), less intense in the simulations, which arises due to the overlap of three distinct ESA contributions (Appendix, roots 8,11,12, Table 3.1).

ESA bands provide an indirect probe of the coherent vibrational dynamics in the ES ($\pi\pi^*$ in this case). According to their electronic structure, they show different sensitivity to the photo-active modes resembled in oscillatory features of the signals' intensity and/or spectral position as a function of the pump-probe delay. All states contributing to PA1 and PA2 show pronounced sensitivity in the low frequency regime to the 606/614 cm^{-1} (benzene shear) and 666 cm^{-1} (CNN bending)
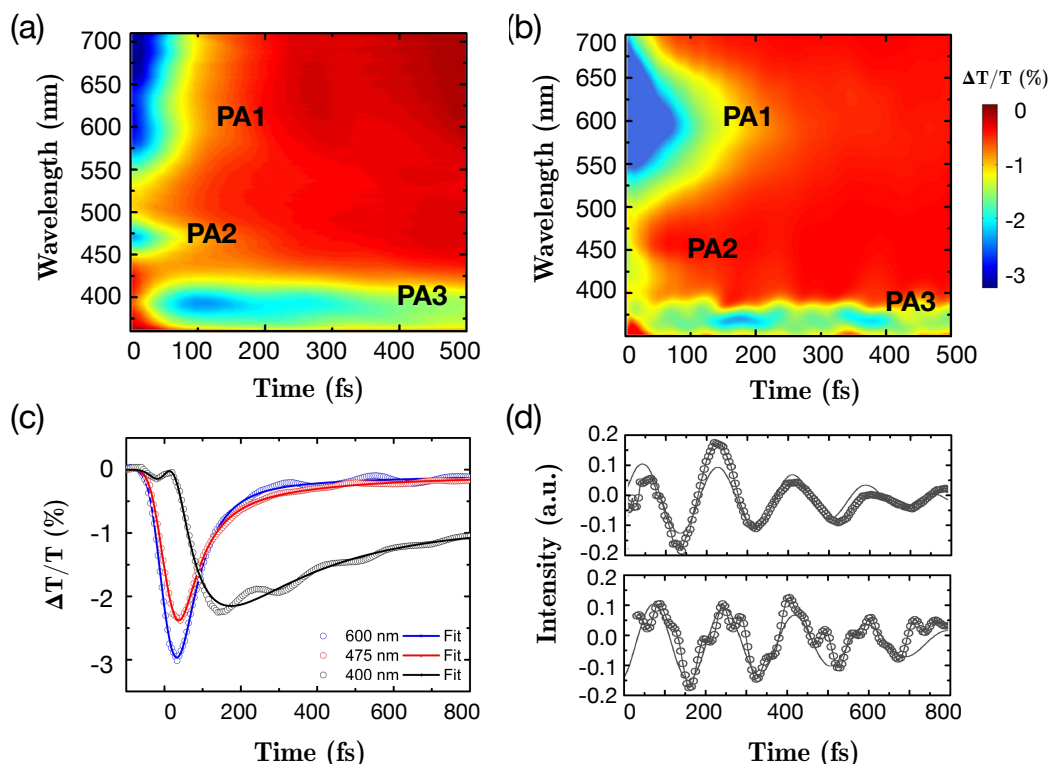
Figure 3.3: (a) Experimental (ethanol) and (b) theoretical (gas-phase) TA maps of *trans*-AB in the visible spectral window during the first 500 fs. The theoretical maps were convoluted with a gaussian-like pulse shape with a standard deviation $\sigma = 16$ fs. (c) Extracted dynamics (from experiment) at 400, 475 and 600 nm. (d) Intensity oscillations (residuals): experimental at 400 nm (top) and computed at 370 nm (bottom). Open dots represent the experimental (theoretical) data and the solid line the fits.

modes, as well as in the high frequency range to modes 924 cm-1 (symmetric CNN bending), 1161 cm^{-1} (CN stretching), 1397 cm^{-1} (NN stretching) and 1628 cm^{-1} (CC stretching in the benzene rings). The ultrafast decay of the population broaden the signals and covers any coherent oscillatory features at early times.

The picture is clearer when looking at the 400 nm trace (Figure 3.3(c)), the fingerprint of the $n\pi^*$. It arises from the ESA contribution of a single higher lying state (Appendix, root 3, Table 3.1). The oscillator strength is facilitated through intraband transitions which promote either the excited electron to a higher π^* orbital ($\pi^* \rightarrow \pi^*$ transition), the generated hole to a lower n-orbital ($n \rightarrow n$ transition) or excite a π-electron thus generating a doubly excited configuration $n\pi\pi^{*2}$. As noted above, PA3 shows clear oscillatory behavior with a 170-fs period. Our simulations (Figure 3.3(d)) reproduce the oscillatory dynamics rather well. Remarkably, only one dominant vibrational mode (195 cm^{-1}) is extracted from the fit of both the experiment and simulation, despite the fact that time-resolved Raman[170] and

photoionization[183] spectroscopies have resolved a plethora of modes involved in the coherent dynamics on the $n\pi^*$ state after selective $n\pi^*$ excitation. Oddly enough, in spite of CASSCF frequencies at the $n\pi^*$ minimum providing a 205 cm^{-1} mode (symmetric CNN bending) that could be tentatively assigned to the experimental observation, our simulations demonstrate that the ES responsible for PA3 should be rather insensitive to the dynamics in this mode (Figure 3.11(a), Appendix). Instead, we find that the coherent oscillations with a 195 cm^{-1} frequency are the result of energy gap dynamics along the 660 cm^{-1} and 852 cm^{-1} modes, both having strong CNN-bending contribution. These frequencies have been reported to be particularly intense by Fujino[168] (635 cm^{-1}, 845 cm^{-1}) and Kovalenko[177] (644 cm^{-1}, 847 cm^{-1}) from time-resolved Raman studies, and by Buma (653 cm^{-1}, 853 cm^{-1}) from photoionization spectroscopy[183]. Together with the 205 cm^{-1} CNN bending and the 300 cm^{-1} CCN bending modes, they constitute a quartet of "hot" modes that accumulate almost 10000 cm^{-1} reorganization energy upon $\pi\pi^* \rightarrow n\pi^*$ decay due to the large out-of-equilibrium displacement along the bending coordinates. Other high frequency modes previously reported in time-resolved resonance Raman spectra by Mathies and co-workers[175] are also well reproduced by our simulations (see Appendix, Section 3.5.5). We also note a second $n\pi^*$ fingerprint PA signal around 600 nm which has been reported previously for selective $n\pi^*$ excitation[171, 177]. Weak coherent oscillations of this ESA are resolved in the ps-range, and we found that three modes, 205 cm^{-1}, 660 cm^{-1} and 852 cm^{-1} can be responsible of them.

A second set of measurements was performed by probing in the UV window (250-380 nm). Figure 3.4(a) shows the TA map during the first 500 fs compared to the theory (panel (b)). In addition to PA3, two new spectral features are observed: the GSB in the range 300-340 nm, which decays with a time constant of 11 ps (Figure 3.4(c)) and a PA band ranging from 245 to 280 nm (PA4). Global analysis of the spectral features around PA4 reveals 0.45, 2.8 and 11 ps time constants. These values match those of PA3, which indicates that the nature of PA4 and PA3 must be similar. This notion is supported by the computations, which resolve also this ESA feature of the $n\pi^*$ state (Figure 3.4(b) and Appendix, Table 3.1). There is however one noticeable difference between PA3 and PA4: by comparing the TA spectra (Figure 3.4(d)), one observes that the signals at 365 nm and 270 nm decrease similarly during the first 2 ps, while at the bluest frequencies (245-260 nm) PA4 increases in amplitude on this timescale, effectively inducing a blue-shift of the ESA from 270 to 250 nm. At longer delay times the entire band relaxes with a lifetime of 11 ps, leaving a finite long-lived offset due to the formed *cis*-AB. Correspondingly, a fit of the signal at 250 nm shows a build-up time of 0.45 ps, and decay constant of 11 ps. A
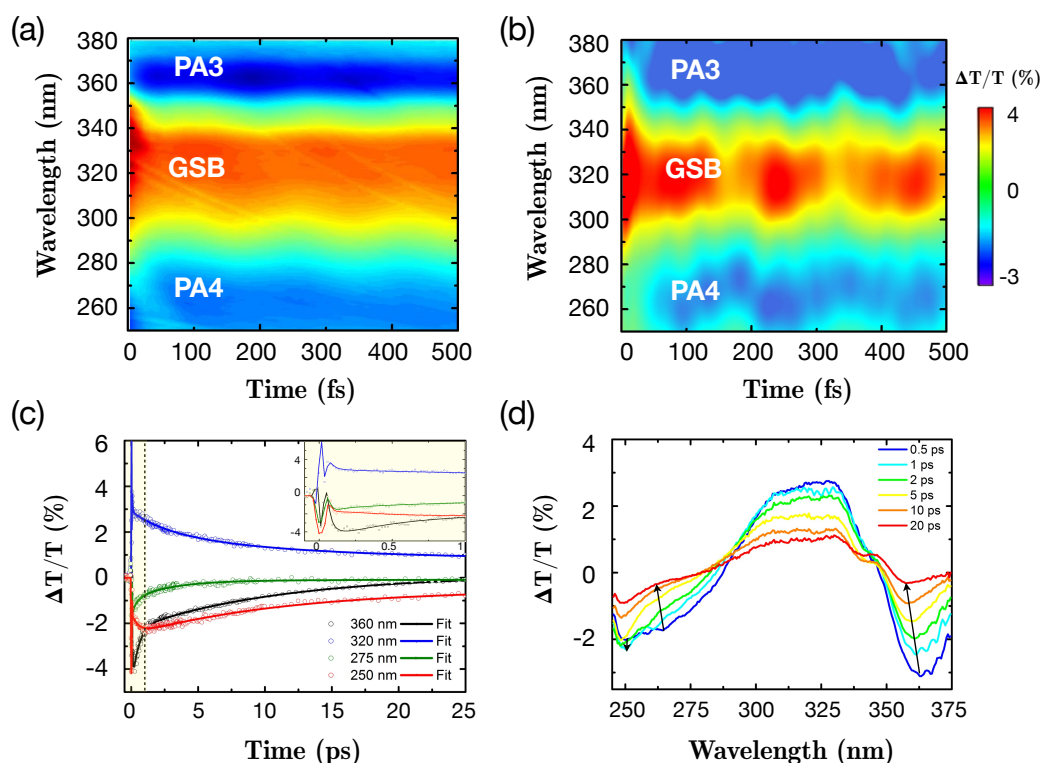
Figure 3.4: (a) Experimental (ethanol) and (b) theoretical (gas-phase) TA data of *trans*-AB probed in the ultraviolet range (245-380 nm). The theoretical maps were convoluted with a gaussian-like pulse shape with a standard deviation $\sigma = 16$ fs. (c) Experimental dynamics at four selected wavelengths (open circles) and fit of the data (solid line). Inset: Dynamics in the first 1 ps. (d) Experimental transient spectra at several delay times. Arrows highlight the blue-shift of the maxima of the transient absorption signals around 270 and 360 nm, and the increase of the signal at $\sim$250.

global analysis of the data reveals that the bluest region (245-260 nm) is dominated by the 0.45 ps and 11 ps components, whereas in the reddest region (260-280 nm) the 0.45 and 2.8 ps DAS present the largest amplitude. Thus, these two spectral regions of PA4 capture different processes whose signatures overlap spectrally and temporally. Let us consider all the signals which are known to fall in that region. By looking at the linear absorption (LA) spectrum of both *trans*- and *cis*- AB in the 200-280 nm interval (see Figure 3.13 in the Appendix), one observes two main contributions:

- An absorption peak at 250 nm for the *cis*-AB;

- A narrow ground state absorption band of *trans*-AB, attributed to the second bright $\pi\pi^*$ transition, peaking at about 230 nm. Our computations show that this band arises due to transferring electronic density between the central

CNNC fragment and the benzene rings.

One might tentatively assign the build-up of intensity at this wavelength to the formation of *cis*-AB in the GS on a sub-ps time scale. However, we argue that what is observed instead is more probably a signature of the "hot" trans-AB reactant. Kovalenko et al. estimated that roughly 50% of the $n\pi^*$ population returns to the GS within the first ps. Even if we assume that all of the *cis*-AB photoproduct (12% QY) is formed through this ultrafast channel, we have to acknowledge that at least four times more "hot" reactant would be recovered simultaneously. It is well known that a "hot" GS wavepacket gives rise to a PA band red-shifted from the GSB band, which decays upon energy dissipation to the environment (cooling) on a ps time
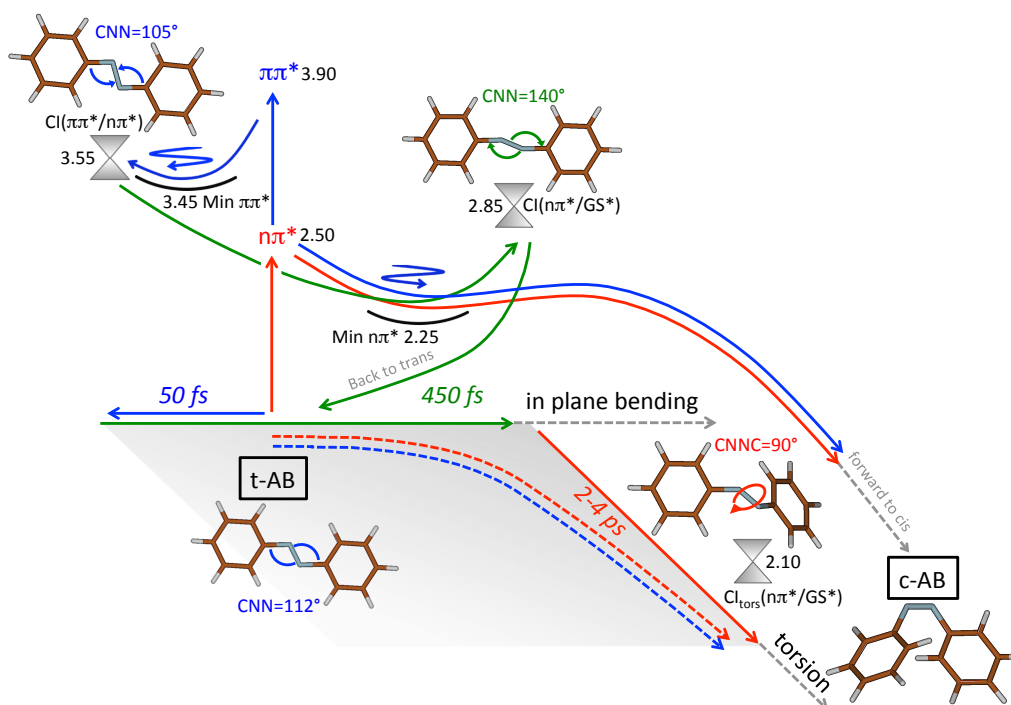
Figure 3.5: Overview of the photochemistry of *trans*-AB in the space of the CNN in-plane bending and CNNC torsion modes. Excitation of the bright $\pi\pi^*$ transition in the UV (320 nm), opens a subps nonreactive decay channel to the GS via $\pi\pi^* \to CI(\pi\pi^*/n\pi^*) \to n\pi^* \to CI(n\pi^*/GS) \to GS$ ("Hot channel" in Figure 3.2a). The coherent dynamics associated with this non-reactive channel driven by the in-plane CNN bending mode is the source of ESA intensity beats in the transient spectra and reduced QY. $trans \to cis$ isomerization requires internal vibrational energy redistribution into the torsional mode, takes an order of magnitude longer (2-4 ps), is incoherent, and proceeds in analogous way upon UV and VIS excitation (500 nm, $n\pi^*$ excitation). Dashed lines show evolution in the bending-torsion plane. Coloring according to Figure 3.2a. Energy values in eV.

scale. Thus, we interpret the band registered around 250 nm as the build-up of the "hot" reactant, whose spectral signature overlaps with the 270 nm ESA of the $n\pi^*$ state.

To validate this interpretation and explain the molecular motions governing the ultrafast (sub-ps) decay of a major part of the ES population, we performed adiabatic ab initio MD simulations, whose results are presented in the published paper.

3.4   Conclusions

In this study we have combined TA spectroscopy with sub-20 fs temporal resolution in the UV range with state-of-the-art computational tools to study the ultrafast photodynamics of trans-AB. We are able to resolve the lifetime of the $\pi\pi^*$ state, the build-up of the $n\pi^*$ population and the following coherent oscillatory dynamics. We observe a single ultrafast lifetime ($\sim$50 fs) of the $\pi\pi^*$ state which is correlated to the build-up of the $n\pi^*$ ESA. Theoretical simulations reproduce with remarkable accuracy the positions of all ESA bands from the $\pi\pi^*$ and $n\pi^*$ states and reveal the origin of the ps-lasting oscillations and, thus, the nature of the vibrational dynamics activated immediately after decay to the $n\pi^*$ state. Four "hot" modes, all characterized by strong symmetric in-plane bending deformations in the central CNNC fragment, were identified: 200 cm^{-1}, 300 cm^{-1}, 650 cm^{-1}, 850 cm^{-1}. Importantly, neither the experimental nor the theoretical results call for additional ESs in order to describe the $\pi\pi^*$ depopulation dynamics. The simulations demonstrate that all spectral features can be already accurately described under the incorporation of only $\pi\pi^*$ and $n\pi^*$ states, accounting for the signals registered experimentally.

Figure 3.5 summarizes the decay channels after $\pi\pi^*$ excitation of trans-AB. A non-reactive decay channel on the $n\pi^*$ PES becomes accessible after excitation to the $\pi\pi^*$ state, which allows the decay to the GS on a sub-ps timescale through an energetically high lying CI seam reached by strong bending deformations. The latter are facilitated only after $\pi\pi^*$ excitation as the AB accumulates nearly 10000 cm^{-1} in the four "hot" bending modes, which allows for exploring a region far away from the equilibrium. Molecular dynamics simulations indicate that the "fastest" molecules could potentially reach the GS within 40 fs.

The interplay between theory and experiment allows us to assign the so-called "CNN-bending" channel as the main reason behind the violation of the Kasha rule and behind the quantum yield reduction at shorter wavelengths, cis-AB being formed only after internal vibrational redistribution from the bending modes into the torsion on the 1 ps time scale.

3.5   Appendix - AZO

3.5.1   Experimental details

The differential transmission ($\Delta T/T$) was measured as a function of probe wavelength and pump-probe delay. For the set of measurements in the visible range parallel polarizations were preferred in order to enhance the oscillatory behavior. In the UV window, perpendicular polarizations were used in order to avoid pump scattering. The experiments were performed at $T = 300$ K.

3.5.2   Spectra simulation

The simulation of the pump-probe spectra for delay times t_2 up to 500 fs within the framework described in Part II, requires the computation of a number of parameters to feed in the lineshape functions for both the high and low frequency sector of the spectral density. These include the strength λ_i and timescale Λ_i^{-1} of the system-bath coupling for the over damped brownian oscillator modeling of the continuum spectral density (Part I, Eq. (3.27)), as well as the normal modes, frequencies ω_m and displacements d_{ij} for the high-frequency sector of the spectral density. From these spectral densities one obtains lineshape functions which modulates the non-linear responses for the different contributions (GSB, SE and ESA). One has to further compute vertical transition energies ε_i and dipole moments μ_{ij}. Finally, the population dynamics must be incorporated by solving the Pauli differential rate equation (Part II, Eq. (2.60)). In the following we elaborate on how the individual parameters were obtained.

3.5.3   Kinetic model and lifetimes

The $\pi\pi^*$ population decays to the $n\pi^*$ state with a lifetime of 60 fs. The $n\pi^*$ population exhibits a biexponential decay. Kovalenko and co-workers estimated that with a time constant of about 300 fs 50% of the $n\pi$ intensity decays. Our molecular dynamics simulations show that this decay is associated with a decay channel to the GS available only to molecules that have accumulated enough vibrational energy in the CNN bending bending modes as the $n\pi^*$/GS energy crossing occurs close to the turning point along a $0K$ trajectory. The remaining $n\pi^*$ population decays to the GS via a torsional mechanism on a few-ps timescale scale after internal vibrational redistribution. To account for the population splitting we consider the $n\pi^*$ population as being formally composed of a fast $\rho_{n\pi^*(F)}$ and a slow $\rho_{n\pi^*(S)}$ component, both exhibiting coherent oscillations and decaying with different rates. The global

analysis of the transient spectra gave lifetime of 270 fs and 2.4 ps for the fast and slow components, respectively.
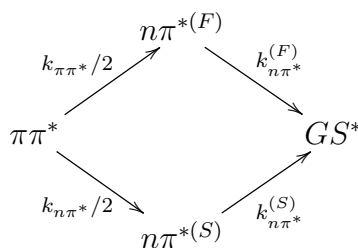
Figure 3.6: Population dynamics.

Figure 3.7 shows the evolution of the population between 0 and 1 ps delay time starting in the $\pi\pi^*$ state (initial population of $\pi\pi^*$ is $\rho_{\pi\pi^*} = 1$). $\rho_{n\pi^*}$ denotes here the combined population of the fast and slow components which shows a peak around 150 fs followed by a biexponential decay. One can see that after 500 fs almost half of the population has returned back to the GS.
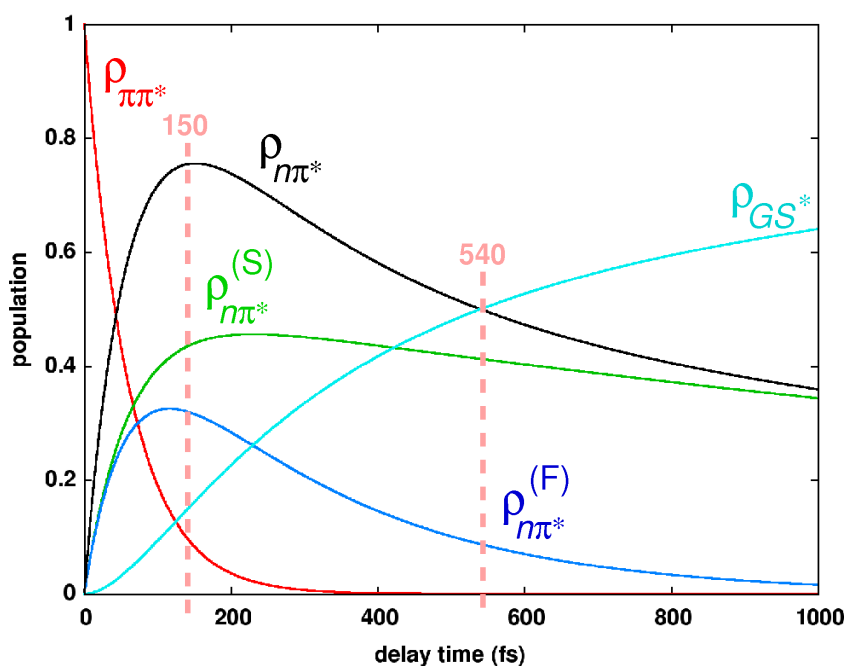
Figure 3.7: Population dynamics in *trans*-azobenzene.

3.5.4   Electronic structure computations: constructing the DHO model

In Part I, Chapter 3 we have shown that the system-bath coupling can be modeled as a set of independent harmonic oscillators linearly coupled to the electronic states. By employing this model, the damping of the vibrations on the $n\pi^*$ state and internal vibrational redistribution into the torsion is neglected, as it is not expected to show in the simulated time window (0-500 fs). The parameters for the DHO model can be obtained from electronic structure computations (normal modes, excitation energies, transition dipole moments and nuclear gradients) at few selected geometries.

The parameters for the $\pi\pi^*$ state were obtained at the GS equilibrium geometry, while the parameters of the $\pi\pi^*$ and $n\pi^*$ fingerprint ESA were obtained at the corresponding ES minima. Gradient projection techniques were utilized to obtain the displacements d_{ij} between the various PES. The parameters for the $n\pi^*$ state were obtained through a projection technique based on the Cartesian coordinate difference of intermediate geometries (minima and conical intersections) along the relaxation mechanism (second method presented in Part I, Section 3.1.4). The frequencies were obtained through a normal mode analysis, at second-order Møller-Plesset perturbation theory (MP2), while we made use of the RASSCF/RASPT2 technique for computing the electronic structure of ESs.

3.5.5   Electronic structure of the $\pi\pi^*$ state and its ESA

Transition energy, transition dipole moment and gradient of the $\pi\pi^*$ state were computed at the MP2 optimized *trans*-AB geometry within D_{2h} symmetry as the second root in the B_u irreducible representation at SS-RASPT2/SA-3-RASSCF $(4, 7|0, 0|4, 15)$/ANO-L[321,21] level where the active space comprises all valence π-orbitals of the system and *eight further virtual orbitals*. The so obtained vertical energy of 3.90 eV (31450 cm^{-1}, 318 nm) matches well the experimental $\pi\pi^*$ absorption band maximum (315 nm). The spectral density in Figure 3.8 is dominated by the NN stretching mode with 1397 cm^{-1} frequency in the high-frequency range and with a notable contribution by the CCN/CNN bending mode with 225 cm^{-1} frequency in the low-frequency range. Several other modes found to contribute as well are shown in the Figure 3.8.

We note that the values of the displacements depend strongly on the method used to compute the gradient. In constructing the spectral densities showed in Figure 3.8 we used the SS-RASPT2/SA-3-RASSCF$(4, 7|0, 0|4, 15)$/ANO-L[321,21] gradient, thereby increasing the values of the displacements for the 225 cm^{-1} mode (from 1.48
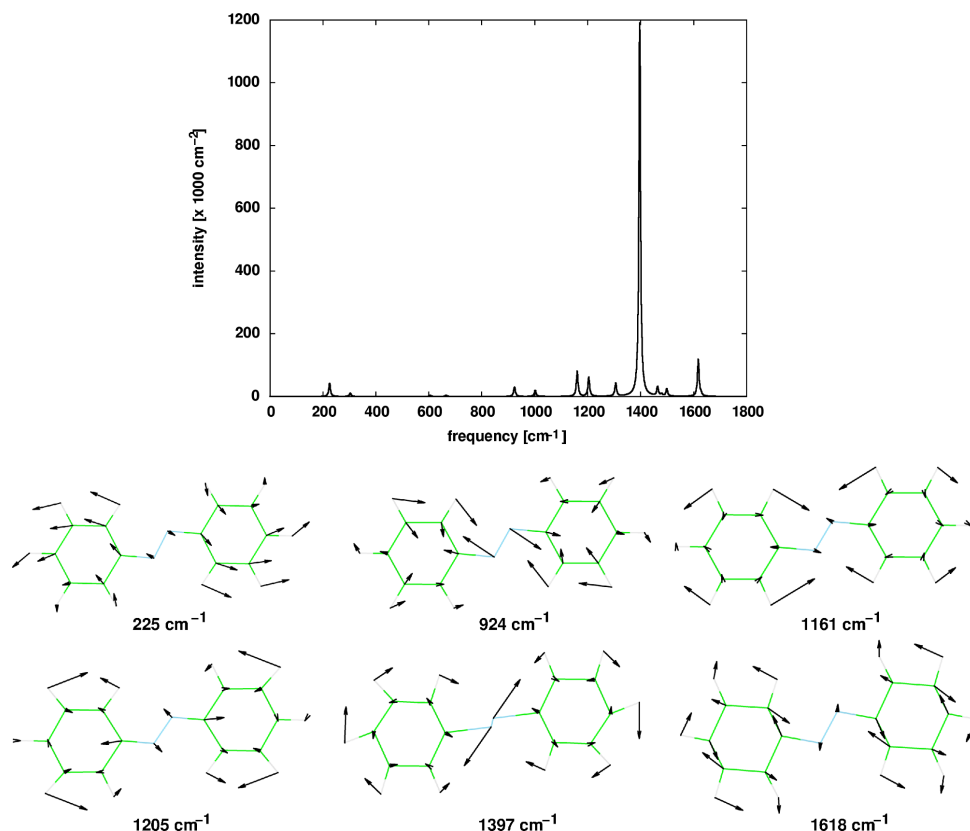
Figure 3.8: Spectral density of the $\pi\pi^*$ state. Most prominent normal modes are shown below. A weak damping factor $\gamma = 5$ cm^{-1} was applied to broaden the transitions.

to 1.75 Bohr$\sqrt{\text{amu}}$) and of the 1397 cm^{-1} mode (from 0.42 to 0.61 Bohr$\sqrt{\text{amu}}$) to match the experimental intensity distribution in their progressions which have their maxima in the fourth members (see LA spectra in Figure 3.12). Integrating over the spectral density one obtains the reorganization energy of the $\pi\pi^*$ state 4950 cm^{-1}. Subtracting the reorganization energy from the vertical transition energy (31450 cm^{-1}) gives an origin for the $\pi\pi^*$-band at 26500 cm^{-1}, in a good agreement with the experimental value of 27660 cm^{-1}[194]. In the simulations we shifted the origin to match the literature value of 27660 cm^{-1}.

The $\pi\pi^*$ state was optimized within D$_{2h}$ symmetry as the first root in the B$_u$ irreducible representation at MS-3-CASPT2/SA-3-RASSCF(4, 7|0, 0|4, 7)/ANO-L[321,21] where the active space comprises all valence π-orbitals of the system. An MS-Ansatz was necessary due to strong state mixing at CASSCF level along the relaxation path.

The ESA spectrum of the $\pi\pi^*$ state was calculated by state-averaging over twelve states in the A$_g$ irreducible representation (i.e. SS-CASPT2/SA-12-RASSCF
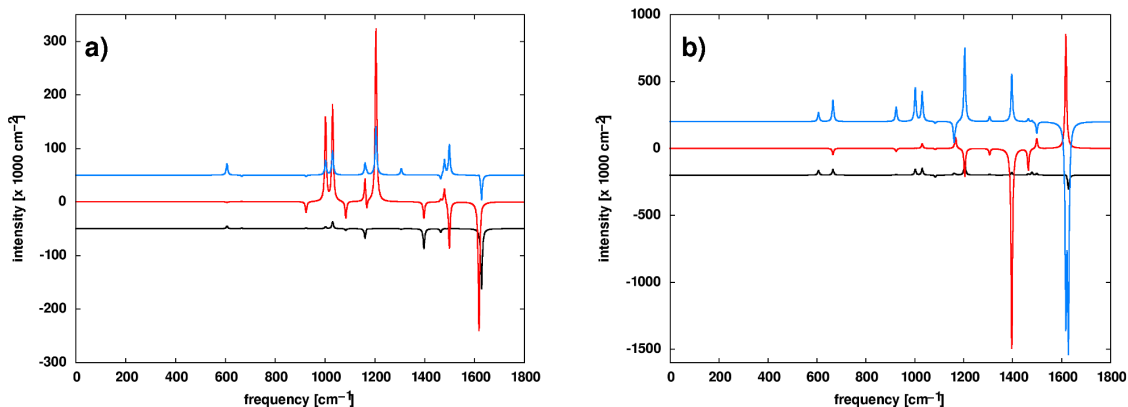
Figure 3.9: Spectral densities of the higher lying ESs 5 (black), 6 (red) and 7 (blue) giving rise to PA1 (a), as well as 8 (black), 11 (red) and 12 (blue) giving rise to PA2 (b) in Figure 3.3 of the main text obtained at SS-CASPT2/SA-12-RASSCF$(4, 7|0, 0|4, 15)$/ANO-L[321,21] level. Displacements d_{fk} used to construct the spectral densities are taken relative to the minimum $\pi\pi^*_{\min}$. Negative contributions arise due to the negative values for of the displacement d_{fk} for mode k. A weak damping factor $\gamma = 5$ cm^{-1} was applied to broaden the transitions.

$(4, 7|0, 0|4, 15)$/ ANO-L[321,21]). Among the twelve higher lying states six were selected as showing large transition dipole moments from the $\pi\pi^*$ state in the simulated spectral window and their gradients were computed at the same level. Figure 3.9 shows the spectral densities of these states with displacements obtained by applying the gradient projection approach. Figure 3.9a) shows the spectral densities of the three states responsible for the broad ESA feature PA1 around 600 nm, Figure 3.9b) shows the spectral densities of the three states responsible for the ESA feature PA2 around 450 nm in Figure 3.1 of the main article. The displacements of the higher lying states $\boldsymbol{d}_f$ can assume both positive and negative values (as already pointed out in Part I, Section 5.4).

3.5.6 Electronic structure of the $n\pi^*$ state and its ESA

The FC point is the doorway for the excited wavepacket to the $\pi\pi^*$ state. Its energy gradient or relative position in coordinate space with respect to the $\pi\pi^*$ minimum allows to extract the active modes governing the vibrational dynamics on the $\pi\pi^*$ state. The conical intersection between the $\pi\pi^*$ state $n\pi^*$ states CI$_{\pi\pi^*/n\pi^*}$ visited during the coherent dynamics on the $\pi\pi^*$ state is the doorway for the wavepacket to the $n\pi^*$ state. Similarly, its analysis can help to extract the active modes governing the vibrational dynamics on the $n\pi^*$ state. Figure 3.10 shows the spectral density of the $n\pi^*$ state. We resort to geometrical difference for the computation of the
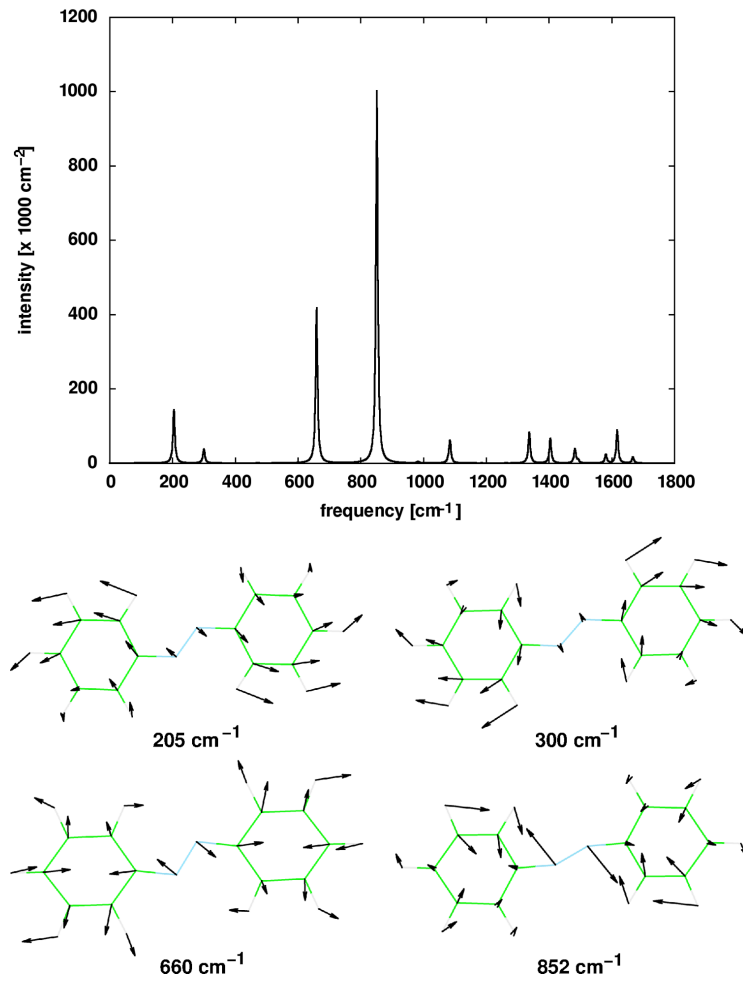
Figure 3.10: Spectral density of the $n\pi^*$ state. Most prominent normal modes are shown below. A weak damping factor $\gamma = 5$ cm^{-1} was applied to broaden the transitions.

displacements in this case as gradients generally show larger fluctuations in the crossing region due to wavefunction mixing. $\Delta \boldsymbol{Q}$ was calculated as the difference between the geometries of the energy minimum on the $n\pi^*$ state $n\pi^*_{\mathrm{min}}$ and $\mathrm{CI}_{\pi\pi^*/n\pi^*}$ as

$$\Delta \boldsymbol{Q} = \boldsymbol{Q}(n\pi^*_{\mathrm{min}}) - \boldsymbol{Q}(\mathrm{CI}_{\pi\pi^*/n\pi^*}) \tag{3.1}$$

$n\pi^*_{min}$ was optimized at the same level of the CI (relying on numerical RASPT2 gradients and employing a SS-CASPT2/SA-4-RASSCF$(4,5|0,0|4,3)$/ANO-L[321,21] level, where the active space comprises six frontier valence π-orbitals and two occupied lone pair orbitals localized on the NN fragment), to avoid method-related artifacts in the evaluation of the spectral density. $n\pi^*$-specific normal modes and frequencies were computed at SA-2-CASSCF(14,12) level, reoptimizing the geometry at this level as RASPT2 frequencies were not affordable. The default scaling
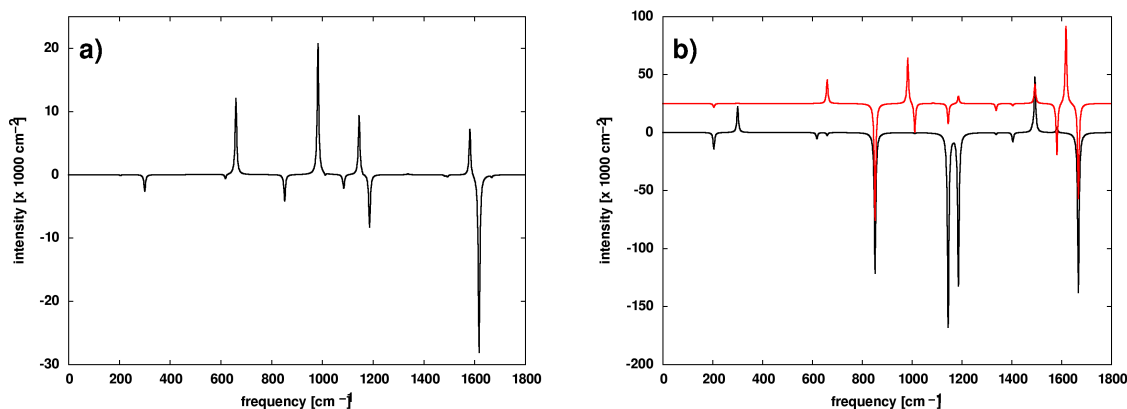
Figure 3.11: Spectral densities of the higher lying ESs 3 (black) giving rise to PA3 (a) in Figure 3.3 of the main article, as well as 6 (black) and 7 (red) giving rise to PA4 (b) in Figure 3.4 of the main article obtained at SS-CASPT2/SA-12-RASSCF$(4, 9|0, 0|4, 13)$/ANO-L[321,21] level. Displacements d_{fk} used to construct the spectral densities are taken relative to the minimum $n\pi^*_{\min}$. Negative contributions arise due to the negative values for of the displacement d_{fk} for mode k. A weak damping factor $\gamma = 5$ cm^{-1} was applied to broaden the transitions.s

factor for CASSCF frequencies of 0.91 was used. In Figure 3.10 it is evident that upon decay to the $n\pi^*$ state energy is stored in four low-to-mid frequency modes: 852 cm^{-1}, 660 cm^{-1}, 205 cm^{-1} and 300 cm^{-1}, all of them showing strong CNN and CCN bending deformations. The overall reorganization energy available to the system upon entering the $n\pi^*$ state is 10380 cm^{-1}.

Prior to computing the $n\pi^*$-specific ESA spectrum a geometry refinement was performed for $n\pi^*_{\min}$ within D$_{2h}$ symmetry as the first root in the B$_g$ irreducible representation at SS-CASPT2/SS-RASSCF$(4, 9|0, 0|4, 7)$/ANO-L[321,21] where the active space comprises all valence π-orbitals of the system and two lone pair orbitals localized on the NN fragment. The purely electronic excitation $\varepsilon_{n\pi^*}$ from the GS equilibrium, was computed with a larger active space comprising six additional virtual orbitals in the active space (i.e. SS-CASPT2/SS-RASSCF $(4, 9|0, 0|4, 13)$/ANO-L[321,21]) to 18250 cm^{-1}. The ESA spectrum was calculated by state-averaging over eight states in the A$_u$ irreducible representation (i.e. SS-CASPT2/SA-8-RASSCF $(4, 9|0, 0|4, 13)$/ANO-L[321,21]). Among the eight states four were selected as showing large transition dipole moments from the $n\pi^*$ state and their gradients were computed. Figures 3.11 shows the spectral densities of these states.

Figure 3.11a) shows the spectral density of the state responsible for the ESA feature PA3 at 360-400 nm in Figures 1 and 3 of the main article, Figure 3.11b) shows the spectral densities of the two states responsible for the ESA feature PA4

around 270-290 nm in Figure 2.

Note, that the 205 cm^{-1} mode shows an almost imperceptible peak in Figure 3.11a), thus, the potential energy surface of the higher lying state responsible for ESA PA3 is *not* displaced along this mode with respect to the $n\pi^*$ state, implying that the energy gap is independent of the dynamics in the 205 cm^{-1} mode. Therefore, within the limits of the applied theoretical model the coherent oscillations with 195 cm^{-1} frequency observed for PA3 cannot originate from the 205 cm^{-1} mode, but are rather the result of the interplay of the 660 cm^{-1} and 852 cm^{-1} modes, both showing appreciable displacements in Figure 3.11a).

3.5.7 Summary of $\pi\pi^*$ and $n\pi^*$ parameters

$\pi\pi^*$			$n\pi^*$		
State	ϵ^a (cm^{-1})	TDM (a.u.)	State	ϵ^a (cm^{-1})	TDM (a.u.)
$\pi\pi^*$	27660	2.55 0.00 1.70^b	$n\pi^*$	18250	0.00 0.00 0.00^b
root 5	43880	2.01 0.0 1.40	root 1	33557	0.52 0.00 0.21
root 6	41447	2.28 0.0 1.70	root 3	44683	1.81 0.00 0.98
root 7	42880	2.15 0.0 1.90	root 6	50814	1.51 0.00 1.21
root 8	50163	1.37 0.0 1.32	root 7	53228	1.23 0.00 1.41
root 11	43023	1.09 0.0 0.70			
root 12	38782	1.45 0.0 1.31			

Table 3.1: (*left*) Parameters for $\pi\pi^*$ and related signals (GSB, SE and ESA PA1 and PA2); (*right*) parameters for $n\pi^*$ and related signals (ESA PA3 and PA4). ^{a} Adiabatic energies with respect to the GS. ^{b} Transition dipoles with respect to the GS, all the other TDM describe $\pi\pi^* \to$ root x (*left*) or $n\pi^* \to$ root y (*right*) transitions.

3.5.8 Linear absorption spectra

Figure 3.12 shows linear absorption spectra measured (dashed red lines) at three different temperatures, room temperature in ethanol (this study, left), 77K in a rigid solvent (middle) and 20K in a dibenzyl crystal (right, [194]) together with the simulated spectra (solid black lines) using the $\pi\pi^*$ spectral density shown in Figure 3.8. While at room temperature the absorption band has no structure, clear vibrational signatures emerge at lower temperatures. In agreement with the computations the vibrational progression in the spectrum comes from the 1397 cm^{-1} NN stretching mode, while the 225 cm^{-1} CCN/CNN bending mode gives the fine-structure. For the simulation of the 20K spectrum the coupling to the continuum λ was reduced by half to 400 cm^{-1}.
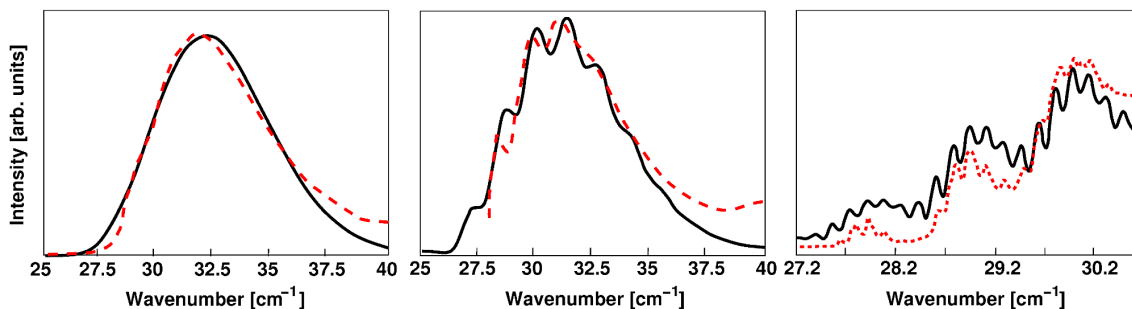
Figure 3.12: Experimental (red dashed) and simulated linear absorption spectra for *trans*-AB obtained at room temperature (left), at 77K (middle) and at 20K (right). Room temperature spectrum measured in this study, 77K spectrum, 20K spectrum (in a dibenzyl crystal taken from ref. 194.

We also report the linear spectra measured by Kovalenko *et al.*[177], which studies both the *cis*- and the *trans*-AB and extends to observed window to 200 nm.
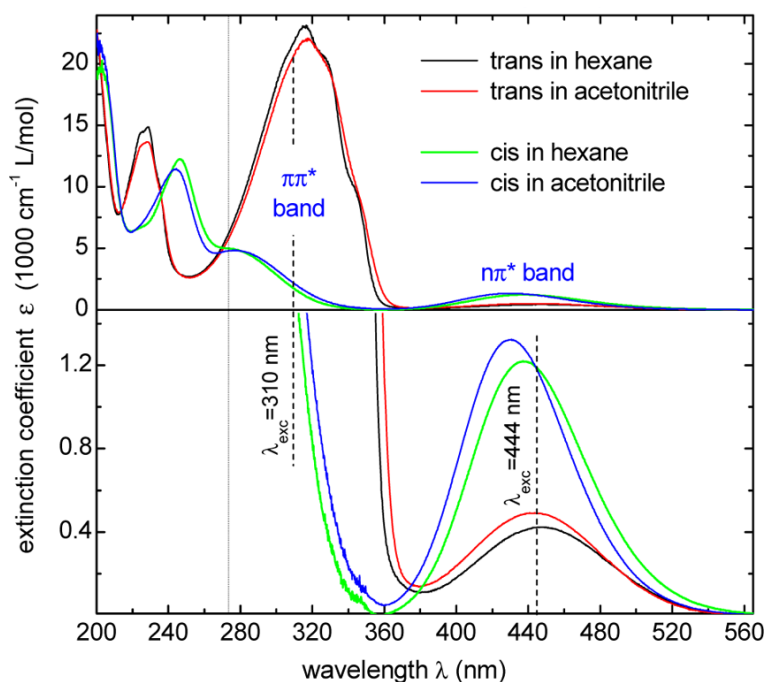
Figure 3.13: *trans*-AB and *cis*-AB absorption spectra in acetonitrile and *n*-hexane. Adapted from ref. 177.

3.5.9 Parameters for the OBO model

The parameters for the OBO model (Part I, Eq. 3.27) were chosen so to reproduce the $\pi\pi^*$ bandwidth in the linear absorption spectrum at room temperature (see Fig-
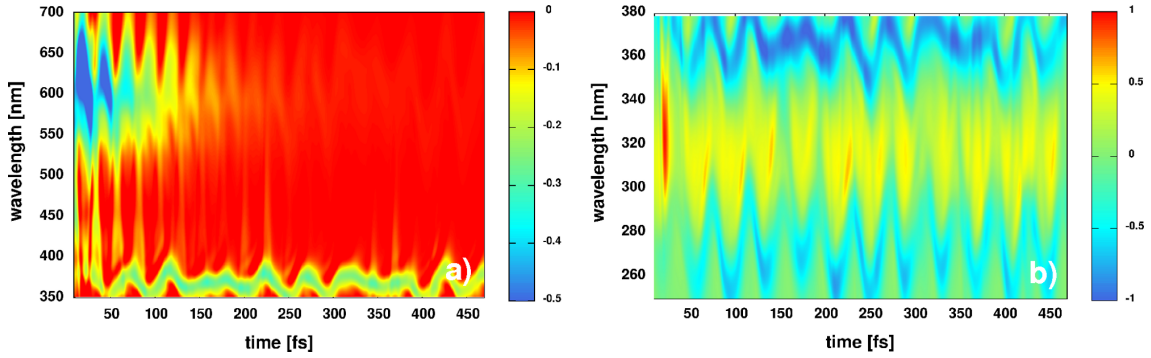
Figure 3.14: Theoretical TA data of *trans*-AB probed in the visible [350-700 nm] (a) and
ultraviolet [250-380 nm] (b) prior to convolution with a Gaussian in the time
domain.

ure 3.12) where inhomogeneous broadening contribution was neglected. The best fit
was obtained for coupling strength $\lambda = 800$ cm^{-1} and timescale $\gamma = 1/50$ fs^{-1}. For
simplification, the same OBO parameters were used for all states.

3.5.10 Accounting for finite pulse duration

Finite pulse duration is accounted for ad-hoc by convoluting the PP signal $S^{(3)}(t_2, \omega_3)$
with a Gaussian function in the time domain

$$S^{(3)}(t_2, \omega_3) = \int_{-\infty}^{+\infty} d\tau \ S^{(3)}(\tau, \omega_3) \ \exp\left(-\frac{(\tau - t_2)^2}{2\sigma^2}\right) \tag{3.2}$$

A standard deviation $\sigma = 16$ fs was used. Figure 3.14 shows the PP signal (Vis and
UV) prior to the convolution. Oscillations of PA1 [550-700 nm] with a period of
ca. 20 fs, i.e. the period of the 1397 cm^{-1} NN stretching mode, are clearly visible.
Furthermore, one can see oscillations of PA3 [350-400 nm] and PA4 [250-300 nm]
with a period of ca. 40 fs, the period of the CNN stretching mode with 850 cm^{-1}
frequency. Upon convolution most of these signatures are washed out.

3.5.11   Active Spaces
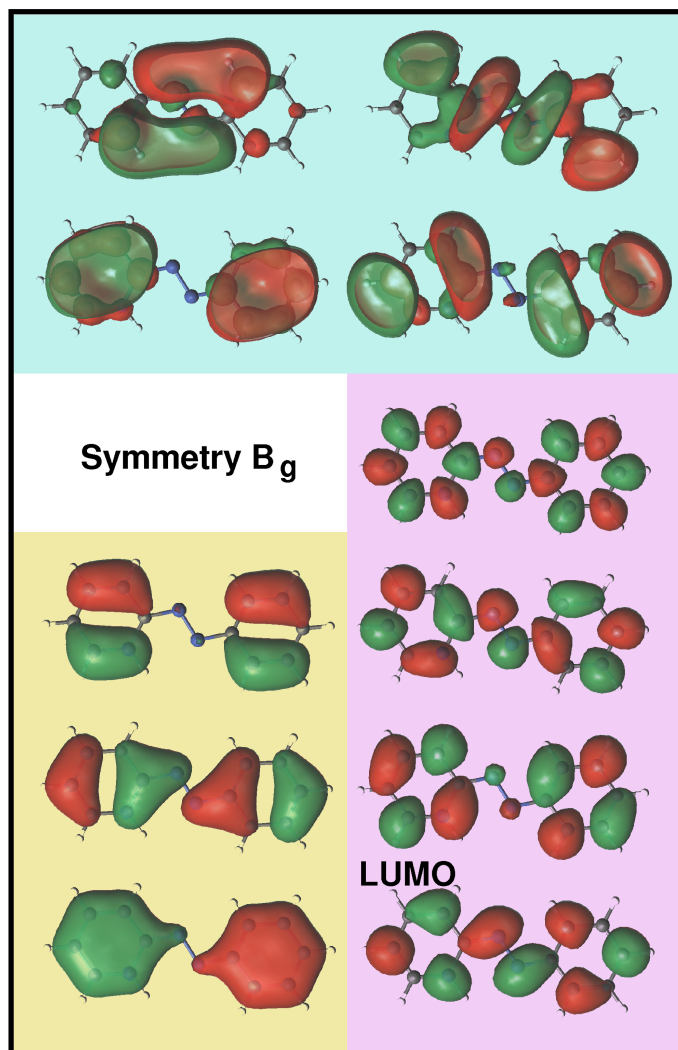
Figure 3.15: *trans*-AB orbitals of symmetry B_g used in the construction of the active spaces.
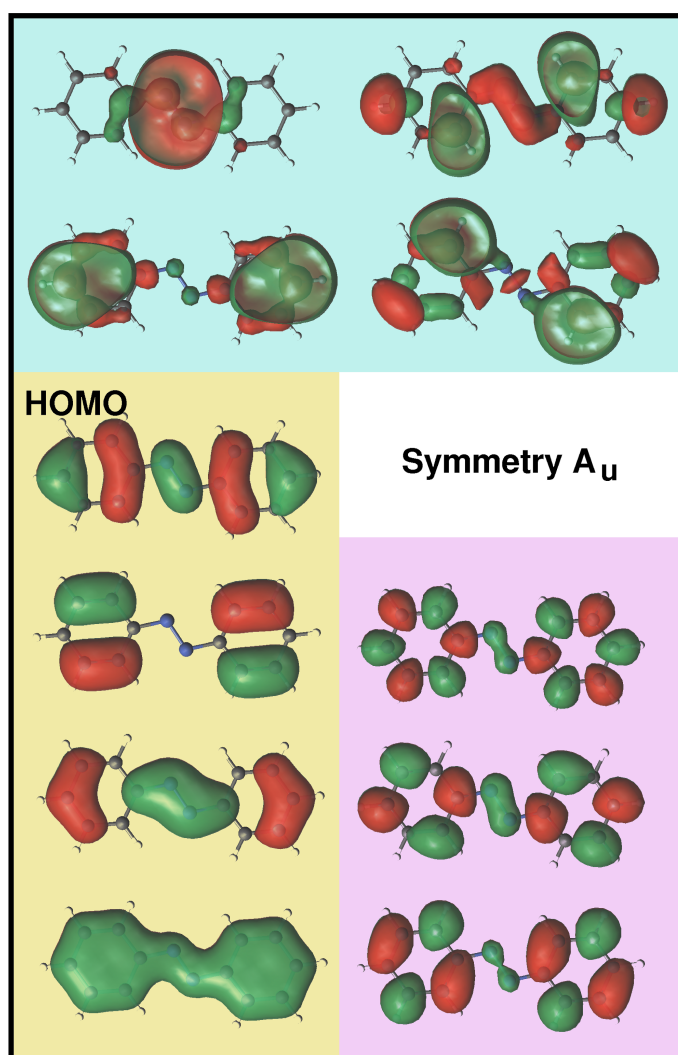
Figure 3.16: *trans*-AB orbitals of symmetry A_u used in the construction of the active spaces.

Concluding Remarks

My three years Phd activity was aimed at understanding the photoinduced reactions that take place when light illuminates samples of interacting organic chromophores, and at developing accurate theoretical and computational tools to simulate their spectroscopy, eventually gaining new physical insight into the novel emerging properties of a multichromophoric system.

Two major lines of research were pursued: the accurate computation of quantum mechanical properties of complex photoactive molecular aggregates (Part I) by state-of-the-art quantum chemistry approaches, and the description of their non-linear spectroscopy (Part II).

The first task was tackled by employing the very accurate multireference perturbative CASSCF/CASPT2 methodology, coupled to the Frenkel Exciton Hamiltonian approach. The coupling of electronic states to system vibrations was also accounted for, within the so-called spectral density functions, and demonstrated to be a key ingredient for a reliable modeling of system properties. The second goal was achieved by studying and applying the theoretical principles of non-linear spectroscopy, and by developing new approaches which allow to overcome many of the limitations of existing methods (as the PLDM-spectroscopy methodology, outlined in Part II, Chapter 3).

The complete parametrization of the Frenkel Exciton Hamiltonian of the LH2 system of *rhodopseudomonas acidophila* (Part III, Chapter 1), with the chromophores in their (electrostatic or polarizable) embedding, was obtained: this includes chromophore properties (e.g., excitation energies) and their electronic couplings (computed at the transition density level). The accuracy of the quantum-chemistry methods here employed and the precise description of intra- and inter- molecular

vibrations were combined to the simulation of non-linear spectroscopy (for the first time extended over the entire VIS-NIR region). This allows to understand the microscopic origin of the measured 2DES spectral signatures, and results in the acquisition of unprecedented physical insight into the photophysical properties of this system.

The relevance of intra-molecular vibrations in assisting inter-molecular energy transport processes, was presented in the study of the xanthorhodopsin carotenoid-to-retinal energy transfer (Part III, Chapter 2). We showed that in this system hot GS vibrations of the donor molecule can provide an enhanced donor-acceptor energy matching condition, and a higher probability for energy transfer. This picture was supported by measured 2DES signals, which reveal the occurred energy transfer process and confirm that vibrationally hot GS levels of the donor are populated during this event.

We have introduced a novel approach that combines the partial linearized density matrix (PLDM) methodology (which describes the system's dynamics) to the response function method of optical spectroscopy. This newly developed scheme, allows for extremely accurate simulation of non-linear optical spectroscopy (Part II, Chapter 3), and has been shown to overcame many of the limitations of existing techniques, in which either the system dynamics or the simulation of its spectroscopy (or both) rely on assumptions that restrict their regime of applicability. This achievement offers an exciting starting point from which to explore the development of accurate, yet computationally efficient, methods for calculating nonlinear electronic spectroscopy.

In conclusion, in this work we have shown that only by combining the "independent" results from accurate quantum chemical based methods and detailed spectroscopic experiments (as pump-probe and 2DES), the complex network of energy transfer routes can be disclosed, and a clear and detailed understanding of the system under scrutiny achieved. In this respect, the combination of state-of-the-art quantum chemical methods and exciton dynamics techniques to the response function theory of non-linear optics, as in the PLDM approach to spectroscopy, represents a fertile ground for the development of electronic spectroscopy in silico, i.e., fully ab-initio approaches to simulate cutting-edge non-linear transient spectroscopy experiments, towards the understanding of complex, biologically relevant, multichromophoric systems.

Acknowledgements

Il giorno prima dell'esame di ingresso al dottorato in Chimica dell'Università di Bologna mi resi conto, improvvisamente, che se non fossi riuscito nell'impresa non avrei probabilmente cercato un'altra possibilità: non mi interessava il dottorato in generale, mi aveva affascinato il progetto che mi era stato proposto da Marco e Simone. Questo mi chiarì che la strada della mia vita, in qualche modo, sarebbe passata da questa città: Bologna. E non solo per quanto riguardava il lavoro, ma proprio tutta la vita. Era tutto vero: quanta strada fatta da allora! Il primo ringraziamento va quindi a Dio che "infondo ha preso lui l'iniziativa" e mi ha accompagnato (e accompagna) continuamente, attraverso il cuore che mi ha dato e i volti di amici che non posso scordare.

First things first: il primo grazie va al mio supervisore, Prof. Marco Garavelli: innanzitutto per avermi voluto nel gruppo, per la costante disponibilità, l'attenzione, l'intelligente consiglio, la simpatia (romagnola)! L'aiuto (necessario per me) a dire "Basta, chiudiamo questo lavoro!". La grande fiducia riservatami. Un grazie altrettanto sentito a Simone Taioli, per la grande pazienza, per avermi sostenuto a distanza, la disponibilità continua a un confronto, i consigli innumerevoli.

Un ringraziamento sincero a tutte le persone del gruppo di ricerca di Bologna. Artur in primis: non è possibile misurare il numero di domande che ti ho fatto (come direbbe Sean, "Sorra-bout-that!"), e quanto ho imparato ogni volta che abbiamo discusso di qualche argomento. Non sarei sicuramente riuscito a fare molta strada senza di te e il tuo aiuto costate (santo subito!). E Anna. Mohsen & Family: it was great to meet you (indeed!), to share our lives, and to become "uncle Francisco"

for your daughters, Hend and Shatha! Angelo (per le cene, il basket..., qualche chiacchierata significativa), Irene (mi hai fatto morire dal ridere quando mi hai detto, dopo una settimana che ero rimasto a Trento: "Ci sei mancato, non c'era nessuno che diceva stupidaggini!!". Eh si, sono fatto così e son contento di diventare pian piano libero di essere me stesso everywhere), Samira (for some true conversations we had), Julieta, Javier, Vishal, Sean. Giulia, per avermi messo alla prova come vice aiuto tutor della tua tesi! Ivan e Baptiste per i periodi condivisi qua a Bologna nelle vostre visite. Last but not least, Flavia (grande voglia di imparare, grinta e simpatia: tanta stima!) e Ettore (il camminatore).

Doverosissimo ringraziamento anche agli amici e colleghi dei gruppi attigui al nostro. Al primo posto, con oscar per interpretazione del ruolo di mamma in seconda, amica, segretaria, consigliera, calendario portatile, conforto nell'ansia, sostegno nella disperazione, positività (nei giorni di sole, s'intende), etc, etc, Signori e Signore: Sofia! Grazie per tutto (per la compagnia, per avermi ricordato $n >> 1$ scadenze, per il frontespizio della tesi... e il codice latex della tesi...! Haha! Mi chiedo a questo punto cosa abbia fatto io per questa tesi!!). Marco Macis e Denise (compagni di avventura ogni giorno per due/tre anni), Marco Dallavalle (bello conoscerti!), Edoardo (grande Edo), Tainah (per il Sanremo continuo...!). Arianna, Otello, Lara.

A special thanks to Prof. David Coker who hosted me for five month in his lab at Boston University (MA, USA): thanks for the always interesting discussions, the 4th of July party (now I know what 4th of July really means!), the passion for science which reawakened my desire to do research. And thanks to all the Coker Group: Justin and Brendan (I'm so happy to have met you guys, and for the friendship with you, and the science we have done together, Justin: let's go on!), Thomas, Alex, Manav, Mi Kyung. I enjoyed very much the time spent there! Thanks.

Grazie per l'ospitalità e il lavoro svolto insieme anche al gruppo Molecolab di Pisa: grazie alla Prof. Benedetta Mennucci, a Sandro, Lorenzo e Daniele!

Grazie per l'accoglienza, ogni volta che sono salito, ai dottorandi FBK di Trento: Tommaso, Martina, Andrea. Sono contento che ci siamo iniziati a conoscere!

Ora gli innumerevoli amici che hanno accompagnato questo percorso, allargandone continuamente l'orizzonte (come direbbe il contadino friulano de *La leggenda del pianista sull'oceano*, riferendo quello che aveva sentito dire dal mare, la prima volta che lui l'aveva visto: "omeni, manega de cornui, la vita s'é immensa, volé capirlo o no.. immensa!").

A Bologna: don Marco (per la fondamentale compagnia, soprattutto nel primo anno), Moro Luca (uno dei primi amici), Nik & famiglia, Andre Silvi (i nostri pranzi),

Bibliography

[1] Kasha, M. *Reviews of Modern Physics* **1959**, *31*(1), 162–169.

[2] Georgi, H. *Annual Review of Nuclear and Particle Science* **1993**, *43*(1), 209–252.

[3] Davydov, A. *Theory of Molecular Excitons;* Mc. Graw-Hill, 1962.

[4] Hu, X.; Ritz, T.; Damjanovic, A.; Autenrieth, F.; Schulten, K. *Quarterly Reviews of Biophysics* **2002**, *35*(01).

[5] Scholes, G. D.; Fleming, G. R. In *Adventures in Chemical Physics;* John Wiley & Sons, Inc., 2005; pages 57–129.

[6] Cogdell, R. J.; Gardiner, A. T.; Microbiology Society, 2001; pages 120–122.

[7] Clegg, R. M.; Sener, M.; Govindjee. In Alfano, R. R., Ed., *Optical Biopsy VII.* SPIE, 2010.

[8] Roos, B. O. *Ab Initio Methods in Quantum Chemistry: Part II;* Wiley: Chicester, UK, 1987.

[9] Andersson, K.; Malmqvist, P.; Roos, B. O.; Sadlej, A. J.; Wolinski, K. *J. Phys. Chem.* **1990**, *94*(14), 5483–5488.

[10] Aquilante, F.; Autschbach, J.; Carlson, R. K.; Chibotaru, L. F.; Delcey, M. G.; De Vico, L.; Fdez. Galván, I.; Ferré, N.; Frutos, L. M.; Gagliardi, L.; Garavelli, M.; Giussani, A.; Hoyer, C. E.; Li Manni, G.; Lischka, H.; Ma, D.; Malmqvist, P.; Müller, T.; Nenov, A.; Olivucci, M.; Pedersen, T. B.; Peng, D.; Plasser, F.; Pritchard, B.; Reiher, M.; Rivalta, I.; Schapiro, I.; Segarra-Martí, J.; Stenrup,

M.; Truhlar, D. G.; Ungur, L.; Valentini, A.; Vancoillie, S.; Veryazov, V.; Vysotskiy, V. P.; Weingart, O.; Zapata, F.; Lindh, R. *J. Comp. Chem.* **2016**, *37*(5), 506–541.

[11] Lee, M. K.; Coker, D. F. *The Journal of Physical Chemistry Letters* **2016**, *7*(16), 3171–3178.

[12] Jelley, E. E. *Nature* **1936**, *138*(3502), 1009–1010.

[13] Kasha, M. *Radiation Research* **1963**, *20*(1), 55.

[14] Modern Quantum Chemistry: Introduction to Advanced Electronic Structure Theory. Szabo, A.; Ostlund, N. S. **1996**.

[15] Cox, S. R.; Williams, D. E. *Journal of Computational Chemistry* **1981**, *2*(3), 304–323.

[16] May, V.; Kühn, O. *Charge and Energy Transfer Dynamics in Molecular Systems;* Wiley-VCH, 2011.

[17] Foresman, J. B.; Head-Gordon, M.; Pople, J. A.; Frisch, M. J. *The Journal of Physical Chemistry* **1992**, *96*(1), 135–149.

[18] Pople, J. A.; Seeger, R.; Krishnan, R. *International Journal of Quantum Chemistry* **2009**, *12*(S11), 149–163.

[19] Bartlett, R. J. *Annual Review of Physical Chemistry* **1981**, *32*(1), 359–401.

[20] Szalay, P. G.; Müller, T.; Gidofalvi, G.; Lischka, H.; Shepard, R. *Chemical Reviews* **2011**, *112*(1), 108–181.

[21] Aquilante, F.; De Vico, L.; Ferré, N.; Ghigo, G.; Malmqvist, P.; Neogrády, P.; Pedersen, T. B.; Pitoňák, M.; Reiher, M.; Roos, B. O.; Serrano-Andrés, L.; Urban, M.; Veryazov, V.; Lindh, R. *J. Comput. Chem.* **2010**, *31*(1), 224–247.

[22] Roos, B. O. In *Advances in Chemical Physics;* John Wiley & Sons, Inc.; pages 399–445.

[23] Malmqvist, P.; Pierloot, K.; Shahi, A. R. M.; Cramer, C. J.; Gagliardi, L. *J. Chem. Phys.* **2008**, *128*(20).

[24] Malmqvist, P. A.; Rendell, A.; Roos, B. O. *The Journal of Physical Chemistry* **1990**, *94*(14), 5477–5482.

[25] Finley, J.; Malmqvist, P.-Å.; Roos, B. O.; Serrano-Andrés, L. *Chemical Physics Letters* **1998**, *288*(2-4), 299–306.

[26] Malmqvist, P.; Roos, B. O. *Chem. Phys. Lett.* **1989**, *155*(2), 189 – 194.

[27] Krueger, B. P.; Scholes, G. D.; Fleming, G. R. *The Journal of Physical Chemistry B* **1998**, *102*(27), 5378–5386.

[28] Lee, M. K.; Huo, P.; Coker, D. F. *Annu. Rev. Phys. Chem* **2016**, *67*, 639–68.

[29] Nitzan, A. *Chemical Dynamics in Condensed Phases;* Oxford Univ. Press, 2006.

[30] Mukamel, S. *Principles of nonlinear optical spectroscopy*, Vol. 523; Oxford Univ. Press, 1995.

[31] Moca, R.; Meech, S. R.; Heisler, I. A. *The Journal of Physical Chemistry B* **2015**, *119*(27), 8623–8630.

[32] Cario, G.; Franck, J. *Z. Physik* **1922**, *11*, 161–166.

[33] Engel, G. S.; Calhoun, T. R.; Read, E. L.; Ahn, T.-K.; Mančal, T.; Cheng, Y.-C.; Blankenship, R. E.; Fleming, G. R. *Nature* **2007**, *446*(7137), 782–786.

[34] Lee, H.; Cheng, Y.-C.; Fleming, G. R. *Science* **2007**, *316*(5830), 1462–1465.

[35] Collini, E.; Wong, C. Y.; Wilk, K. E.; Curmi, P. M. G.; Brumer, P.; Scholes, G. D. *Nature* **2010**, *463*(644–647).

[36] Förster, T. *Annalen der Physik* **1948**, *437*(1-2), 55–75.

[37] Ishizaki, A.; Fleming, G. R. *Annual Review of Condensed Matter Physics* **2012**, *3*(1), 333–361.

[38] Zhang, W. M.; Meier, T.; Chernyak, V.; Mukamel, S. *J. Chem. Phys.* **1998**, *108*(18), 7763–7774.

[39] Min Zhang, W.; Meier, T.; Chernyak, V.; Mukamel, S. *Philos. Trans. R. Soc. A* **1998**, *356*(1736), 405–419.

[40] Yang, M.; Fleming, G. R. *Chem. Phys.* **2002**, *275*(1-3), 355–372.

[41] Huo, P.; Coker, D. F. *J. Chem. Phys.* **2011**, *135*, 201101.

[42] Bonella, S.; Coker, D. F. *J. Chem. Phys.* **2001**, *114*(18), 7778–7789.

[43] Meyer, H.-D.; Miller, W. H. *J. Chem. Phys.* **1979**, *70*, 3214–3223.

[44] Stock, G.; Thoss, M. *Phys. Rev. Lett.* **1997**, *78*(4), 578–581.

[45] Herman, M. F.; Kluk, E. *Chemical Physics* **1984**, *91*(1), 27–34.

[46] Kay, K. G. *Chem. Phys.* **2006**, *322*(1-2), 3–12.

[47] Bonella, S.; Coker, D. F. *J. Chem. Phys.* **2005**, *122*, 194102.

[48] Huo, P.; Coker, D. F. *J. Chem. Phys.* **2012**, *137*, 22A535.

[49] Huo, P.; Coker, D. F. *Molecular Physics* **2012**, *110*(9-10), 1035–1052.

[50] Brixner, T.; Stenger, J.; Vaswani, H. M.; Cho, M.; Blankenship, R. E.; Fleming, G. R. *Nature* **2005**, *434*(7033), 625–628.

[51] Brańczyk, A. M.; Turner, D. B.; Scholes, G. D. *Ann. Phys.* **2014**, *526*(1-2), 31–49.

[52] Segatta, F.; Cupellini, L.; Jurinovich, S.; Mukamel, S.; Dapor, M.; Taioli, S.; Garavelli, M.; Mennucci, B. *Journal of the American Chemical Society* **2017**, *139*(22), 7558–7567.

[53] Provazza, J.; Segatta, F.; Garavelli, M.; Coker, D. F. *Journal of Chemical Theory and Computation* **2018**, *14*(2), 856–866.

[54] Berera, R.; van Grondelle, R.; Kennis, J. T. M. *Photosynthesis Research* **2009**, *101*(2-3), 105–118.

[55] Cerullo, G. *Science* **2002**, *298*(5602), 2395–2398.

[56] Nishimura, K.; Rondonuwu, F. S.; Fujii, R.; Akahane, J.; Koyama, Y.; Kobayashi, T. *Chemical Physics Letters* **2004**, *392*(1-3), 68–73.

[57] Jonas, D. M. *Annual Review of Physical Chemistry* **2003**, *54*(1), 425–463.

[58] Levenson, M. D.; Eesley, G. L. *Applied Physics* **1979**, *19*(1), 1–17.

[59] Fuller, F. D.; Ogilvie, J. P. *Annual Review of Physical Chemistry* **2015**, *66*(1), 667–690.

[60] Halpin, A.; Johnson, P. J. M.; Tempelaar, R.; Murphy, R. S.; Knoester, J.; Jansen, T. L. C.; Miller, R. J. D. *Nature Chemistry* **2014**, *6*(3), 196–201.

[61] Panitchayangkoon, G.; Hayes, D.; Fransted, K. A.; Caram, J. R.; Harel, E.; Wen, J.; Blankenship, R. E.; Engel, G. S. *Proceedings of the National Academy of Sciences* **2010**, *107*(29), 12766–12770.

[62] Hybl, J. D.; Albrecht, A. W.; Faeder, S. M. G.; Jonas, D. M. *Chemical Physics Letters* **1998**, *297*(3-4), 307–313.

[63] Cowan, M. L.; Bruner, B. D.; Huse, N.; Dwyer, J. R.; Chugh, B.; Nibbering, E. T. J.; Elsaesser, T.; Miller, R. J. D. *Nature* **2005**, *434*(7030), 199–202.

[64] Varillas, R. B.; Candeo, A.; Viola, D.; Garavelli, M.; Silvestri, S. D.; Cerullo, G.; Manzoni, C. *Optics Letters* **2014**, *39*(13), 3849.

[65] Fidler, A. F.; Singh, V. P.; Long, P. D.; Dahlberg, P. D.; Engel, G. S. *Nature Communications* **2014**, *5*.

[66] Tannor, D. J. *Introduction to Quantum Mechanics, A Time Dependent Perspective;* University Science Books, 2006.

[67] Hamm, P.; Zanni, M. *Concepts and Methods of 2D Infrared Spectroscopy;* Cambridge University Press, New York, 2011.

[68] Abramavicius, D.; Palmieri, B.; Voronine, D. V.; Sanda, F.; Mukamel, S. *Chem. Rev.* **2009**, *109*(6), 2350–2408.

[69] Abramavicius, D.; Valkunas, L.; Mukamel, S. *EPL-Europhys Lett* **2007**, *80*(1), 17005.

[70] Bonella, S.; Montemayor, D.; Coker, D. F. *P. Natl. Acad. Sci. USA* **2005**, *102*(19), 6715–6719.

[71] Huo, P.; Miller, T. F.; Coker, D. F. *J. Chem. Phys.* **2013**, *139*, 151103.

[72] Dunkel, E.; Bonella, S.; Coker, D. F. *J. Chem. Phys.* **2008**, *129*, 114106.

[73] Wang, H.; Song, X.; Chandler, D.; Miller, W. H. *J. Chem. Phys.* **1999**, *110*(1999), 4828–4840.

[74] Fetherolf, J. H.; Berkelbach, T. C. *The Journal of Chemical Physics* **2017**, *147*(24), 244109.

[75] Lee, M. K.; Bravaya, K. B.; Coker, D. F. *Journal of the American Chemical Society* **2017**, *139*(23), 7803–7814.

[76] Basinskaite, E.; Butkus, V.; Abramavicius, D.; Valkunas, L. *Photosynth. Res.* **2014**, *121*, 95–106.

[77] Engel, G. S.; Calhoun, T. R.; Read, E. L.; Ahn, T. K.; Mančal, T.; Cheng, Y.-C.; Blankenship, R. E.; Fleming, G. R. *Nature* **2007**, *446*(7137), 782–786.

[78] Collini, E.; Wong, C. Y.; Wilk, K. E.; Curmi, P. M. G.; Brumer, P.; Scholes, G. D. *Nature* **2010**, *463*(7281), 644–647.

[79] Zigmantas, D.; Read, E. L.; Mančal, T.; Brixner, T.; Gardiner, A. T.; Cogdell, R. J.; Fleming, G. R. *Proc. Natl. Acad. Sci. U.S.A.* **2006**, *103*(34), 12672–12677.

[80] Rancova, O.; Abramavicius, D. *J. Phys. Chem. B* **2014**, *118*(27), 7533–7540.

[81] Tempelaar, R.; Jansen, T. L. C.; Knoester, J. *J. Phys. Chem. B* **2014**, *118*(45), 12865–12872.

[82] van der Vegte, C. P.; Prajapati, J. D.; Kleinekathöfer, U.; Knoester, J.; Jansen, T. L. C. *J. Phys. Chem. B* **2015**, *119*(4), 1302–1313.

[83] Olbrich, C.; Jansen, T. L. C.; Liebers, J.; Aghtar, M.; Strümpfer, J.; Schulten, K.; Knoester, J.; Kleinekathöfer, U. *J. Phys. Chem. B* **2011**, *115*(26), 8609–8621.

[84] McDermott, G.; Prince, S. M.; Freer, A. A.; Hawthornthwaite-Lawless, A. M.; Papiz, M. Z.; Cogdell, R. J.; Isaacs, N. W. *Nature* **1995**, *374*(6522), 517–521.

[85] Mirkovic, T.; Ostroumov, E. E.; Anna, J. M.; van Grondelle, R.; Govindjee.; Scholes, G. D. *Chem. Rev.* **2017**, *117*(2), 249–293.

[86] Scholes, G. D.; Gould, I. R.; Cogdell, R. J.; Fleming, G. R. *J. Phys. Chem. B* **1999**, *103*(13), 2543–2553.

[87] Tretiak, S.; Middleton, C.; Chernyak, V.; Mukamel, S. *J. Phys. Chem. B* **2000**, *104*(18), 4519–4528.

[88] Jang, S.; Dempster, S. E.; Silbey, R. J. *J. Phys. Chem. B* **2001**, *105*(28), 6655–6665.

[89] Novoderezhkin, V. I.; van Grondelle, R. *J. Phys. Chem. B* **2013**, *117*(38), 11076–11090.

[90] Jang, S.; Rivera, E.; Montemayor, D. *J. Phys. Chem. Lett.* **2015**, *6*(6), 928–934.

[91] Anda, A.; Hansen, T.; De Vico, L. *J. Chem. Theory Comput.* **2016**, *12*(3), 1305–1313.

[92] Stross, C.; van der Kamp, M. W.; Oliver, T. A. A.; Harvey, J. N.; Linden, N.; Manby, F. R. *J. Phys. Chem. B* **2016**, *120*(44), 11449–11463.

[93] Cupellini, L.; Jurinovich, S.; Campetella, M.; Caprasecca, S.; Guido, C. A.; Kelly, S. M.; Gardiner, A. T.; Cogdell, R.; Mennucci, B. *J. Phys. Chem. B* **2016**, *120*(44), 11348–11359.

[94] Damjanović, A.; Kosztin, I.; Kleinekathöfer, U.; Schulten, K. *Phys. Rev. E* **2002**, *65*(3), 031919.

[95] Cogdell, R. J.; Gall, A.; Köhler, J. *Q. Rev. Biophys.* **2006**, *39*(3), 227–324.

[96] Novoderezhkin, V. I.; van Grondelle, R. *Phys. Chem. Chem. Phys.* **2010**, *12*(27), 7352–14.

[97] Ostroumov, E. E.; Mulvaney, R. M.; Cogdell, R. J.; Scholes, G. D. *Science* **2013**, *340*(6128), 52–56.

[98] Ferretti, M.; Hendrikx, R.; Romero, E.; Southall, J.; Cogdell, R. J.; Novoderezhkin, V. I.; Scholes, G. D.; van Grondelle, R. *Sci. Rep.* **2016**, *6*(November 2015), 20834.

[99] Cerullo, G.; Polli, D.; Lanzani, G.; De Silvestri, S.; Hashimoto, H.; Cogdell, R. J. *Science* **2002**, *298*(5602), 2395–2398.

[100] Georgakopoulou, S.; Frese, R. N.; Johnson, E.; Koolhaas, C.; Cogdell, R. J.; van Grondelle, R.; van der Zwan, G. *Biophys. J.* **2002**, *82*(4), 2184–2197.

[101] Papiz, M. Z.; Prince, S. M.; Howard, T.; Cogdell, R. J.; Isaacs, N. W. *J. Mol. Biol.* **2003**, *326*(5), 1523–1538.

[102] Yanai, T.; Tew, D. P.; Handy, N. C. *Chem. Phys. Lett.* **2004**, *393*(1-3), 51–57.

[103] Curutchet, C.; Muñoz Losa, A.; Monti, S.; Kongsted, J.; Scholes, G. D.; Mennucci, B. *J. Chem. Theory Comput.* **2009**, *5*, 1838–1848.

[104] Higashi, M.; Kosugi, T.; Hayashi, S.; Saito, S. *J. Phys. Chem. B* **2014**, *118*(37), 10906–10918.

[105] Higashi, M.; Saito, S. *J. Chem. Theory Comput.* **2016**.

[106] Curutchet, C.; Scholes, G. D.; Mennucci, B.; Cammi, R. *J. Phys. Chem. B* **2007**, *111*(46), 13253–13265.

[107] Pajusalu, M.; Rätsep, M.; Trinkunas, G.; Freiberg, A. *ChemPhysChem* **2011**, *12*(3), 634–644.

[108] Gaussian 09, Revision D.01; gaussian, inc: Wallingford, ct, 2009. Frisch, M. J.; Trucks, G. W.; Schlegel, H. B.; Scuseria, G. E.; Robb, M. A.; Cheeseman, J. R.; Scalmani, G.; Barone, V.; Mennucci, B.; Petersson, G. A.; Nakatsuji, H.; Caricato, M.; Li, X.; Hratchian, H. P.; Izmaylov, A. F.; Bloino, J.; Zheng, G.; Sonnenberg, J. L.; Hada, M.; Ehara, M.; Toyota, K.; Fukuda, R.; Hasegawa, J.; Ishida, M.; Nakajima, T.; Honda, Y.; Kitao, O.; Nakai, H.; Vreven, T.; Montgomery, Jr., J. A.; Peralta, J. E.; Ogliaro, F.; Bearpark, M.; Heyd, J. J.; Brothers, E.; Kudin, K. N.; Staroverov, V. N.; Kobayashi, R.; Normand, J.; Raghavachari, K.; Rendell, A.; Burant, J. C.; Iyengar, S. S.; Tomasi, J.; Cossi, M.; Rega, N.; Millam, J. M.; Klene, M.; Knox, J. E.; Cross, J. B.; Bakken, V.; Adamo, C.; Jaramillo, J.; Gomperts, R.; Stratmann, R. E.; Yazyev, O.; Austin, A. J.; Cammi, R.; Pomelli, C.; Ochterski, J. W.; Martin, R. L.; Morokuma, K.; Zakrzewski, V. G.; Voth, G. A.; Salvador, P.; Dannenberg, J. J.; Dapprich, S.; Daniels, A. D.; Farkas, O.; Foresman, J. B.; Ortiz, J. V.; Cioslowski, J.; Fox, D. J.

[109] Guareschi, R.; Valsson, O.; Curutchet, C.; Mennucci, B.; Filippi, C. *J. Phys. Chem. Lett.* **2016**, *7*, 4547–4553.

[110] Read, E. L.; Schlau-Cohen, G. S.; Engel, G. S.; Georgiou, T.; Papiz, M. Z.; Fleming, G. R. *J. Phys. Chem. B* **2009**, *113*(18), 6495–6504.

[111] Harel, E.; Engel, G. S. *Proc. Natl. Acad. Sci.* **2012**, *109*(3), 706–711.

[112] Ma, Y.; Cogdell, R.; Gillbro, T. *J. Phys. Chem. B* **1997**, *101*(Strain 10050), 1087–1095.

[113] Salverda, J. M.; van Mourik, F.; van der Zwan, G.; van Grondelle, R. *J. Phys. Chem. B* **2000**, *104*(47), 11395–11408.

[114] Ihalainen, J. A.; Linnanto, J.; Myllyperkiö, P.; van Stokkum, I. H. M.; Ücker, B.; Scheer, H.; Korppi-Tommola, J. E. I. *J. Phys. Chem. B* **2001**, *105*(40), 9849–9856.

[115] Pullerits, T.; Hess, S.; Herek, J. L.; Sundstrom, V. *J. Phys. Chem. B* **1997**, *101*(49), 10560–10567.

[116] Agarwal, R.; Yang, M.; Xu, Q.-H.; Fleming, G. R. *J. Phys. Chem. B* **2001**, *105*(9), 1887–1894.

[117] Wendling, M.; Mourik, F. V.; van Stokkum, I. H.; Salverda, J. M.; Michel, H.; Grondelle, R. V. *Biophys. J.* **2003**, *84*(1), 440–449.

[118] Hess, S.; Feldchtein, F.; Babin, A.; Nurgaleev, I.; Pullerits, T.; Sergeev, A.; Sundström, V. *Chem. Phys. Lett.* **1993**, *216*(3-6), 247–257.

[119] Ostroumov, E. E.; Mulvaney, R. M.; Anna, J. M.; Cogdell, R. J.; Scholes, G. D. *J. Phys. Chem. B* **2013**, *117*(38), 11349–11362.

[120] Kleinschmidt, M.; Marian, C. M.; Waletzke, M.; Grimme, S. *J. Chem. Phys.* **2009**, *130*(4), 044708–11.

[121] Polívka, T.; Sundström, V. *Chem. Rev.* **2004**, *104*(4), 2021–71.

[122] Polli, D.; Cerullo, G.; Lanzani, G.; De Silvestri, S.; Hashimoto, H.; Cogdell, R. J. *Biophys. J.* **2006**, *90*(7), 2486–2497.

[123] Cong, H.; Niedzwiedzki, D. M.; Gibson, G. N.; LaFountain, A. M.; Kelsh, R. M.; Gardiner, A. T.; Cogdell, R. J.; Frank, H. A. *J. Phys. Chem. B* **2008**, *112*(34), 10689–10703.

[124] Krueger, B. P.; Scholes, G. D.; Jimenez, R.; Fleming, G. R. *J. Phys. Chem. B* **1998**, *102*(12), 2284–2292.

[125] Curutchet, C.; Mennucci, B. *Chem Rev.* **2017**, *117*(2), 294–343.

[126] *Amber14*; university of california, san francisco., ca, 2015. Case, D.; Berryman, J.; Betz, R.; Cerutti, D.; Cheatham III, T.; Darden, T.; Giese, T.; Gohlke, H.; Goetz, A.; Homeyer, N.; Izadi, S.; Janowski, P.; Kaus, J.; Kovalenko, A.; Lee, T.; LeGrand, S.; Li, P.; Luchko, T.; Luo, R.; Madej, B.; Merz, K.; Monard, G.; Needham, P.; Nguyen, H.; Nguyen, H.; Omelyan, I.; Onufriev, A.; Roe, D.; Roitberg, A.; Salomon-Ferrer, R.; Simmerling, C.; Smith, W.; Swails, J.; Walker, R.; Wang, J.; Wolf, R.; Wu, X.; Zhang, W.; Seabra, G.; Wong, K.; Paesani, F.; Vanicek, J.; Wolf, R.; Liu, J.; Wu, X.; York, D.; Kollman, P.

[127] Hornak, V.; Abel, R.; Okur, A.; Strockbine, B.; Roitberg, A.; Simmerling, C. *Proteins: Struct., Funct., Bioinformatics* **2006**, *65*(3), 712–725.

[128] Ceccarelli, M.; Procacci, P.; Marchi, M. *J. Comput. Chem.* **2003**, *24*(2), 129–142.

[129] Guarnetti-Prandi, I.; Viani, L.; Andreussi, O.; Mennucci, B. *J. Comput. Chem.* **2015**, *37*(11), 981–991.

[130] Wang, J.; Cieplak, P.; Li, J.; Hou, T.; Luo, R.; Duan, Y. *J. Phys. Chem. B* **2011**, *115*(12), 3091–9.

[131] Jurinovich, S.; Curutchet, C.; Mennucci, B. *ChemPhysChem* **2014**, *15*(15), 3194–3204.

[132] Novoderezhkin, V. I.; Rutkauskas, D.; van Grondelle, R. *Biophys. J.* **2006**, *90*(8), 2890–2902.

[133] Novoderezhkin, V. I.; Cohen Stuart, T. A.; van Grondelle, R. *J. Phys. Chem. A* **2011**, *115*(16), 3834–44.

[134] Scholes, G. D. *Annu. Rev. Phys. Chem.* **2003**, *54*(18), 57–87.

[135] Chung, L. W.; Hirao, H.; Li, X.; Morokuma, K. *Wiley Interdiscip. Rev. Comput. Mol. Sci.* **2011**, *2*(2), 327–350.

[136] Scholes, G. D.; Fleming, G. R. *J. Phys. Chem. B* **2000**, *104*(8), 1854–1868.

[137] Ghigo, G.; Roos, B. O.; Malmqvist, P. *Chem. Phys. Lett.* **2004**, *396*(1 - 3), 142 – 149.

[138] Forsberg, N.; Malmqvist, P. *Chem. Phys. Lett.* **1997**, *274*(1), 196 – 204.

[139] Antón, J.; Oren, A.; Benlloch, S.; Rodríguez-Valera, F.; Amann, R.; Rosselló-Mora, R. *International Journal of Systematic and Evolutionary Microbiology* **2002**, *52*(2), 485–491.

[140] Lutnaes, B. F.; Oren, A.; Liaaen-Jensen, S. *Journal of Natural Products* **2002**, *65*(9), 1340–1343.

[141] Koyama, Y.; Rondonuwu, F. S.; Fujii, R.; Watanabe, Y. *Biopolymers* **2004**, *74*(1-2), 2–18.

[142] Gradinaru, C. C.; Kennis, J. T. M.; Papagiannakis, E.; van Stokkum, I. H. M.; Cogdell, R. J.; Fleming, G. R.; Niederman, R. A.; van Grondelle, R. *Proceedings of the National Academy of Sciences* **2001**, *98*(5), 2364–2369.

[143] Mathies, R. A.; Lin, S. W.; Ames, J. B.; Polland, W. T. *Annual Review of Biophysics and Biophysical Chemistry* **1991**, *20*(1), 491–518.

[144] Luecke, H.; Schobert, B.; Stagno, J.; Imasheva, E. S.; Wang, J. M.; Balashov, S. P.; Lanyi, J. K. *Proceedings of the National Academy of Sciences* **2008**, *105*(43), 16561–16565.

[145] Balashov, S. P.; Imasheva, E. S.; Wang, J. M.; Lanyi, J. K. *Biophysical Journal* **2008**, *95*(5), 2402 – 2414.

[146] Balashov, S. P.; Imasheva, E. S.; Boichenko, V. A.; Antón, J.; Wang, J. M.; Lanyi, J. K. *Science* **2005**, *309*(5743), 2061–2064.

[147] Boichenko, V. A.; Wang, J. M.; Antón, J.; Lanyi, J. K.; Balashov, S. P. *Biochimica et Biophysica Acta (BBA) - Bioenergetics* **2006**, *1757*(12), 1649 – 1656.

[148] Zhu, J.; Gdor, I.; Smolensky, E.; Friedman, N.; Sheves, M.; Ruhman, S. *The Journal of Physical Chemistry B* **2010**, *114*(8), 3038–3045.

[149] Polívka, T.; Balashov, S. P.; Chábera, P.; Imasheva, E. S.; Yartsev, A.; Sundström, V.; Lanyi, J. K. *Biophysical Journal* **2009**, *96*(6), 2268 – 2277.

[150] Christensson, N.; Milota, F.; Nemeth, A.; Sperling, J.; Kauffmann, H. F.; Pullerits, T.; Hauer, J. *The Journal of Physical Chemistry B* **2009**, *113*(51), 16409–16419.

[151] Perlík, V.; Seibt, J.; Cranston, L. J.; Cogdell, R. J.; Lincoln, C. N.; Savolainen, J.; Šanda, F.; Mančal, T.; Hauer, J. *The Journal of Chemical Physics* **2015**, *142*(21), 212434.

[152] Hasson, K. C.; Gai, F.; Anfinrud, P. A. *Proceedings of the National Academy of Sciences* **1996**, *93*(26), 15124–15129.

[153] Polli, D.; Altoè, P.; Weingart, O.; Spillane, K. M.; Manzoni, C.; Brida, D.; Tomasello, G.; Orlandi, G.; Kukura, P.; Mathies, R. A.; Garavelli, M.; Cerullo, G. sep **2010**, *467*(7314), 440–443.

[154] Nenov, A.; Borrego-Varillas, R.; Oriana, A.; Ganzer, L.; Segatta, F.; Conti, I.; Segarra-Marti, J.; Omachi, J.; Dapor, M.; Taioli, S.; Manzoni, C.; Mukamel, S.; Cerullo, G.; Garavelli, M. mar **2018**, pages 1534–1541.

[155] In *Molecular Switches;* Wiley-VCH Verlag GmbH & Co. KGaA, 2011; pages I–XXXI.

[156] Ikeda, T.; Tsutsumi, O. *Science* **1995**, *268*(5219), 1873–1875.

[157] Renner, C.; Moroder, L. *ChemBioChem* **2006**, *7*(6), 868–878.

[158] Flint, D. G.; Kumita, J. R.; Smart, O. S.; Woolley, G. *Chemistry & Biology* **2002**, *9*(3), 391–397.

[159] Sporlein, S.; Carstens, H.; Satzger, H.; Renner, C.; Behrendt, R.; Moroder, L.; Tavan, P.; Zinth, W.; Wachtveitl, J. *Proceedings of the National Academy of Sciences* **2002**, *99*(12), 7998–8002.

[160] Mahimwalla, Z.; Yager, K. G.; ichi Mamiya, J.; Shishido, A.; Priimagi, A.; Barrett, C. J. *Polymer Bulletin* **2012**, *69*(8), 967–1006.

[161] Rau, H.; Lueddecke, E. *Journal of the American Chemical Society* **1982**, *104*(6), 1616–1620.

[162] Rau, H. *Photoisomerization of benzenes. In Photoreactive Organic Thin Films;* Academic Press: Boston, 2002.

[163] Cho, J.; Berbil-Bautista, L.; Levy, N.; Poulsen, D.; Fréchet, J. M. J.; Crommie, M. F. *The Journal of Chemical Physics* **2010**, *133*(23), 234707.

[164] Pechenezhskiy, I. V.; Cho, J.; Nguyen, G. D.; Berbil-Bautista, L.; Giles, B. L.; Poulsen, D. A.; Fréchet, J. M. J.; Crommie, M. F. *The Journal of Physical Chemistry C* **2011**, *116*(1), 1052–1055.

[165] Bandara, H. M. D.; Burdette, S. C. *Chem. Soc. Rev.* **2012**, *41*(5), 1809–1825.

[166] Lednev, I. K.; Ye, T.-Q.; Hester, R. E.; Moore, J. N. *The Journal of Physical Chemistry* **1996**, *100*(32), 13338–13341.

[167] Lednev, I.; Ye, T.-Q.; Matousek, P.; Towrie, M.; Foggi, P.; Neuwahl, F.; Umapathy, S.; Hester, R.; Moore, J. *Chemical Physics Letters* **1998**, *290*(1-3), 68–74.

[168] Fujino, T.; Tahara, T. *The Journal of Physical Chemistry A* **2000**, *104*(18), 4203–4210.

[169] Fujino, T.; Arzhantsev, S. Y.; Tahara, T. *The Journal of Physical Chemistry A* **2001**, *105*(35), 8123–8129.

[170] Fujino, T.; Arzhantsev, S. Y.; Tahara, T. *Bulletin of the Chemical Society of Japan* **2002**, *75*(5), 1031–1040.

[171] Satzger, H.; Root, C.; Braun, M. *The Journal of Physical Chemistry A* **2004**, *108*(30), 6265–6271.

[172] Nägele, T.; Hoche, R.; Zinth, W.; Wachtveitl, J. *Chemical Physics Letters* **1997**, *272*(5-6), 489–495.

[173] Satzger, H.; Spörlein, S.; Root, C.; Wachtveitl, J.; Zinth, W.; Gilch, P. *Chemical Physics Letters* **2003**, *372*(1-2), 216–223.

[174] Schultz, T.; Quenneville, J.; Levine, B.; Toniolo, A.; Martínez, T. J.; Lochbrunner, S.; Schmitt, M.; Shaffer, J. P.; Zgierski, M. Z.; Stolow, A. *Journal of the American Chemical Society* **2003**, *125*(27), 8098–8099.

[175] Stuart, C. M.; Frontiera, R. R.; Mathies, R. A. *The Journal of Physical Chemistry A* **2007**, *111*(48), 12072–12080.

[176] Kim, Y.; Phillips, J. A.; Liu, H.; Kang, H.; Tan, W. *Proceedings of the National Academy of Sciences* **2009**, *106*(16), 6489–6494.

[177] Quick, M.; Dobryakov, A. L.; Gerecke, M.; Richter, C.; Berndt, F.; Ioffe, I. N.; Granovsky, A. A.; Mahrwald, R.; Ernsting, N. P.; Kovalenko, S. A. *The Journal of Physical Chemistry B* **2014**, *118*(29), 8756–8771.

[178] Monti, S.; Orlandi, G.; Palmieri, P. *Chemical Physics* **1982**, *71*(1), 87–99.

[179] Ishikawa, T.; Noro, T.; Shoda, T. *The Journal of Chemical Physics* **2001**, *115*(16), 7503–7512.

[180] Conti, I.; Garavelli, M.; Orlandi, G. *Journal of the American Chemical Society* **2008**, *130*(15), 5216–5230.

[181] Casellas, J.; Bearpark, M. J.; Reguero, M. *ChemPhysChem* **2016**, *17*(19), 3068–3079.

[182] Harabuchi, Y.; Ishii, M.; Nakayama, A.; Noro, T.; Taketsugu, T. *The Journal of Chemical Physics* **2013**, *138*(6), 064305.

[183] Tan, E. M. M.; Amirjalayer, S.; Smolarek, S.; Vdovin, A.; Zerbetto, F.; Buma, W. J. *Nature Communications* **2015**, *6*, 5860.

[184] Ootani, Y.; Satoh, K.; Nakayama, A.; Noro, T.; Taketsugu, T. *The Journal of Chemical Physics* **2009**, *131*(19), 194306.

[185] Yuan, S.; Dou, Y.; Wu, W.; Hu, Y.; Zhao, J. *The Journal of Physical Chemistry A* **2008**, *112*(51), 13326–13334.

[186] Tiberio, G.; Muccioli, L.; Berardi, R.; Zannoni, C. *ChemPhysChem* **2010**, *11*(5), 1018–1028.

[187] Cembran, A.; Bernardi, F.; Garavelli, M.; Gagliardi, L.; Orlandi, G. *Journal of the American Chemical Society* **2004**, *126*(10), 3234–3243.

[188] Altoè, P.; Bernardi, F.; Conti, I.; Garavelli, M.; Negri, F.; Orlandi, G. *Theoretical Chemistry Accounts* **2006**, *117*(5-6), 1041–1059.

[189] Conti, I.; Marchioni, F.; Credi, A.; Orlandi, G.; Rosini, G.; Garavelli, M. *Journal of the American Chemical Society* **2007**, *129*(11), 3198–3210.

[190] Böckmann, M.; Doltsinis, N.; Marx, D. *Angewandte Chemie International Edition* **2010**, *49*(19), 3382–3384.

[191] Moreno, M.; Gelabert, R.; Lluch, J. M. *ChemPhysChem* **2016**, *17*(18), 2824–2838.

[192] van Stokkum, I. H.; Larsen, D. S.; van Grondelle, R. *Biochimica et Biophysica Acta (BBA) - Bioenergetics* **2004**, *1657*(2-3), 82–104.

[193] Snellenburg, J. J.; Laptenok, S. P.; Seger, R.; Mullen, K. M.; van Stokkum, I. H. M. *Journal of Statistical Software* **2012**, *49*(3).

[194] Dyck, R. H.; McClure, D. S. *The Journal of Chemical Physics* **1962**, *36*(9), 2326–2345.